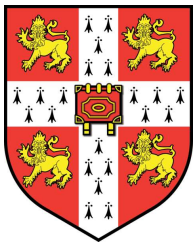
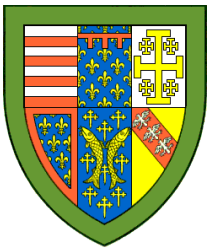

UNIVERSITY OF CAMBRIDGE

INSTITUTE OF ASTRONOMY

A DISSERTATION SUBMITTED TO THE

UNIVERSITY OF CAMBRIDGE FOR THE DEGREE

OF DOCTOR OF PHILOSOPHY

SPATIALLY-RESOLVED STUDIES OF NEARBY STAR-FORMING GALAXIES

NIMISHA KUMARI

QUEENS' COLLEGE

Submitted to the Board of Graduate Studies

April 25, 2018

SUPERVISIORS:

PROF. MICHAEL J. IRWIN & DR. BETHAN L. JAMES

SPATIALLY-RESOLVED STUDIES OF NEARBY STAR-FORMING GALAXIES

NIMISHA KUMARI

SUMMARY

Spatially-resolved studies of nearby star-forming galaxies are essential to understand various physical and chemical phenomena at play in the interstellar medium in the galaxies, and consequently to obtain a comprehensive picture of galaxy formation and evolution. In this thesis, I perform spatially-resolved analyses of chemical abundances and star-formation in nearby star-forming galaxies – blue compact dwarf galaxies (BCDs) and spiral galaxies.

I map various properties of H II regions and the surrounding gas within three BCDs, using integral field spectroscopic (IFS) data from the Gemini Multi-Object Spectrograph-North. While answering questions related to chemical homogeneity, ionisation mechanisms and stellar populations within BCDs, I address more profound issues, which go beyond the characterisation of studied BCDs and aim to explain global phenomena with broader implications.

The BCD NGC 4449 hosts a metal-poor central star-forming region, which I explain by various scenarios related to the interplay between star-formation, metal-distribution and gas-dynamics within galaxies. The BCD NGC 4670 shows an unusual negative relationship between the nitrogen-to-oxygen ratio and oxygen abundance at spatially-resolved scales. I explore this relation with chemical evolution models and by comparison to other star-forming galaxies and suggest that nitrogen enrichment, variations in star-formation efficiency or hydrodynamical effects may be responsible for the observed relation. For another BCD, SBS 1415+437, the spatially-resolved abundances on average agree with the integrated abundance, implying that low-redshift spatially-resolved results may be directly compared with unresolved high-redshift results.

I study spiral galaxies to address long-standing issues related to the reliability of metallicity calibrators and the Schmidt Law of star-formation. Using IFS data of twenty-four spiral galaxies taken with the Multi-Unit Spectroscopic Explorer, I find that the current strong-line metallicity calibrators for H II regions are unsuitable for regions dominated by diffuse ionised gas (DIG). I devise new recipes for estimating the metal-content of the DIG. For another set of nine spiral galaxies, I use multi-wavelength data to show that the spatially-resolved Schmidt relation is very sensitive to the consideration of diffuse background, which is a component unrelated to the current star-formation. Removal of this component from the SFR tracers and the atomic gas results in similar local and global Schmidt relation.

To conclude, the spatially-resolved analyses presented in this thesis have led to discoveries and further questions, which I will address in my ongoing and future works.

Whence this creation has arisen
- perhaps it formed itself, or perhaps it did not -
the One who looks down on it,
in the highest heaven, only He knows
or perhaps even He does not know.

Rig Veda: Nasadiya Sukta *(Hymn of Creation)*
(as translated by Wendy Doniger O'Flaherty)

Dedicated to Nani & Dadi (my grandmothers),
whose struggles always inspire me never to give up!

Contents

DECLARATION OF ORIGINALITY

I, Nimisha Kumari, declare that the work presented in this thesis entitled *'Spatially-resolved studies of nearby star-forming galaxies',* was done wholly while in candidature for a PhD degree at the University of Cambridge, and that this thesis has not previously been submitted for a degree or any other qualification at this University or any other institution. The parts of this thesis based on academic papers are as follows:

- **Chapter 3**
  'A GMOS-N IFU study of the central H II *region in the blue compact dwarf galaxy NGC 4449: Kinematics, Nebular Metallicity and Star-Formation'*
  Kumari, N., James, B., Irwin, M. T, 2017, MNRAS, **470,** 4618

- **Chapter 4**
  'O/H-N/O: the curious case of NGC 4670'
  Kumari, N., James, B., Irwin, M., Amorin, R, Perez-Montero, E., 2018, MNRAS, **476,** 3793

- **Chapter 5**
  'Small-scale chemical abundance analysis in a blue compact dwarf galaxy SBS1415+437'
  Kumari, N., James, B., Irwin, M., Aloisi, A., 2018, MNRAS, to be submitted

- **Chapter 6**
  'Metallicity calibrations for diffuse ionised gas'
  Kumari, N., Maiolino, R., Belfiore, F., 2018, MNRAS, in preparation

- **Chapter 7**
  'A spatially-resolved star-formation study in nearby spiral galaxies'
  Kumari, N., Irwin, M., James, B., 2018, A&A, submitted

I confirm that this thesis is the result of my own research and contains nothing resulting from collaboration, except where explicitly noted. B. James provided the GMOS-IFU data analysed in Chapters 2, 3, 4 and 5. For Fig 4.22, R. Amorin provided the SDSS data and Green Pea galaxies data and F. Vincenzo shared his chemical evolution models. The voronoi binned maps used in Chapter 6 were provided by F. Belfiore. For the work in Chapter 7, R. Kennicutt made data from KINGFISH survey accessible, and M. Irwin provided the images processed by Nebuliser and the best-fit coefficients for Fig 7.14. All other data used in this thesis are public and their sources are cited in respective chapters. The published works incorporate the comments of co-authors. This thesis does not exceed the word limit of 60,000 words.

Nimisha Kumari
April 25, 2018

ACKNOWLEDGEMENTS

Forever I will remain indebted to Mike Irwin for rescuing me at the end of the first year of my PhD and taking me under his wings. A huge thanks to both my supervisors - Mike Irwin and Bethan James - I am very grateful for the training you provided me over the past two and a half years, which will serve me my entire scientific, professional and personal life.

Thanks to all collaborators, members and visitors of the IoA/Kavli, including Roberto Maiolino, Ricardo Amorín, Enrique Pérez-Montero, José Vilchez, Nikku Madhusudhan, Vasily Belokurov, Paul Hewett, Cathie Clarke, Sally Oey, Matt Auger, Alessandra Aloisi, Rob Kennicutt and Extragalactic group members.

Thanks to the college support from Dr Lawrence Tiley, Richard Geddis, Emma Dellar and Dr James Kelly. Thanks to Dr Anil Seal and the Nehru Trust for Cambridge University. Thanks to the IoA support staff - Roderick Johnstone and IT team, Debbie Peterson, Margaret Harding, Joy McSharry, Mark Hurn, Mandy Cockrill, Judith Moss and Emma Hyde.

Thanks to my officemates and classmates particularly Matt Read, Keith Hawkins, Anjali Piette, Luca Matrá, Sebastián Marino, Harley Katz, Bjoern Soergel, Dominika Boneberg and Clare Wethers. Thanks to my students.

Thanks to all friends, specially Darshana Joshi, Aditya Sadhanala, Sapna Shekhar, Swati Bhabhi, Clotilde Laigle, Amal Marogy, Rosalie Moloney, Arindam Biswas, Mukesh Kumar, Megha Agrawal, Florent Brach, Vijay Venugopalan and Fiona Rosette.

Thanks to Rita Chandra Ma'am, and the Miranda House's friends and team. Thanks to Pihu, Noah and other children of the SCA. Thanks to my family - Maa, Papa and Chotu - for an unconditional and everlasting love.

Thanks to everybody who have touched my life - thank you all for everything!

– Nimisha

List of Figures

List of Tables

1 Introduction

1.1 Star-Forming Galaxies

A fundamental goal of human knowledge has been to understand cosmic evolution – "How did the Universe start and evolve?" The Universe was relatively simpler when it was formed. Approximately a billion years after the Big Bang, the first stars and galaxies formed. The star formation rate density peaked at z≈1.9 and then declined exponentially in later times (see Figure 1.1), influencing the physical and chemical state of the Universe, which now hosts a variety of morphologically different galaxies, some actively forming stars, others quiescent. Hence, an approach to understanding our cosmic origin is to study galaxies throughout the cosmic history. However, galaxies in the high-redshift Universe cannot be studied in great detail using present technology. Fortunately, we can characterise the properties of different star-forming galaxies found in the nearby Universe in great spatial details, allowing us to probe and predict the properties of the galaxies that can be measured in a distant or younger Universe. This concept forms the basis of this thesis on the "Spatially-resolved studies of nearby star-forming galaxies".

Star-forming galaxies differ from their non-star-forming counterparts in properties like morphology, luminosity, mass, colour, stellar populations and gas content. The spectra of star-forming galaxies are characterised by strong emission lines while the spectra of non-star-forming galaxies are characterised by absorption features as shown in Figure 1.2. Even star-forming

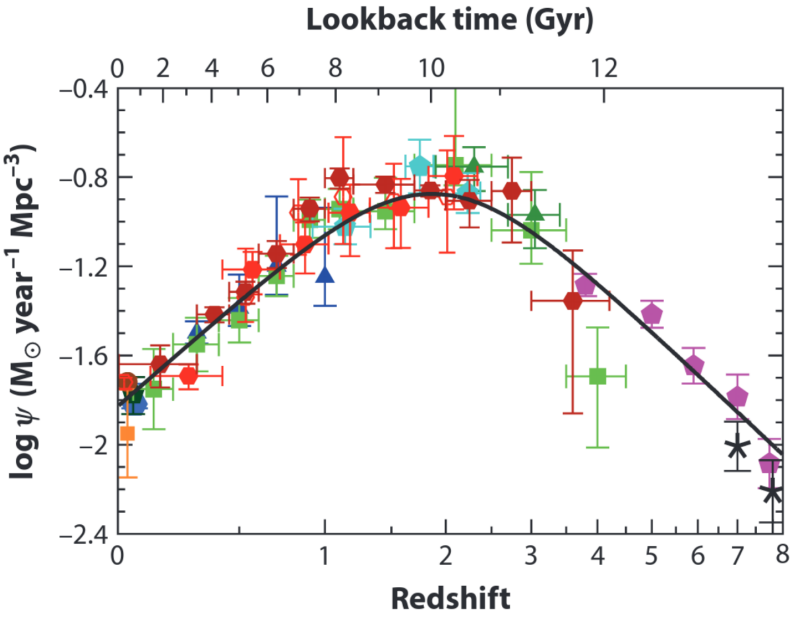

Figure 1.1 – The history of cosmic star formation, showing the star-formation rate per unit volume as a function of redshift (and thus the lookback time in Gyr). The data points include the far-ultraviolet and infrared rest-frame measurements compiled from various studies (See Table 1 of Madau & Dickinson (2014) for the bibliographic references and details of these data points). The solid black curve denotes the best-fit star-formation rate density as a function of redshift. Figure adapted from Madau & Dickinson (2014).

galaxies differ from each other and hence are classified in various sub-groups. This thesis involves the analysis of two types of star-forming galaxies: spiral galaxies and blue compact dwarf galaxies (BCDs). Figure 1.3 shows example images of spiral and blue compact dwarf galaxies. These objects are briefly introduced in the following sub-sections.

1.1.1 Spiral Galaxies

Spiral galaxies are the most common type of star-forming galaxy found in the nearby Universe. Spiral galaxies generally host a supermassive black hole at the centre of a central bulge of mostly old stellar populations, surrounded by a flat rotating disc of young stellar populations, along with a halo of stars and a dark matter halo. For example, the Milky Way (MW) hosts a supermassive black hole Sagittarius A* ($\sim 4.1 \times 10^6$ M$_\odot$), with a central bulge ($\sim 2 \times 10^{10}$ M$_\odot$, $\sim 3 \times 10^9$ L$_\odot$) containing stars of ages $\gtrsim$ 10 Gyr (Minniti & Zoccali, 2008; Freeman & Bland-Hawthorn, 2002), the disc ($\sim 4 \times 10^{10}$ M$_\odot$, $\sim 2 \times 10^{10}$ L$_\odot$) containing metal-rich stars younger than 10 Gyr (Freeman & Bland-Hawthorn, 2002), and the halo ($\sim 1 \times 10^9$ M$_\odot$, $\sim 10^9$ L$_\odot$) containing some of the oldest objects in the Universe, the Globular Clusters, and some of the most metal-poor stars known. Spiral galaxies were first described in "The Realm of Nebulae" (Hubble, 1936) by Edwin Hubble, who classified galaxies with spiral structures into two broad

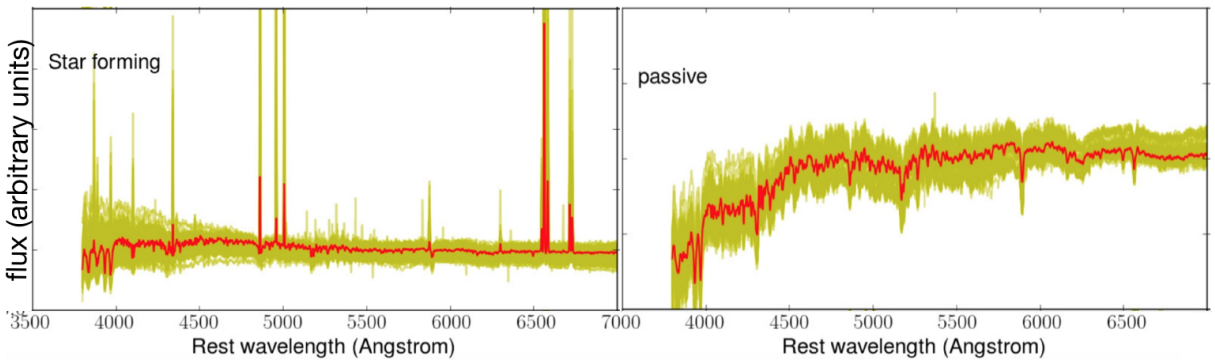

Figure 1.2 – Composite spectra of star-forming (left panel) and passive (right panel) galaxies from the fourth data release of Large Sky Area Multi-Object Fibre Spectroscopic Telescope (LAMOST). Figure adapted from Wang et al. (2018).

Figure 1.3 – Left: Spiral galaxy NGC 5055, image credit & copyright: data - Subaru Telescope, Hubble Legacy Archive, processing: Robert Gendler, Roberto Colombari, Don Goldman. Right: Blue Compact Dwarf galaxy NGC 4449, credit: data - Hubble Legacy Archive, ESA, NASA, processing: Robert Gendler. Figures taken from the website: "Astronomy Picture of the Day".

categories, barred spirals and (unbarred/normal) spirals depending on the presence/absence of a linear central bar-shaped band of stars. In the Hubble classification scheme, normal spirals are listed as "S" and barred spirals as "SB". In this notation, both "S" and "SB" are followed by letters a, b, c where "a" indicates a large bulge and tight arms, "c" indicates a small bulge and loose arms, and "b" indicates a morphology lying between these two extremes. A fourth class of spiral galaxy was introduced by de Vaucouleurs which accounted for spirals with fragmented loose arms in both barred (SBd) and normal spirals (Sd). Our Milky Way is classified as an SBb galaxy. Most spiral galaxies host older stellar populations and high metallicity gas in the centre, with a gradient in their distributions (stellar population and metallicity) towards the outer regions (see e.g. Bell & de Jong, 2000). For example, the nearby spiral galaxy NGC 0628 shows a negative metallicity gradient with a gas-phase metallicity of $12 + \log(\mathrm{O/H}) = 8.43$ in its central region (Berg et al., 2013), which is equivalent to $\sim 0.7(\mathrm{O/H})_{\odot}$, assuming $12 + \log(\mathrm{O/H})_{\odot} = 8.69$ (Asplund et al., 2009).

1.1.2 Blue Compact Dwarf Galaxies

Blue compact dwarf galaxies are nearby, metal-deficient ($\sim$1/40–1/3 $Z_\odot$) star-forming systems (see Kunth & Östlin, 2000, for a review), first described by Sargent & Searle (1970) and Searle & Sargent (1972a). Their definition was first formally given by Thuan & Martin (1981) on the basis of low luminosity ($M_B \geq$ -18), compactness (small optical diameter $D_{25} < 1$ kpc) and the presence of strong narrow emission lines on a blue continuum. However, these criteria have been revised in subsequent studies (see, e.g. Gil de Paz, Madore & Pevunova, 2003; Ann, Seo & Ha, 2015), and, as such, there is no unique definition of BCDs in the literature. BCDs are therefore sometimes confused with "H II galaxies", a class of emission line galaxies which also include high-metallicity objects with spiral structures (Thuan, 2008). Though BCDs have recent bursts of star-formation, they also host older stellar populations. Hence they are not the young star-forming systems as first thought. Due to their high star-formation activity and chemically unevolved nature and proximity, BCDs are excellent local analogues of high-redshift galaxies and hence provide ideal laboratories for probing the high-redshift Universe.

1.2 Interstellar Medium

To carry out spatially-resolved studies of star-forming galaxies, one needs to characterise the interstellar medium (ISM) between the stars in galaxies, which constitutes matter as well as radiation. This matter is comprised of gas and dust, while the radiation is produced by both stars and interstellar matter and is known as the interstellar radiation field (ISRF). Field, Goldsmith & Habing (1969) proposed that the ISM was occupied by gas in two thermally stable static phases, which coexisted in pressure equilibrium, one at T = 10^4 K and the other at T = 300 K. Cox & Smith (1974) suggested the idea of a hot phase ($10^{5.5}$ K) in the ISM as the result of supernovae explosions. Combining the two-phase model with the supernovae-generated hot phase model, McKee & Ostriker (1977) proposed a three-phase model of the ISM consisting of cold, warm and hot gas.

In the subsequent sections, I discuss the currently-accepted characteristic phases of the ISM, and the tracers and techniques used to characterise it.

1.2.1 Phases/Constituents of the ISM

This section describes different phases/constituents of the ISM, along with the observational probes used to trace them. The temperatures and densities of different phases mentioned below are taken from Draine (2011) and may vary slightly from other bibliographic sources.

- **H II gas** is photoionised gas with a density of $\sim$0.1–10^4 cm^{-3} and is observed by optical emission lines and thermal radio continuum. It exists in two forms: dense gas in H II

regions and lower density diffuse ionised gas (DIG). The H II region (also referred to as diffuse emission nebula), is the photoionised hydrogen (H^+) associated with active star-formation. In a typical star-forming region, young and hot massive O/B stars emitting mostly in the far-ultraviolet (FUV) ionise the gas around them, thereby creating an H II region. However, photoionisation may also take place from the radiation of older stellar populations, which leads to DIG, also referred to as the warm ionised medium (WIM).

- **Neutral Atomic gas** is found in two forms: cool H I and warm H I. Cool H I (often referred to as the cold neutral medium, CNM) is at temperatures of $\approx$ 100 K and densities of $\approx$ 30 cm^{-3}. Only $\sim$1% of the volume of the local ISM is filled with the CNM. On the other hand, a large volumetric fraction of $\sim$ 40% of the ISM is filled up with warm H I (often referred to as the warm neutral medium, WNM). It is also neutral atomic gas but at higher temperatures of T $\approx 10^{3.7}$ K and lower densities $\approx$ 0.6 cm^{-3}. Both CNM and WNM are traced by H I 21 cm emission and absorption lines, and optical and UV absorption lines.

- **Molecular gas** can be sub-divided into dense and diffuse molecular gas based on temperature and density. Dense molecular gas is the gravitationally bound component of the ISM, which is cold ($\approx$ 10–50 K) and dense ($\approx 10^3$–10^6 cm^{-3}) and hence, provides sites for star-formation. It fills only $\approx$ 0.01% of the volume of the ISM and is mainly traced by CO 2.6 mm emission, HCN or far infrared emission. Compared to the dense molecular gas, diffuse molecular gas has a lower density ($\approx$ 100 cm^{-3}) with temperatures of $\approx$ 50 K. It fills $\sim$ 0.1% of the volume of the ISM. It is traced by H I 21 cm emission and absorption lines, CO 2.6 mm emission, and optical and ultraviolet (UV) absorption lines.

- Other thermal phases: Approximately 50% of the volume of the ISM is composed of hot ionised medium (HIM) coronal gas at very high temperatures T $\geq 10^{5.5}$ K and low densities $\sim$ 0.004 cm^{-3}. The HIM is produced by supernovae blast waves and can be traced by UV and x-ray emission, and radio synchrotron emission.

- **Interstellar Dust** is another important constituent of the ISM, which decreases the intensity of the observed starlight. Depending on the geometry of the dust and the light source, a decrease in starlight is termed as either extinction or attenuation (see Calzetti, 2013, for details). We generally make use of extinction curves/reddening laws to correct for dust extinction and determine the intrinsic starlight at a given wavelength. Some examples of reddening laws are given in Figure 1.4, where $k_\lambda = A_\lambda/E(B\text{-}V)$, i.e. extinction A_λ at a given wavelength relative to the reddening E(B-V). The effects of dust can also be taken into account by observing the dust-obscured systems in the infrared. This approach has been adopted in Chapter 7 and is described in detail there.

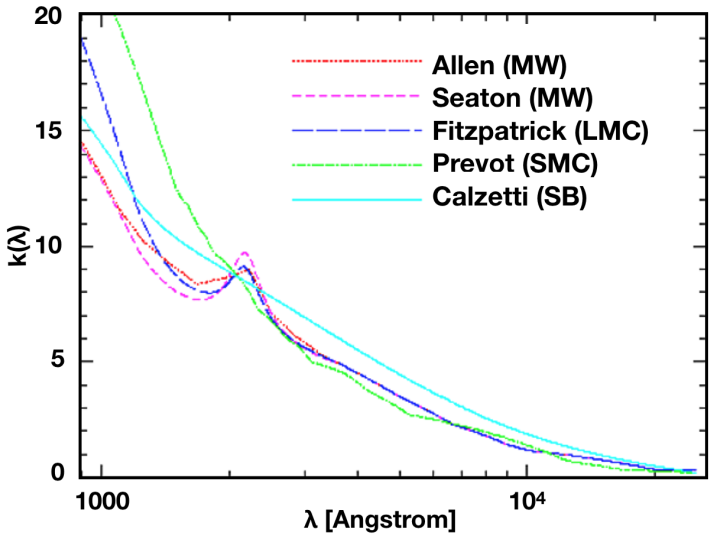

Figure 1.4 – Reddening laws for the Milky Way (Allen, 1976; Seaton, 1979), the Large Magellanic Cloud (Fitzpatrick, 1986), the Small Magellanic cloud (Prevot et al., 1984) and the starbursts (Calzetti et al., 2000). Figure adapted from the website: http://webast.ast.obs-mip.fr/hyperz/hyperz_manual1/node10.html

1.2.2 Ionised gas: Emission Line Spectroscopy

Emission line spectroscopy is a powerful tool in characterising the ionised phase of the ISM, because emission lines provide a wealth of information about the source from which they emanate, such as temperature, density, star-formation activity and chemical abundances. In this thesis, emission line spectroscopy is extensively used to study chemical properties of the star-forming regions (also known as the H II regions). I have also used the Hα emission line to deduce the kinematic and stellar properties which will be discussed in the relevant sections in Chapters 3, 4 and 5. In this Section, I mainly focus on showing how the chemical abundances of H II regions can be derived using emission line spectroscopy.

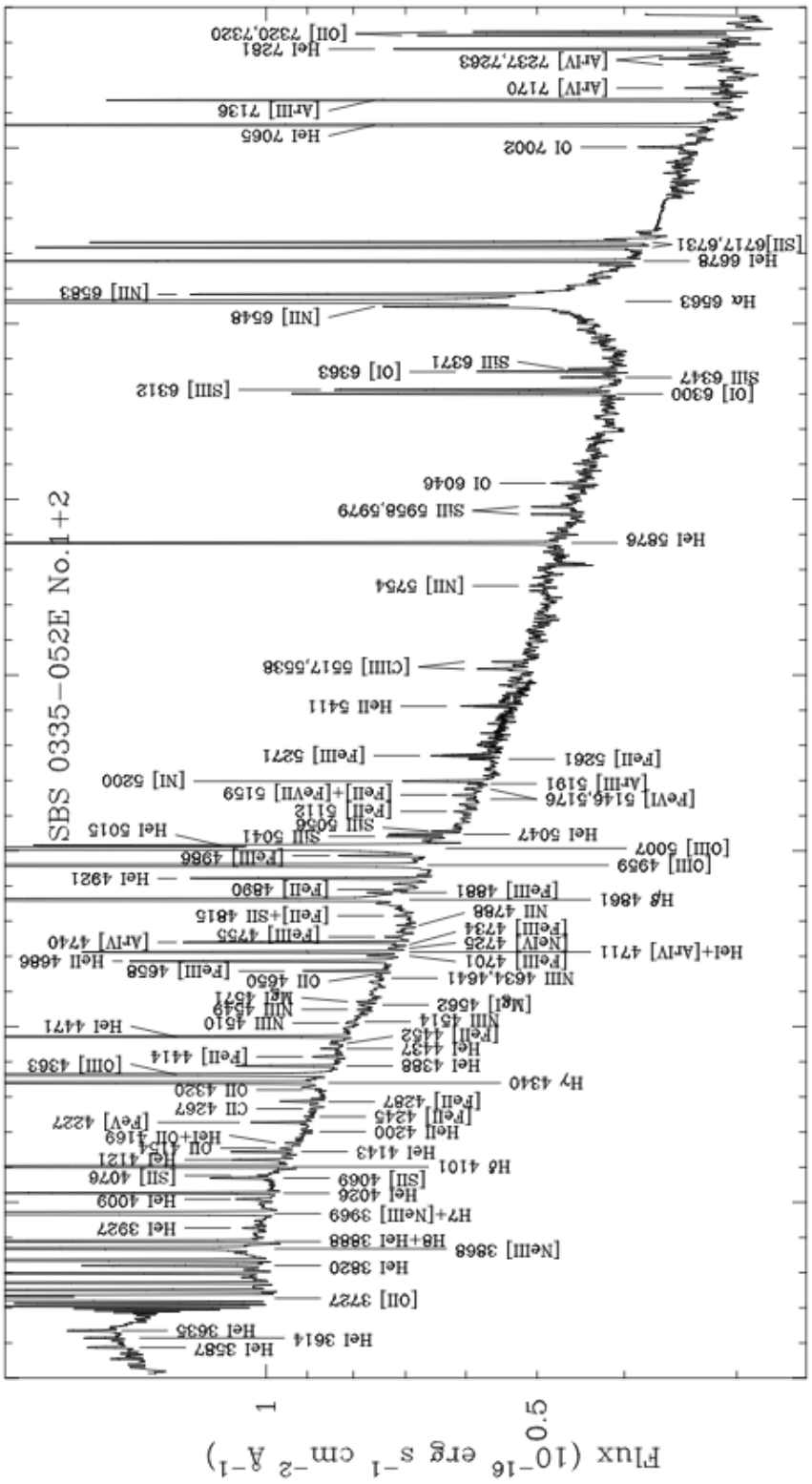

Figure 1.5 – Spectrum of BCD SBS 0335-052, showing a plethora of collisionally-excited lines (CELs) and recombination lines (RLs). Figure taken from Izotov et al. (2009).

Several physical processes occur in the ionised gas of the H II regions, which include photoionisation, recombination, heating, cooling, collisional excitation and fluorescence. Each of these processes help to maintain the local ionisation and thermal equilibrium of the ionised gas. Photoionisation, recombination and collisional excitation processes result in the production of emission lines, which are categorised as recombination lines (RLs) and collisionally excited lines (CELs). RLs are produced when ions capture free electron and emit photons while descending from higher energy levels to the lower ones. Some of the commonly used RLs are Balmer series lines (Hα λ6563, Hβ λ4860, Hγ λ4340), He I lines (He I $\lambda\lambda\lambda$4471, 5876, 6075) and He II λ4471. Examples of CELs include [O II] $\lambda\lambda$3727, 3729, [O III] $\lambda\lambda$4959, 5007, [N II] $\lambda\lambda$6548, 6584 and [S II] $\lambda\lambda$6717, 6731. CELs are produced when collisional excited atoms decay via radiative transitions. Figure 1.5 presents the spectrum of a metal-poor BCD SBS 0335-052 which shows a plethora of emission lines, with both RLs and CELs in the optical wavelength range. By combining the RLs and CELs, we can determine the physical conditions of the ionised gas, i.e. electron temperature (T_e) and density (N_e), also known as "nebular diagnostics". I describe some of the theory involved in the following subsections. The details of the concepts and methods discussed here can be found in the textbooks, e.g. Osterbrock & Ferland (2006a); Draine (2011) and tutorials, e.g. Peimbert, Peimbert & Delgado-Inglada (2017); Pérez-Montero (2017). The adopted notation follows the textbook Draine (2011), and are briefly summarised here:

- k: Boltzmann constant, h: Planck constant, c: Speed of light.
- ν: frequency, T: gas temperature.
- l and u denote the lower and upper levels in an energy transition, respectively, and n_l and n_u denote the level populations.
- E_{ul}: Energy involved in the transition from level u to l.
- A_{ul}: Einstein coefficient of spontaneous emission from level u to l.
- g_i: Degeneracy of level i.
- Ω_{lu}: Collision strength; note that $\Omega_{lu} = \Omega_{ul}$.
- C_{lu}: Collisional Excitation rate, k_{lu}: Rate-coefficient of collisional excitation

$$C_{lu} = k_{lu} N_e. \tag{1.1}$$

$$k_{lu} \propto \frac{1}{\sqrt{T}} \frac{\Omega_{lu}}{g_l} e^{-E_{ul}/kT}. \tag{1.2}$$

- j: Emissivity, the power radiated per unit frequency per unit solid angle per unit volume.

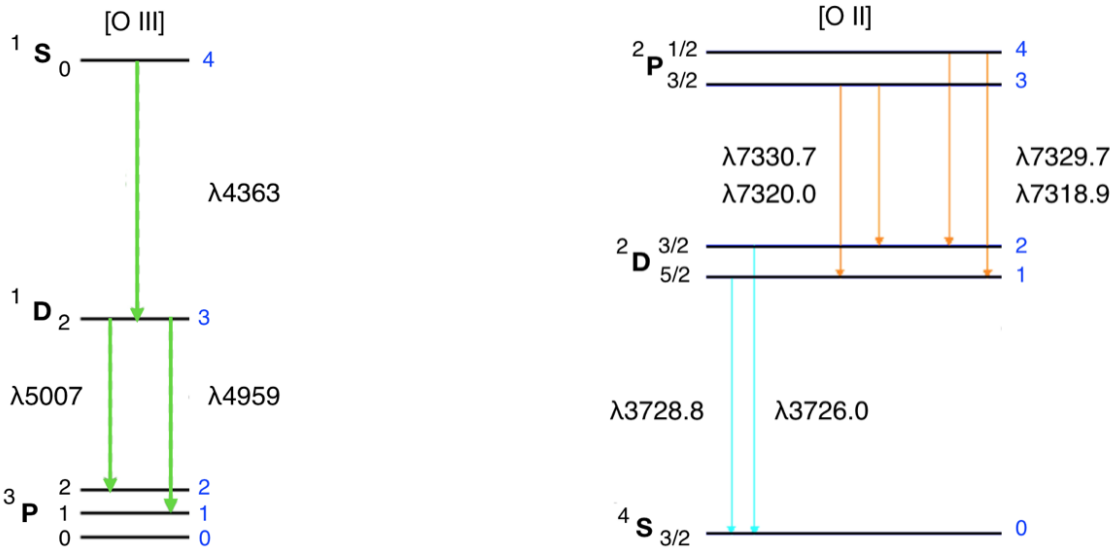

Figure 1.6 – Energy level diagrams of the temperature diagnostic ions, [O III] (left panel) and [O II] (right panel). On both panels, the numerals (0, 1, 2, 3, 4) in blue on the right-hand side are marked to simplify notations in the derivation of electron temperature (see text in Section 1.2.2.1).

- $n(X^{i+})$: Density of the ion (X^{i+}) that emits the line.
- I: Intensity of an emission line given by

$$I = \int j ds \tag{1.3}$$

where ds is the line-of-sight distance.

1.2.2.1 Electron Temperature & Density

An H II region has a complex structure. However, one may simply assume that it can be described with a single T_e and single N_e. In this thesis, I have assumed that the thermal structure of a H II region can be approximated by a three-zone model (Garnett, 1992). This model consists of a high-ionisation zone, a low-ionisation zone and an intermediate ionisation zone. The innermost high-ionisation zone corresponds to species such as O^{2+}, Ne^{2+}, Fe^{2+}, He^{+} and Ar^{3+}. The outermost low-ionisation zone corresponds to species such as O^{+}, N^{+} and S^{+}. The region between the two is the intermediate-ionisation zone and corresponds to species such as Ar^{2+} and S^{2+}. The electron temperature of each zone can be approximated from the temperature of one of the species related to that zone.

- **Electron temperature** can be determined using either CELs, RLs, a combination of an RL and a CEL (Peimbert & Peimbert, 2013), or from the Balmer continuum (Liu &

Danziger, 1993). The CELs that are used to determine T_e have two excited levels with an energy difference between them comparable to kT. As such, the population of these energy levels are sensitive to the temperature of the ionised gas. In this thesis, I have used two such combinations of CELs, the [O III] λ4363 / [O III] $\lambda\lambda$4959, 5007 line ratio and the [O II] $\lambda\lambda$7320, 7330 / [O II] $\lambda\lambda$3727, 3729 line ratio to determine the temperature of the high-excitation zone and the low-excitation zone of the ionised gas, respectively. The energy level diagrams of the two combinations are shown in Figure 1.6. On these diagrams, energy levels are marked in blue numerals (0, 1, 2, 3 and 4 going upwards) to simplify notation for the derivations presented below. For example, when we consider O III ion, E_{43} corresponds to the energy transition from level u = 4 to level l = 3, i.e. the [O III] λ4363 emission line.

Let us consider the O III ion (i.e. doubly ionised O^{2+}), whose energy diagram is shown in Figure 1.6 (left panel). In the low-density limit, when the density of the ionised gas is below the critical density of its excited levels (i.e. $^1D_2$ and $^1S_0$), every collisional excitation from the ground state ($^3P_0$) will be followed by radiative decays which will return the ion from the excited level to the ground level, with branching ratios that are determined by the Einstein coefficients. For example, the probability of a radiative transition from the excited state 4 to the lower level 3 is given by $A_{43}/(A_{41} + A_{43})$. Let the collisional excitation rate from the ground state to the excited levels 3 and 4 be C_{03} and C_{04} respectively. Then, the power radiated per unit volume in the transitions $4 \rightarrow 3$ and $3 \rightarrow 2$, is given by

$$P(4 \rightarrow 3) = E_{43}[n_0 C_{04}] \frac{A_{43}}{A_{41} + A_{43}}, \tag{1.4}$$

$$P(3 \rightarrow 2) = E_{32} \left[n_0 C_{03} + n_0 C_{04} \frac{A_{43}}{A_{41} + A_{43}} \right] \frac{A_{32}}{A_{32} + A_{31}}. \tag{1.5}$$

In the low-density limit (i.e. when $N_e \rightarrow 0$), substituting equations 1.1 and 1.2 into equations 1.4 and 1.5, the emissivity ratio can be expressed as:

$$\frac{j(4 \rightarrow 3)}{j(3 \rightarrow 2)} = \frac{A_{43} E_{43}}{A_{32} E_{32}} \frac{(A_{32} + A_{31}) \Omega_{04} e^{-E_{43}/kT}}{[(A_{41} + A_{43}) \Omega_{03} + A_{43} \Omega_{04} e^{-E_{43}/kT}]}. \tag{1.6}$$

The above ratio depends only on the atomic physics and the gas temperature. Since N_e is generally lower than the critical density of the excited levels ($\sim 10^5$ cm^{-3} and 10^7 cm^{-3} for $^1D_2$ and $^1S_0$, respectively), the assumption of the low-density limit in the above derivation holds in many ionised nebulae (e.g. $N_e \approx 3000$ cm^{-3} for the Orion nebula). Hence, the [O III] lines are useful in determining the temperature of the ionised gas. The

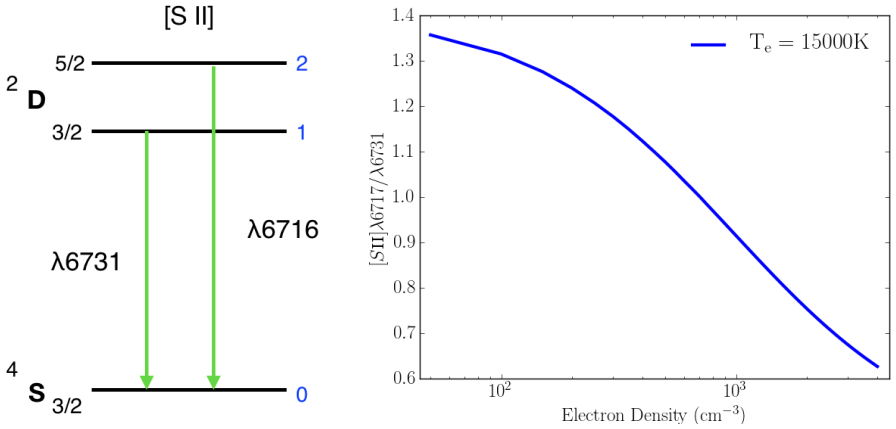

Figure 1.7 – Left panel: Energy level diagram of the density diagnostic ion S II. On this diagram, the numerals (0, 1, 2) in blue on the right-hand side are marked to simplify notations in the derivation of electron density (see text in Section 1.2.2.1). Right panel: [S II] emission line intensity ratio as a function of electron density N_e (at an electron temperature T_e = 15000 K) from Osterbrock & Ferland (2006b).

problem in using the CELs for temperature determination is that the auroral[1] lines (for example, here [O III] λ 4363 resulting from (4 $\rightarrow$ 3)) are very weak, and hence require deep observations to detect.

Let us now consider the O II ion (i.e. singly-ionised O^+), whose energy level diagram is shown in Figure 1.6 (right panel). In this case, the critical density for $^2D^0$ ($\sim 10^3$ cm^{-3}) is relatively low. Hence the [O II] $\lambda\lambda$7320, 7330 / [O II] $\lambda\lambda$3727, 3729 line ratio is sensitive to N_e, and is useful in determining T_e([O II]) only when the electron density is known. It is different from the case of T_e([O III]), for which electron density needs to be considered only when it is large.

The RLs, and the combination of an RL and a CEL are not useful for T_e determination, because RLs of heavy elements are even fainter than the auroral lines (e.g. [O III] λ4363, [N II] λ5755). The strong hydrogen RL cannot be used because it has a nearly homogeneous dependence on T_e (Peimbert, Peimbert & Delgado-Inglada, 2017).

- **Electron density** can also be determined by using the CELs and RLs. The CELs that are used to determine N_e have nearly the same excitation energy, so their intensity ratio does not depend on temperature. Some of the commonly used emission line ratios for determining N_e are [O II] λ3727/λ3729, [S II] λ6717/λ6731, [Cl III] λ5518/λ5538 and [Ar IV] λ4711/λ4740. Below, I describe the use of [S II] for determining N_e as I have used the S II ion in this thesis. Its energy level diagram is shown in Figure 1.7 (left panel), where energy levels are marked in blue numerals (0, 1, 2 going upwards). They

[1]Auroral lines are CELs, and are so called because they are also found in the spectrum of Earth's auroral emissions.

serve to simplify notations in the following derivation. For example, E_{20} corresponds to the energy transition from level $u = 2$ to level $l = 0$, i.e. the [S II] λ6717 emission line.

At low densities, the power radiated during the radiative decay from either of the excited levels ($^2D^0_{3/2}$, $^2D^0_{5/2}$) to the ground level ($^4S^0_{3/2}$) is proportional to the collision rates. Since the fine structure splitting is small ($E_{21} \ll E_{10}$, $E_{21} \ll kT$), the emissivity ratio of the two transitions can be expressed as:

$$\frac{j(2 \rightarrow 0)}{j(1 \rightarrow 0)} = \frac{\Omega_{20} E_{20}}{\Omega_{10} E_{10}} e^{-E_{21}/kT} \approx \frac{\Omega_{20}}{\Omega_{10}}. \tag{1.7}$$

At high densities, the emission lines are thermalised which results in an emissivity ratio:

$$\frac{j(2 \rightarrow 0)}{j(1 \rightarrow 0)} = \frac{g_2}{g_1} \frac{A_{20} E_{20}}{A_{10} E_{10}} e^{-E_{21}/kT} \approx \frac{g_2 A_{20}}{g_1 A_{10}}. \tag{1.8}$$

The lower and upper-density limits differ as shown in Figure 1.7 (right panel), which allows us to either estimate the N_e or establish an upper or lower limit from the line ratios of the doublets.

RLs like He I (Porter et al., 2013) and the lines of the multiplet 1 of O II (e.g. λ4649 relative to the sum of intensities of 8 multiplets, Peimbert & Peimbert, 2005; Storey, Sochi & Bastin, 2017) can also be used to determine N_e.

1.2.2.2 Chemical Abundances of Ionised Gas

Since oxygen is the third most abundant element after hydrogen and helium, its abundance is often used as a proxy for the total metallicity of the system and is expressed as 12 + log(O/H). As a reference, solar oxygen abundance = 12 + log(O/H)$_\odot$ = 8.69 (Asplund et al., 2009). Chemical abundances of the ionised gas (oxygen and other elements) may be determined from the CELs or the RLs. In this thesis, I have used CELs to determine abundances, from the 'direct' and 'indirect' methods, which are discussed below.

- **Direct Method:** This method involves the chemical abundance determination directly from electron temperature and densities (T_e and N_e), combined with the ratio of the intensities of a CEL to a Balmer line. In this thesis, I have used [O III] $\lambda\lambda$4959, 5007/Hβ to determine O^{++}/H^+ abundance and [O II] $\lambda\lambda$3727, 3729/Hβ or [O II] $\lambda\lambda$7320, 7330/Hβ to determine O^+/H^+ abundance. In the following, I show an example case of the physics behind the derivation of O^{++}/H^+ abundance using the intensity ratio of [O III] λ5007/Hβ.

  Following equation 1.3, in the low-density limit ($N_e < 10^4$ cm^{-3}), the intensity of [O III] λ5007 and Hβ are given by

$$I([O\textsc{iii}]) = \frac{1}{4\pi}\int n(O^{++})N_e k_{03} E_{32} \frac{A_{32}}{(A_{31}+A_{32})} ds, \tag{1.9}$$

$$I(H\beta) = \frac{1}{4\pi}\int n(H^{+})N_e \alpha_{eff,H\beta} h\nu_{H\beta}\, ds, \tag{1.10}$$

where $\alpha_{eff,H\beta}$(T) is the effective recombination coefficient, which depends on temperature (T), and $\nu_{H\beta}$ is the frequency of Hβ emission line, respectively. Thus, the ratio of their (reddening-corrected) intensities can be expressed as

$$\frac{I([O\textsc{iii}]\lambda5007)}{I(H\beta)} = \frac{N_e n(O^{++}) k_{03} E_{32} A_{32}/(A_{31}+A_{32})}{N_e n(H^{+}) \alpha_{eff,H\beta} E_{H\beta}}. \tag{1.11}$$

Equation 1.2 shows that k_{03} is a function of temperature. Therefore, the intensity ratio can be written as

$$\frac{n(O\textsc{iii})}{n(H^{+})} = C\frac{I([O\textsc{iii}]\lambda5007)}{I(H\beta)} f(T), \tag{1.12}$$

where C is a constant and $f(T)$ is a function of temperature. Hence, if the temperature is known, we can easily determine the abundance n(O^{++})/n(H^{+}) from the intensity line ratios.

The same concepts apply to the derivation of the ionic abundances of other ions as well. To estimate n(O^{+})/n(H^{+}), the temperature of the low-ionisation zone T_e([O II]) needs to be determined first, which itself depends on N_e. Hence accurate estimates of T_e and N_e are essential in deriving chemical abundances from the direct method. The total elemental abundance is determined by summing the ionic abundances. In a case when all the ions of a particular element are not available, ionisation correction factors (ICFs) must be used (see e.g. Kingsburgh & Barlow, 1994).

In the direct method explained above, T_e is estimated from the auroral line [O III] λ 4363, which is subject to many caveats. This auroral line is difficult to detect even in the low-metallicity H II regions (i.e. when it should be strongest). This emission line is temperature-sensitive and the presence of metals in the ISM leads to cooling. So, it can be observed in high-metallicity environments only with very sensitive, high S/N spectra. Moreover, the direct method can only give reliable metallicity estimates up to roughly 12 + log(O/H) = 8.7, above which this method may underestimate the metallicity if temperature fluctuations or gradients are present within the H II regions (Stasińska, 2002, 2005; Kewley & Ellison, 2008).

- **Indirect Method:** A caveat in using the CELs to determine chemical abundance is the

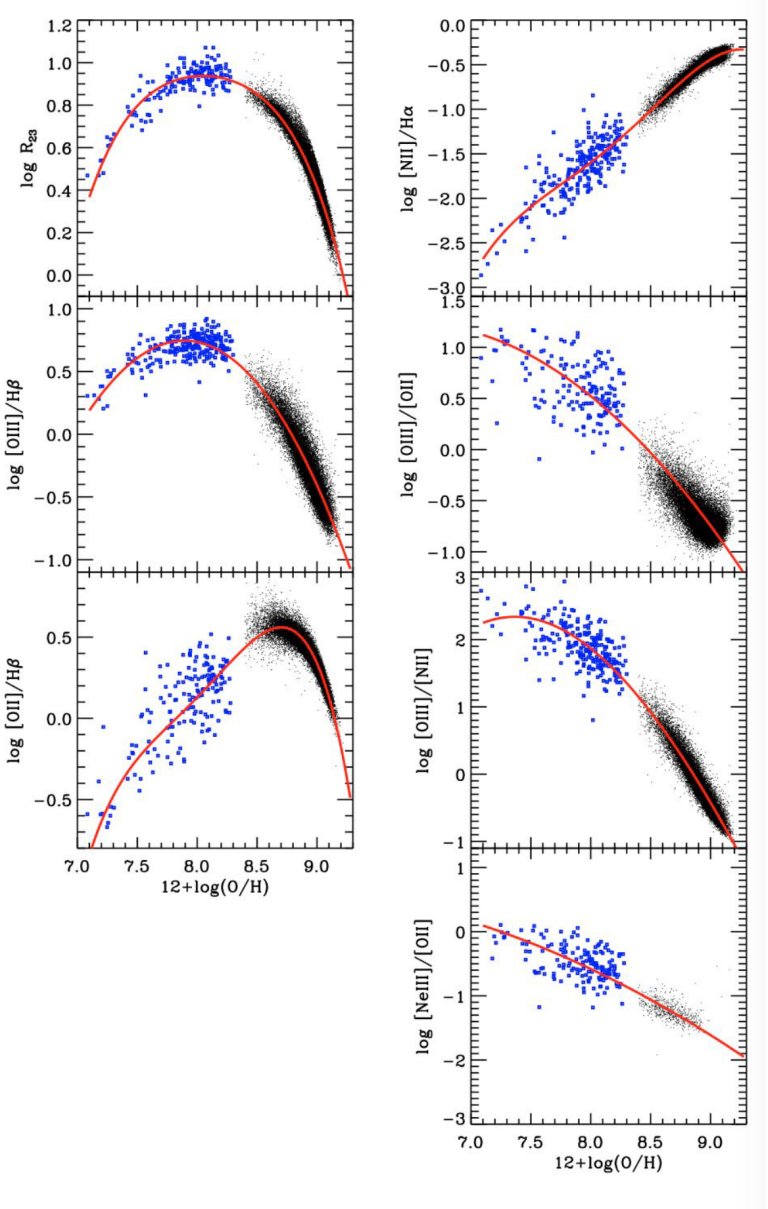

Figure 1.8 – Examples of strong line metallicity calibrations, where different metallicity diagnostics have been calibrated against the metallicities derived from the direct T_e method (blue points) as well as the photoionisation models (black points). Reproduced from Maiolino et al. (2008).

necessity to detect the weak auroral lines, required to estimate T_e. Hence, various recipes have been devised to determine abundances from the stronger CELs (for example, [O II] λ3727, [O III] λ5007, [N II] λ6584). These recipes are generally called "indirect methods" and do not require the estimates of T_e and N_e of the ionised gas.

The indirect method recipes are relations between a combination of emission line ratios and the total metallicity. To establish such relations, the combination of emission line ratios must be calibrated against the metallicity determined from other methods, for example, by the direct method or photoionisation models. Examples of such calibrations are shown in Figure 1.8, where metallicities derived from the direct method have been used for calibration at lower-metallicity values while the metallicities derived from photoionisation models have been used for higher-metallicity values, where auroral lines are difficult to detect. The determination of metallicity from photoionisation models is subject to caveats related to the limited choice of geometry for H II regions (plane-parallel or spherical), unconstrained depletion of metals, the clumpy density distribution of gas and dust (Kewley & Ellison, 2008). This results in a discrepancy of up to 0.2-0.3 dex in the strong line metallicity calibrations based on the photoionisation models.

There are more than a dozen indirect methods available, (see e.g. Alloin et al., 1979; Storchi-Bergmann, Calzetti & Kinney, 1994; Oey & Shields, 2000; Denicoló, Terlevich & Terlevich, 2002; Pettini & Pagel, 2004; Nagao, Maiolino & Marconi, 2006; Stasińska, 2006; Pérez-Montero et al., 2007; Kewley & Ellison, 2008; Marino et al., 2013; Dopita et al., 2016; Curti et al., 2017). In this thesis, I have used four indirect metallicity calibrators N2, O3N2 (Pettini & Pagel, 2004), N2S2Hα (Dopita et al., 2016) and R_{23} (Kobulnicky, Kennicutt & Pizagno, 1999), which will be introduced and discussed in Chapters 3 and 6.

1.2.2.3 Ionisation mechanisms

The ionisation/excitation mechanisms occurring in the ionised gas may be determined from the classical emission line ratio diagrams (Figure 1.9), also known as the 'BPT diagrams' (Baldwin, Phillips & Terlevich, 1981). These diagrams were initially devised to classify galaxies as star-forming, Seyfert, active galactic nuclei (AGN), low-ionisation nuclear line region (LINER) and composite (Figure 1.10), and have been subsequently extended to the analysis of ionised gas within galaxies. For example, diffuse ionised gas (DIG) exhibits properties similar to Seyfert, AGN and LINERs, whereas H II regions exhibit properties similar to star-forming galaxies. The relevant equations used for such classifications can be found in Kewley et al. (2001, 2006); Kauffmann et al. (2003).

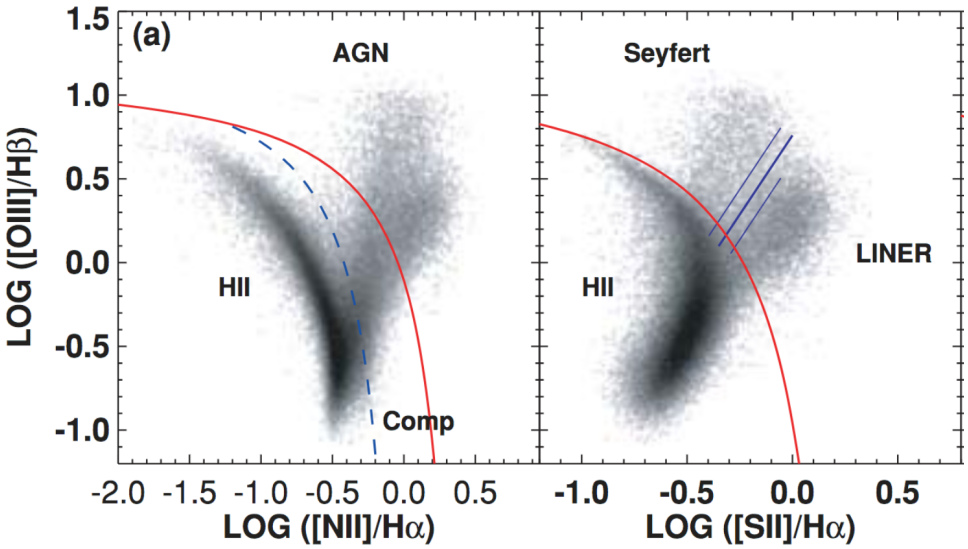

Figure 1.9 – Emission line ratio diagnostic diagrams, i.e. [N II] λ6584/Hα vs [O III] λ5007/Hβ (left panel) and [S II] $\lambda\lambda$6717,6731/Hα vs [O III] λ5007/Hβ (right panel). On each panel, black points represent the galaxies from the Sloan Digital Sky Survey, red line denotes the Kewley line (Kewley et al., 2001) serving as a demarcation between the regions/galaxies with photoionisation by massive stars lying below the Kewley line, and regions/galaxies with ionisation by either hardened radiation or shock excitation lying above the Kewley line (AGN, Seyfert, LINER). The dashed blue line on the left panel represents the curve from Kauffmann et al. (2003). The solid blue line on the right panel separates Seyferts from LINERs. Figure adapted from Kewley et al. (2006).

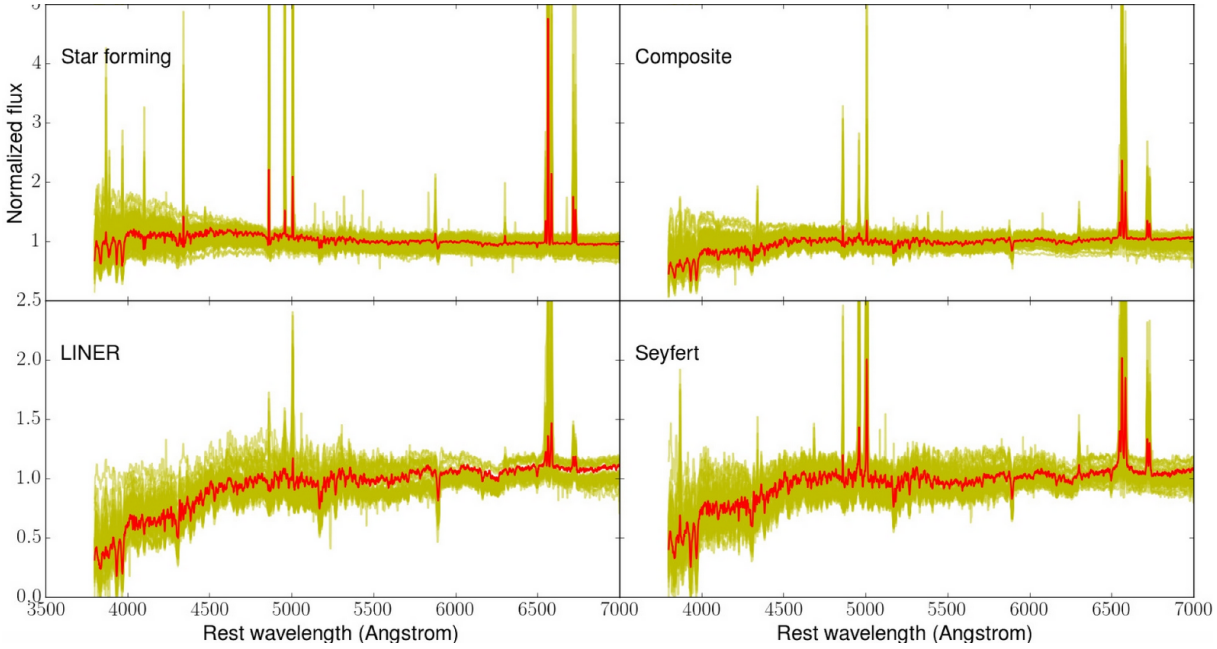

Figure 1.10 – Composite spectra of galaxies from LAMOST DR4, classified using the classical emission line ratio diagrams. Figure adapted from Wang et al. (2018).

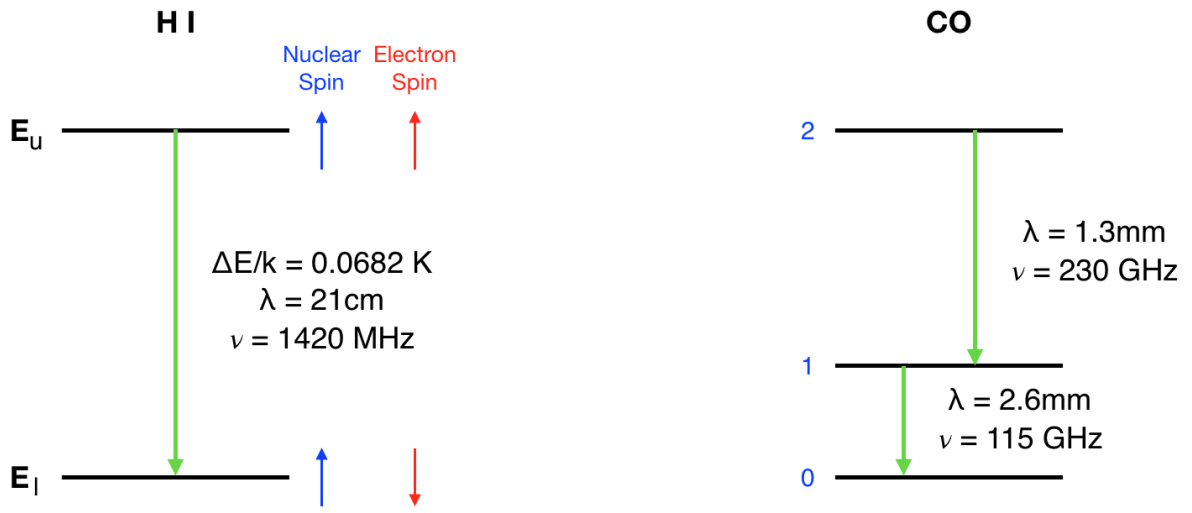

Figure 1.11 – Left panel: Hyperfine splitting of the ground state of the hydrogen atom where E_l and E_u denote energy corresponding to the ground state (l) and excited state (u), respectively. Right panel: Energy level diagram of CO molecule where low-lying rotational levels are denoted by numerals 0, 1 and 2.

1.2.3 Neutral gas: H I and CO

In the Universe, the most abundant element is hydrogen and the most abundant gas phase molecule after hydrogen is CO. Atomic gas is mainly traced by H I 21 cm and the molecular gas by CO. I have used atomic gas data and molecular gas data in Chapter 7. This section describes energy level transitions involved in using H I 21 cm and CO to trace the two neutral gas phases of the ISM. The notations here are similar to those used in the previous Section 1.2.2. Here, I also use the term brightness temperature (T_B), which is a measure of received intensity in radio astronomy. It is the temperature of a blackbody in thermal equilibrium emitting the same intensity as measured.

- **H I 21 cm (Atomic gas)**

  A hydrogen atom has one proton and one electron, both of which have spins (Figure 1.11, left panel). The spin of an electron and proton can be either parallel or anti-parallel to each other. The interaction between the magnetic moments of the electron and the proton results in "hyperfine splitting" of the parallel and anti-parallel spin states. The anti-parallel spin state has a lower energy level and hence is more stable than the parallel spin state. During the transition of an electron to the ground state ($u \rightarrow l$), the spin flips which results in the emission of a photon of wavelength λ =21.11 cm.

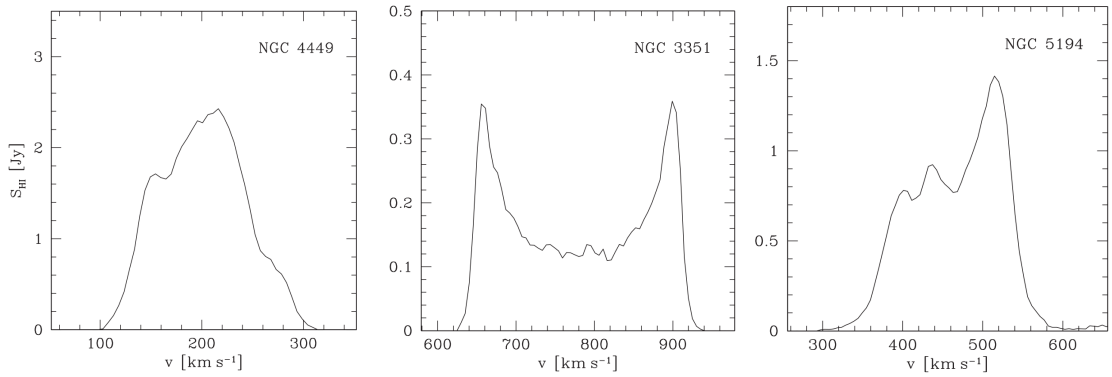

Figure 1.12 – Global H I profiles for example dwarf and spiral galaxies. Left: NGC 4449 (blue compact dwarf), middle: NGC 3351 (spiral galaxy), right: NGC 5194 (spiral galaxy). Figure adapted from Walter et al. (2008).

The energy corresponding to the emission of a photon at 21 cm is

$$E_{ul} = E_u - E_l \simeq \frac{hc}{[21\ cm]} \simeq h[1.4\ GHz] \simeq k[0.0682\ K]. \tag{1.13}$$

By the definition of excitation temperature, T_{exc}[2] (or its H I analogue, spin temperature T_s), the ratio of the population of upper (n_u) and lower (n_l) levels is given by

$$\frac{n_u}{n_l} = \frac{g_u}{g_l} e^{-h\nu_{ul}/kT_{exc}} = 3e^{-0.0682K/T_{spin}} \approx 3. \tag{1.14}$$

The last approximation can be made since the temperature of the gas in the ISM is large ($T \approx T_s \approx 150$ K) compared to the temperature involved in the transition. Thus, if $n_u + n_l = n(H\,I)$, then

$$n_u \approx \frac{3}{4} n(H\mathrm{I}), n_l \approx \frac{1}{4} n(H\mathrm{I}). \tag{1.15}$$

Substituting n_u in the definition of emissivity j_ν gives

$$j_\nu = n_u \frac{A_{ul}}{4\pi} h\nu_{ul}\phi_\nu \approx \frac{3}{16} \frac{A_{ul}}{\pi} h\nu_{ul} n(H\mathrm{I})\phi_\nu. \tag{1.16}$$

Here ϕ_ν represents the normalised line profile ($\int \phi_\nu d\nu = 1$) and is determined by the velocity distribution of H I. The column density of H I is obtained by integrating n(H I) along the line of sight distance (ds), i.e. N(H I) = $\int$ n(H I) ds. The intensity of a line is related to the emissivity, and is estimated from the brightness temperature.

For an optically thin atomic gas cloud, the column density of atomic hydrogen is obtained

[2] T_{exc}: Temperature at which the thermodynamic equilibrium distribution of the population (i.e. the Boltzmann distribution) equals the actual distribution.

by integrating the observed brightness temperature over the entire 21 cm line profile with respect to the line-of-sight velocity (v):

$$N(H\textsc{i}) = 1.823 \times 10^{18} \int [T_B(v)]dv \tag{1.17}$$

where N(H I) is in cm^{-2} and the expression inside the integral is in units of K km s^{-1}.

Figure 1.12 shows the H I profile of dwarf and spiral galaxies. Due to the low H I content and low dynamical mass of dwarf galaxies, their H I profiles are generally narrow and faint and can be characterised by a Gaussian profile. However, H I profiles of the spiral galaxies are broad and strong, which may sometimes be a double-horned profile.

- **CO (Molecular gas)**

  The most abundant molecule in the Universe is H_2. However, it is not used to trace the molecular gas since it does not emit a significant amount of radiation. This is because the H_2 molecule is not significantly excited at the typical temperature of the molecular gas in the ISM (T $\sim$ 10–40 K). However, at such low temperatures, the rotational transition lines of CO molecule can be easily excited as these lines are closely spaced due to the large moment of inertia of the massive CO molecule. The low-lying rotational energy levels of the CO molecule are shown in Figure 1.11 (right panel). The energy of the first rotationally excited level of CO ($J = 1 \rightarrow 0$) is given by

$$\Delta E \equiv E(J=1) - E(J=0) \simeq hc[2.6\ mm]^{-1} \simeq h[115\ GHz] \simeq k[5.5\ K]. \tag{1.18}$$

  For an optically thick molecular gas cloud, the integrated intensity of the CO ($J = 1 \rightarrow 0$) line is obtained by integrating brightness temperature over the line-of-sight velocity (v):

$$I_{CO} = \int_{line} T_B(v)dv \tag{1.19}$$

  The column density of the molecular gas (N(H_2) in cm^{-2}) is related to the integrated intensity of the CO line emission (I_{CO} in K km s^{-1}) via an X-factor, thus

$$N(H_2) = X_{CO} \times \int_{line} T_B(v)dv. \tag{1.20}$$

  The value of X_{CO} is a subject of intense discussion, for which see Bolatto, Wolfire & Leroy (2013). The most reliable estimate of the X_{CO} factor in the solar neighbourhood is $(1.8 \pm 0.3) \times 10^{20}$ cm^{-2} (K km s^{-1})$^{-1}$ (Dame, Hartmann & Thaddeus, 2001). To determine molecular gas content from CO (2→1) transition rather than from the CO (1→0),

generally, a constant ratio is assumed between the two. For example, a typical value of 0.8 is reported by Leroy et al. (2009) for this ratio.

1.3 Star-Formation in Galaxies

Star-formation is a multi-scale process, comprising various physical processes happening at different physical scales, encompassing megaparsecs to astronomical units (Kennicutt & Evans, 2012). These processes include gas being accreted onto the star-forming galaxies from the circumgalactic/intergalactic medium or accompanying star-forming galaxies, cooling of the accreted gas, the formation of molecular clouds, which fragment into clumps and cores, and contraction of the cores to form stars and planetary systems. Hence the study of star-formation is a complex topic which has significant implications in various other areas, including galaxy formation and evolution, cosmochemistry, and even the existence of life elsewhere in the Universe (Ward-Thompson, Fraser & Rawlings, 2002). Consequently, star-formation has been a subject of much interest for both theoreticians and observers who continue to explore various aspects.

The Schmidt Relation is one of the active topics of star-formation studied extensively at both large galactic scales and local sub-galactic scales. In 1959, Maarten Schmidt theorised a power-law relation between the volume densities of star-formation rate (SFR) and gas, i.e. ρ_{SFR} and ρ_{gas}, respectively. In 1963, he modified this relation to a power-law relating the surface densities of the two quantities, simply to overcome the difficulty in measuring the volume densities. Hence the Schmidt relation is expressed as

$$\Sigma_{SFR} = A\Sigma_{gas}^{N} \tag{1.21}$$

where N is the power-law index, A is the star-formation efficiency, and Σ_{SFR} and Σ_{gas} are the surface-densities of the star-formation rate and gas, respectively. "Gas" here refers to the neutral component of the ISM, which includes both the atomic as well as the molecular components and are traced as described in Section 1.2.3. Various methods have been explored and devised to trace the "SFR". Some of the commonly used SFR tracers in the low redshift star-formation studies include far-ultraviolet, Hα and infrared (IR) (see Kennicutt, 1998a; Kennicutt & Evans, 2012, for details on various SFR tracers), and are briefly mentioned here:

- FUV continuum: The FUV is produced from stars with masses of several solar masses formed over the past 10–100 Myr. As such, the FUV continuum is one of the direct tracers of recent SFR.

- Recombination lines: These lines are produced from the ionised gas surrounding massive stars ($\gtrsim$ 15 $M_\odot$ and mostly in the range of 30–40 $M_\odot$), thus tracing stars of age $\sim$ 3–10 Myr. As such, these lines give an instantaneous measure of the SFR.

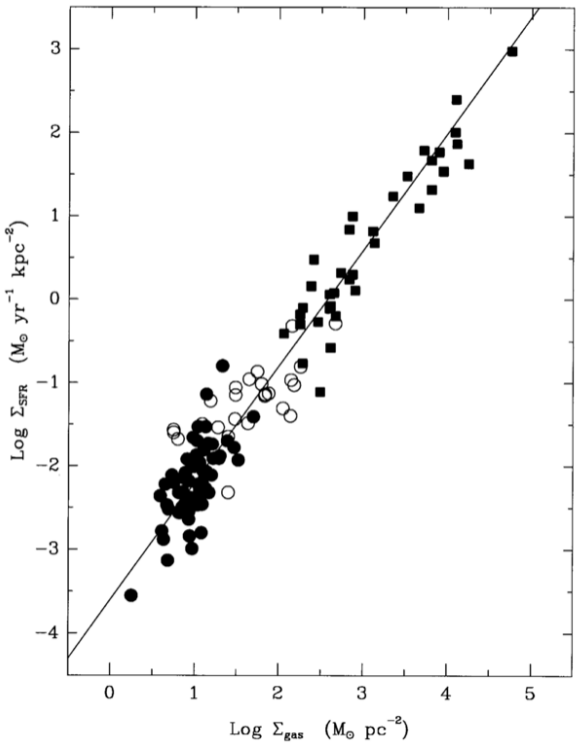

Figure 1.13 – Global Schmidt relation for the normal disk (filled circles), starbursts (squares), centres of the normal disk galaxies (open circles). Figure adapted from Kennicutt (1998b).

- IR emission: Nearly half of the stellar light (optical and UV) is absorbed by the interstellar dust and re-emitted in the IR, so measurements in the IR provides an estimate of the dust-obscured component of SFR.

1.3.1 Large Galactic Scales

In 1998, Rob Kennicutt combined measurements of Hα, H I and CO distribution in 61 normal spiral galaxies and, far-infrared and CO measurements of 36 starburst galaxies, to study the Schmidt law. He derived an empirical value of N = 1.4 $\pm$ 0.15 in the equation 1.21, and established the disk-averaged star-formation law, called the "Kennicutt-Schmidt Law" (Figure 1.13).

The power-law index N $\approx$ 1.5 at the galactic scale can be explained by a simple self-gravitational model where the large-scale SFR is proportional to the growth rate of perturbations in the gas disk (Kennicutt, 1998b). The characteristic time scale for such perturbations is equal to the free-fall time in the gas disk, given by $\tau_{ff} \propto \rho_{gas}^{-0.5}$. Hence $\rho_{SFR} \propto \frac{\rho_{gas}}{\rho_{gas}^{-0.5}} \propto \rho_{gas}^{1.5}$. For the spiral galaxies and starbursts considered in Kennicutt (1998b), a constant mean scale height is a reasonable approximation, which implies that the volume densities are proportional to surface densities. Hence,

$$\Sigma_{SFR} \propto \Sigma_{gas}^{1.5}. \tag{1.22}$$

The Kennicutt-Schmidt law can explain plausible scenarios of galaxy formation and evolution and hence is used as an essential prescription in models and simulations (Thacker & Couchman, 2000; Kay et al., 2002; Marri & White, 2003; Tasker & Bryan, 2006; Schaye & Dalla Vecchia, 2008) involving galaxy formation and evolution. However, we do not know yet if the disk-averaged Kennicutt-Schmidt law explains the local relationship between SFR and gas densities at sub-galactic scales. This empirical law may be a consequence of a causal physical relationship, or it may be an empirical consequence of other relationships between different quantities (Kennicutt, 2008). We note here that the disk-integrated or disk-averaged star-formation law implies the averaging out of large local variations in the stellar population (age and initial mass function (IMF)) and gas/dust geometry (Kennicutt & Evans, 2012), implying that the currently-established law might not follow from a fundamental and causal physical relationship. To answer these questions and to better understand the physics of star-formation, requires a spatially-resolved analysis of the star-formation law, which forms Chapter 7 of this thesis.

1.3.2 Local Sub-Galactic Scales

The study of the Schmidt-law at the local sub-galactic scales for nearby galaxies has been revolutionised with the advent of the heterodyne receiver array (HERA at the IRAM[3] 30m telescope) which allowed mapping of the CO gas in nearby galaxies, and the space-based infrared telescopes (e.g. Spitzer and Herschel) which allowed mapping of the dust-content in these galaxies. Such technological advancements have enabled a number of detailed studies at different physical scales exploring various aspects of the physics of star-formation. However, the plethora of studies has led to different results, and there has been much debate particularly on the power-law index N at local sub-galactic scales. In the following, I provide a summary of spatially-resolved star-formation studies and also possible causes of the discrepancies between them.

- **Causes of discrepancies in Schmidt relations at local scales.** A study of the Schmidt relation at local scales requires SFR tracers or diagnostics that are valid on the scales under consideration. On galactic-scales, the following assumptions are made while converting fluxes to the respective SFR : (1) fluxes are mainly from massive, young stars and scale with the stellar mass of the clusters and thus with SFR; (2) star formation is approximately constant over the time period probed by the corresponding SFR tracer, e.g. 5 Myr for Hα emission; (3) the stellar IMF is known meaning that the number of low and

[3]Institut de Radioastronomie Millimètrique

high mass stars are known or can be approximated; (4) the stellar IMF is fully sampled which means that there is at least one star in the highest mass bin (typically $\sim$ 100 $M_\odot$) described by the IMF. On sub-galactic scales, all the approximations made while establishing the SFR diagnostics for integrated-galactic measurements break down. While the variation of the stellar-age mix, IMF and the gas/dust geometry averages out in galactic studies, there are significant variations at local scales. Compared to the galactic scale, the observed flux on local scales is dominated by a few young stars which leads to high scatter in the conversion of luminosity to SFR, and hence uncertainties in the determination of star-formation properties are higher. At these local scales, the IMF is not fully populated, which results in considerable random and systematic errors in the SFR. Moreover, gas and dust are often separated from the stars, so their tracers do not necessarily trace the same system if the region of study is not chosen carefully. Since the distribution and geometry of dust shows much variation at local scales, SFR calibration needs further consideration with a dust-attenuation correction. Thus, measuring star-formation rate at sub-galactic scales is a significant challenge.

Estimating molecular gas content is also not straightforward. Section 1.2.3 explains the use of CO to trace the molecular gas. However, its use as a gas tracer is subject to many caveats. CO is sensitive to photodissociation at low column densities and needs a minimum column density of molecular gas to excite emission. On the other hand, the emission gets saturated at very modest column densities. In cold regions of higher column density, CO freezes out and gets converted to CO_2 ice which complicates its use as a molecular gas tracer. Hence, CO measurements cover a limited dynamic range of molecular gas column densities. Moreover, the X(CO) conversion factor (required to convert the observed CO intensity to the H_2 column density) is known to be a source of systematic uncertainty in estimating molecular gas. X(CO) varies with galaxy properties, such as volume density, turbulence and metallicity of the gas (Bolatto, Wolfire & Leroy, 2013). It appears to drop in the central, bright regions of some galaxies, but not all. A metallicity-dependent X(CO) will result in a decrease of the molecular gas density by a factor of 2 to 3 in the central regions compared to disk regions of nearby galaxies (Boissier et al., 2003; Narayanan et al., 2012).

Since the measurement of the SFR and molecular gas are subject to systematic uncertainties, one needs to take them into account while determining the best-fit parameters of the Schmidt relation. There can be systematic uncertainties of up to 30–50% on both axes. Moreover, instead of fitting a power law of the form (equation 1.21), it is customary to do a linear fit to the Schmidt relation in log-log space, i.e. log Σ_{SFR} = N log Σ_{gas} + log A to determine N and log A. Though log-log space allows us to cover a broad dynamic range and it simplifies the determination of parameters, the main problem is that the observables

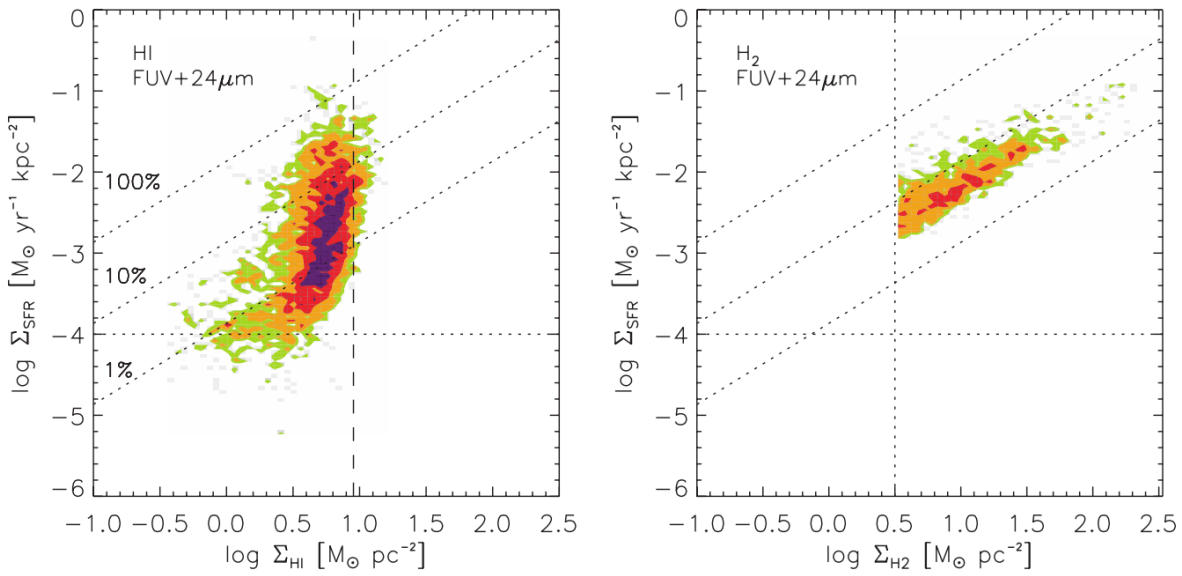

Figure 1.14 – Spatially-resolved Schmidt relation for atomic gas (left panel) and molecular gas (right panel) (Bigiel et al., 2008). Contours indicate the density of data, i.e. 25% (magenta), 50% (red), 75% (orange) and 90% (green). On both panels, the diagonal dotted lines correspond to constant star-formation efficiencies of 1%, 10% and 100%.

are not what is being fit. Different fitting techniques have also led to a variation of best-fit parameters and are also a source of discrepancies in Schmidt relation studies.

- **Molecular gas Schmidt relation.** The molecular gas Schmidt relation, i.e. the relationship between the surface densities of the SFR and the molecular gas has been found to be noticeably tighter at sub-kiloparsec scales ($\sim$ 0.5–1 kpc) than at global scales (Kennicutt, 1998b). Some studies suggest that the star-formation rate surface density scales linearly (N $\sim$ 1) with the molecular gas surface density at local scales (Figure 1.14, right panel), and is independent of the atomic gas surface density which saturates at $\sim$ 10 $M_\odot$ pc^{-2} (Figure 1.14, left panel) (see e.g. Bigiel et al., 2008; Schruba et al., 2011; Leroy et al., 2013). However, other studies have also found that the molecular gas Schmidt relation is sub-linear (N $<$ 1 Shetty, Kelly & Bigiel, 2013; Shetty et al., 2014; Shetty, Clark & Klessen, 2014) and super-linear (N $>$ 1, e.g. Kennicutt et al., 2007). Each of these findings has different interpretations and implications:

  A super-linear molecular gas Schmidt relation is explained by the dominance of non-linear processes at play, e.g. gravitational collapse (N=1.5) or cloud-cloud collision (N=2), in the regions of high gas density and for the systems with a constant scale height (Madore, 1977; Elmegreen, 1994; Tan, 2000; Bigiel et al., 2008; Momose et al., 2013). A linear relation is explained by the formation of stars in giant molecular clouds with approximately uniform properties (Bigiel et al., 2008). A sub-linear relation is explained by the presence of CO-bright diffuse molecular gas (Shetty, Clark & Klessen, 2014). A

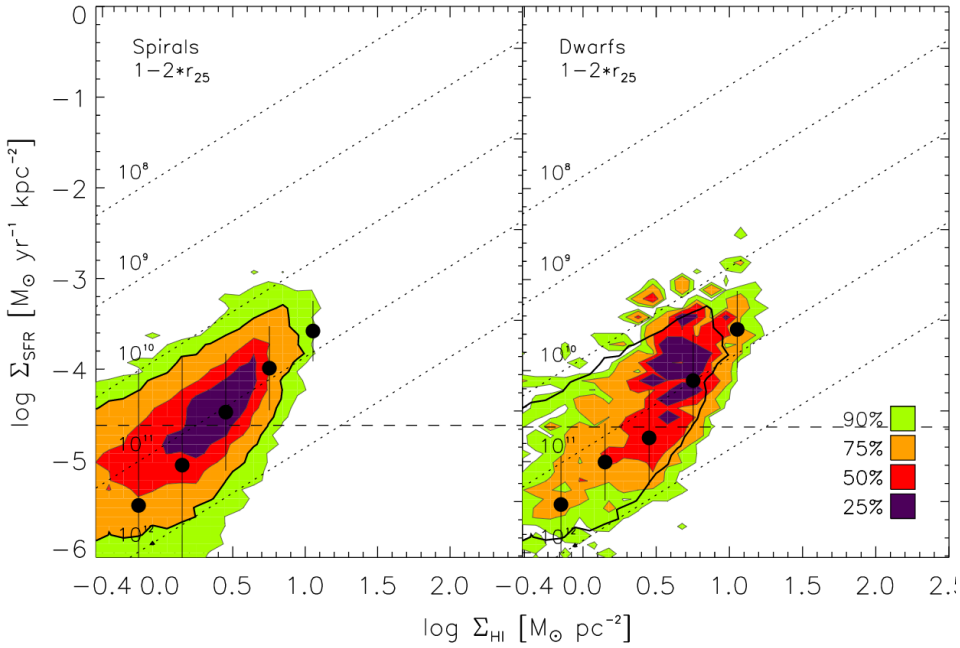

Figure 1.15 – Relation between surface densities of star-formation rate ($\Sigma_{\rm SFR}$) and atomic gas ($\Sigma_{\rm HI}$) on a pixel-by-pixel basis in the outer regions (1–2r_{25}) of spiral galaxies (left panel) and dwarf galaxies (right panel). Coloured contours indicate the density of data, i.e. 25% (magenta), 50% (red), 75% (orange) and 90% (green). On both panels, the dotted diagonal lines correspond to constant H I depletion time of 10^8–10^{12} yr. Though irrelevant here, black dots with error bars are the median FUV and dispersion in bins of $\Sigma_{\rm HI}$, respectively. Figure adapted from Bigiel et al. (2010).

linear or non-linear dependence of molecular gas Schmidt relation implies a constant or varying gas depletion time (or star-formation efficiency) estimated with respect to the molecular gas. Though there has been many discrepancies between different works, the correlation between the spatially-resolved SFR and molecular gas is evident.

- **Atomic gas Schmidt relation.** The atomic gas surface density is found to saturate at ~ 10 $M_\odot$ pc^{-2} at sub-kiloparsec scales and is uncorrelated with the SFR in the inner regions of galaxies (Figure 1.14, right panel). However, in the outer regions of galaxies (both spirals and dwarfs), a correlation does exist between the atomic gas content and star-formation, though there is a significant scatter in the relation (Figure 1.15). Note here that in the outer regions, no molecular gas is detected, though star-formation is still taking place. Hence the role of atomic gas cannot be discarded entirely. In this regime, parameters such as the metallicity of the gas and the stellar surface density seem to play a non-negligible role in star-formation. Several theoretical (Glover & Clark, 2012; Krumholz, 2012) and observational (Michałowski et al., 2015; Cortese, Catinella & Janowiecki, 2017) works suggest that atomic gas contributes to star-formation and hence needs to be explored further.

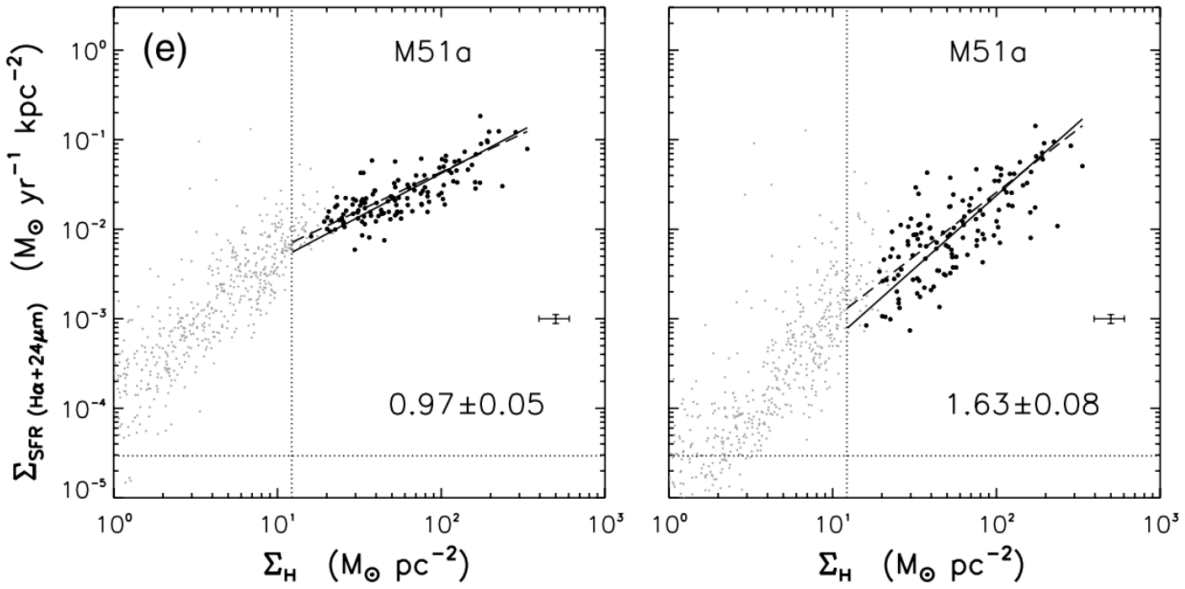

Figure 1.16 – Spatially-resolved relation between surface densities of star-formation rate (Σ_{SFR} estimated by combining Hα and 24μm measurements) and total gas (Σ_H) before (left panel) and after (right panel) subtraction of diffuse background in SFR tracers for the grand spiral M51a. Figure adapted from Liu et al. (2011).

- **Diffuse background and Schmidt relation.** The role of the diffuse background in the Schmidt relation studies began to be considered and explored after two contemporary spatially-resolved studies: aperture photometric analysis of the grand spiral M51 by Kennicutt et al. (2007) who found a super-linear molecular gas Schmidt relation; and the pixel-by-pixel analysis on seven spiral galaxies by Bigiel et al. (2008) who found a linear relation. A follow-up study by Liu et al. (2011) demonstrated that the subtraction of diffuse background in the SFR tracers leads to an increase in the slope of the Schmidt relation (Figure 1.16). Though the diffuse background is proposed to be a component of the ISM unrelated to current star-formation, its nature is not understood completely. Various statistical methods have been used to determine and remove the diffuse background from various tracers. It has been found that its effect is more prominent in the lower-luminosity regions than the higher luminosity regions, and as such the slope of the Schmidt relation (N) is affected. Chapter 7 further explores the role of diffuse background in local Schmidt relation determinations.

1.4 Integral Field Spectroscopy

Integral Field Spectroscopy (IFS) is a powerful technique developed over the past several decades, which provides spatially-resolved spectroscopy across the whole field of view (FOV) in a single exposure. It is crucial in investigating the spatially-resolved properties of extended

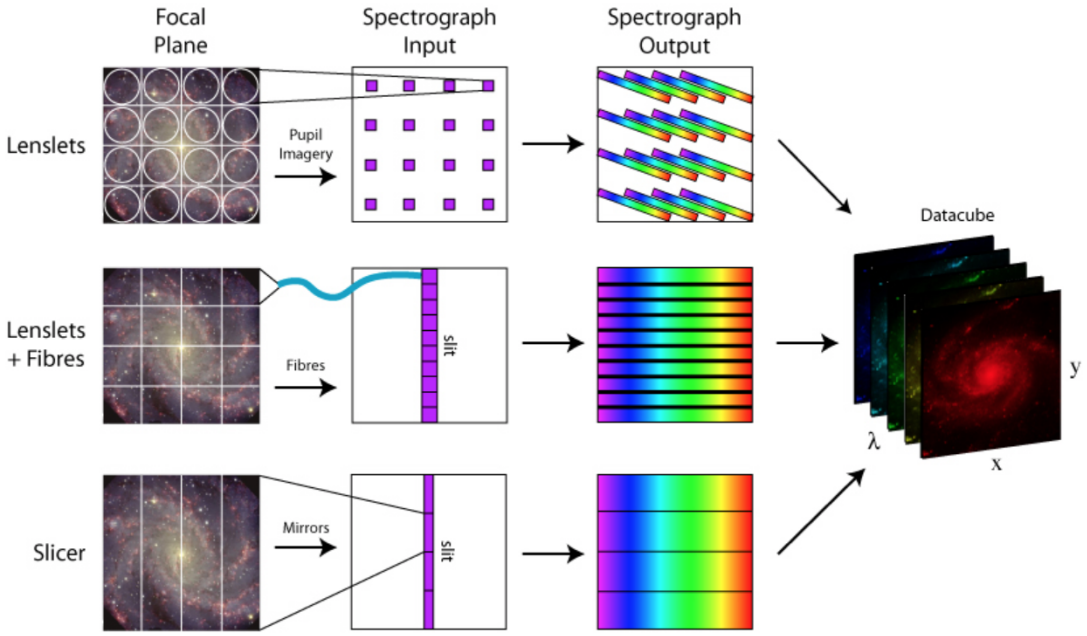

Figure 1.17 – Three IFU techniques employed to divide a two-dimensional spatial plane into a continuous three-dimensional cube in x, y and wavelength (λ). Figure credit: Mark Westmoquette

systems, which may span from pre-main sequence objects (e.g. protostellar discs) to groups and clusters of galaxies at both low- and high-redshifts. To this end, major observatories, both ground-based (Keck, Gemini, William Herschel Telescope(WHT), Very Large Telescope (VLT)) and space-based (Herschel, James Webb Space Telescope (JWST)) have integral field units (IFUs) installed on them, leading to a large number of spatially-resolved galaxy surveys both at low- and high-redshifts. The future of astronomy has and will continue to be revolutionised by IFS.

1.4.1 Basics of IFS

An integral field spectrograph consists of an integral field unit (IFU) along with a spectrograph. The IFU serves the purpose of dividing a two-dimensional spatial plane into a continuous three-dimensional cube in x, y and wavelength (λ), which can be achieved by one of the three techniques shown in Figure 1.17 and described below.

- Lenslets: This technique (Bacon et al., 1995, Figure 1.17, upper panel) involves the use of microlens arrays, which split the image of the observed object into many elements. Light from each element is then concentrated onto a small dot on the spectrograph which disperses the light to produce the spectra of each element. The microlens array may be

tilted to avoid the overlap of spectra and hence sample the observed object contiguously. Example instrument: SAURON on the WHT.

- Lenslets & Fibres: This technique (Barden & Wade, 1988; Allington-Smith et al., 1997, Figure 1.17, middle panel) relies on the use of optical fibres which transfer the light from different parts of the detected object to a slit of the spectrograph. Densely packed lenslets may be used along with the fibres to sample the observed object contiguously. Example instrument: GMOS[4]-IFUs on Gemini Telescopes.

- Slicer: This technique (Content, 1997, Figure 1.17, lower panel) involves the use of two segmented mirrors, which results in a continuous sampling with high spatial resolution. The horizontal segments of the first mirror slice the light from the detected object and send them in slightly different directions. The segments of the second mirrors receive these slices and reformat them so that slices are now arranged end to end to form the slit of the spectrograph. Example instrument: MUSE[5] on the VLT.

1.4.2 IFS & Star-forming Galaxies

IFS has been used to study various aspects of star-forming galaxies. IFS allows us to map various physical properties of the star-forming systems simultaneously and study their spatial correlation. There have been numerous individual IFS studies on star-forming galaxies, BCDs (see e.g. James et al., 2009; James, Tsamis & Barlow, 2010; James et al., 2013a; Lagos et al., 2012, 2014, 2016; Pérez-Montero et al., 2011; Cairós et al., 2009, 2012) as well as spirals (e.g. Sánchez et al., 2011; Kaplan et al., 2016). Entire surveys have been dedicated to exploring hundreds of star-forming galaxies, such as: the Calar Alto Legacy Integral Field Area Survey (CALIFA) (Sánchez et al., 2012); the Mapping Nearby Galaxies at APO (MANGA) survey (Bundy et al., 2015); the SAMI galaxy survey (Green et al., 2017); the MUSE Atlas of Disks (MAD) survey; KMOS3D (Wisnioski et al., 2015) and KROSS (Magdis et al., 2016). The aim of these IFS works includes, but is not limited to, the study of chemical element distribution, the ionised gas kinematics dominated by rotation or dispersion, mapping of stellar populations, their age, star-formation activity, ionisation mechanisms. In my thesis, I have used IFS data to map these physical properties and study their spatial correlation, which is essential to understand different mechanisms at play in the star-forming systems and is aimed at gaining a deeper understanding of galaxy formation and evolution.

[4]Gemini Multi Object Spectrograph
[5]Multi-unit Spectroscopic Explorer

1.5 This Thesis

In this thesis, I have carried out spatially-resolved analyses of star-forming galaxies using optical IFS data and multi-wavelength data from FUV to radio. The star-forming galaxies studied here are either BCDs or spirals. These studies are driven by some of the fundamental questions of galaxy formation and evolution. According to the bathtub model, star-formation, chemical abundance and gas kinematics (inflow and outflow of gas) are the three vital elements of galaxy formation and evolution (Lilly et al., 2013). In this thesis, I have touched on each of these three essential elements, with the aim of answering some of the related questions. In the following, I present a chapter-wise structure of the thesis along with the questions addressed in each chapter.

- Chapter 2 describes the IFS data reduction on which further analysis is based. Chapters 3, 4 and 5 concern the IFS analyses of star-forming regions in three individual BCDs, aimed at answering the following three questions:

  1. Do chemical inhomogeneities exist in the ionised gas within BCDs?
  2. What is the primary physical mechanism responsible for the ionisation in the star-forming regions and the surrounding gas?
  3. What is the age of stellar populations that are currently ionising the gas?

  Building upon the answers to these questions, I investigate more profound issues in each Chapter as mentioned below.

  - Chapter 3 inspects what could cause the observed inverse metallicity gradient in the BCD 'NGC 4449'.
  - Chapter 4 investigates the star-forming regions not only in the BCD 'NGC 4670' but also nine more BCDs, along with green pea galaxies and low-mass star-forming galaxies. The question asked here concern understanding why a negative trend exists between the nitrogen-to-oxygen ratio and oxygen abundance.
  - Chapter 5 presents the IFS analysis of the BCD 'SBS 1415+437' and explores how spatially-resolved and integrated chemical abundances are related.

- Chapter 6 involves the IFS analyses of 24 nearby spiral galaxies. The questions asked here are as follows:

  1. How does DIG affect the different indirect metallicity diagnostics?
  2. How can we robustly measure the metallicity content of spiral galaxies irrespective of its DIG content?

- Chapter 7 concerns a spatially-resolved study of the Schmidt relation in nine nearby spiral galaxies, where the following questions are explored:

    1. How does the inclusion and removal of diffuse background in the SFR tracers and atomic gas affect the spatially-resolved Schmidt relation?
    2. How does the slope of the spatially-resolved Schmidt relation depend on the analysis method, pixel-by-pixel analysis or aperture photometry?

- Chapter 8 summarises the primary results of this thesis. The plans for future work are also presented in this last chapter.

2

GMOS-IFU Data Reduction

2.1 The GMOS IFU

A significant part of my thesis is based on integral field spectroscopic (IFS) data. The analyses presented in Chapters 3, 4 and 5 are based on the IFS data of blue compact dwarfs (BCDs) taken with the Gemini Multi-Object Spectrograph (GMOS; Hook et al., 2004) and integral field unit (IFU) (GMOS-N IFU; Allington-Smith et al., 2002) at Gemini-North telescope in Hawaii. For the work in Chapter 6, I have used the IFS data of 24 spiral galaxies taken with the Multi-Unit Spectroscopic Explorer on the Very Large Telescope. Although there is in principle a GMOS pipeline, it requires a significant amount of manual intervention whereas the MUSE pipeline is more reliable. I reduced GMOS-IFS data not only for my thesis work but also for collaborative work on another BCD, Mrk 71 (Oey et al. in prep). This Chapter describes GMOS-IFS data observation and reduction specifically for BCDs analysed in Chapters 3, 4 and 5. However, I also include any relevant information related to the other BCD Mrk 71. I first briefly describe the GMOS instrument, then observation of IFS data in Section 2.2 and finally in Section 2.3, I describe the data-reduction steps, and highlight the problems encountered using the standard GMOS pipeline. For details of data-reduction using MUSE pipeline, see Chapter 6.

The GMOS detector is a mosaic of three buttable CCDs (2048 $\times$ 4608 pixels), with chip-gaps of approximately 37 pixels, equivalent to 1.87Å. Each CCD has two readout amplifiers (see Figure 2.1). The GMOS-IFU is based on the fibre-lenslet technique described in Section 1.4.1

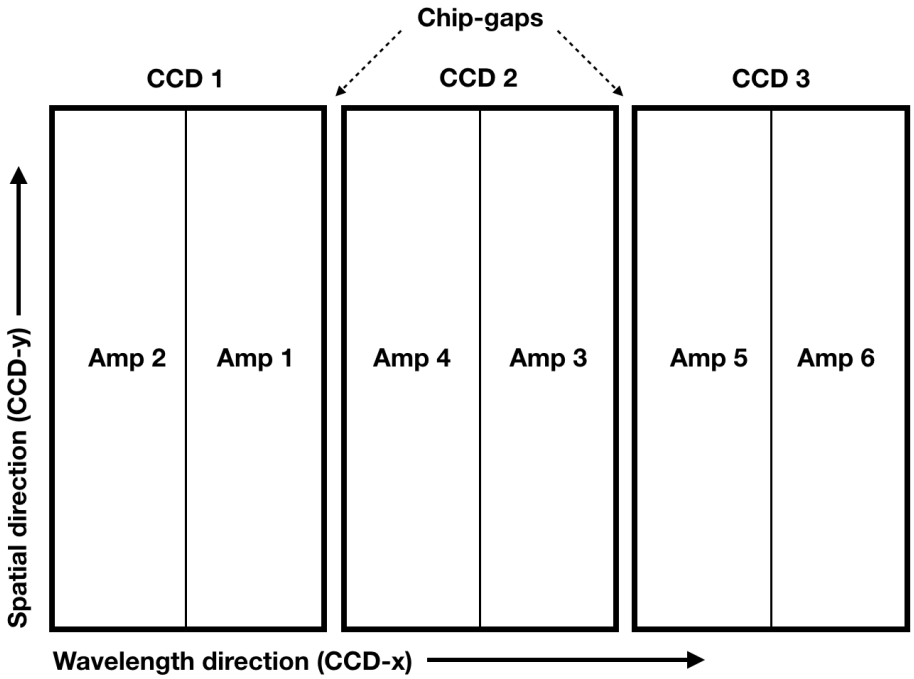

Figure 2.1 – Schematic diagram of the GMOS detector mosaic showing three CCDs, each consisting of two amplifiers (denoted by Amp 1, Amp 2, Amp 3, Amp 4, Amp 5 and Amp 6). The x- and y-axes of the CCD mosaic denote the wavelength and spatial direction of observations, respectively.

Table 2.1 – Differences between one-slit and two-slit modes

	One-slit mode	Two-slit mode
Object (FOV)	5” × 3.5” (500 lenslets)	5” × 7” (1000 lenslets)
Sky (FOV)	5” × 1.75” (250 lenslets)	5” × 3.5” (500 lenslets)
Advantage	Extended wavelength coverage	Maximum FOV
Disadvantage	Smaller FOV	Limited wavelength coverage

and has 1500 hexagonal lenslets of projected angular diameter on sky of 0.2 arcsec for sampling the field of view (FOV), including both target and sky. The instrument is designed to take observations in the wavelength range of 0.4–1.1 micron, and in two different configurations: one-slit mode and two-slit mode. The main differences of each slit mode are given in Table 2.1.

2.2 GMOS Observations

Information from the data observing log for the BCDs analysed in Chapters 3, 4 and 5 is presented in Table 2.2. Observations were taken in one-slit queue-mode in 2012. For NGC 4449 and NGC 4670, observations were carried out in four different settings which involved two gratings each for blue (B600) and red (R600) observations. To have a better wavelength coverage and limit the problems due to two chip gaps between the three detectors of GMOS-N IFU, two

Table 2.2 – GMOS-N IFU observing log for NGC 4449, NGC 4670, SBS 1415+437

Grating	Central wavelength (Å)	Wavelength range (Å)	Exposure time (s)	Average airmass	Standard star
			NGC 4449		
B600+_G5307	4650	3202 – 6067	1200	1.148	Hz44
B600+_G5307	4700	3252 – 6119	2×1200	1.099, 1.108	Wolf1346
R600+_G5304	6900	5345 – 8261	1100	1.097	Wolf1346
R600+_G5304	6950	5397 – 8314	1100	1.103	Wolf1346
			NGC 4670		
B600+_G5307	4650	3196 – 6067	2×1550	1.16, 1.24	Hz44
B600+_G5307	4700	3250 – 6118	3×1550	1.015, 1.034, 1.066	Wolf1346
R600+_G5304	6900	5345 – 8261	2×1400	1.013, 1.008	Wolf1346
R600+_G5304	6950	5397 – 8314	2×1400	1.12, 1.038	Wolf1346
			SBS 1415+437		
B600+_G5307	4700	3250 – 6118	2×1850	1.098, 1.092	Wolf1346
R600+_G5304	6900	5443 – 8361	2×1800	1.161, 1.121	Wolf1346

Note: Seeing FWHM was not available for the above dataset. Hence, I estimated seeing FWHM of 0.6 arcsec for each object by comparing its GMOS continuum image with the corresponding HST image. An example case of SBS1415+437 is shown in Chapter 5.

sets of observations were taken with spectral dithering of 50 Å. For SBS 1415+437, observations in only two settings were available, corresponding to the blue and red gratings. Unlike the observations of these three BCDs, Mrk 71 was observed in the two-slit mode.

2.3 Data Reduction

I performed the necessary reduction steps by interactive use of the standard GEMINI pipeline written in Image Reduction and Analysis Facility (IRAF)[1]. However, the standard pipeline does not provide satisfactory results for some procedures. I therefore, had to develop and implement several codes to deal with these issues. The following sections describe the overall processing stages highlighting where necessary the additional procedures I had to develop. The essential steps of data-reduction include bias-subtraction, flat fielding, sky subtraction, wavelength calibration and flux calibration.

2.3.1 Raw Data

Along with science data of target objects, we also need a set of observations for calibration and twilight flats, CuAr lamp (arc) for wavelength calibration and standard stars for flux calibration taken in the same configuration (for example, grating, wavelength, IFU-slit configuration, CCD binning) as science data. Figure 2.2 shows an example CCD image of each of these raw

[1]IRAF is distributed by the National Optical Astronomy Observatory, which is operated by the Association of Universities for Research in Astronomy (AURA) under a cooperative agreement with the National Science Foundation.

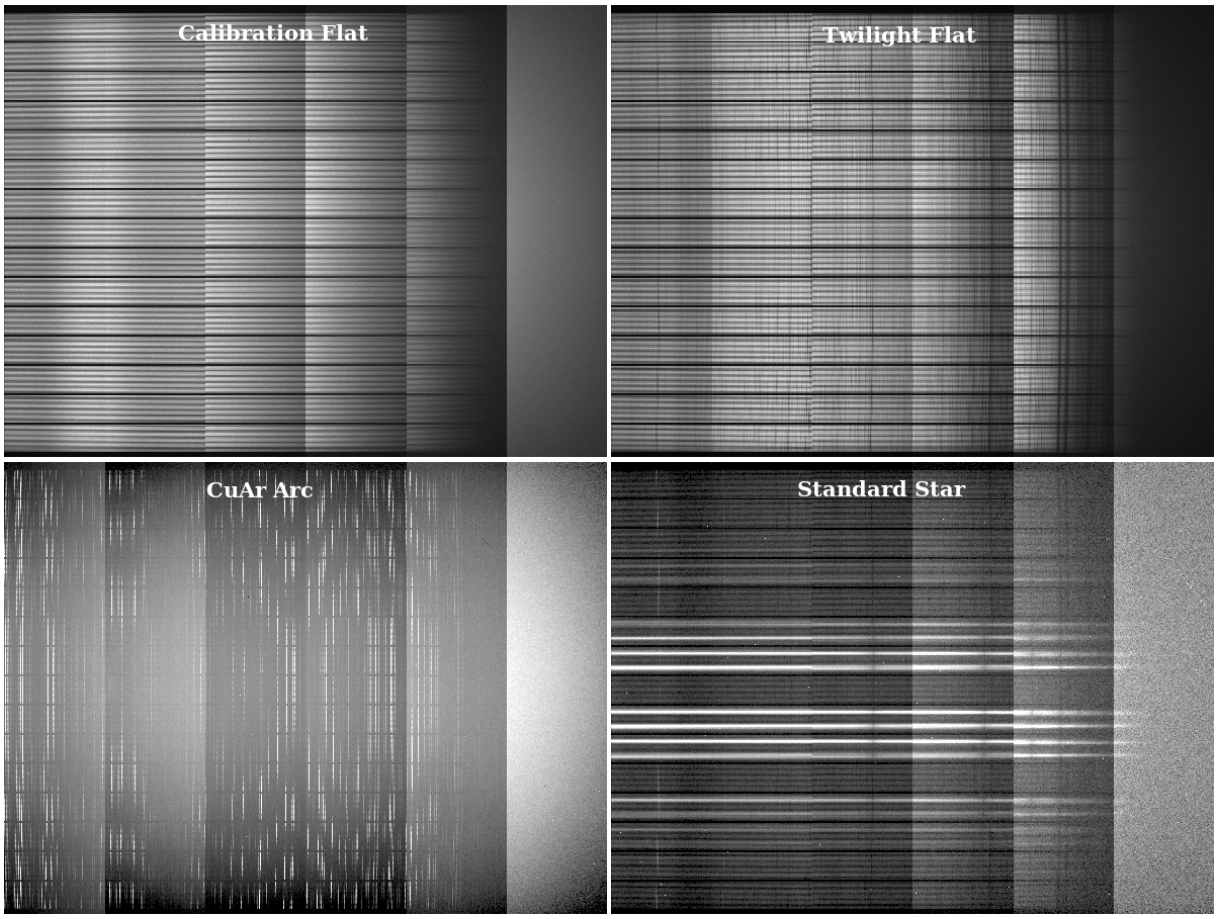

Figure 2.2 – Raw calibration data as registered on CCDs. Upper-left panel: calibration flat, upper-right panel: twilight flat, lower-left panel: CuAr arc, lower-right panel: standard star. On each panel, the six amplifiers readouts illustrated in Figure 2.1 can be easily seen. The CCD image appears featureless at right left end of each panel because the sensitivity of GMOS instrument is low at the blue end. On the CuAr CCD image (lower-left panel), multiple emission lines from the CuAr arc can be seen as bright vertical lines.

calibration data taken using a blue grating (B600). Figure 2.3 shows an example CCD image of science data taken in the one-slit mode using blue and red gratings. A set of bias frames is also needed to create the master bias for determining the noise level of CCD and bias-correcting the data. All raw data (science and calibration) must be first pre-reduced which includes bias-subtraction and internal gain correction of the amplifiers. Since arcs are acquired in fast read mode, pre-reduction of arcs involves only overscan-subtraction rather than full bias-subtraction.

2.3.2 Reducing flats & creating the response curve

The lenslets/fibres correspond to the spatial position of each observed element of science object. While reducing the calibration flat, I first inspected each of the 750 fibres in one-slit mode (and 1500 fibres in two-slit mode), and masked missing fibres and assigned the correct identification number to each fibre (Figure 2.4). This is a critical step of GMOS IFS data reduction and if

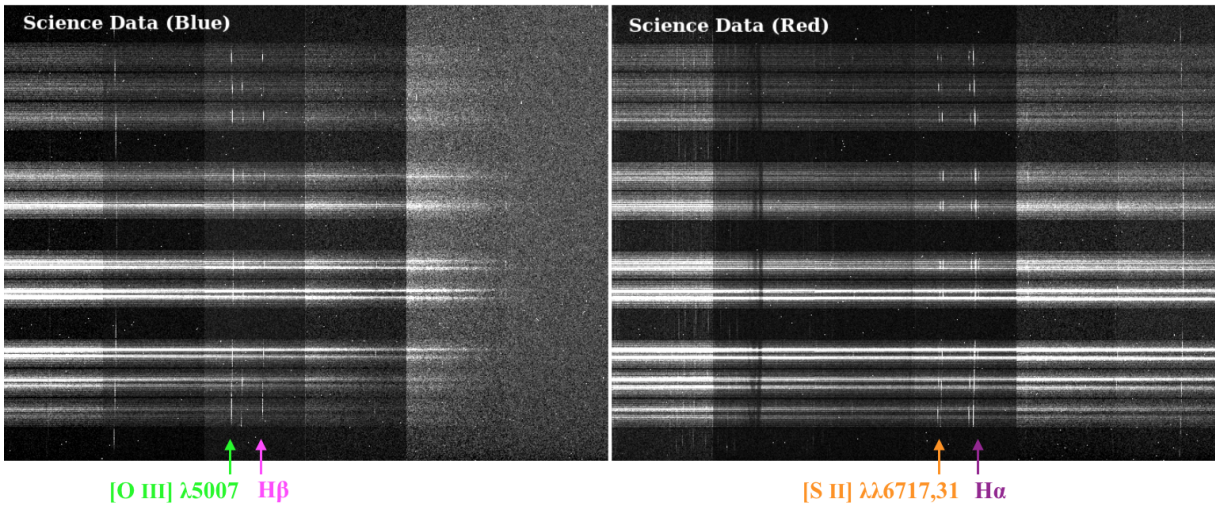

Figure 2.3 – Raw science data taken in the one-slit mode using blue (left panel) and red gratings (right panel). On both panels, 'bright' vertical straight lines are emission lines (for example, Hβ, [O III] λ5007, Hα, [S II] $\lambda\lambda$6717, 6731) as indicated. Note that wavelength is increasing left-ward on the CCD image. On the right panel, 'dark' vertical lines denote telluric/atmospheric absorption lines. The sensitivity of the blue end of GMOS-IFU is weaker than the red end, which is evident from a comparison of the two raw science frames. Cosmic ray hits appear as random bright marks in science data but are negligible in calibration files in Figure 2.2.

incorrect, fibre mis-identification cannot be identified until the datacube is made (Figure 2.5). The next step is to trace apertures corresponding to each fibre, which is primarily mapping their exact positions on the CCDs by fitting a suitable function (for example Chebyshev). In doing so, it is essential to choose a suitable number of rows and columns to be summed to identify and trace apertures, otherwise problems may occur due to oversampling or cross-talk between fibres (Figure 2.6, upper panel). Since the blue end of the GMOS-instrument has low sensitivity, I also tuned the range of columns used for tracing apertures (Figure 2.6, lower panel). After correctly tracing the apertures, the spectrum stored in each fibre is extracted by summing pixels within $\pm$2.5 pixels of the centre of each fibre, and stored as row-stacked spectra (Figure 2.7).

Using the calibration flat as the reference, the same steps are applied to reduce twilight flats as well, though an interactive procedure at this step is generally not needed. Using the extracted spectra from the calibration flats and twilight flats, a response map of relative fibre throughputs can now be created.

2.3.3 Wavelength calibration

To establish the wavelength calibration, I first pre-reduced the CuAr arcs and extracted arc spectra corresponding to each fibre using calibration flat spectra as the reference. To establish a wavelength-solution for each fibre, I chose approximately 20 emission lines using NASA's

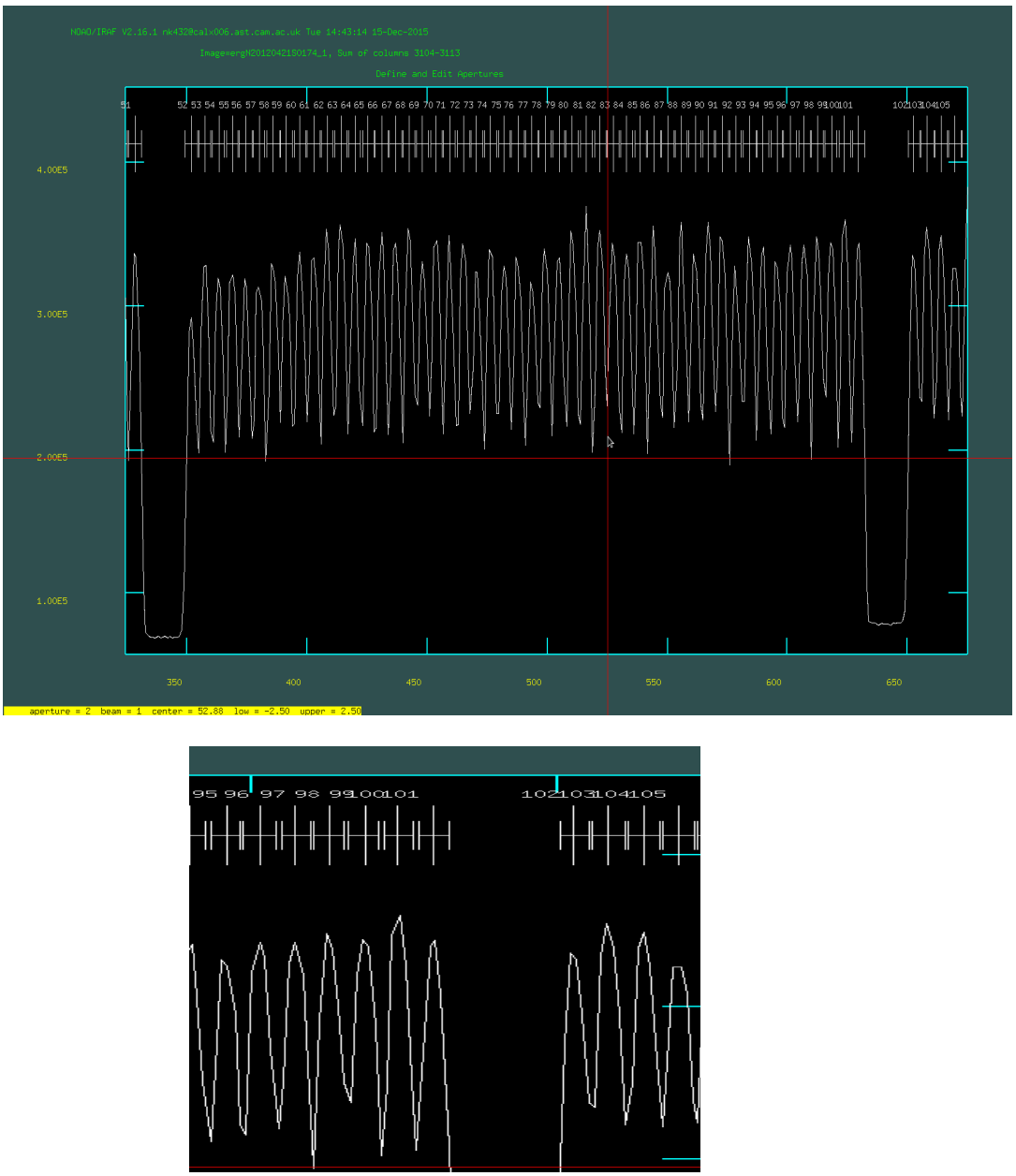

Figure 2.4 – Fibres in GMOS-IFU are arranged in blocks of 50 fibres, with the first one in each block starting with x1 (1, 51, 101, ...) and the last one with x0 (50, 100, 150,...). Upper panel: interactive IRAF window showing zoomed-in to a block of 50 fibres. Lower-panel: a small section of IRAF window showing that each fibre's position is misaligned (shifted by one). Fibres must be assigned the correct identification numbers for subsequent spatial mapping to create the correct data cubes.

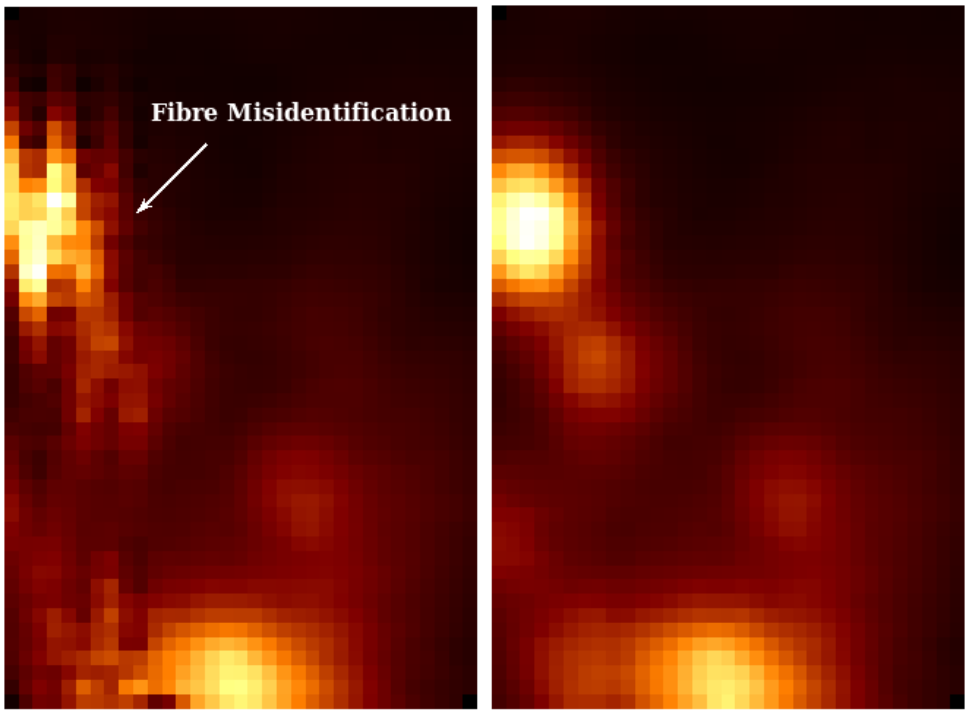

Figure 2.5 – Both panels show the same wavelength plane ($\lambda \sim 5007$ Å) in the final data cubes of NGC 4670 before (left panel) and after (right panel) correct fibre identification. The GMOS-FOV covers four H II regions. On the left panel, the two H II regions can hardly be seen as almost one-third of the fibres are misidentified, whereas the right panel shows all of the regions very clearly.

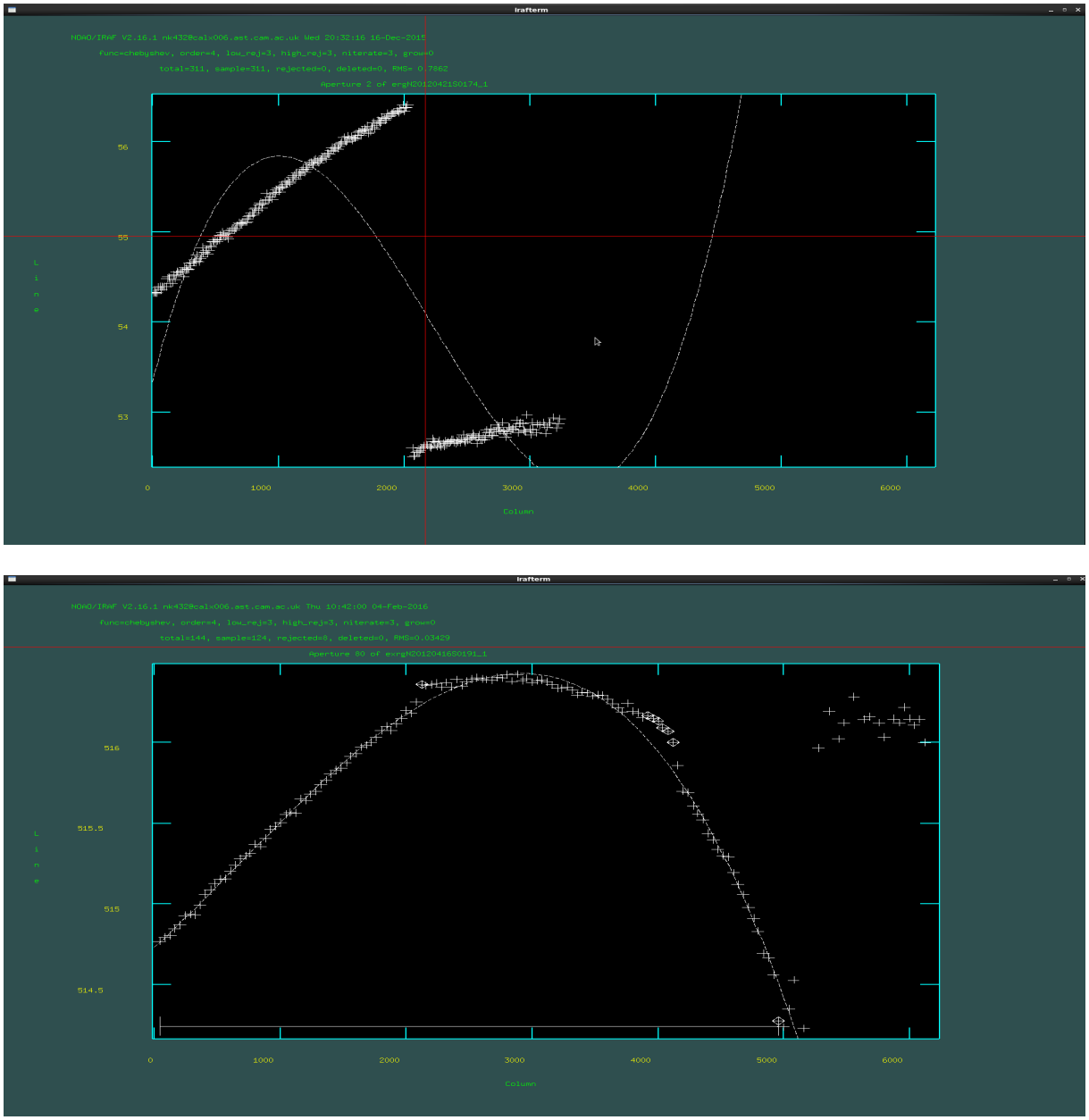

Figure 2.6 – Upper panel: An example of incorrect fibre trace due to oversampling of columns and cross-talk of fibres. Lower panel: Aperture trace is determined only in a selected column range and excluding the pixels corresponding to the less sensitive blue end of the GMOS-instrument (right end in above figure).

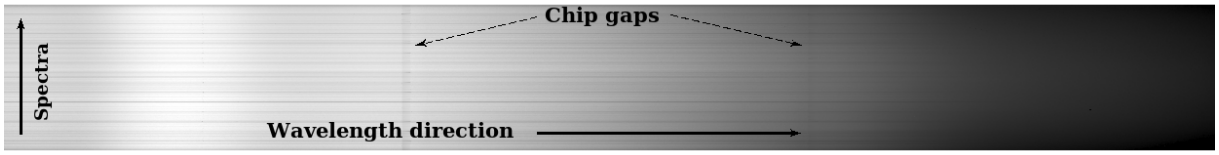

Figure 2.7 – An example of row-stacked spectra (RSS) for a calibration flat. 750 spectra are stacked on top of each other. Interpolation across chip gaps between two CCDs can also be seen in the RSS.

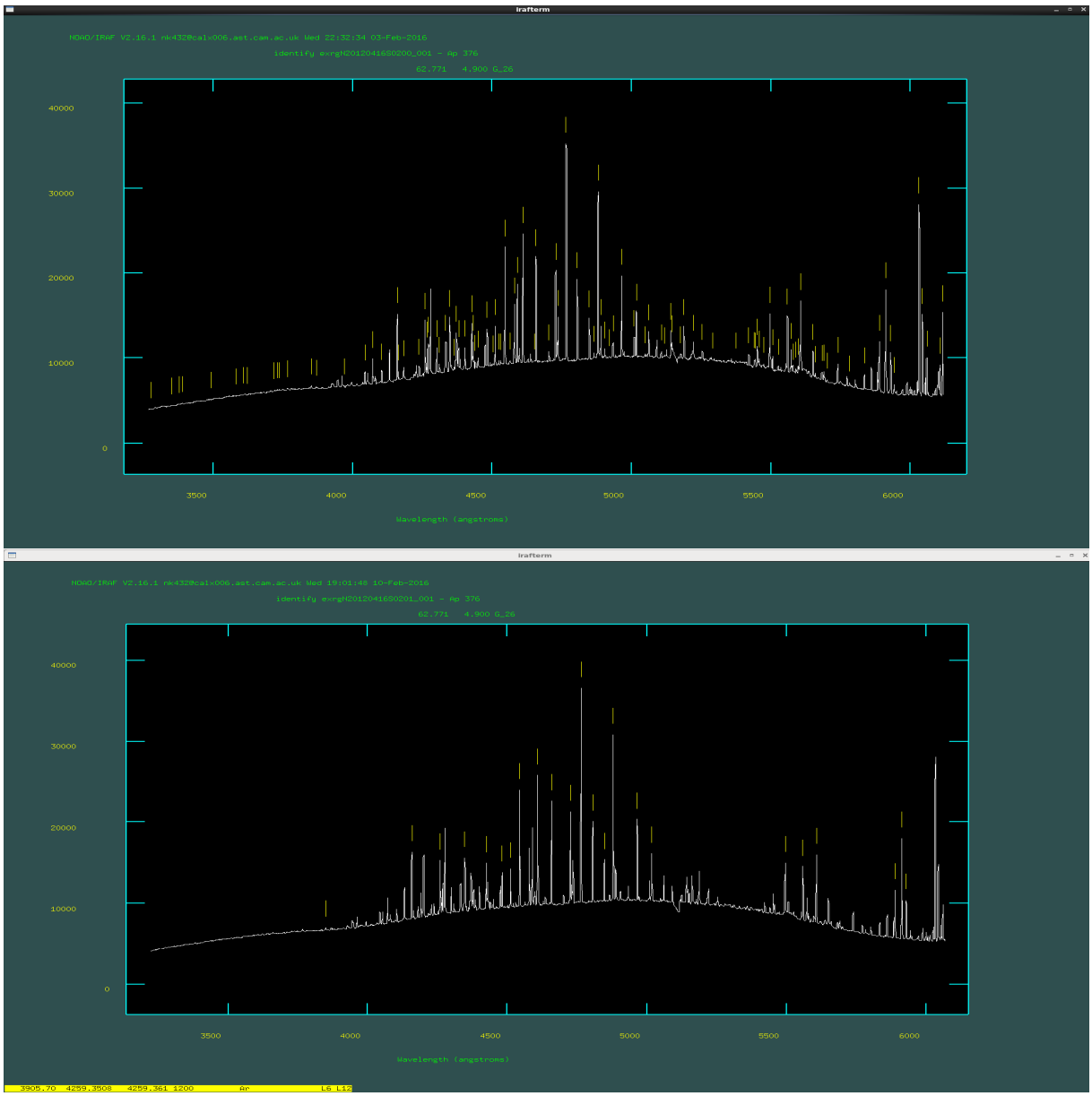

Figure 2.8 – Upper panel: the GEMINI database for CuAr arc lamp identifies emission lines (marked as yellow lines), many of which are spurious. Lower panel: For wavelength calibration, roughly 20 emission lines were chosen, most lines were selected in the centre and a few lines at the two wavelength ends. It is essential to select at least a few lines at the ends to ensure that the wavelength calibration is not skewed near the extremities.

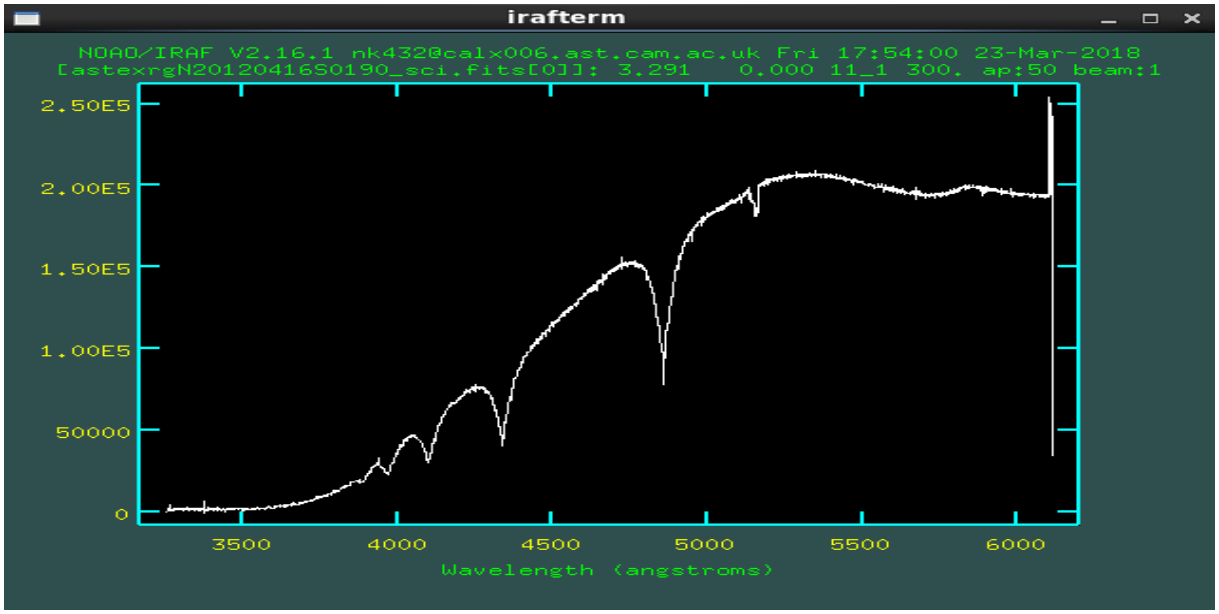

Figure 2.9 – Standard star spectrum obtained after summing all spectra of standard star observation.

CuAr database (Figure 2.8) and used a Chebyshev function (of a suitable order) to map the transformation between the arcline wavelengths and pixel coordinates. The choice of emission lines and function is important to have a reasonable rms (root mean square) error in the fit. For example, the typical rms value for my analysis was < 0.1 Å for all spectra. This rms value combined with the number of fitted emission lines corresponds to velocity errors of ~ 3 km s^{-1} and ~ 2 km s^{-1} at the (approximate) central wavelengths 5000 Å and 7500 Å respectively of the blue and red gratings. These rms values are less than the typical velocity dispersion or rotational velocity in the interstellar medium. Hence, in general, the wavelength calibration accuracy is sufficient for the science requirements. Sometimes the zero-point of wavelength calibration (generally for the red grating) was found to have drifted from arc lamp solution. This problem can be corrected by comparing redshifts obtained from other sets of observations, or by applying wavelength calibration to the twilight flat and inspecting skylines.

The value of the instrumental broadening (full width at half maximum) was determined by fitting a Gaussian profile to several emission lines of the extracted row-stacked spectra of the arc lamp and found to be ~ 1.7 Å for both blue and red settings, corresponding to a resolution of ~ 102 km s^{-1} and ~ 85 km s^{-1} at 5000 Å and 6000 Å, respectively.

2.3.4 Flux calibration

After pre-reduction, the standard star data were reduced using spectra of calibration flats as a reference, flat-fielded by applying the response map from the throughput functions and finally extracting spectra corresponding to the 750 apertures. Reduction of the standard star also in-

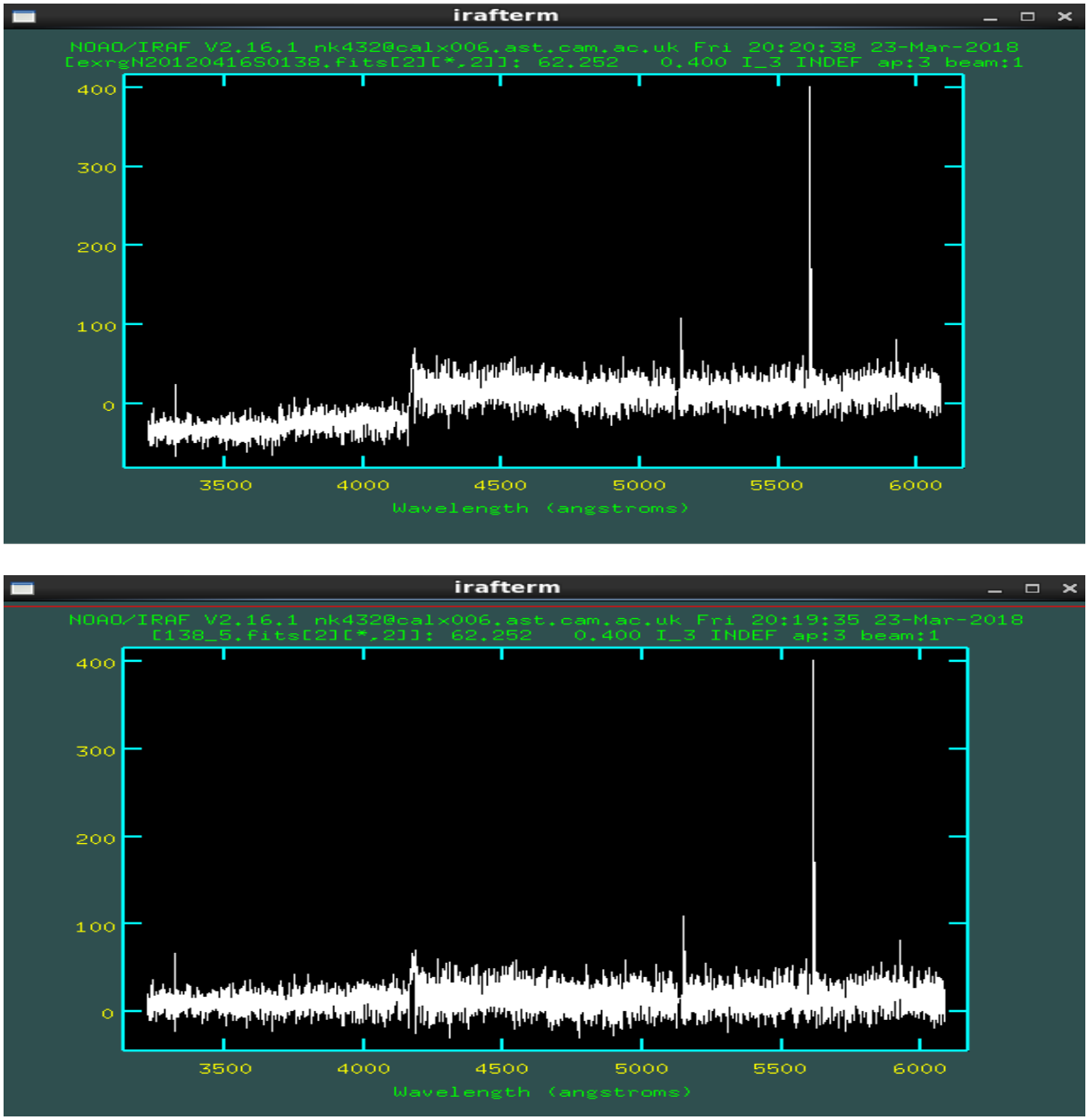

Figure 2.10 – Upper panel: an example spectrum in science data which shows offsets of approximately 50 counts (left-hand side). Lower panel: same spectrum after offset correction.

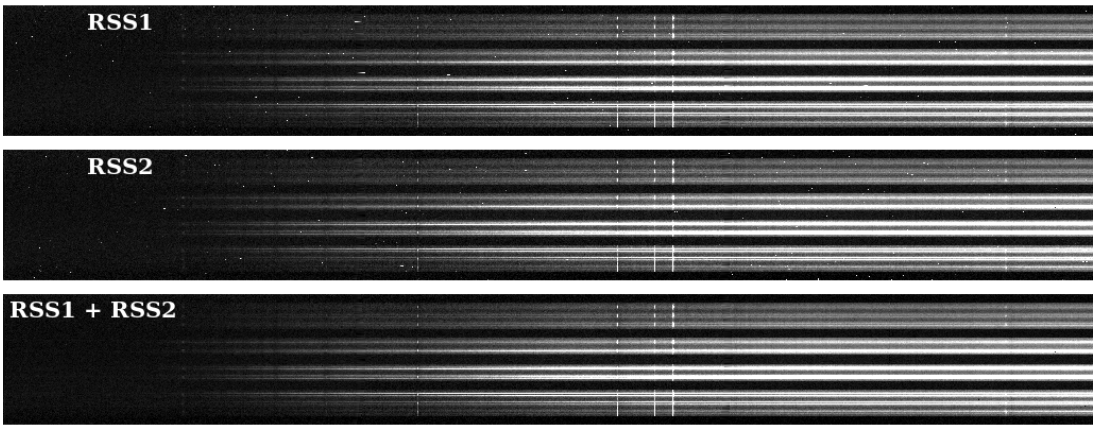

Figure 2.11 – An example of removing cosmic rays while combining two row-stacked spectra (RSS 1 in the upper panel and RSS 2 in the lower panel) to get the final RSS. Cosmic ray hits can be identified as random white marks in the two upper panels.

volved subtraction of the mean sky spectrum and the usual wavelength calibration. Finally all spectra were summed to get the standard star spectrum (Figure 2.9), which was used to determine the sensitivity function, i.e. the instrumental sensitivity as a function of wavelength. This step was carried out interactively to correctly define the band passes and exclude any unphysical feature.

2.3.5 Science data reduction

To reduce the science data, the aperture traces from the calibration flats were used, followed by flat-fielding using the throughput function derived from the twilight flat and then the spectra were extracted. Inspecting each of the spectra individually, I found that there was an offset of approximately 50 counts between the branches of spectra from the second and the third detectors. A similar but mild jump was also observed between the spectra from the fifth and sixth amplifiers. I statistically determined the jump correction between the three amplifiers and corrected the spectra before performing the flux calibration (Figure 2.10). Note here that these jumps were also observed in the spectra of the standard star, but were not corrected because the effect was nullified in the summed spectrum of the standard star which was eventually used for generating sensitivity functions for flux calibration. After correcting for the jumps, the flux calibration from the standard star was applied to the science observation in the corresponding setting, yielding the flux calibrated spectra of the science targets.

When multiple observations were taken in a setting, the wavelength- and flux-calibrated RSSs were combined by taking the average of multiple RSSs. Cosmic rays (CRs) were also removed by a sigma-clipping method (Figure 2.11). CRs can also be removed through a sigma-clipping routine implemented in IRAF. After CR rejection, the RSS are converted into three-dimensional data cubes using a standard IRAF procedure which also takes into account the

differential atmospheric refraction. A spatial sampling of 0.1 arcsec is adequate to preserve the critical sampling of GMOS-IFU. However, for the analysis in this thesis, I tuned the data cube spatial sampling according to the science objectives, and took into account the seeing FWHM when needed. For example, the data cube of NGC 4449 (Chapter 3) was created with a spatial sampling of 0.3 arcsec, to confirm the shock ionisation on the emission-line diagnostic diagram, i.e. data points lying beyond the Kewley curve (see Figure 3.9).

2.3.6 Aligning and combining data cubes

For NGC 4449 and NGC 4670, at the end of the above reduction procedure, four data cubes were obtained: two in the blue settings with spectral and spatial offsets, and similarly two more in the red settings with similar offsets. For each wavelength setting, the cubes were combined to create a larger cube covering the complete FOV from each cube and corrected for spectral dithering through linear-interpolation between wavelength planes. The FOV covered by the red and blue gratings also showed spatial offsets (0.1–0.3 arcsec) on one or both axes for some observations. The offsets were determined either by cross-correlating the continuum maps in each setting or by comparing the contours of Hα and Hβ emission line maps. Each combined data cube was then trimmed and the analysis concentrated on the overlapping area of the FOVs covered by the two wavelength settings. The data cubes were then converted to row-stacked spectra for spectral line fitting and flux extraction in the required emission lines for the analysis presented in Chapters 3, 4 and 5.

3

Central H II region in NGC 4449

3.1 Introduction

Galaxy formation and evolution is regulated by a complex interplay between star-formation, chemical abundance and gas dynamics. Stars form from cool gas, which is either formed in-situ in the galaxy or is accreted from the circum/inter-galactic medium or the merger progenitors. Metals form in stars and are ejected into the interstellar medium (ISM) by subsequent supernova explosions. The metal-enriched gas can get dispersed in the ISM due to the internal gas dynamics of the ISM or get transported out of the galaxy via supernova-driven outflows or galactic winds. This intricate ballet of gas flows in to, out of and within galaxies can lead to chemical inhomogeneities in the gas across the star-forming galaxies (Cresci et al., 2010; Kewley et al., 2010; Davé, Finlator & Oppenheimer, 2011; Sánchez Almeida et al., 2013, 2014b, 2015; Ceverino et al., 2016), and manifest itself in the form of ordered/disordered kinematics and photo/shock-ionisation of the ISM. Detailed spatially-resolved kinematical and chemical studies of star-forming regions can hence unravel some of the secrets of the key mechanisms involved in galaxy formation and evolution. However, a definitive picture can only be obtained by carrying out detailed analyses in star-forming systems across cosmic history – at low and high redshifts. The limited sensitivity and precision of present technology prevent us from studying the high-redshift star-forming systems in detail. Fortunately, the local Universe hosts a variety of analogues to the high-redshift star-forming galaxies, such as blue compact dwarf

galaxies (BCDs), tadpole galaxies, extremely metal-poor galaxies (XMPs), green pea galaxies etc., which can be studied in great detail because of their proximity and hence enable us to probe and predict the properties of high-redshift galaxies. BCDs are low metallicity (1/40 – 1/3 $Z_{\odot}$; Kunth & Östlin, 2000) star-forming galaxies, as such, they are thought to be excellent local analogues/proxies for high-redshift galaxies (Searle & Sargent, 1972b) and hence provide the best local laboratories to study the primordial Universe in detail.

BCDs have been the focus of many imaging (e.g. Papaderos et al., 1996b,a; Cairós et al., 2001b,a; Gil de Paz, Madore & Pevunova, 2003; McQuinn et al., 2010; Roychowdhury et al., 2012; Janowiecki & Salzer, 2014), spectroscopic (e.g. Izotov & Thuan, 1999, 2004, 2016; Bergvall & Östlin, 2002; Wu et al., 2006; Guseva et al., 2011) and integral field spectroscopic (IFS) studies (e.g. James et al., 2009; James, Tsamis & Barlow, 2010; James et al., 2013a; Kehrig et al., 2016; Lagos et al., 2016) for over two decades. IFS is the best available technique to study these galaxies which host H II (star-forming) regions, because it not only allows us to access information encoded in the emission lines from the star-forming regions but also enables us to *map* the spatial distribution of the information (i.e. physical and chemical properties) from them.

NGC 4449 is a nearby ($\sim 3.79 \pm 0.57$ Mpc), spectacularly luminous ($M_B = -18.2$) BCD (Ann, Seo & Ha, 2015), which has been studied extensively using multiwavelength data. In this Chapter, I present spatially-resolved observations of the central H II region in NGC 4449 taken with the integral field unit (IFU) on the Gemini Multi Object Spectrograph North (GMOS-N). Please see Chapter 2 for details of data observation and reduction. At the end of data reduction, data cubes were produced with a spatial-sampling of 0.3 arcsec per spaxel. The IFS data has enabled the study of the chemical and physical properties of this star-forming region at a resolution of 0.6 arscec, 11 pc (i.e. seeing FWHM) and a spatial scale of 5.5 pc per spaxel. In addressing the questions related to homogeneity, ionisation mechanisms and stellar properties asked in Chapter 1, I aim to spatially-resolve the chemical and kinematic patterns in the central star-forming region of NGC 4449, and explore the interplay between star-formation, chemical abundance and gas kinematics/dynamics.

Figure 3.1 shows the Sloan Digital Sky Survey (SDSS) image of NGC 4449 taken in r band with the region of the *Hubble Space Telescope (HST)* cutout shown in Figure 3.2 (highlighted). General properties of NGC 4449 are given in Table 3.1. It is also classified as a Magellanic-type irregular galaxy, with a high star formation rate (SFR) [current SFR $\sim$ 0.5–1.5 $M_{\odot}$ yr^{-1}, Hill et al. (1998); Hunter et al. (1998); Thronson et al. (1987)] and low metallicity [12 + log(O/H) $\sim$ 8.3, Lequeux et al. (1979); Martin (1997)]. High-resolution imaging of this galaxy by the HST (Figure 3.2) reveals populations of young and old stellar clusters which is indicative of an active star-formation history (Annibali et al., 2011). Long-slit échelle spectroscopy has revealed interesting kinematic features in NGC 4449 - expanding bubbles, supergiant shells and high-velocity filaments, along with diffuse ionised gas (Bomans & Weis, 2014; Hunter & Gal-

Table 3.1 – General Properties of NGC 4449

Parameter	NGC 4449
Other designation	UGC 07592
Morphological Type	IBm
R.A. (J2000.0)	12:28:11.09
DEC (J2000.0)	44:05:37.06
Redshift (z)[a]	0.00069±0.00001
Distance (Mpc)[a]	3.79±0.57
inclination (°)[a]	60
Helio. Radial Velocity(km s^{-1})[a]	207±4
E(B-V)[b]	0.017±0.001

[a] Taken from NED
[b] Foreground Galactic extinction (Schlafly & Finkbeiner, 2011)

lagher, 1997). The heavy-element (O I, Si II, Fe II) absorption lines of NGC 4449 suggest the occurrence of turbulent broadening within the neutral gas (James et al., 2014). Radio observations of this galaxy suggest that it is embedded in a large halo of H I gas which is rotating in the opposite direction to that of the main stellar component (Bajaja, Huchtmeier & Klein, 1994). The H I morphology and the velocity field indicate that the galaxy might have undergone an interaction with DDO 125 which is at an apparent separation of 41 kpc from the centre of NGC 4449) and is hypothesised to channel gas into the centre of NGC 4449 (Hunter et al., 1998). Martínez-Delgado et al. (2012) resolved a stream of red giant branch stars in the halo of NGC 4449 and thus speculated a scenario of "stealth" merger which possibly triggered the starburst in this galaxy. The merger events can also possibly lead to variation in the metal content of the galaxy. Hence, NGC 4449 is an excellent target to study the three questions mentioned in Chapter 1, linking star-formation, metallicity and gas kinematics.

The Chapter is organised as follows: Section 3.2 presents the preliminary procedures required for data analysis. Section 3.3 gives the spectral decomposition of the strong Hα emission line, kinematics of different components, and their role in the ionisation of the surroundings of the H II region is presented in Section 3.4. In Section 3.5, I give a detailed chemical abundance analysis by mapping metallicity using direct and indirect strong line methods; and also explore the chemical variation. Section 3.6 presents the analysis on age-dating the stellar population, and star-formation. I present the interpretation of this analysis in Section 3.7. Section 3.8 summarises the major findings. Throughout this work, I have assumed the solar metallicity of 12 + $\log(O/H)_{\odot}$ = 8.69 (Asplund et al., 2009).

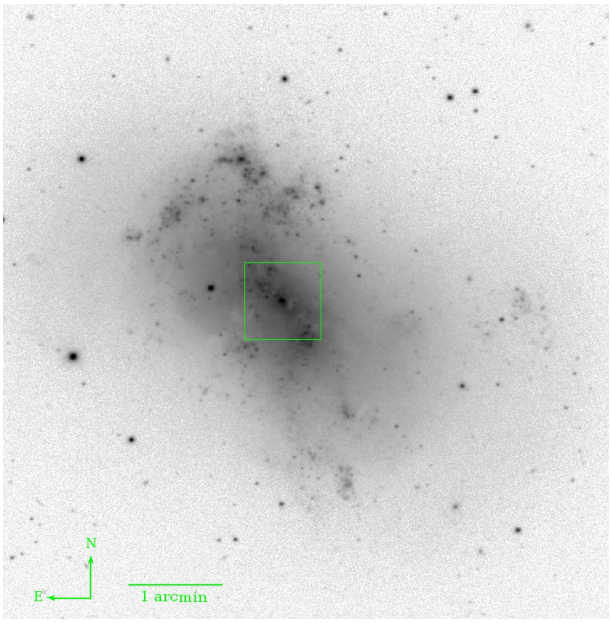

Figure 3.1 – SDSS image of NGC 4449 taken in r-filter. The green square box denotes the region covered by the HST image shown in Figure 3.2.

3.2 Observed and Intrinsic Fluxes

3.2.1 Integrated Spectra & Flux Maps

Figure 3.2 shows the HST image of NGC 4449 taken in the filter F660N. The green box in the central region of the galaxy represents the GMOS aperture (3.5 arcsec $\times$ 5 arcsec), and the magenta box inside the green box shows the main emission region covering an area of 1.2 arcsec $\times$ 1.2 arcsec ($\sim$ 22 $\times$ 22 pc). Figure 3.3 shows the GMOS-IFU integrated spectra of NGC 4449 integrated over the main (bright) emission region of 1.2 arcsec $\times$ 1.2 arcsec (upper two panels), and integrated over the remaining spaxels in the FOV (Whole FOV – main emission region, lower two panels) to highlight the difference, e.g. some of the weaker lines e.g. [O I] λ5577, He I λ6678, [O II] λ 7319) are present either in the main emission region or in the integrated spectra over the remaining spaxels of the FOV. The principal emission lines are over-plotted at their rest wavelengths in air.

I measure the emission line fluxes for all the main recombination and collisionally excited lines within the spectra by integrating the fluxes within the line after subtracting a local linear continuum and absorption features (in recombination lines) modeled by either a Gaussian or a parabola in the spectral range of interest. The uncertainty on fitting the continnum is negligible compared to the uncertainty on the estimated flux in the emission line. The observed flux for the emission lines used in the present analysis for the main emission region is given in Table 3.2. Figure 3.4 shows the observed flux maps of NGC 4449 of the continuum, [O III] λ5007, Hβ and [O II] $\lambda\lambda$3726, 3729 (summed as they are blended), [S II] λ6731 and [N II] λ6583. The

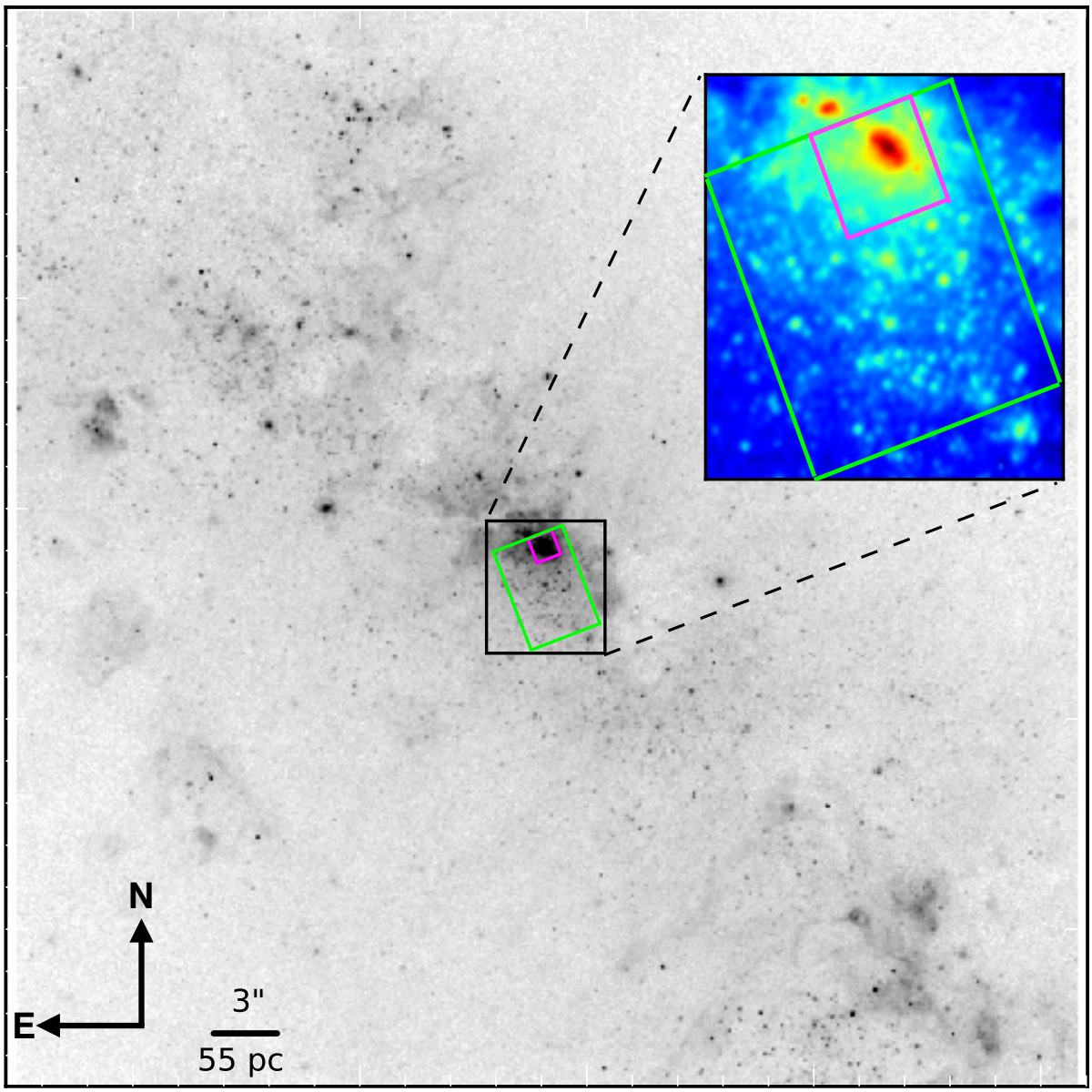

Figure 3.2 – HST image of NGC 4449 taken in the filter F660N centred at (RA, Dec) : (187.04657, 44.093941). The green box in the central region of the galaxy represents the GMOS aperture (3.5 arcsec $\times$ 5 arcsec). The magenta box inside the green box shows the main emission region. The HST image has a spatial scale of 0.05 arcsec pixel^{-1} (0.92 pc pixel^{-1}) and are 51.2 arcsec $\times$ 51.2 arcsec in size. The upper-right inset is obtained by superimposing HST images in three filters F502N (blue), F550M (green) and F660N (red) and is in log scale.

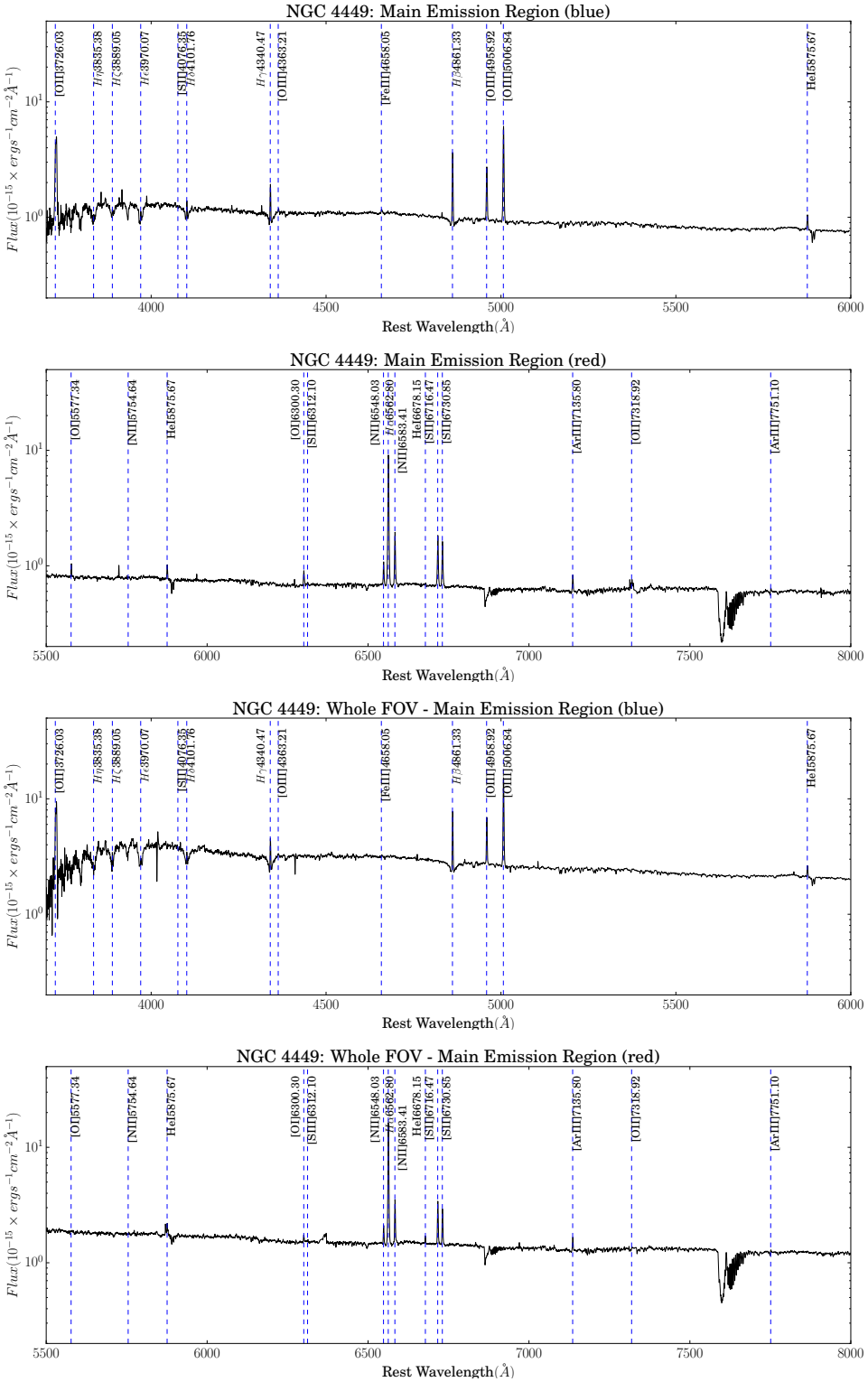

Figure 3.3 – GMOS-IFU integrated spectra of NGC 4449 integrated over the main (bright) emission region of 1.2 arcsec × 1.2 arcsec (upper two panels), and integrated over the remaining spaxels in the FOV (whole FOV – main emission region, lower two panels) for each grating (red and blue) (see Figure 3.2). The principal emission lines are over-plotted at their rest wavelengths.

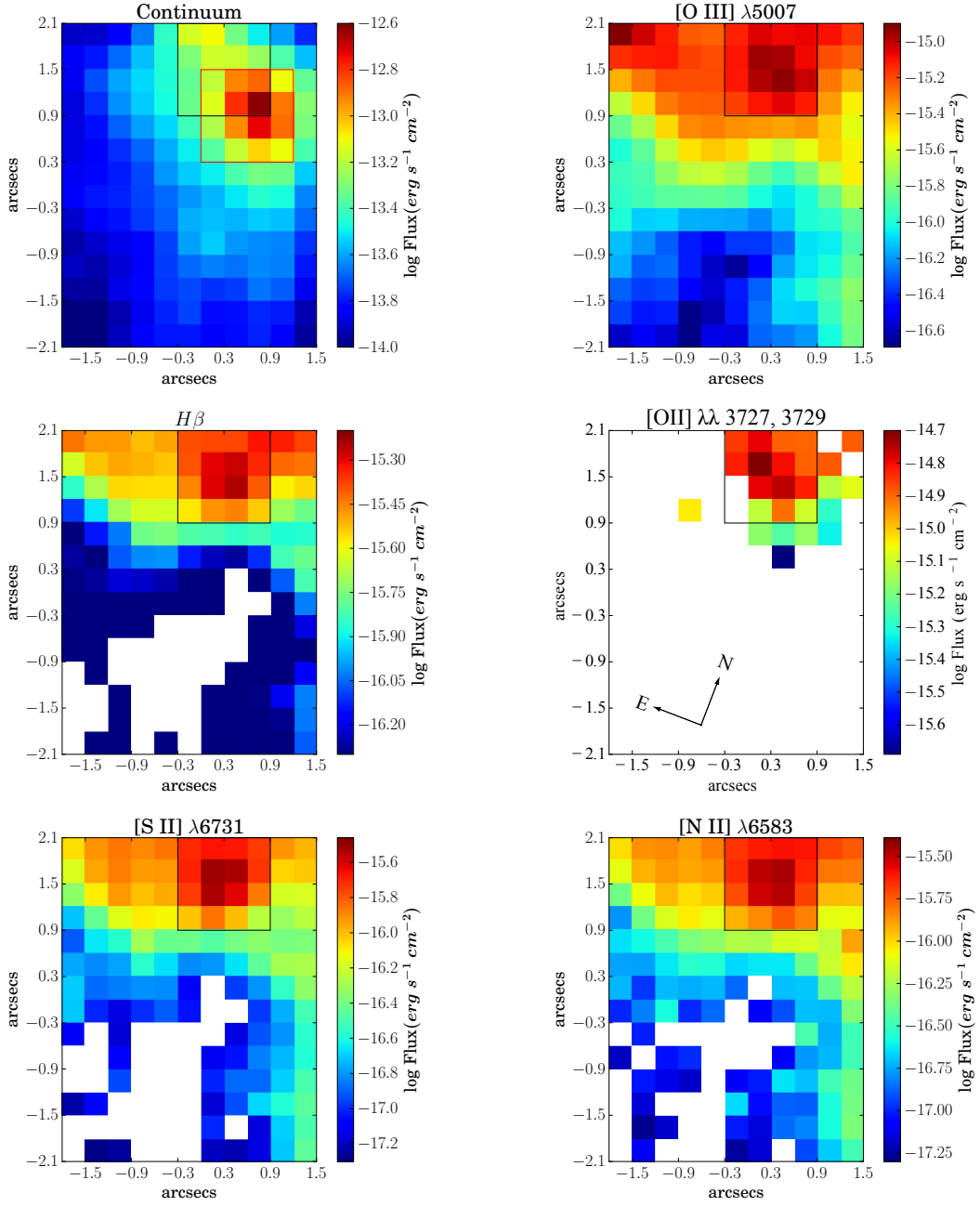

Figure 3.4 – Observed emission line flux maps of NGC 4449: Continuum (5216.03–5971.46 Å), [O III] λ5007, Hβ, [O II] $\lambda\lambda$3726, 3729, [S II]λ6731, [N II] λ6583.An offset ($\sim$ 15 pc) is observed in the continuum (red box) and emission line (black box) peaks. White spaxels correspond to the spaxels in which emission/flux have S/N $<$ 3.

Table 3.2 – Emission line measurements (relative to Hβ = 100) for the summed spectrum of the main emission region. Line fluxes (F_λ) were extinction corrected to calculate I_λ using the c(Hβ) shown at the bottom of the table.

Line	λ_{air}	F_λ	I_λ
$[OII]$	3726.03	319.54 ± 5.52	397.20 ± 15.70
$[OIII]$	4363.21	4.05 ± 0.94	4.44 ± 1.04
$H\beta$	4861.33	100.00 ± 0.66	100.00 ± 2.26
$[OIII]$	4958.92	71.03 ± 0.76	69.95 ± 2.24
$[OIII]$	5006.84	214.22 ± 1.58	209.20 ± 6.46
$[NII]$	6548.03	17.02 ± 0.34	13.68 ± 0.45
$H\alpha$	6562.8	356.61 ± 2.41	286.00 ± 7.73
$[NII]$	6583.41	55.93 ± 0.51	44.77 ± 1.24
$[SII]$	6716.47	53.50 ± 0.49	42.27 ± 1.16
$[SII]$	6730.85	45.90 ± 0.45	36.20 ± 1.00
c(Hβ)		0.31 ± 0.01	
F(Hβ)		6.61 ± 0.04	13.35 ± 0.30

Notes: F(Hβ) in units of $\times$ 10^{-15} erg cm^{-2} s^{-1}
c(Hβ)= log(I$_\lambda$/F$_\lambda$).

continuum map is created by integrating the blue cube in the emission-free wavelength range 5216.03–5971.46 Å (V-band). A spatial offset ($\sim$ 15 pc) is observed in the continuum and emission line peaks.

The following main sources of errors in the flux measurement were checked: photon noise, readout noise and any uncertainty in the data processing. Since the data acquisition was carried out in slow readout mode, the readout noise ($\sim$ 3 e$^-$ with respect to $\sim$ 500–1000 e$^-$ in emission lines including continuum) is negligible. The continuum levels of the same regions in the FOV (e.g. main emission region) obtained from the red and blue gratings, agree with each other which suggest that the error in defining the continuum level is negligible. Hence, for calculating the error on the observed flux, I assume that photon noise is the dominant source of error. Since photon noise is Poissonian, I calculate the relative error (σ_{rel}) as the inverse of square root of the uncalibrated flux (f_{uncal} in e$^-$) and scale the corresponding calibrated flux to calculate the absolute error (σ_{abs}) on calibrated flux (f_{cal} in ergs cm^{-2} s^{-1} Å^{-1}), i.e.

$$\sigma_{abs} = \sigma_{rel} \times f_{cal} = \frac{\sqrt{f_{uncal}}}{f_{uncal}} \times f_{cal} \tag{3.1}$$

The uncertainties on all quantities in this work are computed by propagating the error on the observed calibrated flux.

3.2.2 Dust attenuation

To estimate dust attenuation, I derive E(B–V) using the relationship between the nebular emission line colour excess and the Balmer decrement given by:

$$E(B-V) = \frac{E(H\beta - H\alpha)}{k(\lambda_{H\beta}) - k(\lambda_{H\alpha})} = \frac{2.5}{k(\lambda_{H\beta}) - k(\lambda_{H\alpha})} log_{10}\left[\frac{(H\alpha/H\beta)_{obs}}{(H\alpha/H\beta)_{theo}}\right] \quad (3.2)$$

where $k(\lambda_{H\beta})$ and $k(\lambda_{H\alpha})$ are the values from the LMC (Large Magellanic Cloud) attenuation curve (Fitzpatrick, 1999) evaluated at the wavelengths $H\beta$ and $H\alpha$ respectively[1], $(H\alpha/H\beta)_{obs}$ and $(H\alpha/H\beta)_{theo}$ are the observed and theoretical[2] $H\alpha/H\beta$ line ratios, respectively. This curve is chosen because the metallicity of NGC 4449 is similar to that of LMC. Lequeux et al. (1979) reports a metallicity of 12+log(O/H) = 8.3, which is close to that of LMC, 8.35±0.06 (Russell & Dopita, 1992).

Figure 3.5 shows the map of E(B-V), which varies from 0.2 to 0.4 mag in the main emission region (black square box). E(B-V) goes as high as 0.8 mag in the south-west of the main emission region. Using the calculation for E(B-V) above, I calculate the extinction in magnitudes at wavelength λ, given by $A_\lambda = k(\lambda)E(B-V)$ and finally calculate the intrinsic flux maps using the following equation:

$$F_{int}(\lambda) = F_{obs}(\lambda) \times 10^{0.4A_\lambda} \quad (3.3)$$

Some spaxels away from the main emission region have negative values of E(B-V) due to stochastic error and shot noise (Hong et al., 2013). I force E(B-V) in these spaxels to the Milky Way "foreground" value (Table 3.1) before calculating intrinsic flux. The intrinsic emission line fluxes derived from the integrated spectra of the main emission region are tabulated in Table 3.2.

3.3 Emission Line Kinematics

I perform a detailed kinematic analysis of the central H II region of the galaxy by separating different spectral components of the strong Hα emission line. Figure 3.6 shows different types of kinematic structure present at various locations in the Hα map of the GMOS FOV. I used an IDL-based curve-fitting software PAN (Peak ANalysis) to fit multiple spectral components to the Hα emission line, which is based on χ^2–minimisation. To determine the optimal number of spectral components, I experiment with single, double, and triple Gaussian fits. I found that a double Gaussian fit resulted in the value of χ^2 significantly lower than that of the single Gaussian fit, while an attempt to fit the third component resulted in the Gaussian fits with either the FWHM of the third Gaussian less than the instrumental FWHM or unreasonable fits for a

[1]Note here that it is customary to calculate the total E(B-V) by averaging the E(B-V) from Hα/Hβ and Hγ/Hβ in the ratio 3:1. However, I have only used Hα/Hβ here as the Hγ emission line is excessively noisy.

[2](Hα/Hβ)$_{theo}$ was assumed to be 2.86.

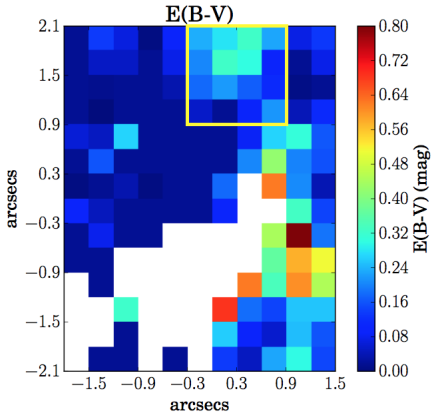

Figure 3.5 – E(B-V) map of the FOV, which varies from 0.2–0.4 mag in the main emission region (yellow square box). E(B-V) goes as high as 0.8 mag to the south-west of the main emission region. White spaxels correspond to the spaxels in which emission line fluxes had S/N < 3.

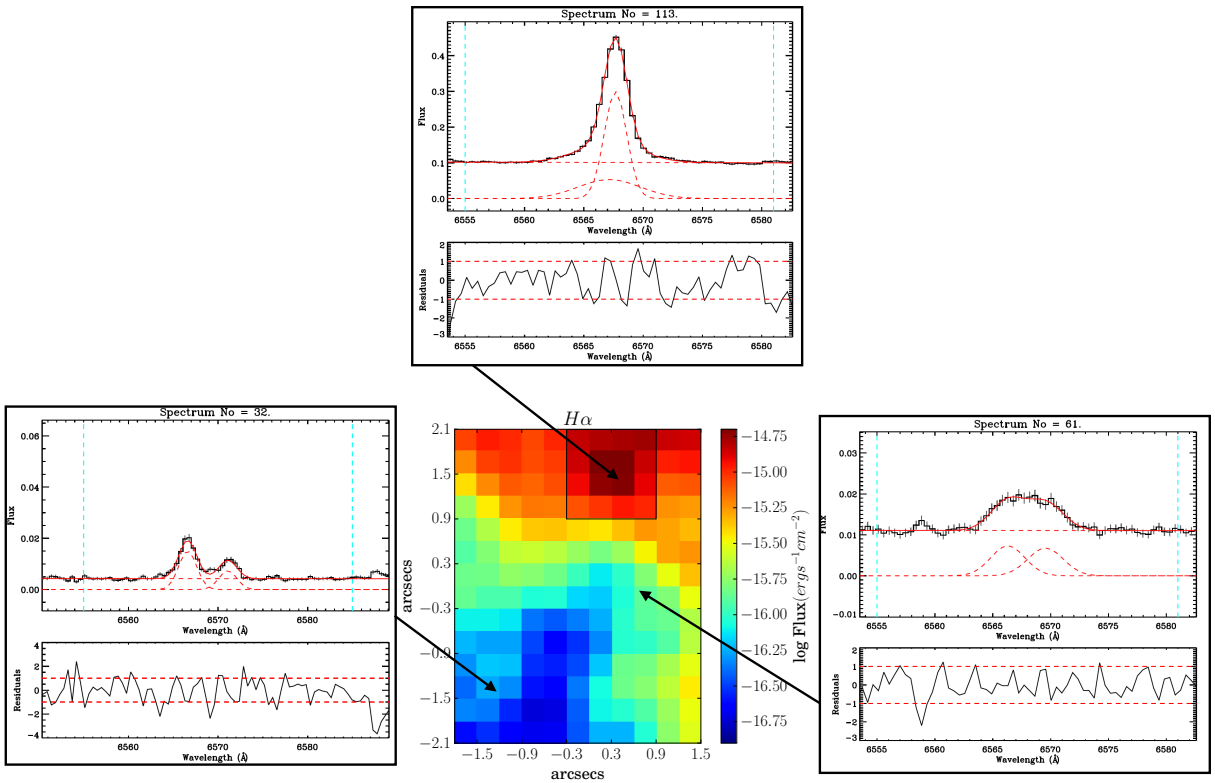

Figure 3.6 – Spectral decomposition of the Hα emission line showing different kinematic structures at different locations of the FOV. The Hα emission line map is created by summing the flux in the spectral region of interest and takes into account the flux in both of the spectral components. The black square box on the Hα emission line map shows the main emission region. In each of the panels showing the Gaussian fits, flux is in units of 10^{-15} erg cm^{-2} s^{-1} Å^{-1}, and residuals are normalised to be in σ-noise units.

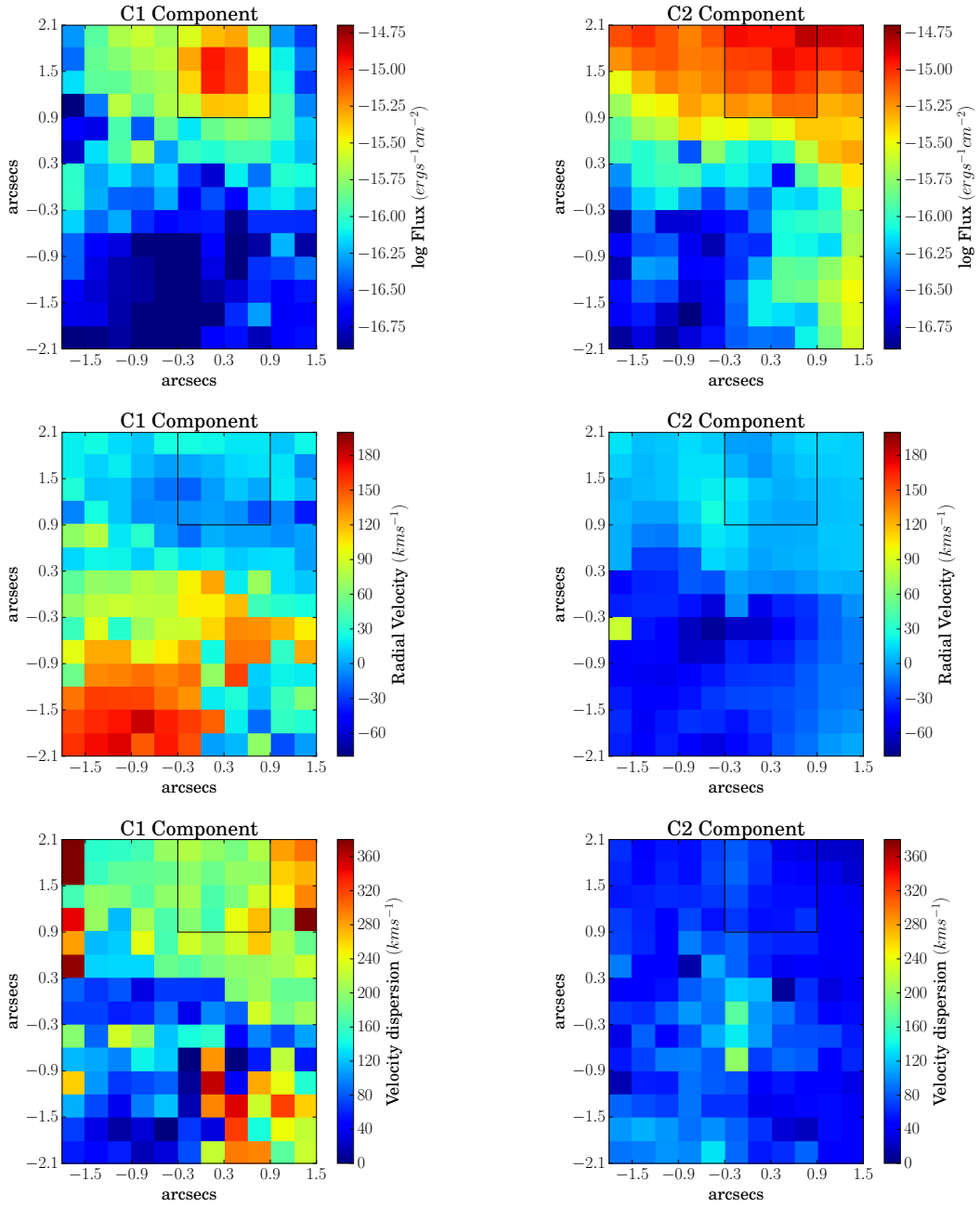

Figure 3.7 – Hα maps of the two spectral components: C1(left) and C2(right). I assign the broad spectral component to C1 and the narrow spectral component to C2. When spaxels have two spectral components with comparable velocity widths, I assign the component with higher radial velocity to C1 and the component with lower radial velocity to C2. Observed flux (upper panel); radial velocity (middle panel) relative to systemic velocity of v_{sys} = 207 km s^{-1}; and velocity dispersion/FWHM (bottom panel) corrected for instrumental broadening. The black square box shows the main emission region. The North-East orientation is shown in Figure 3.4.

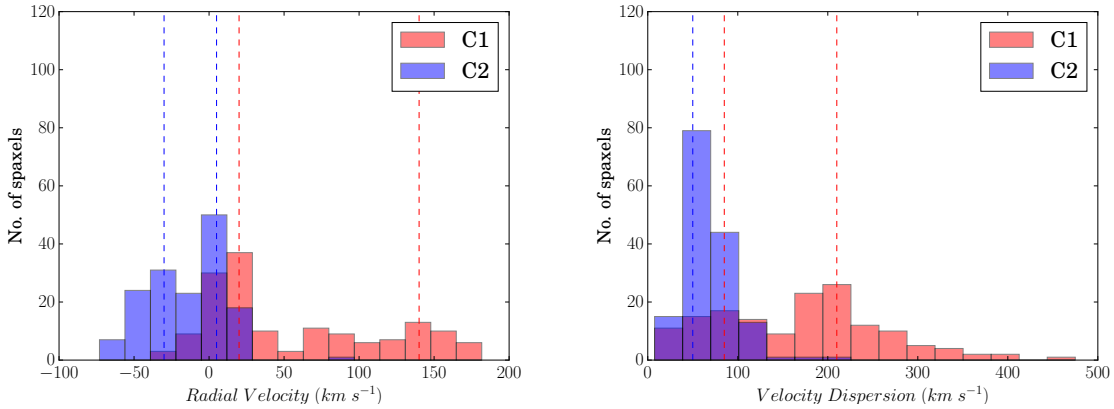

Figure 3.8 – The distributions of radial velocity (left) and velocity dispersion (FWHM) (right) of the two kinematic components of Hα emission line. C1: red, C2: blue for both distribution and the dashed vertical lines denote approximate modes for the distributions. Both C1 and C2 components show bimodal distribution in radial velocity (left plot). The C1 component is probably bimodal while the C2 component follows a unimodal distribution in velocity dispersion (right plot).

large number of spectra. Hence, a double Gaussian provides the most suitable description of the Hα emission line across the entire FOV. The double Gaussian component emission has a variety of structure throughout the FOV. The main emission region shows a narrow and a broad component, while the regions farther away show two separate as well as blended components which are best fit by two similar Gaussians.

Figure 3.7 shows the maps of the observed flux, radial velocity and velocity dispersion of the two components of the Hα emission line. An attempt to separate the components on the basis of velocity dispersion leads to discontinuous/patchy maps. I, therefore, assign broad spectral component to C1 and narrow spectral component to C2. For the spaxels which show two spectral components of comparable velocity widths, I assign the component with higher radial velocity to C1 and the component with lower radial velocity to C2. The distributions of radial velocity and velocity dispersion (FWHM) of different kinematic components of Hα are shown in Figure 3.8. The radial velocities take into account the barycentric correction (= -14.41 km s^{-1}) and are relative to the systemic velocity of 207 km s^{-1} (Schneider et al., 1992). The FWHM values are corrected for the instrumental broadening of 1.7 Å.

The flux maps of Hα (Figure 3.7, upper panel) show that the C1 component peaks in the central part of the main emission region (11 pc $\times$ 11 pc) and decreases by a factor of 2 in the surrounding $\sim$ 5.5 pc region, whereas the C2 component is uniform over an area of 22 pc $\times$ 22 pc of the main emission region. The size of the central part of the main emission region is consistent with being a point source (i.e. the size of the seeing disk). Compared to C1, the C2 component shows a region of higher flux in the south-west of the main emission region.

The radial velocity maps of Hα (Figure 3.7, middle panel) show rotating structures in both

C1 and C2 components about an axis of rotation below the main emission region. The radial velocity of C1 varies between ~ -40 and 180 km s^{-1}. This component of the ionised gas has lower velocity in the main emission region (north-west) and, increases smoothly in the region farther away (south-east) - which could indicate a region of local shear stress between the layers of ionised gas at different velocities, that can lead to turbulence. The C2 component shows a slower and smoother rotation compared to C1, with the radial velocity varying between ~ -70 and 25 km s^{-1}. This component is blueshifted in the main emission region (north-west) and redshifted in the region below it (south-east). The typical uncertainties on the velocity of C1 and C2 components are $\sim$7 km s^{-1} and $\sim$2 km s^{-1}, respectively. Both C1 and C2 components show bimodal distribution (Figure 3.8, left panel) in radial velocity.

From FWHM maps of Hα (Figure 3.7, bottom panel) and the FWHM distribution (Figure 3.8, right plot), I find that the C1 component spans a wide range of velocity dispersion varying between $\sim$ 10 and 400 km s^{-1}; while the C2 component is mostly narrow varying between $\sim$ 10 and 200 km s^{-1} with a mean value of $\sim$ 70 km s^{-1}. The typical uncertainties on the velocity dispersion of C1 and C2 components are $\sim$18 km s^{-1} and $\sim$4 km s^{-1}, respectively. The C1 component is probably bimodal while the C2 component follows a unimodal distribution in velocity dispersion (Figure 3.8, right plot).

3.4 Ionisation Conditions

3.4.1 BPT diagrams

In order to understand different excitation or ionisation mechanisms responsible for the kinematic components observed in Section 3.3, I use the classical emission line diagnostic diagram by Baldwin, Phillips & Terlevich (1981). Such diagrams are commonly known as the BPT diagrams, and are shown in Figure 3.9 ([O III]/Hβ versus [S II]/Hα (left), and [O III]/Hβ versus [N II]/Hα (right)). Note here that the line fluxes used to calculate the line ratios in the BPT diagram are not corrected for reddening due to their closeness in wavelength. The "Kewley line" (Kewley et al., 2001) indicating the theoretical maximum starburst line is over-plotted as the solid black curve on these diagrams. The emission line ratios of the region lying below and to the left of the Kewley line can be explained by the photoionisation of gas by massive stars alone while the emission line ratio in the region above this line requires a contribution from non-photoionised emission. The red dot denotes the line ratios derived from the summed spectrum fluxes of the main emission region (Tables 3.2) shown by the black square box in all maps. As expected, the red dot (with very small error bars) lies well below the Kewley line on both diagnostic plots as it corresponds to a photoionised H II region. The blue points with error bars denote the line-ratios and their uncertainties respectively for individual spaxels. In the [N II] diagnostic plot (Figure 3.9, right) all the points lie below the Kewley line,

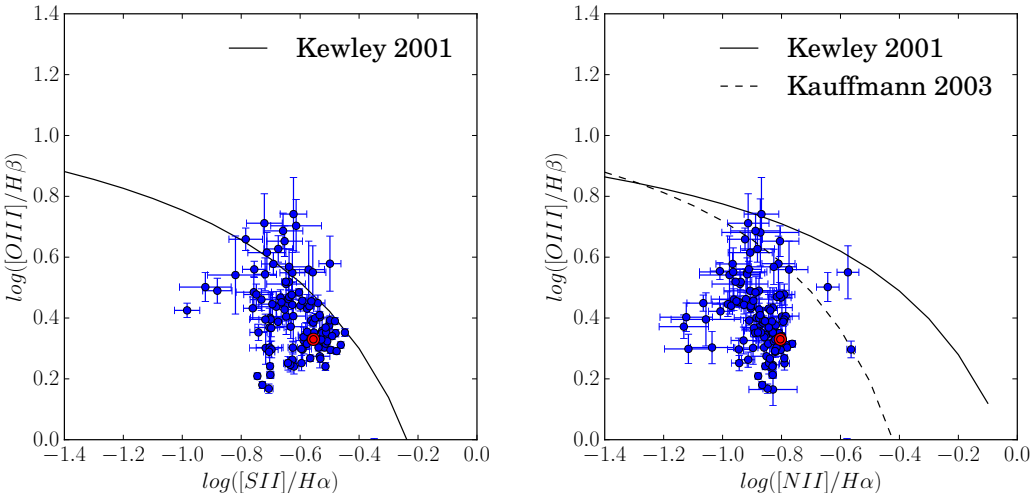

Figure 3.9 – Emission line ratio diagnostic diagrams: [O III]/Hβ versus [S II]/Hα (left), and [O III]/Hβ versus [N II]/Hα (right). Black solid curve and dashed curve represent the theoretical maximum starburst line from Kewley et al. (2001) and Kauffmann et al. (2003), respectively, showing a classification based on excitation mechanisms. The points lying below and to the left of the Kewley line are those objects whose emission line ratios can be explained by the photoionisation by massive stars while the points above this line are those objects where some other source of ionisation is needed to explain their line ratios. The outliers above the Kewley line are the $\sim$ 2–σ events but there are enough of them to argue for an additional mechanism. Red dot (with small error bars) denotes the corresponding ratios of the summed spectrum of the main emission region shown by the black square box in all maps.

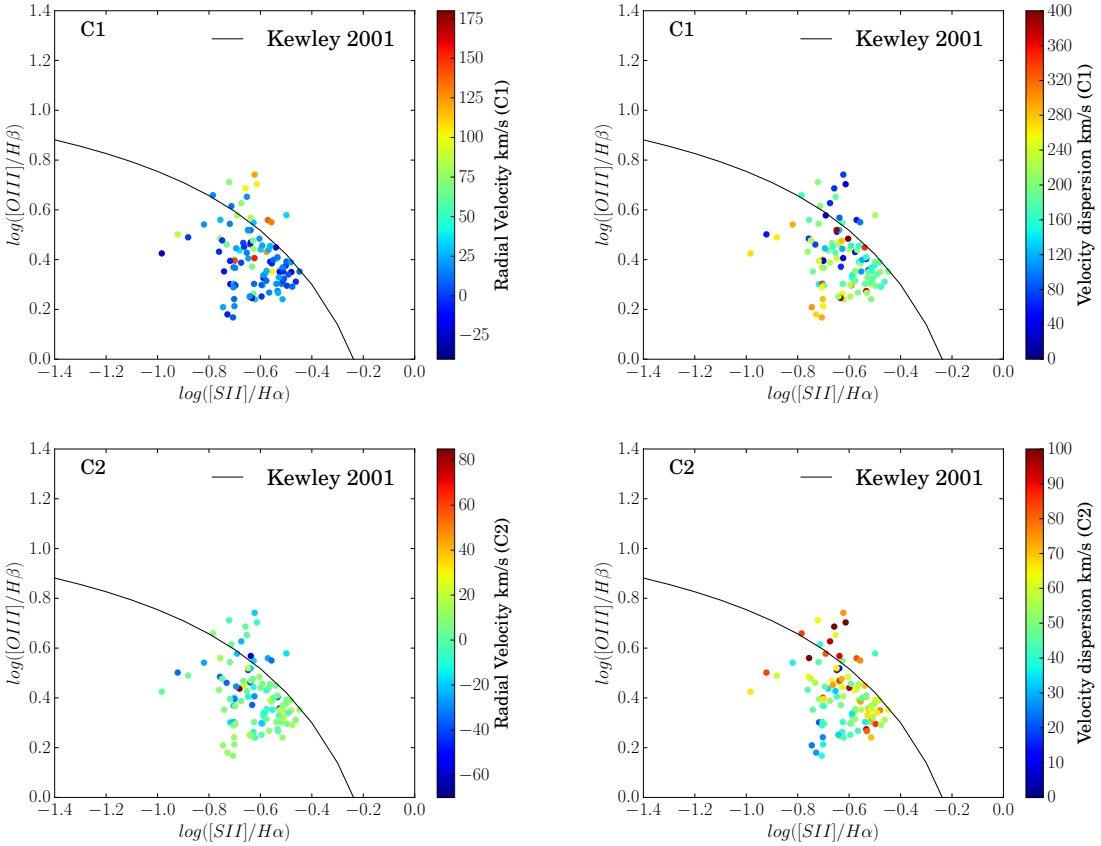

Figure 3.10 – [O III]/Hβ versus [S II]/Hα diagnostic plots, where points are colour-coded with respect to radial velocity (left) and velocity dispersion (right) of the two spectral components of Hα - C1 (upper panel) and C2 (lower panel). There is no unambiguous evidence of correlation/dependence between the points on the [S II] diagnostic plot and radial velocity. Though there are possible hints of correlation between the points on the [S II] diagnostic plot and velocity dispersion, there are too few points to be confident about such a correlation.

indicating photoionisation as the primary ionisation mechanism even in the region surrounding the star-forming region. This is an interesting observation because the gas surrounding a star-forming region may or may not be photoionised, and can be ionised by non-photoionising sources (e.g. mechanical shocks by supernovae, stellar winds, expanding H II regions). On the [N II]/Hα diagnostic plot, I also plot the line derived by Kauffmann et al. (2003) (referred to as the "Kauffmann line") based on the SDSS spectra of 55 757 galaxies. The region enclosed between the Kewley line and the Kauffmann line is thought to be ionised either by photons or by shocks. On the [S II]/Hα diagnostic plot (Figure 3.9, left), I find points lying both below and above the Kewley line, which indicates that the surroundings of the H II region may not be primarily photoionised but may also be shock ionised.

The identification of shocks and turbulence in the surrounding of a star-forming region is important because shocks can have a strong impact on the evolution of gaseous clouds which are the sites of star-formation, and hence can affect the star formation rate and efficiency in the star-forming regions. Hence, I further investigate different ionisation mechanisms depicted in the [S II] diagnostic plot by using the information on radial velocity and velocity dispersion obtained from multi-component line fitting to the strong Hα emission line. Figure 3.10 shows this analysis where points on the [S II] diagnostic plot are colour-coded with respect to radial velocity (left) and velocity dispersion (right) of the two spectral components of Hα - C1 (upper panel) and C2 (lower panel). The points above the Kewley line show velocity widths $\sim$ 50–100 km s^{-1} for both of the components (Figure 3.10, right plots), which suggests that the gas ionised by shock excitation is primarily cool. The diagnostic plot corresponding to the velocity width of the C2 component (bottom right plot) shows that the velocity dispersion is slightly increasing as we go above the Kewley line, which suggests the shock ionised gas might be broadened. However, this behaviour is not observed in the broad C1 component of the gas (upper right plot). Moreover, there are too few data points to establish a correlation between points on [S II] diagnostic plot and velocity dispersion. Hence overall there is no unambiguous evidence of correlation/dependence between the position of the points on the [S II]/Hα diagnostic plot and radial velocity or velocity dispersion.

3.4.2 Emission line ratio maps

Interestingly, the points above the Kewley line on the [S II] diagnostic plot (Figure 3.9) show higher [O III]/Hβ rather than [S II]/Hα, suggesting highly ionised gas ([O III]) along the shock front. I investigate this further through the line ratio maps of [O III]/Hβ, [S II]/Hα and [O III]/[S II] in Figure 3.11. Comparing doubly- and singly-ionised gas of the same species (e.g. [O III]/[O II]) would give a better estimate of the relative amount of gas in the two ionisation states. However, [O III]/[S II] is used instead because [S II] map has larger number of spaxels with sufficient S/N ($>$ 3) than [O II] (Figure 3.4), and [S II] has similar ionisation potential

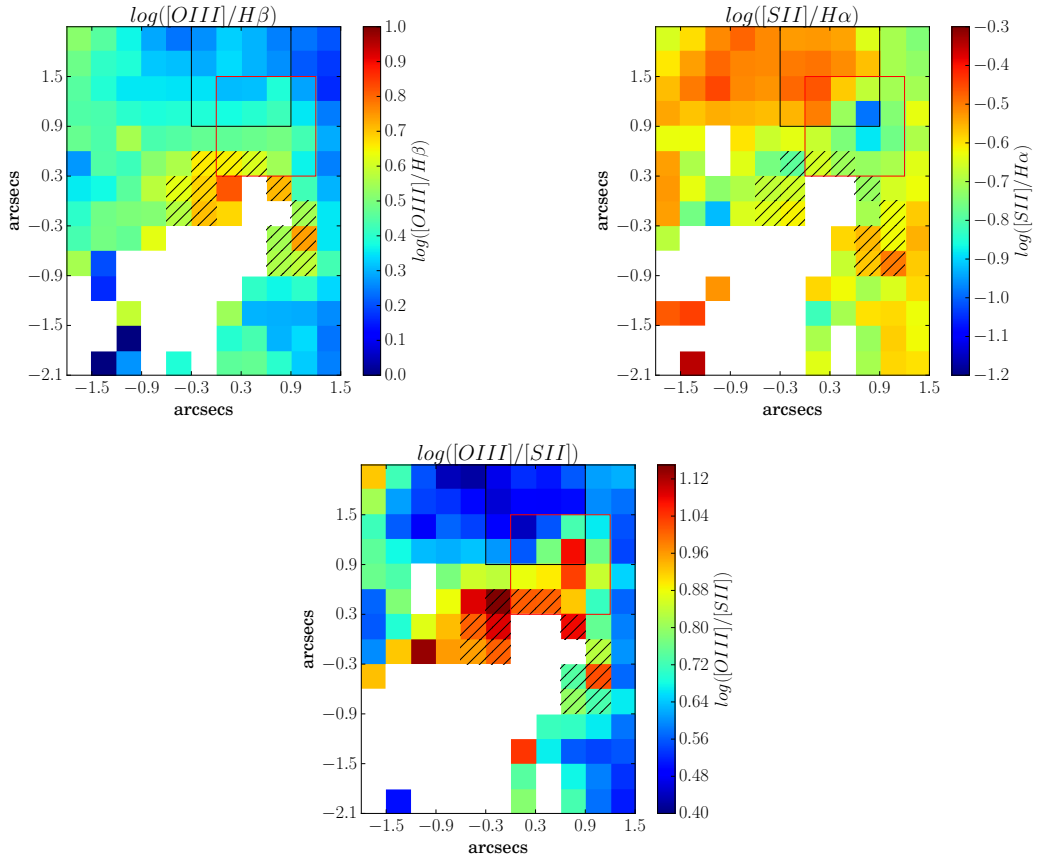

Figure 3.11 – Emission line ratio maps of [O III]/Hβ, [S II]/Hα and [O III]/[S II]. The hatched region corresponds to the spaxels with line-ratios above the theoretical Kewley line in the [S II] diagnostic plot (Figure 3.9, left). The black and red square boxes show the main emission region and the continuum region, respectively, for reference. The white spaxels correspond to the spaxels in which emission/flux had S/N < 3. The shape of the hatched region corresponds to the presence of highly ionised gas along the shock ionised front.

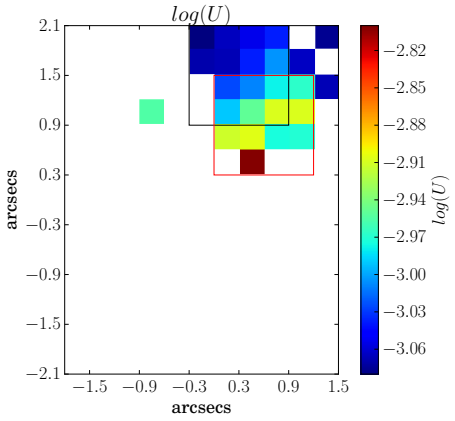

Figure 3.12 – Ionisation parameter $\mathcal{U} \equiv q/c$ as mapped from the diagnostic method of Kewley & Dopita (2002) based on the ratio of [O III] λ5007 and [O II] $\lambda\lambda$3726, 3729. The black and red square box show the main emission region and the continuum region for reference respectively. White spaxels correspond to the spaxels in which emission/flux had S/N < 3.

as that of [O II]. In the emission line maps in Figure 3.11, the hatched regions correspond to the spaxels with line-ratios above the theoretical Kewley line in the [S II] diagnostic plot (Figure 3.9, left). Overall, the regions appear to be bow-shaped. The cause of this bow-shock remains unknown, however, since there are no stellar clusters on the south-east of this region which could lead to supersonic local random motion and create the apparent bow-shock. The continuum map instead shows the presence of the stellar cluster in the north of the shock-ionised region. This suggests that the gas is ionised by the stellar winds originating from this stellar cluster. It is also possible that the shock-front has been triggered by the recent interaction of NGC 4449 with DDO 125 present in the south of this galaxy (Hunter et al., 1998) or due to a tidal interaction with another dwarf as evidenced by tidal stellar stream in the south-east (Martínez-Delgado et al., 2012) of this galaxy. The spectra of shock-ionised gas are generally characterised by double Gaussians. Figure 3.6 shows that the spectra corresponding to the shock-ionised region on the Hα emission line map consist of these expected double Gaussians of equal velocity widths and are blended.

3.4.3 Ionisation Parameter

The ionisation state of a medium is characterised by the ionisation parameter (q), which controls the ratio of the number of particles in the ionised state to that in the non-ionised state. For the photoionised gas, it is simply the ratio of the surface density of ionising photon flux (radiation pressure) to the local neutral gas number density (gaseous pressure), and is interpreted as the maximum velocity at which the local radiation field can drive an ionisation front (Kewley & Dopita, 2002). It is generally expressed as a dimensionless parameter $\mathcal{U} \equiv q/c$ where c is the speed of light. Using the ionisation parameter diagnostic devised by Kewley & Dopita

Table 3.3 – Metallicities derived using direct and indirect methods for integrated spectrum of the bright emission region as well as on spaxel-by-spaxel basis.

Diagnostic	R_{23}	N2	O3N2	Direct
		Integrated Spectrum Abundance		
12 + log(O/H)[a]	8.16 ± 0.15	8.39 ± 0.18	8.37 ± 0.14	7.88 ± 0.14
Z ($Z_\odot$)	$0.29\ ^{+0.12}_{-0.08}$	$0.50\ ^{+0.27}_{-0.17}$	$0.48\ ^{+0.19}_{-0.13}$	$0.15\ ^{+0.06}_{-0.04}$
		Spatially-resolved Abundance		
Mean metallicity[b]	8.17 ± 0.15	8.35 ± 0.06	8.33 ± 0.06	7.89 ± 0.08
Maximum deviation Δ	0.58	0.35	0.34	0.32
Calibration uncertainty	0.15	0.18	0.14	–

Notes: [a] The quoted error on each metallicity estimate takes into account both the statistical error (in flux measurement) and the calibration error associated with each of the empirical calibrators (given in the last row). Section 3.5.1.2 details the error estimate on the direct method metallicity. [b] Mean metallicity along with standard deviation across the FOV.

(2002) which relates O32 (flux ratio of [O III] λ5007 to [O II] $\lambda\lambda$3726, 3729) and log (q) with the metallicity-dependent constants, log $\mathcal{U}$ (Figure 3.12) is mapped. Note here that in order to calculate $\mathcal{U}$, I use the metallicity map derived from the direct T_e method which is the most robust metallicity estimator. log $\mathcal{U}$ is found to be highest at the peak of the stellar continuum (see first plot of Figure 3.4) and decreases as we go toward the main emission region. $\mathcal{U}$ is expected to be highest at the inner edge of the ionised region and falling to zero at the outer edge in case of full depletion of ionising flux (Nicholls et al., 2013), i.e. when the source of ionising radiation (indicated by the continuum) is aligned with respect to the ionised gas. In the present case, the peak of the continuum is not aligned with the peak of the main emission region. Hence, I do not find the expected decrease from the inner to outer region of the H II region. I find one spaxel on the outer edge of the continuum which has unusually high log $\mathcal{U}$ = − 2.8 and also high error bar 0.19 compared to the standard error ($\sim$ 0.01) of measurement on log $\mathcal{U}$. Moreover, we do not expect a high log $\mathcal{U}$ region to be confined to one spaxel. A variation of ~ -3.08 to -2.80 is observed across the region with S/N $>$ 3, with an average value of log $\mathcal{U}$ = -3.00 ± 0.07. The estimated values of log $\mathcal{U}$ lie in the range of its value found for extragalactic H II regions ($-3.5 <$ log $\mathcal{U} < -2.5$, Dopita et al., 2000). However, Stasińska et al. (2015) showed that extreme BCDs with high [O III]/[O II] have volume-averaged ionisation parameter as high as -1.5 or even -1 (depending on the nebular geometry used in the photoionisation models), which is higher than galaxies with lower values of [O III]/[O II] ratios. The central H II region studied here exhibits [O III]/[O II] (= 0.52 ± 0.03), which is much smaller than that of BCD sample ([O III]/[O II] >5) of Stasińska et al. (2015).

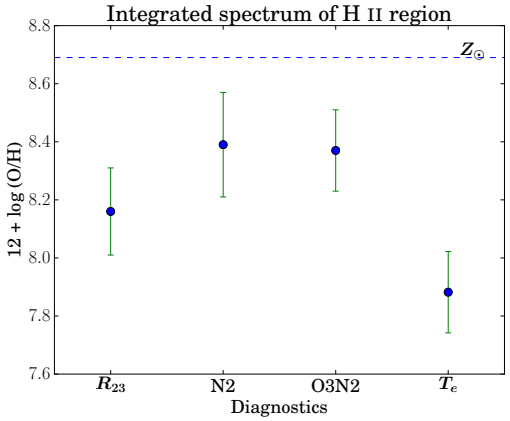

Figure 3.13 – Comparison of metallicities derived from the integrated spectrum of the main emission region using direct and indirect methods. The error bar on each indirect metallicity estimates takes into account both the statistical error (in flux measurement) and the calibration error associated with each of the empirical calibrators. See Section 3.5.1.2 for the error estimate on the direct-method (T_e) metallicity. The horizontal blue dashed line corresponds to the solar abundance of 12 + log(O/H) $\sim$ 8.69 (Asplund et al., 2009).

3.5 Chemical Abundance Analysis

3.5.1 Integrated spectrum chemical abundances

In this section, I present a chemical abundance analysis of the integrated spectrum of the main emission region (Figure 3.3, upper two panels) based on direct and indirect metallicity diagnostic methods. The direct method involves the measurement of the abundance *directly* from the electron temperature T_e combined with the relative emission flux of collisional-to-Balmer emission lines (Section 3.5.1.2), while the indirect method involves the ratio of strong emission lines (Section 3.5.1.3). Since oxygen is the most prominent heavy element commonly observed in the optical spectrum in the form of O^0, O^+, O^{2+} and O^{3+}, it is used as a proxy for total metallicity. This analysis primarily includes oxygen abundance determination, however, I also briefly mention nitrogen-to-oxygen abundance ratios.

3.5.1.1 Electron Temperature and Density

The electron temperature T_e is derived from the dereddened [O III] line ratio, [O III] (λ5007+λ4959) / λ4363 and the calibrations based on the MAPPINGS IV photoionisation code which uses up-to-date atomic data (Nicholls et al., 2013). Unfortunately, the S/N ratio of [O III] λ4363 and the [S II] doublet in the individual spectrum across the FOV was too low on an individual spaxel basis to map the spatially-resolved electron temperature T_e and electron density N_e. We can, however, calculate the T_e and N_e from the integrated spectrum of the main emission region which has S/N $>$ 3 for [O III] λ4363 and the [S II] doublet. From the integrated spectrum of the

main emission region, I obtain an electron temperature of $\sim$ 15100$\pm$1700 K. Using the derived T_e value and the [SII] doublet ratio $\lambda6717/\lambda6731$ from the integrated spectrum of the main emission region, I compute an electron density N_e of $\sim$ 316$\pm$47 cm^{-3} for the main emission region. The derived values of electron temperature and density correspond to those of typical H II regions (T_e([O III]) $\sim$ 7000–14000, $N_e \approx 10^2$ cm^{-3}; Osterbrock & Ferland, 2006a). Since metal leads to cooling, metal-poor systems exhibit higher values of electron temperature and vice-versa. For example, H II regions studied in Chapter 4 are metal-rich compared to the main emission region studied here, and hence exhibit lower temperatures. The electron densities derived for the main emission region in this Chapter and those of H II regions presented in Chapter 4 lie in the low-density limit, as these electron densities are lower than the critical densities of ^2D_o levels of [S II] (Draine, 2011).

3.5.1.2 Direct method

To calculate the total elemental abundance, ionic abundance ratios are calculated using the electron temperature of the ionisation zone dominated by the corresponding ion. I estimate O^+/H^+ and O^{2+}/H^+ using T_e ([O II]) and T_e ([O III]), respectively, using the formulations of Nicholls et al. (2014). Using the empirical relation between T_e([O II]) and T_e ([O III]) given in López-Sánchez et al. (2012a), I calculate T_e([O II]) $\sim$ 12300 $\pm$ 900 K. The O^+/H^+ and O^{2+}/H^+ are finally summed to calculate the elemental O/H. I derive a metallicity 12 + log(O/H) = 7.88 $\pm$ 0.14 $\sim$ 0.15 $^{+0.06}_{-0.04}$ $Z_\odot$ from the integrated spectrum of the main emission region. Note here that the error estimate on T_e([O II]) obtained by the error propagation on flux measurement error is underestimated because of the shape of the empirical model of López-Sánchez et al. (2012a) at the required T_e([O II]). Hence, I estimated the error on T_e([O II]) through a Monte Carlo simulation (100,000 samples) by using a Gaussian distribution of T_e([O III]) with a sigma (width) equal to the error on T_e([O III]). This error is hence propagated to obtain error on metallicity measurements.

Assuming the same T_e for [O II] and [N II], and that N^+/O^+ = N/O, I use the formulation from Nicholls et al. (2014) and derive N/O = -1.03 ± 0.07.

3.5.1.3 Indirect methods

Although the direct method is deemed the most reliable to estimate chemical abundances, it is sometimes difficult to calculate because it requires the detection of usually weak auroral lines (e.g. [O III] λ4363, [N II] λ5755). This has led to the development of theoretical and empirical calibrations of metallicity based on ratios of strong lines. I estimate metallicity from the following three widely used methods:

1. The R_{23} parameter was first defined by Pagel et al. (1979) as R_{23} = ([O II] $\lambda\lambda$3727,29 + [O III] $\lambda\lambda$4959,5007)/Hβ. Since oxygen is one of the principle coolants in H II nebulae,

R_{23} is in turn sensitive to the oxygen abundance. However, it has some drawbacks and requires caution. One of the main problems is the degeneracy of R_{23} with abundance, i.e. a single value of R_{23} corresponds to two values of the O abundance. From the abundance measurement using the direct method (Section 3.5.1.2), I could break the degeneracy and decide to use the calibrations corresponding to the lower-metallicity branch. The second problem arises due to the dependence of R_{23} on the ionisation parameter. Hence, of the many calibrations available (Zaritsky, Kennicutt & Huchra, 1994; Kewley & Dopita, 2002; Kobulnicky & Kewley, 2004), I use the metal-poor (lower) branch calibration from Kobulnicky, Kennicutt & Pizagno (1999) which takes into account the effect of the ionisation parameter and is based on a set of H II region models of McGaugh (1991) using the photoionisation code Cloudy (Ferland et al., 1998). From the integrated spectrum of the main emission region, I find 12+log(O/H) = 8.16 $\pm$ 0.02 (statistical) $\pm$ 0.15 (calibration).

2. The *N2* parameter was initially defined as N2 = log ([N II] λ6584/Hα) and proposed as an abundance estimator for low-metallicity galaxies by Denicoló, Terlevich & Terlevich (2002). Since the two emission lines involved in the N2 parameter are very close to each other spectrally, the use of this parameter requires neither reddening correction nor flux calibration. I use the calibration relating N2 and metallicity from Pettini & Pagel (2004) and find 12 + log(O/H) = 8.39 $\pm$ 0.01 (statistical) $\pm$ 0.18 (calibration).

3. The *O3N2* parameter was defined as O3N2 = log([OIII] λ5007/Hβ / [N II] λ6584/Hα) and introduced as an abundance estimator by Pettini & Pagel (2004). Using their calibration, I find 12 + log(O/H) = 8.37 $\pm$ 0.01 (statistical) $\pm$ 0.14 (calibration) for the integrated spectrum of the main emission region.

Table 3.3 and Figure 3.13 summarise the metallicity estimates of the main emission region from all the methods described above. The error on each of the metallicity estimates takes into account both the statistical error (i.e. in flux measurement) and the calibration error associated with each of the empirical calibrators. I find that the metallicity estimates using all indirect methods agree with each other within the errors, and all of them are at significant offsets (0.3–0.5 dex) from the metallicity obtained using the direct method. The observed offset is consistent with other works (e.g. Kewley & Ellison, 2008) which show that the theoretical and empirical calibrations produce oxygen abundances higher than those derived from the direct method. Such offset is likely due to the limitations on the photoionisation models mentioned in Chapter 1 used to calibrate strong line metallicity calibrators. It may also be possible that the intrinsic properties of H II regions used for empirical calibrations are different than those of H II regions for which these calibrators are used.

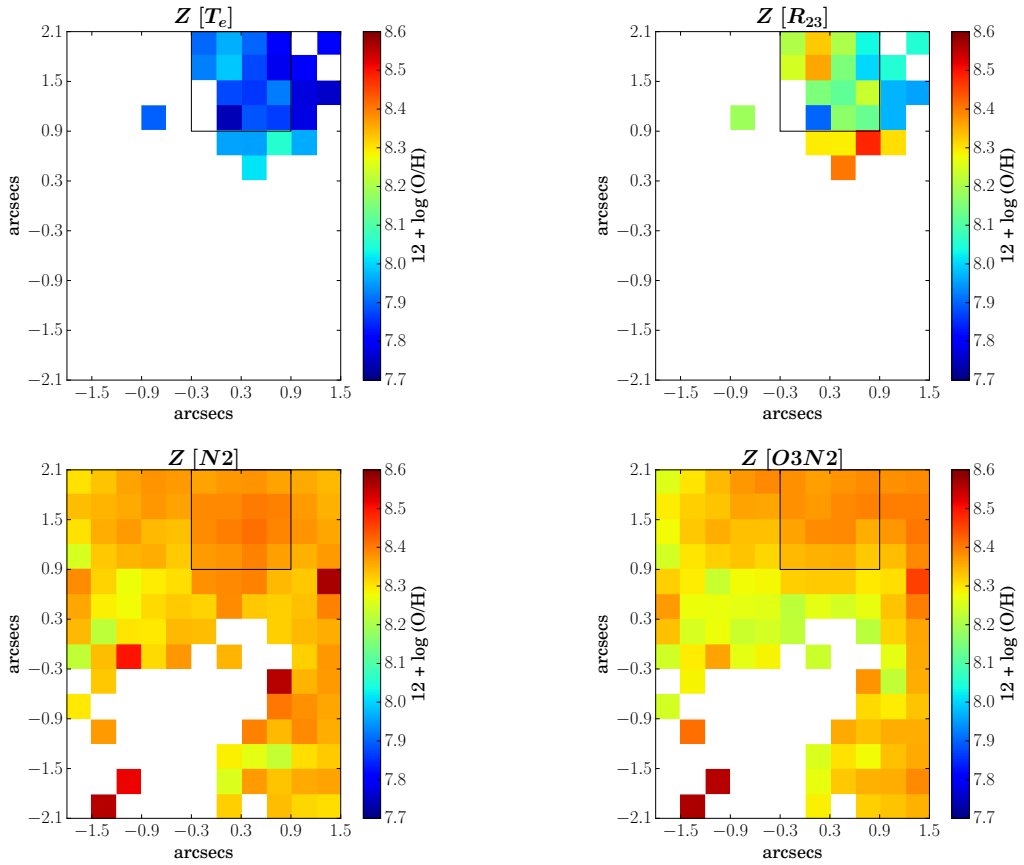

Figure 3.14 – Metallicity maps derived from the direct Te method (Z [T_e]) and indirect methods (Z [R_{23}], Z [N2] and Z [O3N2]). The scales of all maps are adjusted to the same limits so that the obvious offsets between metallicities from different methods and relative variation within maps are clear. The black square box shows the main emission region and white spaxels correspond to the spaxels in which emission line fluxes had S/N < 3.

3.5.2 Spatially-resolved chemical abundances

I create the metallicity maps of the FOV using the three indirect diagnostic methods described in Section 3.5.1. The metallicity could not be mapped from the direct method due to poor S/N in the [O III] λ4363 line required to map T_e. Hence, I assume a constant temperature H II region and map Z [T_e] using the constant T_e of the integrated spectrum of the main emission region and the maps of relative intensities of collisional-to-Balmer emission lines (i.e. O^+/H^+ and O^{2+}/H^+). Figure 3.14 presents the metallicity maps obtained from the four methods. Scales of all maps are adjusted to the same limits so that the relative offsets between metallicities from different methods and variations across the FOV are clear. Due to the low S/N of [O II] $\lambda\lambda$3727,29 (see Figure 3.4), the Z [T_e] and Z [R_{23}] maps only show the values for the main emission region and $\sim$ 5–10 pc area surrounding it. The metallicity maps obtained from N2 and O3N2 parameters (Z [N2] and Z [O3N2] respectively) cover a larger area and are mainly limited by the low S/N of [N II] λ6584 in the low-brightness region to the south-east of the H II region.

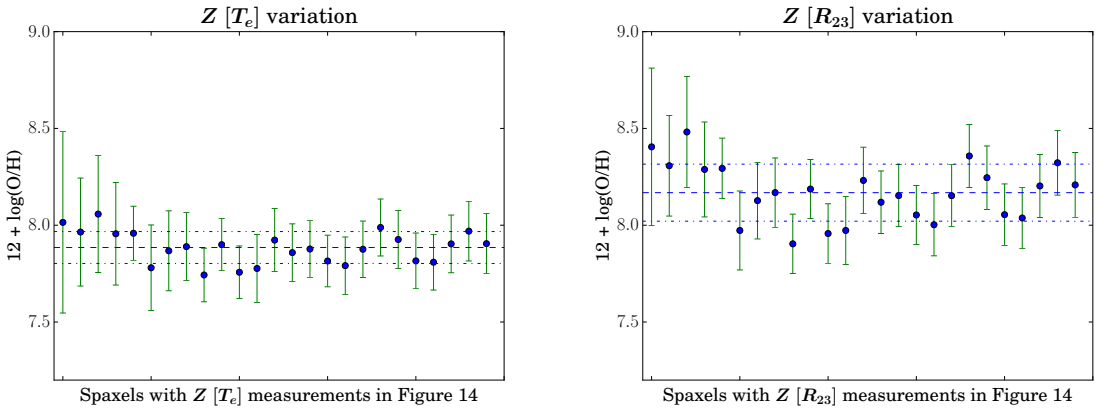

Figure 3.15 – Scatter plots of metallicity values in each spaxel of Z [T_e] (left) and Z [R_{23}] (right) maps. Section 3.5.1.2 details error estimate on the direct-method (T_e) metallicity. It is possible that the uncertainties on Z[Te] are over-estimated while doing Monte-Carlo simulation due to the shape of the empirical relation between Te ([O II]) and Te ([O III]). The error bar on each metallicity value Z [R_{23}] in the right plot also includes calibration error of 0.15 dex along with the propagated error on the flux measurement. The dashed and dotted line in each of the plots indicates the mean and standard deviation of all metallicities in the corresponding metallicity maps. In both plots, I find that all the individual metallicity values with error bars lie within the 1-σ standard deviation of the mean metallicity value, indicating chemical homogeneity throughout the regions.

Large offsets between metallicity maps obtained from indirect method and direct method are clearly seen from the colour scale. Table 3.3 presents the mean metallicities, the maximum deviation within each metallicity map, along with the calibration uncertainty associated with each indirect method employed. The quoted error on the mean is the 1-σ standard deviation across each map. These values are particularly useful in identifying any chemical variation of the ionised gas in the star-forming region and its surroundings. I find that the standard deviation (σ) and maximum variations (Δ) are comparable in Z [T_e], Z [N2] and Z [O3N2] ($\sigma \sim 0.07$ dex and $\Delta \sim 0.3$ dex) while they are a factor of 2 higher in Z [R_{23}] ($\sigma \sim 0.15$ dex and $\Delta \sim 0.6$ dex).

I further investigate the possible chemical variation in Figure 3.15, which shows scatter plots of metallicity values with error bar in each spaxel of Z [T_e] (left) and Z [R_{23}] (right) maps. The error bar on each point in both of the plots includes the error on flux measurement as well as the calibration error. The dashed and dotted line in each of the plots indicate the mean and standard deviation of all metallicities in the corresponding metallicity maps. In both of the panels, I find that the individual metallicity values with error bars lie within the 1-σ standard deviation of the mean metallicity value. The scatter plots for Z [O3N2] and Z [N2] are not shown because the calibration uncertainties on these metallicity calibrations errors are very high ($\sim$0.14 dex and $\sim$0.18 dex on O3N2 and N2 respectively), due to which all metallicity values are within the 1-σ standard deviation of the mean metallicity value. Hence, I conclude that the ionised gas in the

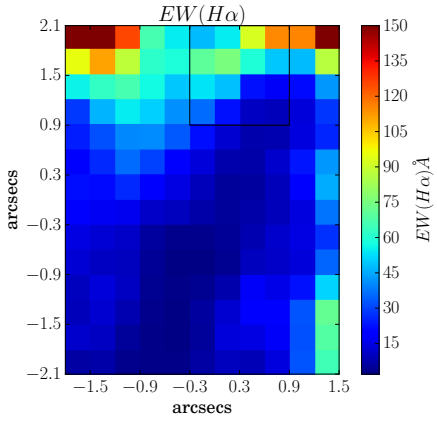

Figure 3.16 – Map of the equivalent width of Hα. The black square box shows the main emission region.

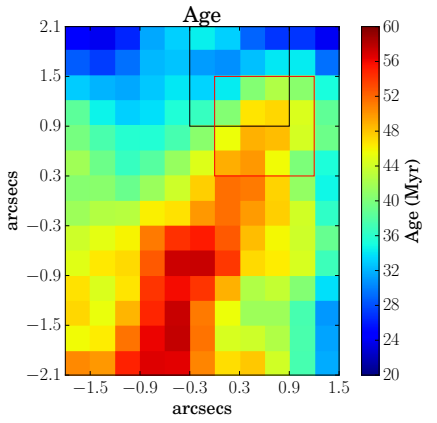

Figure 3.17 – Age map in Myr calculated from Starburst99 models at the "constant" metallicity Z = 0.15 $Z_{\odot}$ (calculated from the integrated spectrum of the main emission region). The black and red square boxes show the main emission region and the continuum region for reference, respectively.

central H II region in NGC 4449 and its surrounding is chemically homogeneous.

3.6 Stellar Properties

3.6.1 Age of stellar population

The integrated spectra of the main emission region (Figure 3.3, upper two panels) as well as its surroundings (i.e. whole FOV - main emission region; lower two panels) show Balmer emission which are indicative of young stellar systems (O and B stars) embedded in gas, and absorption lines are characteristic of early-type (A-type) stars. None of these spectra show any obvious Wolf-Rayet (WR) features, despite previous reports of WR stars in other regions of NGC 4449 (Milisavljevic & Fesen, 2008; Sokal et al., 2015).

To determine the age of the current ionising population, I first map the equivalent width (EW) of the strongest hydrogen recombination line Hα as shown in Figure 3.16. The EW values vary from 15–150 Å across the entire FOV. Note here that the EWs of other recombination lines (Hβ, Hγ) can also be used for age-dating, but these lines in my spectra also show broad photospheric absorption which can introduce considerable uncertainties on the age determined from their equivalent widths.

I employ a metallicity-dependent age-dating method in which, the age of the currently ionising stellar population is estimated by comparing the measured EW(Hα) with those predicted by the evolutionary synthesis models of Starburst99 (Leitherer et al., 1999) at a constant metallicity of 0.15 $Z_{\odot}$ across the chemically-homogeneous FOV (Section 3.5). Each spatial pixel in the FOV has a size of 5.5 pc, which is smaller than the size of an individual giant H II region ($\sim$ 100–1000 pc). This is small enough that the free-fall time at this spatial scale is much less than the evolutionary timescale of the massive stars, and hence the star-formation activity can be described by an instantaneous starburst (Leitherer & Heckman, 1995). For generating models, I assume instantaneous star-formation with the epoch of the onset of star-formation as 0.01 Myr and the oldest age of the model as 100 Myr. I adopt a Salpeter-type initial mass function (IMF) (Salpeter, 1955) with the mass boundaries 1 $M_{\odot}$ and 100 $M_{\odot}$ and total stellar mass of 10^6 $M_{\odot}$ (the default mass). I choose Geneva tracks with standard mass-loss rates over Padova tracks, though note here that a different choice of the evolutionary tracks produces a relatively small change in the predicted ages ($\sim$20–23% as found by James, Tsamis & Barlow, 2010; James et al., 2013a). I use recommended more realistic models of Pauldrach/Hiller of expanding atmosphere. At the specified metallicity and IMF, the Starburst99 code first generates the mass-distribution of the stellar population. The stellar evolutionary track is then used to predict the EW(Hα) and its variation in specified time-steps of 0.1 Myr in the time-period between the zero-age main sequence and the end-point of the stellar evolution. These time steps are representative of the age at a given EW(Hα). When stellar rotation in the starburst models is taken into account, I find an insignificant increase of $\sim$ 3% in the age.

Figure 3.17 shows the resulting age map which varies between 20–60 Myr. This result is quite interesting since it is longer than the ionisation lifetime of an H II region (up to 5 Myr, Kennicutt & Evans, 2012). These results should be interpreted with caution because of the systematic uncertainties involved in modelling. For example, I do not take into account the internal attenuation due to dust present in the region of study, which will affect the continuum level and the emission line fluxes. EW(Hα) may be 30% lower in typical star-forming galaxies if dust effects are taken into account (Levesque & Leitherer, 2013), which will affect the estimated age from EW($H\alpha$). Note also that Starburst99 does not account for dust either. Moreover, the observed continuum in a region is the combination of the nebular continuum and stellar continuum resulting from the stellar population of different ages in the same region (see for example, Cantin et al., 2010). Note here that at a given EW(Hα), the derived age will be

even longer if the star-formation history is assumed to be continuous rather than instantaneous. This is because a continuous star-formation history will result in a continuous production of younger stars as well as an increased fraction of older stars, which will decrease the EW(Hα) and increase the derived age. I find that the age of the main emission region (black box) is relatively younger than the continuum region (red box). The spatial distribution of older stars with respect to the younger stellar population has approximately the same shape as the bow-shock region found earlier in Section 3.4.2, and hence the older stellar population could be the possible cause of the shock.

The age of the stellar population in NGC 4449 has been estimated in various observational studies at global and spatially-resolved scales using different modelling techniques. For example, Karczewski et al. (2013) analysed the global optical spectrum of NGC 4449 by using the spectral fitting code STARLIGHT and found that only 1% of the mass fraction of the stellar populations in NGC 4449 have age $<$ 10 Myr, 20–25% is $\sim$ 100 Myr old and 60-75% of $>$ 1000 Myr. Spatially-resolved stellar mass-estimates of the entire galaxy are required to compare the ages derived in their work with this one. However, considering that the region of NGC 4449 studied in the present work is very bright (see Figure 3.1), young and massive stars must be present there, which is likely to correspond to the mass-bin of 20-25% corresponding to the age of $\sim$ 100 Myr. This is in good agreement with the age range of 20–60 Myr obtained from the current analysis. Böker et al. (2001) reports the detection of very deep Calcium triplet (CaT) in absorption based on their optical échlette spectra of the nucleus of NGC 4449 and hence predicts a younger cluster age between 5–20 Myr, which is in relatively good agreement with the current results of the main emission region whose average age is found to be $\sim 30 \pm 3$ Myr. This age-estimate is consistent with the results of Gelatt, Hunter & Gallagher (2001) who report the detection of ^{12}CO(2, 0) and ^{12}CO(3, 1) absorption features in the near-infrared spectrum of the central cluster of NGC 4449, indicative of the presence of cool stars (7–100 Myr). However, the current age-estimate is higher than the age-limit of 8–15 Myr derived in Gelatt, Hunter & Gallagher (2001), obtained by comparing the colour of central region with cluster evolutionary models fitted to the clusters in the galaxy. The discrepancy in the results is likely due to the metallicity Z = 0.4 $Z_{\odot}$ assumed in Gelatt, Hunter & Gallagher (2001) which is significantly higher than the metallicity (Z = 0.15 $Z_{\odot}$) of NGC 4449. I analyse the age-estimates in light of the star-formation history of NGC 4449 derived by McQuinn et al. (2010) using a colour-magnitude diagram of the stellar population in the entire galaxy. These authors report a lower average activity in the last 50 Myr than that in the last 4–10 Myr. This time bin is smaller than their inherent temporal resolution ($\sim$25–50 Myr) of star-formation history and hence should be interpreted with caution. In the case where the galaxy has undergone starbursts in the last 10 Myr, we expect the stellar age of the corresponding star-forming regions to be younger. The distribution of stellar populations younger than $\sim$ 10 Myr is presented in Figure 20 of Annibali et al. (2008), which shows that the majority of the younger stellar population does not reside in

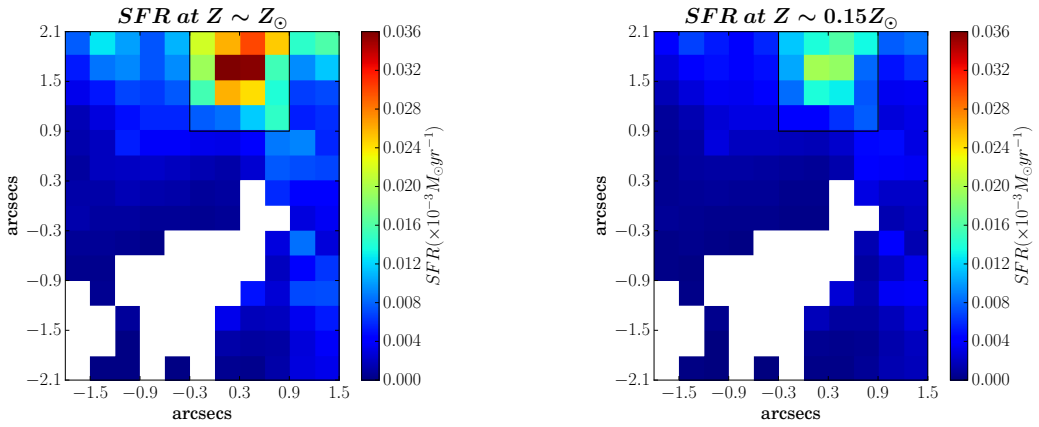

Figure 3.18 – SFR maps of the FOV in units of $\times\ 10^{-3} M_\odot\ yr^{-1}$ assuming $Z_\odot$ (left) and 0.15 $Z_\odot$ (right). The black square box shows the main emission region and white spaxels correspond to the spaxels in which emission line fluxes had S/N < 3.

the central star-forming region. Moreover, Annibali et al. (2008) also note that over-crowding prevents the detection of the older stellar population in the central star-forming region. Thus the results of McQuinn et al. (2010), combined with those of Annibali et al. (2008) are in agreement with the average age-estimate of the central star-forming region found in this analysis. It may be possible that the central star-forming region is in a post-starburst regime.

3.6.2 Star Formation Rate

I map the SFR assuming Z = 0.15 $Z_\odot$ (Figure 3.18, right panel) using the following metallicity-dependent relation between the dereddened luminosity of Hα, L(Hα) and SFR from Ly et al. (2016): $log[\frac{SFR}{L(H\alpha)}] = -41.34 + 0.39y + 0.127y^2$, where y = log(O/H) + 3.31[3]. This relation is derived from the Starburst99 models assuming a Padova stellar track and Chabrier IMF (Chabrier, 2003). I also map the SFR derived assuming the solar metallicity (Figure 3.18, left panel) for comparison using the L(Hα)–SFR relation: $SFR = \frac{L(H\alpha)}{1.26\times10^{41} ergs s^{-1}}$. This formula was initially calibrated by Kennicutt (1998b) for Salpeter IMF and I multiplied it by a factor of 0.63 to convert it to Chabrier IMF. The chosen IMF has more realistic distribution at lower stellar masses and matches the IMF assumption of Ly et al. (2016). Figure 3.18 shows that when Z is assumed to be $Z_\odot$, SFR varies from 0–0.04 $\times\ 10^{-3}$ $M_\odot$ yr^{-1} (left panel), while it varies from 0–0.02 $\times\ 10^{-3}$ $M_\odot$ yr^{-1} it is assumed that Z = 0.15 $Z_\odot$ (right panel). The spatially-resolved (spaxel-by-spaxel) values of SFR given here should be interpreted with caution because the SFR recipes fail at these scales because of the stochastic sampling of IMF. From the integrated spectrum of the main emission region, I find SFR = 0.328 $\pm$ 0.005 $\times 10^{-3}$ $M_\odot$ yr^{-1} assuming solar metallicity and SFR = 0.176 $\pm$ 0.003 $\times\ 10^{-3}$ $M_\odot$ yr^{-1} assuming Z = 0.15 $Z_\odot$, which correspond to the SFR surface density (SFRD) of 0.67 $M_\odot$ yr^{-1} kpc^{-2} and 0.34 $M_\odot$ yr^{-1}

[3] y = 0 is the solar oxygen abundance.

kpc^{-2} respectively. There is a good agreement between the SFRD estimated assuming solar metallicity ($\sim$ 0.67 M $_{\odot}$ yr^{-1} kpc^{-2}) and that found by Buckalew, Kobulnicky & Dufour (2005, $\sim$ 0.76 M $_{\odot}$ yr^{-1} kpc^{-2})[4]. For both the integrated spectrum of the main emission region and the spatially-resolved data, I find that the SFR estimated assuming solar metallicity is higher than SFR at sub-solar metallicity in the H II region and its surroundings. This is because the atmosphere of the metal-poor O stars are less-blanketed at sub-solar metallicity which results in an increased escape fraction for the ionising photons and hence requires a lower SFR.

The SFR of the central star-forming region in NGC 4449 estimated assuming both solar and sub-solar metallicity, is comparable to the SFR of star-forming regions in other BCDs, e.g. Buckalew, Kobulnicky & Dufour (2005) reports SFR of 0.208 $\times$ 10^{-3} M$_{\odot}$ yr^{-1} and 1.53 $\times$ 10^{-3} M$_{\odot}$ yr^{-1} for two different star-forming regions in Mrk 178, a BCD found at approximately the same distance ($\sim$ 4.5 Mpc) and has similar metallicity (12 + log(O/H) = 7.82) as NGC 4449. The literature suggests that the SFRs of BCDs might span a range of 10^{-3} to 10^{2} M$_{\odot}$ yr^{-1}, with the mean SFR varying from 0.1 M$_{\odot}$ yr^{-1} to 10 M$_{\odot}$ yr^{-1} (Fanelli, O'Connell & Thuan, 1988; Sage et al., 1992; Hopkins, Schulte-Ladbeck & Drozdovsky, 2002).

3.7 Discussion: Possibility of chemical inhomogeneities

Comparing the metallicity values of the integrated spectrum of the main emission region and the average values of all the metallicity maps in Table 3.3, I find that the global values agree very well with the spatially-resolved values irrespective of the metallicity diagnostic used. For both integrated spectra and spatially-resolved analysis, I find that the indirect metallicity values (Table 3.3) are offset by about 0.3–0.5 dex from the direct method metallicity (12 + log(O/H) = 7.88 $\pm$ 0.14) estimates. This offset has been observed before for different data sets (e.g. Kewley et al., 2001; Sánchez et al., 2011) and depends on many factors including the assumptions on the photoionisation models employed for calibrating the indirect diagnostics.

Figure 3.19 shows the variation of metallicity estimates with respect to distance from the centre, and includes the metallicity estimate from the integrated spectrum of the central star-forming region from this study as well as from the literature for different regions. In this figure the "Central nucleus (3 studies)" refers to the central H II region (RA, Dec: 187.046567, +44.0934) from the present study (7.88 $\pm$ 0.14, direct method), Böker et al. (2001, 7.8 $\pm$ 0.3) and Buckalew, Kobulnicky & Dufour (2005, 7.96 $\pm$ 0.16[5]). "Martin1997" refers to the average metallicity of two long-slit spectroscopic observations from Martin (1997) at two different locations from the central star-forming region. Here I have approximated distance and the error bar as the mean and the standard deviation of the distances between the central star-forming region and the mid-points of the two long-slit position. Note here that the metallicity measurements

[4]The SFRD value takes into account the IMF conversion from Salpeter to Chabrier.

[5]We estimated this metallicity from the flux measurements given in Buckalew, Kobulnicky & Dufour (2005).

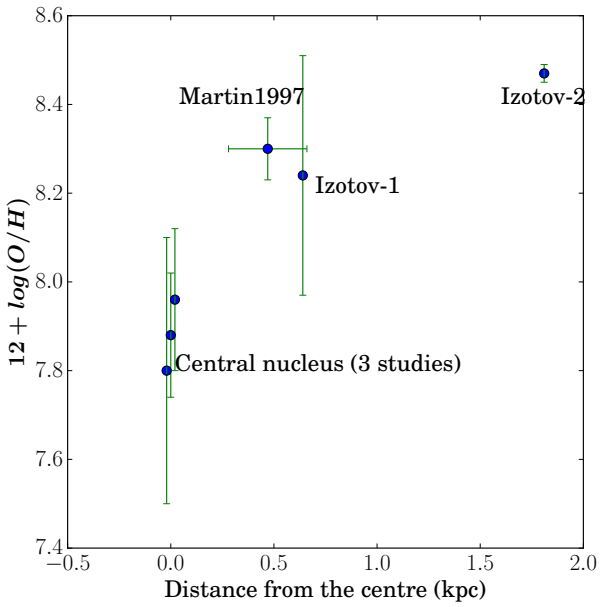

Figure 3.19 – Variation of metallicity estimates with respect to projected distance from the centre. "Central nucleus (3 studies)" refers to the central H II region (RA, Dec: 187.046567, +44.0934) from present study (7.88 ± 0.14), Böker et al. (2001, 7.8 ± 0.3) and Buckalew, Kobulnicky & Dufour (2005, 7.96 ± 0.16). Note here that the two data points (excluding this study) corresponding to the central nucleus have been shifted on the x-axis to avoid overlap at 0 kpc. "Martin1997" refers to the average metallicity of two long-slit spectroscopic observations from Martin (1997) at two different locations from the central star-forming region. "Izotov-1" and "Izotov-2" refer to the other two pointings in NGC 4449 ((RA,Dec): (187.03861, +44.08556) and (187.05776, +44.11956)) from Izotov et al. (2006).

of Martin (1997) are ambiguous with respect to the number of slits (two or three) used in the measurement. The trend in the plot is unaffected even if I assume three instead of two slits for measuring distance, hence the conclusion remains the same. "Izotov-1" and "Izotov-2" refer to the other two pointings in NGC 4449 in the north and south-west of the centre respectively. This plot suggests an overall increase in metallicity with respect to the distance from the centre.

The above comparison indicates that chemical inhomogeneities do exist across NGC 4449. Metallicity inhomogeneities have been observed before in other galaxies. Sánchez Almeida et al. (2014b) observed low metallicity inner regions with enhanced star-formation activity in two out of five dwarf star-forming galaxies with measurable metallicities. Sánchez Almeida et al. (2015) found low-metallicity starburst regions in nine out of ten extremely-metal poor galaxies. Elmegreen et al. (2016) reported a drop in metallicity at the star-forming head in the tadpole galaxy Kiso 5639. All these previous works interpret their finding of metallicity drops in the star-forming regions as a result of accretion of metal-poor gas. However, other mechanisms such as gas outflows, supernova blowout and fallback can also lead to chemical inhomogeneities as are discussed by Werk et al. (2010) in the case of BCD NGC 2915. In the following sections, I discuss possible alternative mechanisms that may yield a more metal-poor central star-forming region.

3.7.1 Metal-poor gas accretion from merger-event or cosmic web

Low metallicity at low-redshift can be caused by the accretion of either low-metallicity gas from a merger event or the pristine gas from the cosmic web mixed with the metal-rich gas of the galaxy. The accretion of gas onto the galaxy will not only dilute the metallicity but also may increase the star-formation rate.

To investigate the scenario of increased star-formation and decreased metallicity caused by the accretion of gas in NGC 4449, I compared the Hα fluxes (from the HST narrow band F658N image) in the central star-forming region as well as the two pointings of Izotov et al. (2006) (e.g. see Figure 3.19). I find that the central star-forming region is the brightest of all the three star-forming regions[6], which indicates that star-formation is enhanced in the centre compared to other regions in the galaxy. Moreover, the central star-forming region also shows an increased concentration of atomic gas as revealed by the H I map of this galaxy obtained from Very Large Array (VLA) in Hunter et al. (1998), indicating the possible inflow of gas in the centre.

Merger events can cause an inflow of gas in a galaxy, particularly in very dense environments, as demonstrated by numerical simulations. For example, Bekki (2008) shows that a merger event between gas-rich dwarf galaxies can lead to the formation of a BCD, leading to the transfer of metal-poor gas from the outer parts of the merger progenitors to the centre of BCDs. NGC 4449 is quite likely currently interacting with a nearby dwarf galaxy (Martínez-

[6]The flux estimates take into account the attenuation correction.

Delgado et al., 2012) and has potentially undergone interactions in the past (Hunter et al., 1998; Theis & Kohle, 2001). The low-metallicity gas in the central star-forming region could well be from a now disrupted gas-rich satellite.

Cosmic-web gas can also feed galaxies with low-metallicity gas, sustaining the star-formation and creating chemical inhomogeneities, as suggested by cosmological simulations (Ceverino et al., 2016) and several observational studies. An inverse metallicity gradient is observed in three rotationally-supported star-forming galaxies at z=3 by Cresci et al. (2010), who conclude that the low-metallicity centre in these galaxies is the result of dilution by accreted primordial gas ("Cold flow model" Dekel et al., 2009). The finding of low-metallicity in the central star-forming region of NGC 4449 is similar to the finding of Sánchez Almeida et al. (2015) who reports localised starbursts associated with low-metallicity gas in extremely metal-poor galaxies in the local universe and suggests its origin to be the infall of low-metallicity cosmic clouds. However, the infall of gas may not always lead to chemical inhomogeneities as is the case in BCD NGC 5253, where a flat metallicity profile is observed (Westmoquette et al., 2013) despite an infall of low-metallicity H I gas (López-Sánchez et al., 2012b). Hence accretion of cosmic gas may or may not be the cause of the observed low-metallicity in the central star-forming region in NGC 4449.

3.7.2 Metal-rich gas loss via supernovae-driven blowout or galactic winds

High-metallicity gas can be easily lost from low-mass galaxies like NGC 4449 because of the shallow gravitational potential. The gas loss can take place via supernova explosions (Mac Low & Ferrara, 1999), galactic winds generated by supernovae (Tremonti et al., 2004), or energy-driven outflows (Davé et al., 2013) in dwarf galaxies.

Although supernova remnant candidates have been proposed for NGC 4449 (Summers et al., 2003), no supernova explosion/remnant or outflows are reported near the central star-forming region of NGC 4449. The closest suggested supernova remnant is about 1 arcmin north of the central star-forming region (Seaquist & Bignell, 1978; Kirshner & Blair, 1980), with size $>$ 1.2 pc, age $<$ 100 yr and expansion velocity of 6000 km s^{-1} (Milisavljevic & Fesen, 2008). With this expansion velocity, this supernova is unlikely to affect the central star-forming region at a distance of 1.1 kpc from the explosion. However, the age of the stellar populations of the central star-forming region is $\sim$ 20–60 Myr, which is old enough to harbour earlier core-collapse supernovae and hence cannot be ruled out as a possible cause of metal-rich gas loss leading to low-metallicity in the centre of NGC 4449.

Galactic superwinds can occur when supernova explosions occur in galaxies with a high local star formation rate, which may trigger chimneys ejecting the metals out of the galaxy. Similarly, stellar winds from massive stars can also lead to metal-enriched gas loss. The gas loss in NGC 4449 has been predicted based on the Hα morphology, but outflows could also

be prevented by the low-density neutral gas around the galaxy (Ott, Walter & Brinks, 2005). This scenario is somewhat similar to BCD NGC 5253, where the unusually high densities and pressures in the supernebula and the surrounding medium stalls the ionised gas outflow from the supernebula cluster winds (Westmoquette et al., 2013). However, galactic winds may cause outflows in BCDs as suggested by various observational studies, e.g. Meurer et al. (1992) report an outflow Hα morphology in the nucleated BCD NGC 1705, suggesting that stellar winds and supernova from recent cluster-formation in the nucleus power the outflow. Large-scale outflows have been reported in another BCD, Mrk 71 possibly caused by the winds from massive stars (Roy et al., 1991; James et al., 2016). Thus, galactic winds can transport metal-rich gas out of galaxies depending on the environment, and hence cannot be ruled out as a possible cause of the chemical inhomogeneity in NGC 4449.

Alternative Mechanisms: Two possible scenarios are presented in the above discussion where the transport of gas in and out of the galaxy can lead to metallicity inhomogeneities. It is also possible that the metal-rich star-forming region on the outskirts of the galaxy could have been formed from the pre-enriched gas accreted from a past-merger event, for example from DDO 125. There can also be another scenario where low-metallicity gas is formed in-situ and has remained un-enriched within the galaxy. In this case, supernova explosions may eject the metal-enriched gas into the galactic halo which may rain back to the outskirts of the galaxy causing a higher metallicity in the outer regions without any gas loss. Such a scenario is proposed for BCD NGC 2915 by Werk et al. (2010) where they find the outer disk to be overabundant and the central star-forming core to be underabundant for the gas fraction in the respective regions. The low-metallicity central star-forming region in NGC 4449 can be explained by this alternative mechanism without invoking any accretion or loss of gas from the galaxy.

A spatially-resolved kinematic and chemical abundance study complemented by a detailed star-formation study of NGC 4449 is required to determine the cause of observed low-metallicity central star-forming region in this galaxy. This can be achieved by carrying out a spatially-resolved spectroscopic (IFU) study of the entire galaxy, along with the central star-forming region. The Keck Cosmic Web Imager (KCWI) would be an excellent instrument available in the northern hemisphere for this type of study because of its large FOV and full wavelength coverage, which allow mapping important emission lines ([O II] $\lambda\lambda$3727, 3729) in the blue-end of the optical spectrum. This can be complemented by multiwavelength data, particularly H I which provide signatures of cold-flow streams (if present) and CO (e.g. using Very Large Baseline Array), which will trace the cool gas fuelling star-formation. This would allow us to confirm the chemical inhomogeneity across the galaxy from a single study and also determine its cause by mapping the gas kinematics and signatures of gas flows - in, out and within the

galaxy.

3.8 Summary

I have carried out a spatially-resolved study of the central H II region in the blue compact dwarf galaxy NGC 4449 using GMOS-N IFS data. I summarise the main results concerning the questions posed in Chapter 1.

(a) Do chemical inhomogeneities exist at the parsec-scale in this star-forming region? To investigate the possibility of chemical inhomogeneity across the central star-forming region, metallicity maps of the entire region of the study were created using both direct and indirect methods. The region under study is chemically homogeneous. The average values of metallicity across the FOV agree with the values obtained from the integrated spectrum of the main emission region for each diagnostic (T_e, R_{23}, N2 and O3N2). I find a metallicity of 12 + log(O/H) = 7.88 $\pm$ 0.14 from the integrated spectrum of the main emission region from the direct T_e method. Comparison with direct-method metallicity measurements (from the literature) of other regions in this galaxy shows a radial increase in metallicity and hence signatures of chemical inhomogeneity at kiloparsec-scales.

(b) What are the possible ionisation mechanisms at play in the gas surrounding this H II region? A complex velocity structure of ionised gas is found in the central H II region of NGC 4449 and its surroundings. This includes distinct and blended shell structures indicating turbulence in the star-forming region, which could be due to stellar winds from a nearby stellar cluster or bow shocks possibly triggered by recent merger events from satellite galaxies to the south of NGC 4449. A BPT diagnostic diagram using [N II]/Hα flux ratios showed photoionisation to be the dominant source of ionisation, as expected for an H II region. However, I also find signatures of shock ionisation in the BPT diagram from the [S II]/Hα line flux ratio, confirming the shock signatures in the velocity structure of the ionised gas. I also mapped the ionisation parameter (log $\mathcal{U}$) using the O32 diagnostic and find a radial decrease of log $\mathcal{U}$ from the peak of the continuum source.

(c) What is the age of the stellar population currently ionising the gas in this region? The age of the current ionising stellar population was mapped by comparing the equivalent widths of the recombination line (Hα) to that predicted by evolutionary synthesis models from Starburst99. The age of the stellar population in the region of study is found to vary between 20–60 Myr, which is old enough to harbour supernovae explosions in the past. The distribution of older stellar population appears to have approximately the same shape as the apparent bow-shock in this region, suggesting that the bow-shock may in-fact be linked to the stellar population in the surrounding area.

The central star-forming region of NGC 4449 appears to be metal-poor compared to other regions in the galaxy. Though it is more likely due to the accretion of low-metallicity gas due to an ongoing merger-event, other hypotheses such as the outflow of metal-rich gas, or gas loss via galactic winds or supernova-driven blowout cannot be discarded. An extensive spatially-resolved study of the entire galaxy NGC 4449 would provide a complete picture presenting the interplay between star-formation, chemical abundance and gas kinematics at spatially-resolved scale in the local universe. NGC 4449, being an excellent local analogue of high redshift galaxies, will also shed light on our understanding of the complex interplay in the high redshift Universe.

4

O/H-N/O: the curious case of NGC 4670

4.1 Introduction

Chemical evolution of the Universe is one of the most explored topics in astrophysical research and is essential to unravel the secrets of cosmic origin. All chemical elements result from nucleosynthetic processes, which happened either after a few seconds of the Big Bang or in the first stars after the Dark Ages and then during the subsequent evolutionary stages of stars and are still happening today in the present-day galaxies. Consequently, this topic has been the subject of innumerable observational and theoretical studies, as we continue to investigate various aspects of chemical evolution (see e.g. Pagel, 1997; Izotov & Thuan, 1998; Matteucci, 2003; Tremonti et al., 2004; Erb et al., 2006; Maiolino et al., 2008; Steigman, 2007; Mannucci et al., 2010; Davé, Finlator & Oppenheimer, 2012; Mollá et al., 2015).

The study of the relation between nitrogen-to-oxygen ratio and oxygen abundance has been a topical subject of investigation and debate in both observing (e.g. McCall, Rybski & Shields, 1985; Thuan, Izotov & Lipovetsky, 1995; Izotov et al., 2006; Amorín, Pérez-Montero & Vílchez, 2010; Berg et al., 2012; James et al., 2015; Belfiore et al., 2017) and modelling (e.g. Edmunds, 1990; Henry, Edmunds & Köppen, 2000; Köppen & Hensler, 2005; Mollá et al., 2006; Vincenzo et al., 2016) communities working on chemical evolution. Nitrogen is of special interest as its origin is both primary and secondary. It may be produced from stars whose gas mixture contains only H and He (primary origin), and also from stars whose initial gas mix-

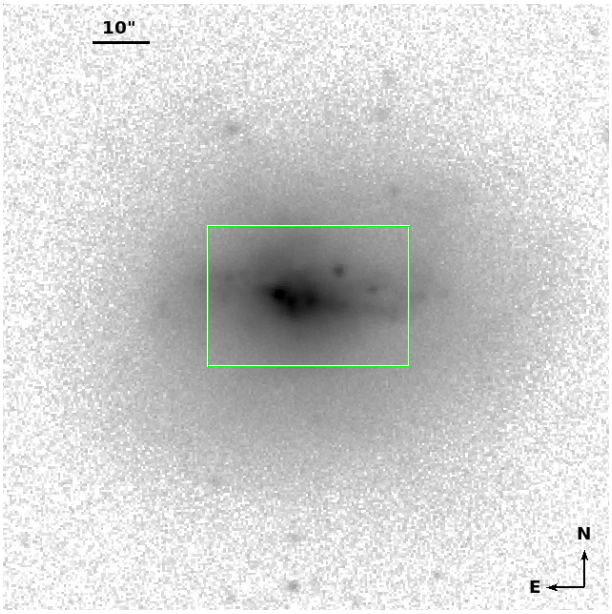

Figure 4.1 – SDSS r-band image, showing the bright central region and an elliptical halo of older stellar population in NGC 4670. The green rectangular box shows the region covered by the HST image shown in Figure 4.2.

ture contain metals (secondary origin). Thus, the production of nitrogen may or may not depend on the initial metallicity of the gas. The relative abundance of nitrogen and oxygen is regulated by various factors such as star formation history, presence of low- and high-mass stars, local chemical pollution possibly due to supernovae or Wolf-Rayet (WR) stars, and the flow of gas in, out and within the galaxies (Edmunds, 1990; Henry, Edmunds & Köppen, 2000; Köppen & Hensler, 2005; Mollá et al., 2006; Vincenzo et al., 2016). Hence, mapping the distribution of physical properties of the ionised gas within galaxies is essential in understanding not only the nucleosynthetic origin of nitrogen but also the chemical enrichment and recycling processes.

Chemical abundances of galaxies can be robustly estimated and mapped by using the direct T_e method, which requires the detection of weak auroral lines (e.g. [O III] λ4363, [N II] λ5755). In the absence of such detections, indirect methods are used for estimating the chemical abundances, which involve the use of strong emission lines. These indirect methods may be either the well-established calibrations involving the emission line ratios (e.g. Pettini & Pagel, 2004; Maiolino et al., 2008; Pérez-Montero & Contini, 2009; Dopita et al., 2016; Curti et al., 2017), or using the emission line fluxes in the photoionisation models of the ionised nebulae, such as CLOUDY (Ferland et al., 2013), and MAPPINGS (Sutherland & Dopita, 1993). Some examples of the codes that use such models to calculate abundances are HII-CHI-mistry (Pérez-Montero, 2014), IZI (Blanc et al., 2015) and BOND (Vale Asari et al., 2016).

Blue compact dwarf galaxies (BCD, Searle & Sargent, 1972b; Thuan & Martin, 1981) in the local Universe are ideal laboratories for mapping chemical abundance as they host luminous H II regions that emit in the visible range, hence providing a plethora of the emission lines re-

quired for chemical abundance analysis. Moreover, BCDs are low-metallicity (1/50–1/3 $Z_{\odot}$), starbursting dwarf galaxies in the nearby Universe, whose properties (e.g., metallicity, compactness, specific star formation rate, and gas fraction) resemble those which are observed in primeval galaxies at high redshift (see Kunth & Östlin, 2000, for a review). Their proximity enables detailed in-depth analyses of a variety of physical properties for both the young (Hunter & Thronson, 1995; Papaderos et al., 1998; Thuan, Izotov & Foltz, 1999) and more evolved stellar components (Papaderos et al., 1996a; Gil de Paz, Madore & Pevunova, 2003; Cairós et al., 2007; Amorín et al., 2009). However, most of these analyses are based on either long-slit and/or photometric observations (e.g. Izotov & Thuan, 1999; Cairós et al., 2001b,a; Hägele et al., 2012), which do not allow us to simultaneously map the chemical abundances and other physical properties within the BCDs. As such, any information on the spatial correlation between different physical properties and chemical abundance patterns are lost.

With the advent of integral field spectroscopy (IFS), the study of BCDs have been revolutionised (e.g. James et al., 2009; James, Tsamis & Barlow, 2010; James et al., 2013a,b; Westmoquette et al., 2013; Lagos et al., 2012, 2014, 2016) as IFS has enabled us to spatially resolve the distribution of the physical properties of the ISM within the BCDs. This has allowed statistical analysis of these distributions to explore the spatial uniformity or homogeneity of such properties within BCDs (Pérez-Montero et al., 2011, 2013; Kehrig et al., 2013, 2016). IFS also allows us to analyse the spatial correlation between different properties: for example, using IFS, Kehrig et al. (2008) detected both a WR population and an excess N/O across the BCD IIZw70; López-Sánchez et al. (2011) detected WR features and He II λ4686 emission line at the same location in the BCD Ic10, and Kumari, James & Irwin (2017) reported signatures of shock ionisation in the spatially-resolved emission line ratio diagrams and the velocity structure of the ionised gas of the central H II region of the BCD NGC 4449. Hence, IFS studies are essential in understanding the cause and effect of various physical processes taking place in the ISM of the BCDs.

In this Chapter, I have targeted the central region of a blue compact dwarf NGC 4670 (Figure 4.1). NGC 4670 is an ideal target for addressing the questions posed in Chapter 1 and specifically for studying the relation between N/O and O/H. Beside being classified as a BCD, it has also been recognised as a WR galaxy (Mas-Hesse & Kunth, 1999). As such, we expect local chemical pollution resulting from the winds of the WR stars, which may lead to chemical enrichment of the ISM and an enhanced N/O. Being a BCD, it is expected to have a low-metallicity and high star-formation rate (SFR). In fact, neutral hydrogen observations of NGC 4670 show a high concentration of the gas in the centre of the galaxy (Hunter, van Woerden & Gallagher, 1996), which may also increase the star-formation. A multi-wavelength analysis of the galaxy by Huchra et al. (1983) indicates the presence of several hundred O stars in giant H II region complexes, which indicate that the galaxy hosts young stellar populations. It is therefore possible that the metallicity, star-formation or stellar properties might be spatially correlated

Table 4.1 – General Properties of NGC 4670

Parameter	NGC 4670
Other designation	UGC 07930, Haro 9, Arp 163
Galaxy Type	BCD, WR
R.A. (J2000.0)	12h45m17.1s
DEC (J2000.0)	+27d07m31s
Redshift (z)[a]	0.003566 ± 0.000013
Distance (Mpc)[a]	18.6
inclination (°)[b]	28
Helio. Radial Velocity(km s^{-1})[a]	1069 ± 4
E(B-V)[c]	0.0128 ± 0.0003
M_B^b	-18.6
U-B[b]	-0.49
12 + log(O/H)[d]	8.30
M_* ($M_\odot$)[e]	$10^{8.78^{+0.2}_{-0.17}}$

[a] Taken from NED
[b] Hunter, van Woerden & Gallagher (1996)
[c] Foreground galactic extinction (Schlafly & Finkbeiner, 2011)
[d] Hirashita, Tajiri & Kamaya (2002)
[e] SDSS

with the WR stellar population or N/O. Moreover, this galaxy is relatively close ($\sim$ 18.6 Mpc), as such the high spatial sampling (0.1 arcsec) provided by the integral field unit (IFU) on the Gemini Multi-Object Spectrograph North (GMOS-N) has allowed to study the spatial correlation between these properties at a spatial scale of 9 pc. A previous IFS study of the entire galaxy was performed using Visible Integral Field Replicable Unit Spectrograph (VIRUS-P), but had a spatial sampling of 4.2 arcsec or 350 pc Cairós et al. (2012). This study presents for the first time the IFS observation of NGC 4670, at a spatial sampling of 0.1 arcsec hence allowing a more detailed analysis of spatial properties. Moreover the IFS data has enabled the identification of four new luminous H II regions in this galaxy. General properties of NGC 4670 are given in Table 4.1. The GMOS data observing log for this galaxy and data-reduction methods are presented in Chapter 2.

The Chapter is organised as follows: Section 4.2 presents the preliminary procedures required for data analysis and the main results, which include the gas kinematics, chemical abundances and stellar properties. In Section 4.3, I explore the relation between the nitrogen-to-oxygen ratio and oxygen abundance at the spatially-resolved scale, and for the H II regions in this BCD. I also do a comparative analysis with a sample of H II regions within nine more BCDs compiled from the literature, a sample of green peas and also a large sample of star-forming galaxies from the Sloan Digital Sky Survey (SDSS). I explore the observed trend in the relation with the chemical evolution models. I finally summarize the results in section 4.4.

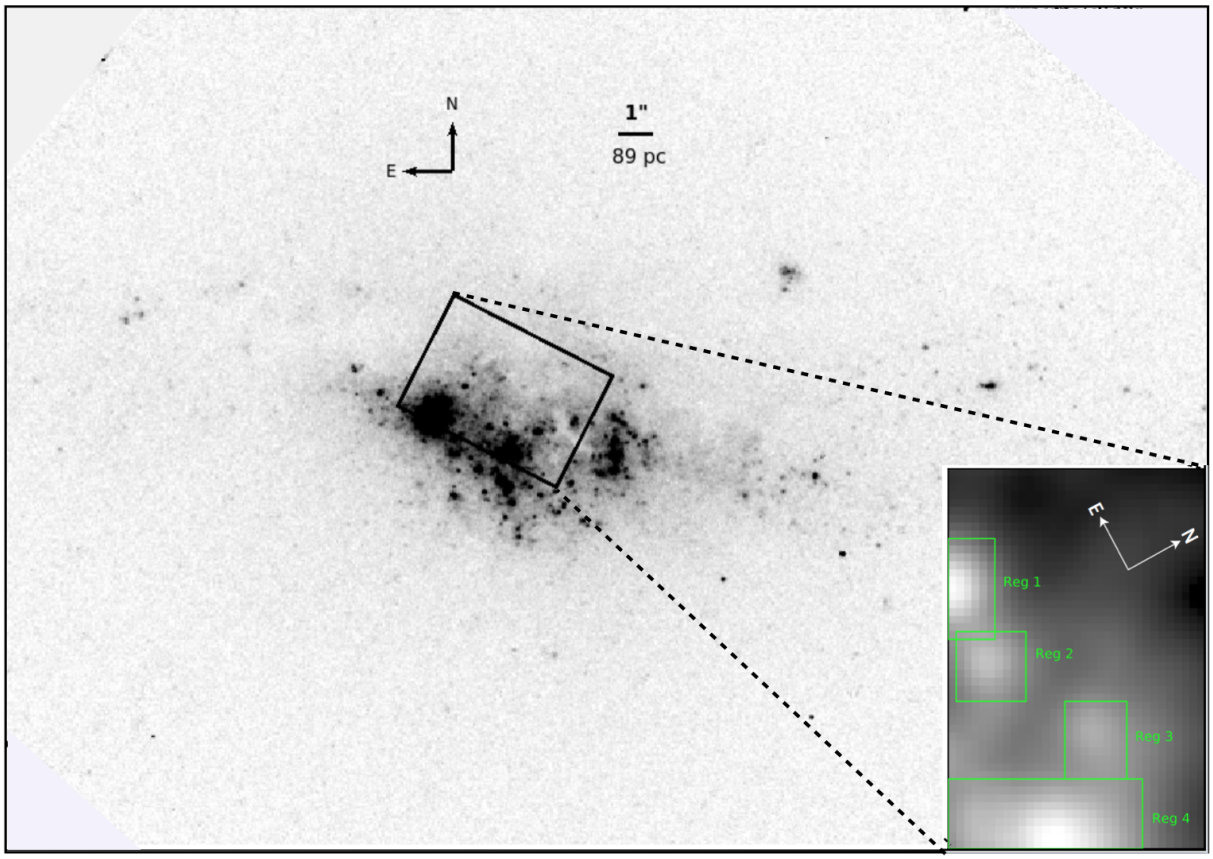

Figure 4.2 – Left panel: HST image of NGC 4670 taken in the filter F439W. The black rectangular box in the centre represents the GMOS aperture (3.5 arcsec $\times$ 5 arcsec). The HST image has a spatial scale of 0.05 arcsec pixel^{-1}. North and east on the image is shown by the compass on the top-left of the figure. Right panel: Hα map of the FOV obtained from the GMOS-IFU shows the four H II regions (Reg 1, Reg 2, Reg 3, Reg 4) in green rectangular boxes. The compass on this panel shows north and east on the FOV.

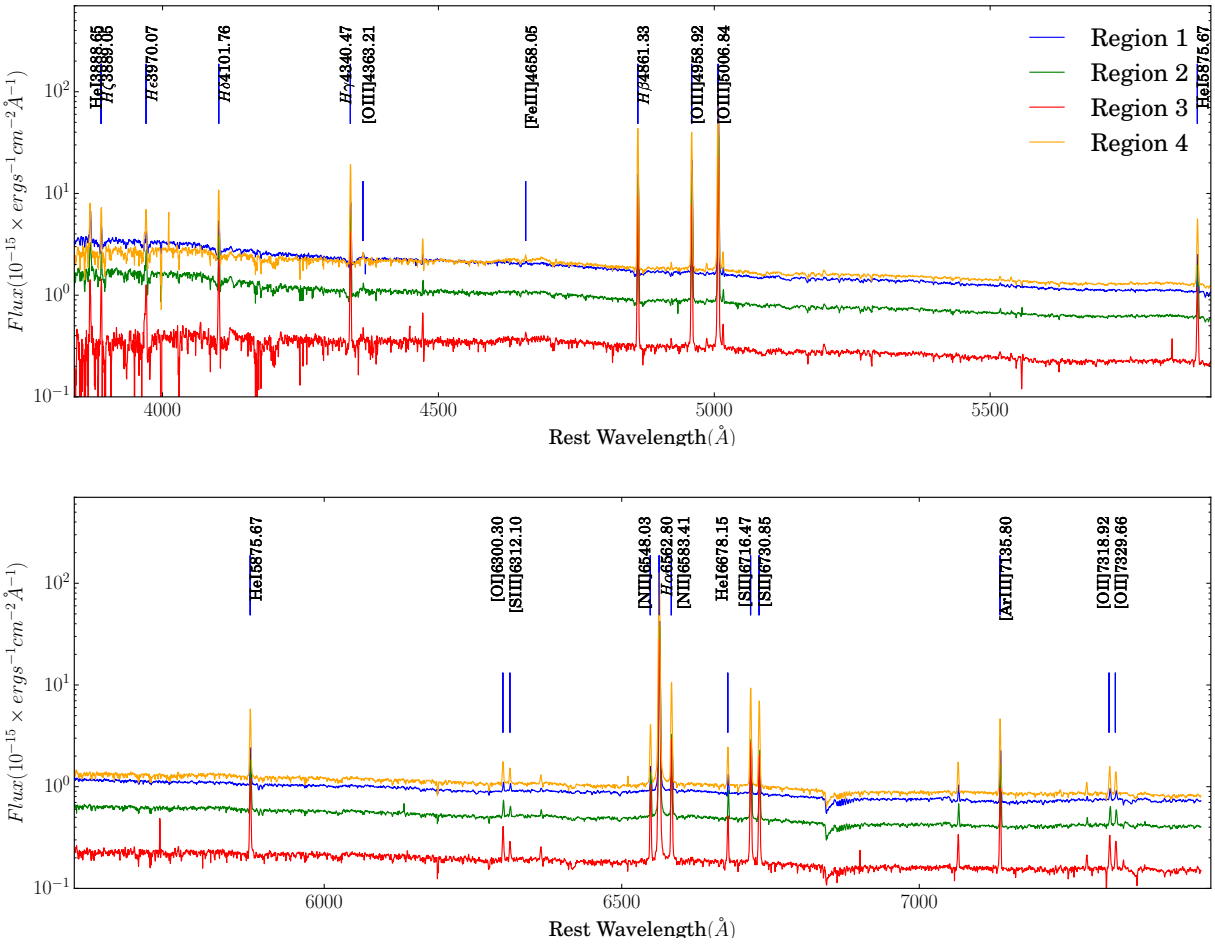

Figure 4.3 – GMOS-IFU integrated spectra of individual H II regions in the FOV in the blue (upper panel) and red (lower panel) settings. The spectra of the four H II regions are colour-coded as follows: region 1: blue, region 2: green, region 3: red, region 4: orange. The blue ends of the spectra are noisier due to the low sensitivity of GMOS-IFU, which makes it difficult to show [O II] λ3727,3729 line in log scale. I show the [O II] λ3727,3729 line for all regions in Figure 4.4, along with the spectral line fitting.

4.2 Results

4.2.1 Observed and Intrinsic Fluxes

4.2.1.1 Flux measurement

Figure 4.2 (left-hand panel) shows the *Hubble Space Telescope (HST)* image of NGC 4670 taken in the filter F435W. The black rectangular box represents the GMOS aperture (3.5 arcsec $\times$ 5 arcsec). The lower right panel presents the distribution of Hα emission line (obtained from GMOS) across the FOV, and clearly shows four regions (green rectangular boxes labelled as "Reg 1", "Reg 2", "Reg 3" and "Reg 4") of current/increased star-formation activity. These regions have been selected by visually inspecting the Hα emission line map, and roughly identifying isophotal regions. The present analysis includes the spatially-resolved and integrated properties of these four H II regions, which are referred to as Regions 1, 2, 3 and 4 in the following. Note here that all analysis related to regions 1 and 4 should be treated with more caution since the GMOS-FOV does not cover these regions completely. In Figure 4.3, I show the GMOS-IFU integrated spectra of these four regions in the blue and red parts of the optical spectrum. The principal emission lines are overplotted at their rest wavelengths in air.

I measure the emission line fluxes for all the main recombination and collisionally excited lines within the spectra by fitting Gaussian profiles to emission lines after subtracting the continuum and absorption features in recombination lines in the spectral region of interest. A single Gaussian profile was used to fit each emission line. Figure 4.4 shows the Gaussian fits for the [O II] doublet, where the peaks of the two emission lines [O II]$\lambda\lambda$3727,3729 could be hardly resolved for the four star-forming regions. In the spaxels where the peaks of the two emission lines in the [O II] doublet could not be resolved at all, I fitted a single Gaussian. While fitting Gaussian to the emission lines, I gave equal weight to flux in each spectral pixel since the dispersion in the continuum flux is found to be constant in the spectral region of interest both in the calibrated and uncalibrated spectra. This shows that the uncertainty of flux-determination within a spectral window is constant. The error estimates on fluxes are the errors obtained while fitting Gaussians to the emission lines. The uncertainty related to the level of continuum is very small, hence the error on the flux is dominated by the error on the Gaussian fitting. The error estimates are consistent with those estimated from a Monte Carlo simulation. The fitting errors have been propagated to the other quantities using Monte Carlo simulations in subsequent analysis.

Figure 4.5 shows the observed flux maps of the GMOS FOV of B-band continuum, [O II] $\lambda\lambda$3727,3729, [O II] λ5007, Hα, [N II] λ6584 and [SII] λ6731. White spaxels in all maps correspond to the spaxels in which emission lines have S/N $<$ 3. The B-band continuum map is obtained by integrating the blue cube in the wavelength range of 3980–4920 Å (in the rest-

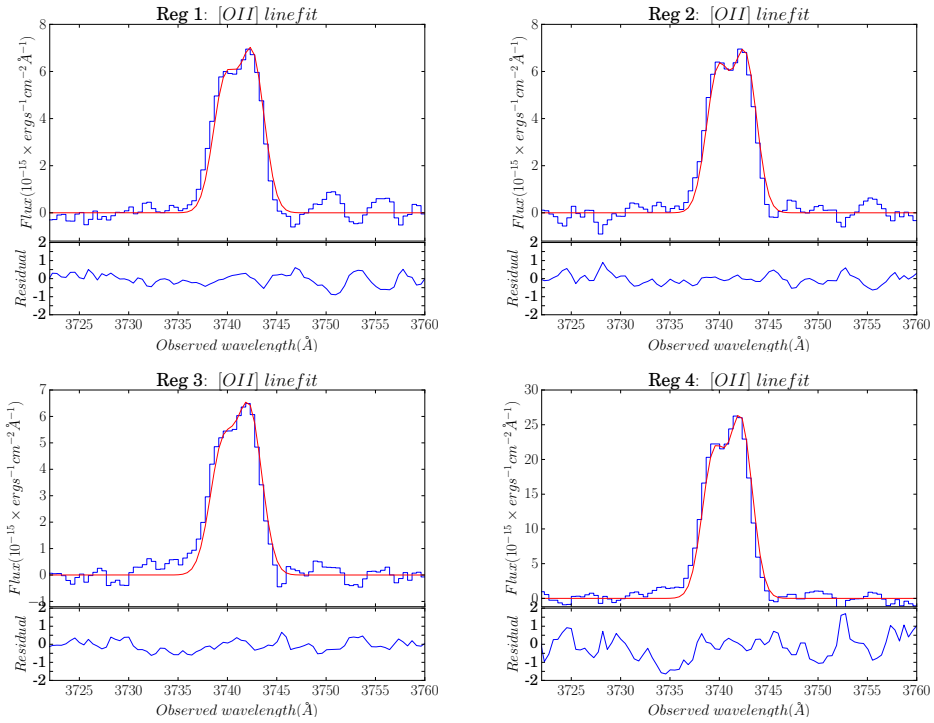

Figure 4.4 – In the four panels corresponding to four H II regions, the upper panel shows the continuum-subtracted [O II] $\lambda\lambda$3727,3729 line (blue curve) detected in each region along with the 'Gaussian' fit (red curve) to extract flux, and the lower panels show the residuals normalised to be in σ-noise units.

frame). The spatial profile of the continuum map remains same irrespective of the masking of emission lines. Table 4.2 presents the observed fluxes for the main emission lines used in the present analysis obtained from the integrated spectra of the four H II regions (Figure 4.3; "Reg 1", "Reg 2", "Reg 3" and "Reg 4" shown in Figure 4.2).

4.2.1.2 Dust attenuation

I estimate E(B-V) by using the relationship between the nebular emission line colour excess and the Balmer decrement given by equation 3.2 in Chapter 3 and the extinction curve of the Large Magellanic Cloud (LMC) (Fitzpatrick, 1999)[1]. I chose the LMC attenuation curve because the metallicity of NGC 4670 is reported to be 12+log(O/H) = 8.30 (Hirashita, Tajiri & Kamaya, 2002), which is close to that of LMC, 8.35±0.06 (Russell & Dopita, 1992).

Following the above procedure, I found negative values of E(B-V) for some spaxels in random regions of the FOV, which I forced to the "Galactic foreground" E(B-V) value (= 0.0128). The negative values of E(B-V) could be due to dominance of shot noise in the low-extinction regions (Hong et al., 2013; Kumari, James & Irwin, 2017). Figure 4.6 shows the map of E(B-V),

[1]The choice of attenuation curves is of little importance here as the attenuation curves of LMC, SMC, starburst or the MW have similar values in the optical range.

Table 4.2 – Emission line measurements (relative to Hβ = 100) for the integrated spectra of the four H II regions shown in Figure 4.2. Line fluxes (F_λ) are extinction corrected using E(B-V) to calculate I_λ for each of the individual H II regions.

Line	λ_{air}	$F1_\lambda$	$I1_\lambda$	$F2_\lambda$	$I2_\lambda$	$F3_\lambda$	$I3_\lambda$	$F4_\lambda$	$I4_\lambda$
$[OII]$	3726.03	127.88 ± 3.63	135.57 ± 6.02	147.14 ± 4.43	154.48 ± 7.10	178.38 ± 6.28	197.62 ± 8.68	153.60 ± 3.22	169.56 ± 5.85
$H\gamma$	4340.47	44.82 ± 0.80	45.97 ± 1.66	43.88 ± 0.56	44.82 ± 1.54	43.08 ± 0.52	45.03 ± 1.22	42.76 ± 0.35	44.63 ± 1.18
$[OIII]$	4363.21	2.78 ± 0.35	2.84 ± 0.37	1.84 ± 0.24	1.88 ± 0.25	1.64 ± 0.24	1.72 ± 0.26	1.26 ± 0.15	1.31 ± 0.16
$H\beta$	4861.33	100.00 ± 0.58	100.00 ± 2.15	100.00 ± 0.56	100.00 ± 2.18	100.00 ± 0.41	100.00 ± 1.65	100.00 ± 0.42	100.00 ± 1.71
$[OIII]$	4958.92	141.05 ± 1.00	140.47 ± 4.19	99.58 ± 0.71	99.24 ± 3.02	81.17 ± 0.46	80.59 ± 1.86	91.76 ± 0.51	91.13 ± 2.18
$[OIII]$	5006.84	418.30 ± 3.02	415.64 ± 12.33	294.67 ± 2.24	293.11 ± 8.89	242.41 ± 1.53	239.72 ± 5.53	273.50 ± 1.71	270.57 ± 6.48
HeI	5875.67	12.28 ± 0.24	11.81 ± 0.39	12.95 ± 0.18	12.54 ± 0.38	13.18 ± 0.14	12.31 ± 0.28	12.66 ± 0.14	11.85 ± 0.29
$[NII]$	6548.03	4.88 ± 0.47	4.60 ± 0.46	7.09 ± 0.58	6.75 ± 0.58	9.66 ± 0.49	8.72 ± 0.47	7.80 ± 0.54	7.07 ± 0.51
$H\alpha$	6562.8	303.46 ± 1.97	286.00 ± 7.42	300.48 ± 1.99	286.00 ± 7.57	317.31 ± 1.59	286.00 ± 5.72	316.16 ± 1.65	286.00 ± 5.96
$[NII]$	6583.41	15.30 ± 0.48	14.41 ± 0.58	22.40 ± 0.60	21.31 ± 0.79	30.07 ± 0.51	27.08 ± 0.69	24.11 ± 0.55	21.79 ± 0.66
$[SII]$	6716.47	13.96 ± 0.16	13.10 ± 0.36	19.92 ± 0.21	18.90 ± 0.52	28.14 ± 0.22	25.18 ± 0.52	20.99 ± 0.18	18.86 ± 0.41
$[SII]$	6730.85	10.37 ± 0.15	9.73 ± 0.28	14.73 ± 0.19	13.96 ± 0.40	20.39 ± 0.20	18.24 ± 0.39	15.24 ± 0.17	13.68 ± 0.31
$[OII]$	7318.92	1.80 ± 0.06	1.67 ± 0.07	2.09 ± 0.07	1.95 ± 0.08	2.28 ± 0.11	1.99 ± 0.10	2.09 ± 0.11	1.84 ± 0.10
$[OII]$	7329.66	1.34 ± 0.05	1.24 ± 0.06	1.70 ± 0.06	1.59 ± 0.07	1.87 ± 0.10	1.63 ± 0.09	1.64 ± 0.09	1.44 ± 0.08
E(B-V)		0.057 ± 0.006		0.048 ± 0.006		0.099 ± 0.005		0.096 ± 0.005	
F(Hβ)		28.46 ± 0.17	34.37 ± 0.74	25.20 ± 0.14	29.50 ± 0.64	19.31 ± 0.08	26.90 ± 0.44	87.11 ± 0.36	119.92 ± 2.06

Notes: F(Hβ) in units of $\times\ 10^{-15}$ erg cm^{-2} s^{-1}

which varies from 0.012–0.60 mag across the FOV. I find that the four H II regions have relatively lesser dust attenuation than the rest of the regions in the FOV. The E(B-V) map appears to be similar to the continuum map (Figure 4.5, upper right panel), i.e. the region to north-west of the group of H II regions with weak continuum is more extincted. To investigate this further, I compared the continuum maps of NGC 4670 in the B- and R-bands, the colour (B-R) map resembles the E(B-V) map. The Balmer decrements $(H\alpha/H\beta)$ observed for the four H II regions are in agreement with the results of Huchra et al. (1983), who report it to be approximately 3 from the broad-band photometric data of NGC 4670. These results are consistent with works of Huchra et al. (1983), whose optical data indicate little internal extinction.

Using E(B-V) obtained above, I calculate the extinction in magnitudes for the emission line fluxes and finally calculate the intrinsic flux maps using equation 3.3 as done in Chapter 3. The intrinsic emission line fluxes calculated from the integrated spectra of the four H II regions are presented in Table 4.2.

4.2.2 Gas Kinematics

Figure 4.7 shows the maps of radial velocity and velocity dispersion (FWHM) of the Hα emission line, obtained from the centroid and width of the Gaussian fit to the emission line. I correct the radial velocity map for the barycentric correction (= -13.74 km s^{-1}) and systemic velocity of 1069 km s^{-1} of NGC 4670 (Wolfinger et al., 2013). I also correct the FWHM maps for the instrumental broadening of 1.7 Å of GMOS-IFU.

The radial velocity map (Figure 4.7, left panel) shows that the ionised gas is slowly rotating about an axis of rotation going diagonally (NE-SW) through the FOV. The radial velocity varies between ~ -10 and 30 km s^{-1}. The gas is redshifted in H II regions 1 and 2 while it is blueshifted in regions 3 and 4. The velocity map shows an isovelocity S-shaped contour, which

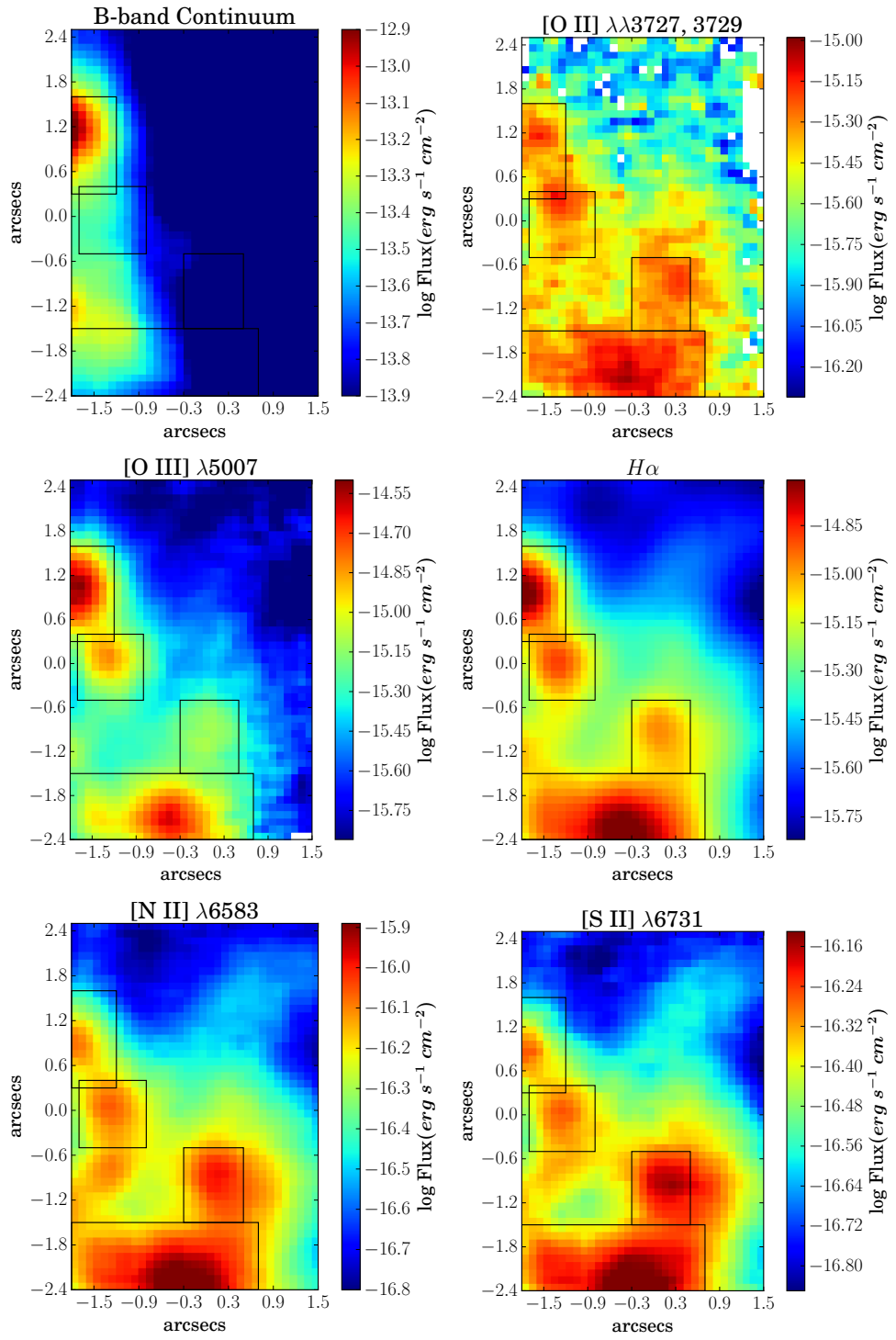

Figure 4.5 – Observed B-band continuum map and the emission line flux maps ([O II]$\lambda\lambda$3727,3729, [O II]λ5007, Hα, [N II]λ6584 and [SII]λ6731) of NGC 4670. The four black rectangular boxes denote the location of the four H II regions. White spaxels correspond to the spaxels in which emission line fluxes had S/N < 3.

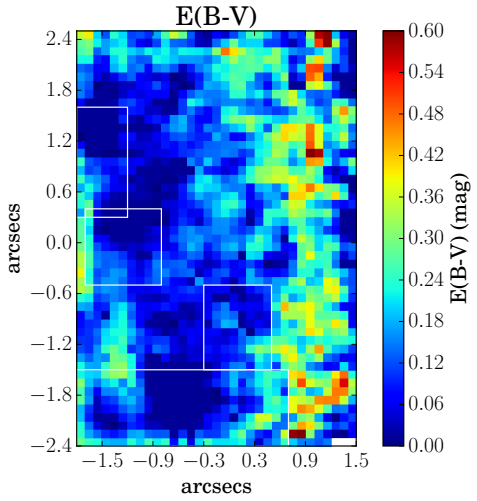

Figure 4.6 – E(B-V) map created assuming the LMC extinction curve. Spaxels with E(B-V) $<$ 0 are set to E(B-V) of the Galactic foreground. The four white rectangular boxes denote the location of the four H II regions. White spaxels correspond to the spaxels in which emission line fluxes had S/N $<$ 3.

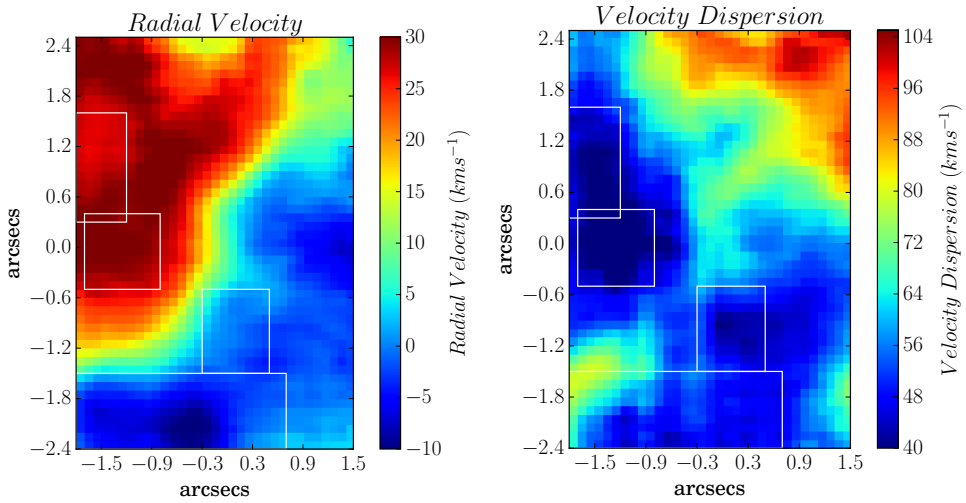

Figure 4.7 – Radial velocity (left) and FWHM (right) maps of the ionised gas obtained from the Hα emission line. Radial velocity is corrected for systemic (= 1069 km s^{-1}) and barycentric velocities (= $-$13.74 km s^{-1}). FWHM is corrected for instrumental broadening (= 1.7 Å). The four white rectangular boxes denote the location of the four H II regions.

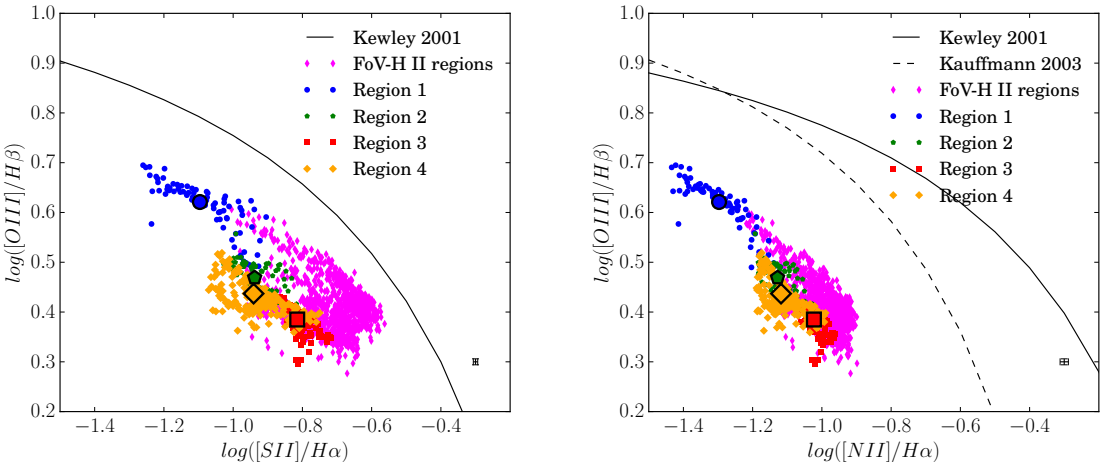

Figure 4.8 – Emission line ratio diagnostic diagrams: [O III]/Hβ versus [S II]/Hα (left), and [O III]/Hβ versus [N II]/Hα (right). Black solid curve and dashed curve represent the theoretical maximum starburst line from Kewley et al. (2001) and Kauffmann et al. (2003), respectively, showing a classification based on excitation mechanisms. The line ratios of the four H II regions are colour-coded as follows: region 1: blue circle, region 2: green pentagon, region 3: red square, region 4: orange diamond. Smaller markers denote the spatially-resolved (spaxel-by-spaxel) line-ratios and the bigger markers denote the line-ratios obtained from the integrated spectrum of the corresponding regions. Magenta coloured markers denote the spatially-resolved line-ratios of the regions of FOV excluding the four H II regions. The size of errorbars varies for line ratios and the median error bars are shown in the right corner of each panel. The error bars on the line ratios obtained from the integrated spectra of the four H II regions are smaller than the markers used here.

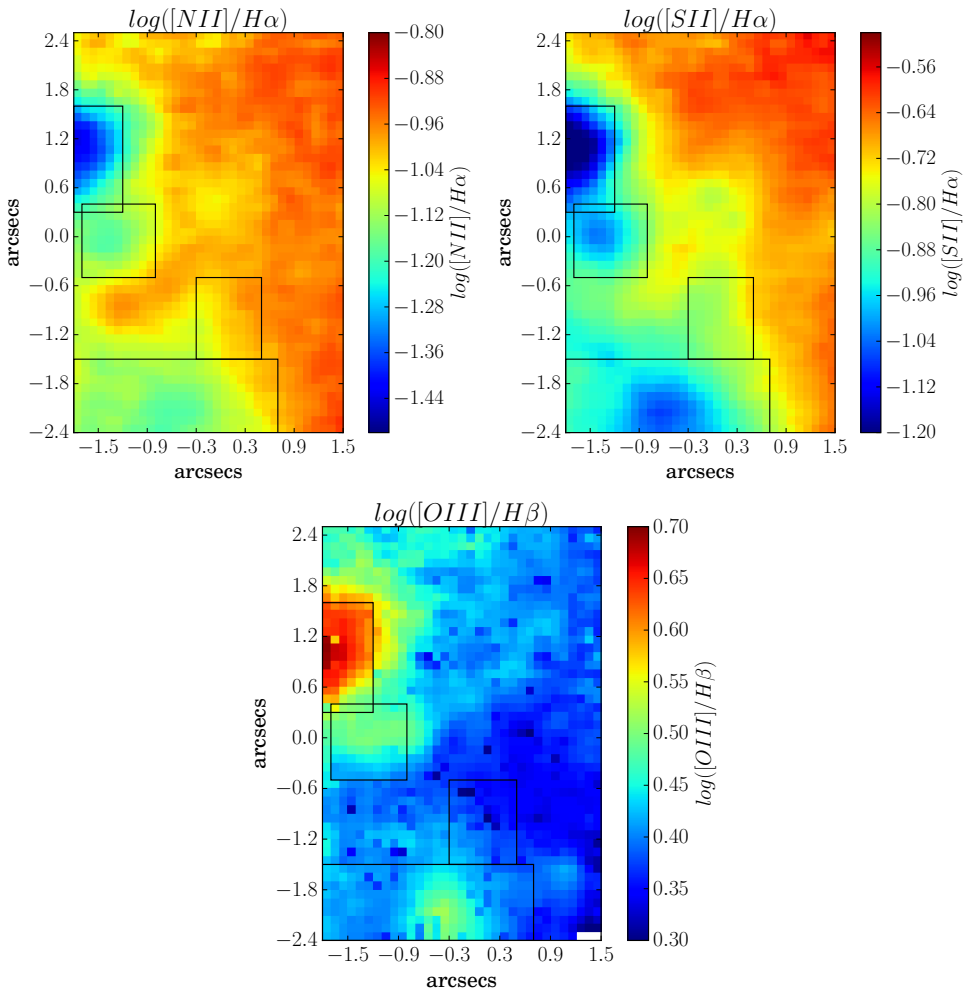

Figure 4.9 – Emission line ratio maps of $[N\,\textsc{ii}]\lambda6583/H\alpha$, $[S\,\textsc{ii}]\lambda\lambda6717,6731/H\alpha$ and $[O\,\textsc{iii}]\lambda5007/H\beta$. The four black rectangular boxes denote the location of the four H II regions. White spaxels correspond to those spaxels with emission line fluxes having S/N $<$ 3.

Table 4.3 – Integrated properties of the four H II regions of NGC 4670 in the GMOS-FOV

	Ionisation Conditions			
	Region 1	Region 2	Region 3	Region 4
log ($[OIII]\lambda5007/H\beta$)	0.621 ± 0.003	0.469 ± 0.003	0.385 ± 0.003	0.437 ± 0.003
log ($[NII]\lambda6583/H\alpha$)	-1.297 ± 0.013	-1.128 ± 0.011	-1.023 ± 0.007	-1.118 ± 0.01
log ($[SII]\lambda\lambda6717,6731/H\alpha$)	-1.096 ± 0.004	-0.938 ± 0.003	-0.815 ± 0.003	-0.941 ± 0.003
	Abundance Analysis			
	Region 1	Region 2	Region 3	Region 4
T_e(O III) (K)	10100 ± 400	9900 ± 400	10200 ± 500	9200 ± 300
T_e(O II) (K)	10500 ± 400	11000 ± 400	9700 ± 300	10000 ± 200
N_e (cm^{-3})	80 ± 30	70 ± 30	<50	<50
12 + log(O^+/H^+)	7.58 ± 0.06	7.55 ± 0.07	7.89 ± 0.06	7.77 ± 0.05
12 + log(O^{++}/H^+)	8.17 ± 0.06	8.05 ± 0.06	7.91 ± 0.07	8.12 ± 0.05
12 + log (O/H)	8.27 ± 0.05	8.17 ± 0.05	8.21 ± 0.05	8.28 ± 0.04
log(N/O)	-1.16 ± 0.07	-1.02 ± 0.08	-1.11 ± 0.07	-1.11 ± 0.06
y^+ (He I 5876)	0.088±0.003	0.093±0.003	0.092±0.002	0.086±0.002
	Stellar Properties			
	Region 1	Region 2	Region 3	Region 4
EW(Hα) (Å)	∼97	∼152	∼334	∼265
Age (sub-$Z_\odot$) (Myr)	∼24	∼22	∼16	∼17
SFR ($Z_\odot$)($\times10^{-3}$M$_\odot$yr^{-1})	20.3 ± 0.3	17.5 ± 0.3	15.9 ± 0.2	70.9 ± 0.8
SFR (sub-$Z_\odot$)($\times10^{-3}$M$_\odot$yr^{-1})	13.4 ± 0.2	10.8 ± 0.2	10.1 ± 0.1	47.1 ± 0.6

is in agreement with the [O III] velocity map of the entire galaxy presented by Cairós et al. (2012). Note here that their one spatial element covers the entire FOV of GMOS-IFU.

The FWHM map (Figure 4.7, right panel) shows a variation of 40–104 km s^{-1} across the FOV [2]. All the H II regions have a relatively lower velocity dispersion compared to the rest of the FOV.

4.2.3 Emission line ratio diagnostics

Figure 4.8 shows the classical emission line ratio diagnostic diagrams ([O III]λ5007/Hβ versus [S II]$\lambda\lambda$6717,6731/Hα (right panel) and [O III]λ5007/Hβ versus [N II]λ6584/Hα (left panel)), commonly known as BPT diagrams (Baldwin, Phillips & Terlevich, 1981) which present a powerful tool to identify the ionisation mechanisms at play in the ionised gas. On both diagnostic diagrams, the solid black line represents the maximum starburst line, known as the "Kewley line" (Kewley et al., 2001) showing classification based on excitation mechanisms. The emission line ratios lying below and to the left of the Kewley line can be explained by the photoionisation by massive stars, while some other source of ionisation [e.g. active galactic nuclei (AGNs) or mechanical shocks] is required to explain the emission line ratios lying above the Kewley line. On the [N II]λ6584/Hα diagnostic diagram (Figure 4.8, right panel), the dashed

[2]One may also estimate the thermal contribution to the velocity dispersion (Amorín et al., 2012b). From the mean T_e values of the four H II regions (Table 4.3), I estimated this contribution as, $\sqrt{\frac{kT_e}{m_H}} \sim 9$ km s^{-1}. This correction leads the velocity dispersion to decrease by only ~ 1 km s^{-1}.

black curve indicates the empirical line derived by Kauffmann et al. (2003) based on the SDSS spectra of 55 757 galaxies. The zone enclosed between this empirical curve and the theoretical "Kewley line" is referred to as the composite zone. The emission line ratios corresponding to the four H II regions (see Table 4.3) derived from their integrated spectra are shown as blue circle (region 1), green pentagon (region 2), red square (region 3) and orange diamond (region 4). The spatially-resolved (spaxel-by-spaxel) emission line ratios in the FOV for different regions are shown using the same colour and markers but smaller sizes. In addition, I also show the line ratios in the spaxels which are not covered by any of the four star-forming regions by magenta coloured markers. I find that both the integrated and spatially-resolved data lie below and to the left of the Kewley line. Evidently no data lies in the composite region, hence confirming photoionisation by massive stars as the dominant ionisation mechanism in the target region of NGC 4670. Note here that the composite zone may also be assigned to pure H II regions with very high N/O (Pérez-Montero & Contini, 2009). Although there is some local N pollution in and around some H II regions in the sample (Figure 4.11), this is not enough to make the regions lie in the composite zone. Previous IFS studies of resolved H II regions in BCDs have shown that low-excitation spaxels can lie in the AGN region (see e.g. Pérez-Montero et al. (2011) and Kumari, James & Irwin (2017) for BCDs HS0128+2832, HS 0837+4717 and NGC 4449, respectively). However, this is not the case for the spatially-resolved data in the BCD under study, NGC 4670.

I study the spatial structure of the ionisation through the relevant line ratio maps shown in Figure 4.9. The H II regions, particularly Regions 1, 2 and 4 show low values of [N II]λ6584/Hα (upper-left panel) and [S II]$\lambda\lambda$6717,6731/Hα (upper-right panel), and high values of [O II]λ5007/Hβ (lower panel), indicating that the corresponding regions have relatively high excitation. This is likely due to the presence of a harder ionising field from hot massive stars in the respective H II regions. These regions are also brighter in the B-band continuum (Figure 4.5, upper-left panel), supporting the inference of the presence of massive stars.

4.2.4 Chemical Abundances

4.2.4.1 Integrated spectra chemical abundances

I estimate chemical abundances of the four H II regions in the target region of NGC 4670 from their integrated spectra (Figure 4.3) by the direct method (i.e. using electron temperatures and collisionally excited lines). All emission line fluxes are reddening-corrected for chemical abundance determination. Table 4.3 summarises the chemical properties of the four H II regions.

Electron Temperature and Density: The first step in estimating chemical abundance by the direct method is the determination of electron temperature(T_e) and density (N_e). I derive T_e ([O III]) from the dereddened [O III] line ratio, [O III] (λ5007 +λ4959)/[O III]λ4363 and

the expression from Pérez-Montero (2017), which is obtained assuming a five-level atom, using collision strengths from Aggarwal & Keenan (1999), and is valid in the range of 7000-25000 K. The estimated T_e ([O III]) for the four H II regions vary from ∼9200 to 10200 K (Table 4.3).

Using the derived T_e ([O III]) value for each star-forming region and the corresponding [S II] doublet ratio $\lambda6717/\lambda6731$ from the integrated spectra, I compute N_e ([S II]) of the four H II regions (Table 4.3). I find N_e to be low in all the four H II regions, with values < 50 cm^{-3} in regions 3 and 4. Such low densities and derived T_e ([O III]) are common within H II regions (Osterbrock & Ferland, 2006b).

To derive the temperature of the low-ionisation zone T_e ([O II]), I employ the expression given in Pérez-Montero (2017)[3], which uses the ratio of oxygen doublets, ([O II] ($\lambda3726$ + $\lambda3729$)/ [O II]($\lambda7319$ + $\lambda7330$)), in combination with the electron density N_e (derived above). The expression is valid in the range of 8000–25000K, where the collision coefficients are taken from Pradhan et al. (2006) and Tayal (2007). The estimated T_e ([O II]) of the four H II regions vary from ∼9700 to 11000 K (Table 4.3).

Oxygen abundance: Oxygen is used as a proxy for total metallicity because it is the most prominent heavy element observed in the optical spectrum in the form of O^0, O^+, O^{2+} and O^{3+}. I employ the formulations of Pérez-Montero (2017) to calculate O^+/H^+ and O^{2+}/H^+ using T_e ([O II]) and T_e ([O III]), respectively, i.e. the electron temperatures of the ionisation zone dominated by the corresponding ions. The O^+/H^+ and O^{2+}/H^+ are combined to calculate the elemental O/H for all four H II regions given in Table 4.3. The values of 12+log(O/H) vary between 8.17 and 8.28, with a mean = 8.23 and standard deviation = 0.04. These values fall in the transition region between the intermediate- and the high-metallicity regime that I discuss further in Section 4.3.

Previous studies reported the metallicity of NGC 4670 using only indirect methods. For example, Mas-Hesse & Kunth (1999) estimates 12+log(O/H) = 8.4 from a 11 arcsec slit spectrum, while Cairós et al. (2012), calculated metallicity using another strong-line calibration, the P-method (Pilyugin & Thuan, 2005) and reported 12 + log(O)/H = 8.29 for the entire galaxy (∼ 80 arcsec × 80 arcsec) and 12+log(O/H) = 8.37 for the nuclear region (∼ 40 arcsec × 40 arcsec). The mean metallicity of 12+log(O/H) = 8.23 calculated from the direct method in this work is lower than all those values, which is consistent with the systematic offsets existing between different metallicity diagnostics as noted by Kewley & Ellison (2008). Moreover the region under study in this work is much smaller (∼ 3.5 arcsec × 5 arcsec) than the previous studies.

Nitrogen-to-oxygen ratio: Assuming the low-ionisation zone temperature T_e ([O II]) and density N_e ([S II]) derived above, I use the emission line ratio of ([N II]($\lambda6584$ + $\lambda6584$)/ Hβ formulation from Pérez-Montero (2017) to derive log(N^+/H^+) for all four H II regions.

[3]See Appendix 4.5.1 for updated formulae.

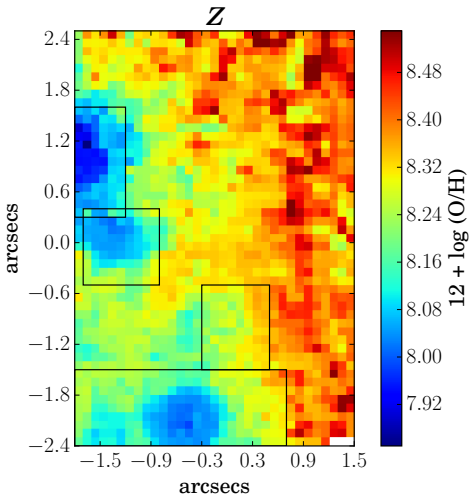

Figure 4.10 – Metallicity map obtained using the HII-CHI-mistry code. The four black rectangular boxes denote the location of the four H II regions. White spaxels correspond to the spaxels in which emission line fluxes had S/N < 3.

Assuming that $N^+/O^+ = N/O$, I use $\log(N^+/H^+)$ and $\log(O^+/H^+)$ to derive log(N/O). These values agree with those derived directly from ([N II]λ6584/ [O II] (λ3726 + λ3729)) using the log(N/O) formula from Pérez-Montero (2017)[3]. The log(N/O) values of the four H II regions vary between -1.02 and -1.16, with a mean of -1.10 and a standard deviation of 0.05.

Helium abundance: I use the reddening-corrected He I 5876 line in combination with T_e ([O II]) and N_e ([S II]) derived above, to calculate the helium abundances (y^+) of the four H II regions. Other helium lines are not used as they are either weak (S/N < 3) or affected by absorption of underlying stellar populations in one or more H II regions. The expression for theoretical emissivities are taken from Pérez-Montero (2017), and the optical depth function is assumed to be one. This assumption on optical depth along with the contamination of He lines due to underlying absorption feature would result in an uncertainty of only $\sim$2% in the helium abundance (Hägele et al., 2008). The y^+ values for the four H II regions vary between 0.086 and 0.093, with a mean of 0.090 and standard deviation of 0.003.

4.2.4.2 Spatially-resolved chemical abundances

To map chemical abundance using the robust T_e-method, the detection of a weak auroral line is required throughout the FOV. Unfortunately, the S/N ratio of [O III]λ4363 in the individual spectrum across the FOV was too low (< 3) to use the direct T_e-method. Various indirect methods involving the use of strong emission lines have been devised to estimate chemical abundances to overcome this problem. Some of the popular indirect methods involve the use of the N2 parameter (Denicoló, Terlevich & Terlevich, 2002), O3N2 parameter (Pettini & Pagel, 2004), R_{23} (Pagel et al., 1979) N2S2Hα (Dopita et al., 2016) or a combination of them (e.g. Maiolino et al., 2008; Curti et al., 2017). I used three of these strong line methods in the analysis

of another BCD, NGC 4449 (Kumari, James & Irwin, 2017) and found the well-known problem of the offsets between the metallicities from the direct and indirect method Kewley & Ellison (2008). In this work, instead, I make use of the publicly-available python-based code HII-CHI-mistry (v3.0)[4]. This code takes the dereddened fluxes, follows a χ^2-based methodology on a grid of photoionisation models, including CLOUDY and POPSTAR, and outputs chemical-abundances (O/H, N/O). The grid of photoionisation models assume 17 different values of the ratio log(N/O) in the range [0.0, -2.0], 11 different values of log $\mathcal{U}$[5] [-1.5, 4.0] and 21 different values of metallicity [7.1, 9.1]. Please see Pérez-Montero (2014) for details of the models and code. The errors on the output abundances are calculated by the code using a Monte Carlo iteration from the reported errors of the measured lines. By using this code, I aim to remove the dependence of oxygen abundance on the nitrogen-to-oxygen ratio, which is an inherent assumption in some of the strong line calibrators. This becomes useful when I study the spatially-resolved (O/H) versus (N/O) later in Section 4.3.

Oxygen abundance: Figure 4.10 shows the metallicity map of the FOV obtained from the HII-CHI-mistry code. The value of 12 + log(O/H) varies between $\sim$ 7.80 and 8.56 with a mean value of = 8.29 and standard deviation = 0.13. I find that region 1 is metal-poor compared to the other three H II regions. However, metallicity estimates obtained from the integrated spectra of the four H II regions show that regions 1 and 4 have comparable metallicities. This is likely due to an aperture effect, i.e. when we integrate over the large regions, the temperature and metallicity gets dominated by the brightest regions and becomes luminosity-weighted. Thus even though region 4 hosts a range of metallicities, it is dominated by the large low-metallicity blob that has similar metallicity to that of region 1 as inferred from the integrated spectra. The mean value of spatially-resolved log(O/H) agrees with the mean value calculated from the integrated spectra of the four H II regions within $\pm$1 standard deviation.

Nitrogen-to-oxygen ratio: Figure 4.11 shows the log(N/O) map of the FOV from the HII-CHI-mistry code. The value of log(N/O) varies between $-$1.4 and $-$1.08, with a mean value of = $-$1.23 and standard deviation = 0.06. I find that there is an increase in log(N/O) values in the region surrounded by the three H II regions 2,3 and 4. This is probably a region which formed stars in the past but is quiescent now, resulting in a relatively chemical-enriched ionised gas. The log(N/O) map also shows that region 3 has a relatively lower log(N/O) value compared to other H II regions, however it is the integrated spectrum of region 1 that shows the highest log(N/O) (Table 4.3). This is likely due to aperture effects as explained above. The mean value of spatially-resolved log(N/O) agrees with the mean value calculated from the integrated spectra of the four H II regions within $\pm$2 standard deviations.

The maps of log(O/H) and log(N/O) show signatures of chemical inhomogeneity though the significance is low because of high error bars. I will explore the homogeneity of chemical

[4]http://www.iaa.es/ epm/HII-CHI-mistry.html
[5]Ionisation parameter

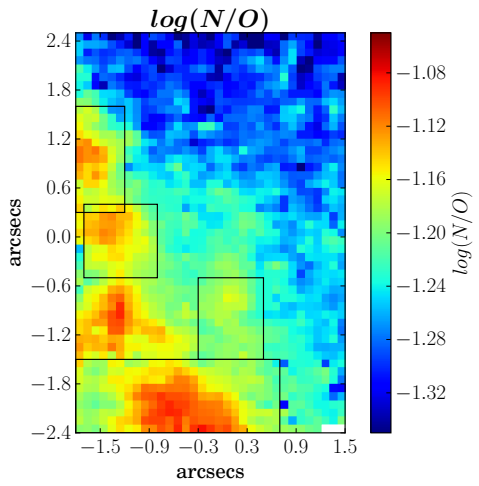

Figure 4.11 – log(N/O) map obtained using the HII-CHI-mistry code. The four black rectangular boxes denote the location of the four H II regions. White spaxels correspond to the spaxels in which emission line fluxes had S/N < 3.

abundances in future as discussed in Chapter 8.

Helium abundance: For mapping helium abundance (y^+), spatially-resolved electron temperature and density measurements are needed. As mentioned earlier, such maps could not be made because of the low S/N of the weak auroral line [O III] λ4363. So I create the T_e ([O III]) map by using the HII-CHI-mistry derived metallicity map (Figure 4.10), and the relation between log(O/H) and T_e ([O III]) from Pérez-Montero (2017) (proposed initially in Amorín et al. (2015)). I use the T_e ([O III]) map in conjunction with spatially-resolved [S II] doublets to map N_e across the FOV [6]. Among all the He lines detected in the data (He I 4471, 5876, 6678 and 7065Å , He II 4686), the flux map corresponding to He I λ5876 has the highest S/N across the entire FOV. Hence, I use the dereddened flux map of He I λ5876 along with the T_e ([O III]) and N_e maps to create the helium abundance map (Figure 4.12). The theoretical emissivities and the optical depth function are same as described in Section 4.2.4.1. Comparing the helium abundance map (Figure 4.12) with the B-band continuum (Figure 4.5), I find that there is a relative increase of y^+ in the regions surrounding the continuum. Given that the continuum indicates the region with a relatively older population, it is likely that these stars or cluster of stars lost their He envelope, thus the winds emanating from their outer atmosphere resulted in an increase in y^+ in the surrounding regions. Note that more massive WR stars lose H and He before processing to CNO elements, which might be the reason for no apparent enhancement of other elements in that region.

[6]The maps of T_e ([O III]) and N_e derived in this section are presented in Appendix 4.5.2

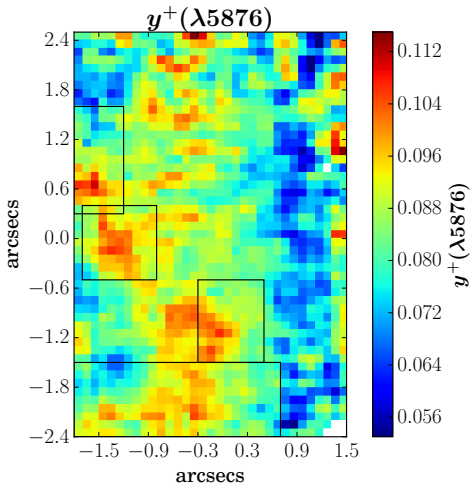

Figure 4.12 – Helium abundance map obtained from He I λ5876 flux map. The four black rectangular boxes denote the location of the four H II regions. White spaxels correspond to the spaxels in which emission line fluxes had S/N < 3. The typical uncertainty on y+ map is 0.005 dex.

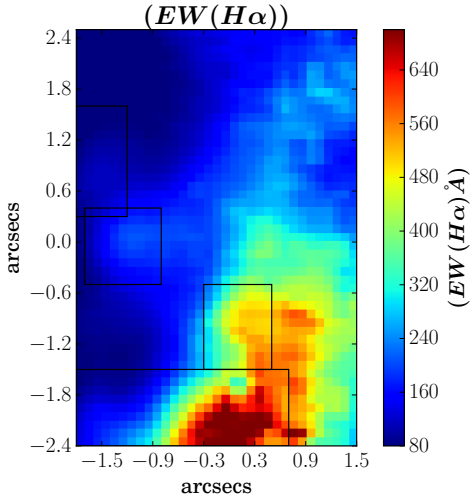

Figure 4.13 – Map of equivalent width of Hα. The four black rectangular boxes denote the location of the four H II regions.

4.2.5 Stellar Properties

4.2.5.1 Age of stellar population

The integrated spectra of the four H II regions (Figure 4.3) show Balmer emission lines indicating the presence of young, hot and massive O and B stars, and Balmer absorption lines (Hβ, Hγ etc.) indicating the presence of early-type A stars. For age-dating the current ionising population, I first map the equivalent width (EW) of Hα recombination line as shown in Figure 4.13. The EW values show a variation of 48–776 Å across the FOV. Such high values of EW(Hα) have been found in H II regions in the local BCDs (e.g. I Zw 18, Mrk 475, Mrk 1236, NGC 2363 by Buckalew, Kobulnicky & Dufour, 2005). Considering higher redshifts, Shim et al. (2011) found EW(Hα) = 140–1700 Å for a galaxy sample in the redshift range of $3.8 < z < 5.0$, although with higher star-formation rates ($\sim$20–500 $M_{\odot}yr^{-1}$). High EW(Hα) (697–1550Å) are also found in the extreme green peas (GPs) (Jaskot & Oey, 2013). Thus NGC 4670 may be similar to the GPs and high redshift galaxies, with respect to EW(Hα).

To find the age of the stellar population, I next estimate the EW(Hα) from the evolutionary synthesis models of Starburst99 (Leitherer et al., 1999) at a constant mean metallicity ($\sim$ 0.35 $Z_{\odot}$) of the four H II regions (calculated in Section 4.2.4.1). For generating models corresponding to the properties typical of H II regions, I adopt Geneva tracks with standard mass-loss rates assuming instantaneous star-formation. The choice of evolutionary tracks results in a relatively small change in the estimated age, with Padova tracks predicting higher ages by up to 20% (James, Tsamis & Barlow, 2010). I assume a Salpeter type initial mass function (IMF) (Salpeter, 1955) and the total stellar mass extent between the upper and lower cut-offs fixed to default value of 10^6 $M_{\odot}$. The expanding stellar atmosphere is taken into account by using the recommended and realistic models of Pauldrach/Hiller. I have also taken into account the stellar rotation in the models though that leads to an insignificant increase of 3% in age (Kumari, James & Irwin, 2017). I compare the modelled EW with the observed EW (Figure 4.13) and, hence map the corresponding age shown in Figure 4.14 which shows a variation of 10–30 Myr across the FOV. The map shows that the stellar population of approximately same age is present in each star-forming region, except region 4 where stellar population of different ages are present, with the youngest at the peak of region 4. The older-age stellar population also seems to align with the two peaks of B-band continuum map (Figure 4.5, upper-left panel). An interesting observation is the similarity of the age map and the velocity map (Figure 4.7, left panel) i.e. on both maps, we see higher velocity/older age populations in one half and lower velocity/younger age in the other half. This probably indicates that the ionised gas near the same-age stellar population have similar velocities, or it may be simply due to the large scale rotation effects.

I also measure EW(Hα) from the integrated spectra of the four H II regions and calculate

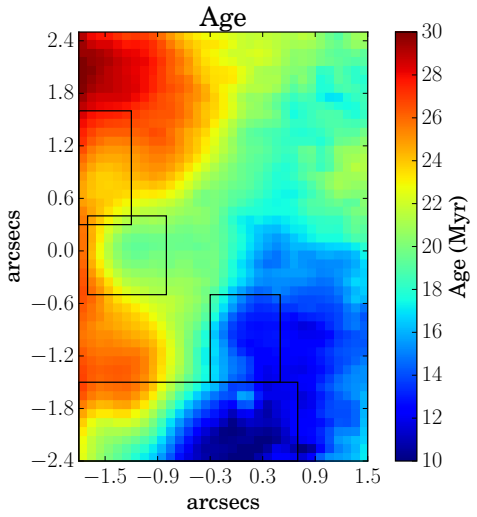

Figure 4.14 – Age map in Myr calculated from Starburst99 models at the constant metallicity of Z = 0.35 $Z_{\odot}$ (mean of metallicities of the four H II regions tabulated in Table 4.3).

the age of the stellar population residing in those regions at sub-solar metallicities (found for each region). The results are tabulated in Table 4.3. The age of these regions are in agreement with the spatially-resolved age shown in Figure 4.14.

The age range of 10–30 Myr derived here, is higher than the age of ∼4 Myr estimated by the Mas-Hesse & Kunth (1999) from their evolutionary population synthesis models. The difference is mainly because the models of Mas-Hesse & Kunth (1999) are weakly sensitive to previous star-formation episodes but rather to the ones younger than 10 Myr. Their calculation had been for a period of only 20 Myr since they were mainly interested in the evolution of massive stars. In contrast, the upper age limit on the models in this work is 100 Myr. In spite of all evident explanations of the difference in results, readers are cautioned to interpret the results in light of the various systematic uncertainties involved in the modelling, e.g. those related to the internal dust attenuation, determination of continuum level that is the combination of the nebular and stellar continuum resulting from different age stellar populations existent in the same region (see e.g. Pérez-Montero et al., 2007; Cantin et al., 2010). Note here that Starburst99 do not take into account the binary population, though ∼ 50% of stars are found in binaries. Ignoring the binary population is another source of systematic uncertainty on the determined age.

4.2.5.2 Wolf-Rayet stars

WR stars are the evolved O stars, which have lost substantial mass to expose their H or He-burning core. They are very hot with effective temperatures of 25,000 K to 100,000 K, and emit winds at speeds ranging between 800 km s^{-1} and 3000 km s^{-1}, which result in broad emission features instead of the narrow absorption lines characteristic of normal stars. WR stars are

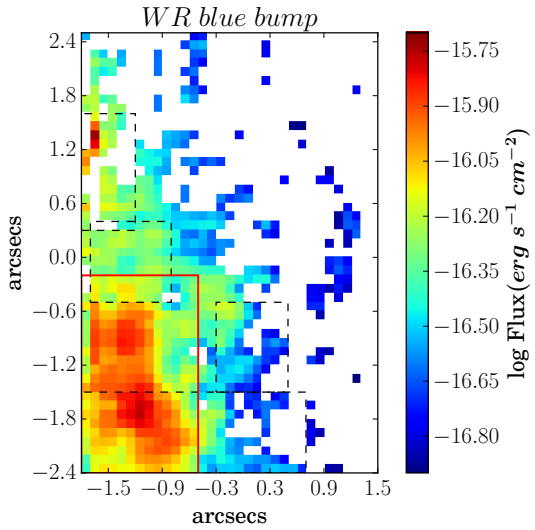

Figure 4.15 – Emission map of the blue WR feature (created by integrating over the full emission feature from 4600–4700Å), showing the distribution of WR stars in the FOV. The red rectangular box shows the peak of the WR distribution which I use for subsequent analysis. The four black dashed rectangular boxes denote the location of the four H II regions. White spaxels correspond to the spaxels in which WR emission fluxes had S/N < 3.

mainly of two types: WN stars characterised by strong emission lines of He and N, and WC or WO stars characterised by strong He, C and O lines, respectively. WN stars are further classified as early-type WN stars lacking H and late-type WN stars with H present on their surfaces.

Figure 4.15 shows the emission map of the blue WR feature showing the distribution of WR stars in the FOV. The map is created by integrating over the full emission feature from 4600 to 4700 Å after subtracting the underlying continuum. The blue bump of the WR feature is mainly composed of N V, N III, C III/IV blends and the He II λ4686 line, and is generally contaminated by nebular line [Fe III] λ4658 line. However, this contaminating line is not strong enough (S/N < 3) at the spatially-resolved scale in the data[7]. Hence I do not remove its contribution while mapping the WR feature shown in Figure 4.15. In this map, all white spaxels correspond to the spaxels in which the combined WR blend or feature has S/N < 3, and the black dashed rectangular boxes denote the location of the four H II regions. I find that the WR feature becomes prominent in the region to the south-east of the peak of region 4, and to the south-west of region 2. I mark the corresponding region (WR region) of peak WR emission by the red rectangular box in Figure 4.15. This region does not contain the peak of any of the four H II regions but lies close to regions 2 and 4. This may indicate the propagation of star-formation from the current WR region to the current H II regions and has been observed before in a dwarf galaxy Mrk 178 (Kehrig et al., 2013). The region of prominent WR emission also shows an increase in log(N/O) (Figure 4.11). This observation is expected because WR stars are the

[7]Taking the ratio of summed fluxes of WR map with S/N>3 and summed fluxes of [Fe III] λ4658 with S/N>1, I find an upper-limit of 6% as contribution of [Fe III] λ4658 in the WR map.

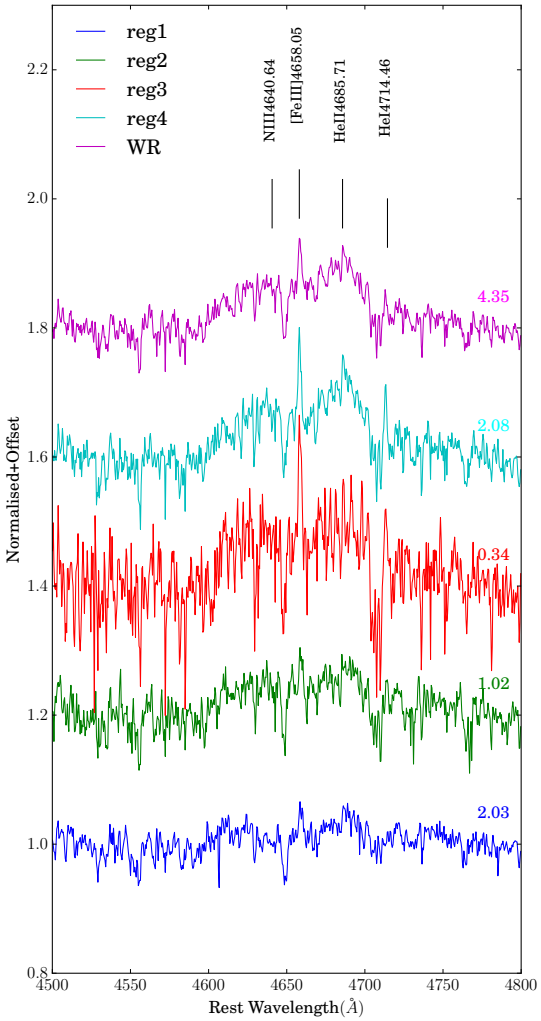

Figure 4.16 – WR 'blue bump' features (N V λ4620, N III λ4640 and He II λ4685) in the integrated spectra of all H II regions along with the region showing the peak in WR distribution (red box in Figure 4.15). The integrated spectra are normalised by the continuum in the respective region and then offset by 0.2 with respect to each other for better visibility. On the right hand side above each spectrum, I show the average level of continuum (in units of 10^{-15} erg s^{-1} cm^{-2} Å^{-1}) in the given wavelength range corresponding to each region in the same colour. The blue bump indicates the presence of late-type WN and WC stars. All these spectra also show a gap between the broad λ4640 feature and the nebular iron line [Fe III] λ4658.05Å.

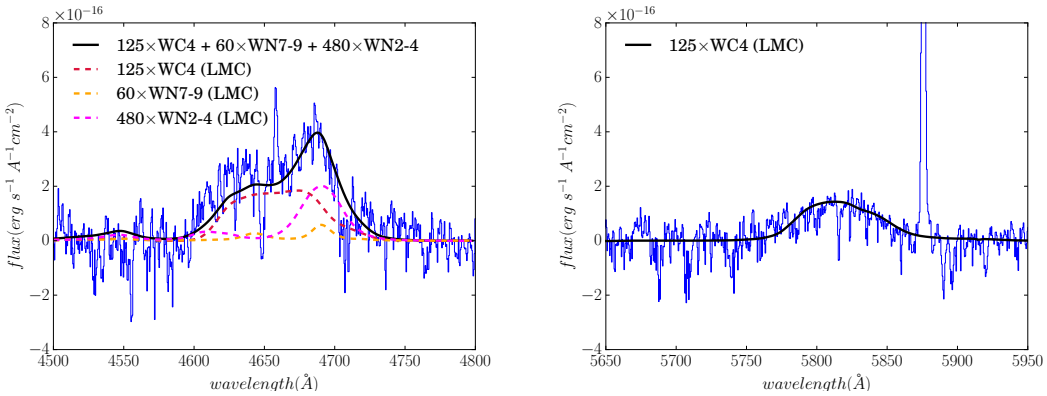

Figure 4.17 – Left: Continuum-subtracted WR 'blue bump' feature summed over the peak of WR distribution (red box in Figure 4.15). Overplotted is the combined fit (solid black curve) for 125 WC4 stars (red dashed curve), 60 WN7-9 stars (orange dashed curve) and 480 WN2-4 stars (magenta dashed curve), using the LMC templates of Crowther & Hadfield (2006). Right: Continuum-subtracted WR 'red bump' feature summed over the peak of WR distribution (red box in Figure 4.15). Overplotted (solid black curve) is the scaled LMC template of WC4 star from Crowther & Hadfield (2006), denoting the presence of 125 WC4 stars.

evolved phases of massive O stars which lose N to the interstellar medium via stellar winds. These winds may also explain the slight increase in the y^+ map (Figure 4.12) surrounding the WR region. The age of WR stars are expected to be in the range ∼3–8 Myr (Meynet, 1995). However, the age map (Figure 4.14) reveals a slightly older (∼10–30 Myr) ionising stellar population in this region. This might simply indicate the existence of an older stellar population along with the younger WR stars. However, note also that the estimated age in this region has further uncertainties related to the implementation of WR evolution in the stellar evolution models since accounting for it properly requires binary evolution. The understanding of the WR evolution is not complete, and the predictions for the line spectrum emitted by a WR population is rather speculative (Leitherer et al., 2010).

Figure 4.16 presents the WR "blue bump" feature in integrated spectra of all H II regions along with the WR region, which shows the peak in the WR distribution (red box in Figure 4.15). In all these spectra, I find a gap between the broad 4640 feature and the [Fe III] λ4658.05 emission line. This rare feature was first identified strongly in NGC 3049 (Schaerer, Contini & Kunth, 1999) and explained as a real feature by Schmutz & Vacca (1999). Basically, the gap arises because the 4640 feature is not one broad feature but a combination of at least three emission components (N V λλ4604, 4620, N III λλ4634, 4641, C III λλ4647, 4650). Except region 4, none of the star-forming regions show a prominent WR "blue bump" feature. Inspecting the spectra of region 4, I find the observed blue bump is mainly due to the common region which it shares with the WR region. Hence I concentrate on the WR region for subsequent analysis of WR stars.

I estimate the number of WR stars in the region showing the peak of the WR distribution (red box in Figure 4.15), by fitting WR templates to the integrated spectrum of the corresponding region. Since the mean metallicity of the FOV (12 + log(O/H) = 8.23) is closer to that of LMC than the Small Magellanic Cloud [i.e. 12 + log(O/H) = 8.35 and 12 + log(O/H) = 8.03, respectively, (Russell & Dopita, 1992)], I use the WR LMC templates (Crowther & Hadfield, 2006). The specific LMC templates are selected on the basis of the relative strength of different components of the WR blue and red bumps revealed by the spectrum. For modelling the red bump, both WC4 and WO templates are available. I did a χ^2 minimization using the two templates separately for the red-bump, and found that the WC4 template produced a better fit. Moreover, the spectrum has a clear C IVλ5808 feature indicating the presence of WC4 stars, but no O Vλ5990, a signature of WO stars. Hence I selected WC4 template for the rest of the template fitting. For fitting the more complex blue bump, I selected the WN7-9 template over the WN5-6 template, because the relative strength of He IIλ4686 and and the broad emission $\sim$4640 Å in the spectrum are similar to WN7-9 template. I also include the WN2-4 template for modelling the N Vλ4604, 4620 feature revealed in the spectrum. Finally, I perform a χ^2 minimization using the above selected templates and simultaneously fit all spectral regions of interest, i.e. the red bump and the three clear features of blue bump (N V $\lambda\lambda$4604, 4620, N III $\lambda\lambda$4634, 4641, He IIλ4686). In χ^2 minimization, I used the dispersion in the emission-free continuum region as the uncertainty on the input WR fluxes. I calculated the uncertainty on the number of WR stars obtained from a Monte-Carlo simulation using the dispersion in the emission free region. Hence I estimate $\sim$125$\pm$4 carbon-type (WC4) stars, $\sim$60$\pm$20 late-type (WN7-9) stars and $\sim$480$\pm$50 early-type (WN2-4) stars. The corresponding fit is shown in Figure 4.17 for both blue (left panel) and red bump (right panel). The blue wing of the blue bump in Figure 4.17 appears to be under-estimated in the best-fit. This underestimate is probably because of the presence of a different sub-group of WR stars than the ones for which WR templates are available. For example, no WR templates are available for WN10-11 stars or WC stars other than WC4. Cairós et al. (2012) reports WR signatures in the central region of NGC 4670 that approximately overlaps with the GMOS-FOV, though there is no estimate of the number of WR stars available for comparison with the study. I have found $\sim$670$\pm$50 WR stars over a region of 212 pc $\times$ 116 pc. This density is lower ($\sim$ a factor of 2) in comparison to another BCD Mrk 996 where $\sim$ 3000 WR stars are reported in an area of 4.6 $\times$ 10^4 pc^2 (James et al., 2009). However, these densities are higher in comparison to a nearby WR galaxy Mrk 178, where 20 WR stars are found in a region of $\sim$ 300 $\times$ 230 pc (Kehrig et al., 2013).

4.2.5.3 Star Formation Rate

Assuming a constant metallicity throughout the FOV, I map the SFR assuming Z = 0.35 $Z_\odot$ (Figure 4.18) using the metallicity-dependent relation between dereddened luminosity of Hα,

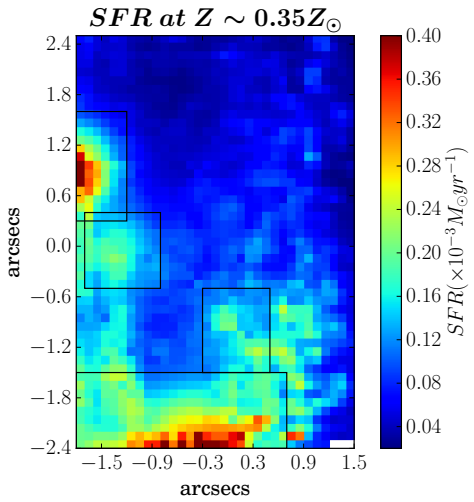

Figure 4.18 – SFR Map of the FOV in units of $\times$ 10^{-3} $M_\odot$ yr^{-1} at 0.35 $Z_\odot$. The four black rectangular boxes denote the location of the four H II regions.

L(Hα) and SFR from Ly et al. (2016) derived from the Starburst99 models assuming a Padova stellar track and Chabrier IMF(Chabrier, 2003). The SFR values vary between 0.02–0.49 $\times$ 10^{-3} $M_\odot$ yr^{-1} at sub-solar metallicity. I also map the SFR assuming solar-metallicity using the L(Hα)–SFR relation given in Kennicutt (1998b) for a Salpeter IMF. I include a multiplicative factor of 0.63 in the SFR map at solar metallicity to account for the Chabrier IMF, which has a more realistic distribution at the lower end of stellar masses. I find that the SFR varies between 0.03–0.77 $\times$ 10^{-3} $M_\odot$ yr^{-1} at solar metallicity. The SFR map at solar metallicity shows a similar pattern as the one at sub-solar metallicity.

I also estimate the SFR for the four H II regions assuming solar and sub-solar metallicities for each region using the recipes mentioned above. The results are given in Table 4.3. For both integrated data of the four H II regions and spatially-resolved data, I find that the SFR estimated assuming sub-solar metallicity is lower than those at solar metallicity. This is because the atmosphere of metal-poor O stars are more transparent resulting in an increased escape fraction for the ionising photons and hence lower SFR. These results are in agreement with the SFRs of other BCDs, which span a range of 10^{-3} to 10^{2} $M_\odot$ yr^{-1} (Hopkins, Schulte-Ladbeck & Drozdovsky, 2002).

4.3 Discussion

4.3.1 N/O Conundrum revisited

The relationship between the nitrogen-to-oxygen ratio and the oxygen abundance in H II regions has been the subject of intense debate (e.g. see McCall, Rybski & Shields, 1985; Thuan, Izotov & Lipovetsky, 1995; Henry, Edmunds & Köppen, 2000; Izotov et al., 2006; López-Sánchez &

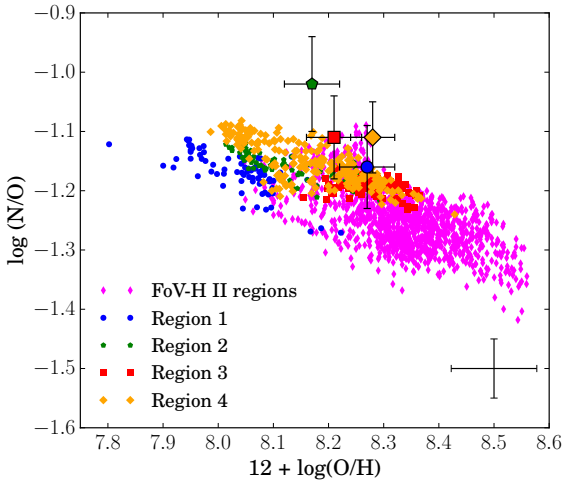

Figure 4.19 – The relationship between log(N/O) versus 12 + log(O/H) for the four H II regions as well as the whole FOV (on spaxel-by-spaxel basis). The four regions are colour-coded as follows: region 1: blue circle, region 2: green pentagon, region 3: red square, region 4: orange diamond. Smaller markers denote the spatially-resolved (spaxel-by-spaxel) relation where the two quantities [log(N/O) and 12 + log(O/H)] are calculated from the HII-CHI-mistry code whereas the bigger markers denote quantities calculated from the direct T_e-method for the four H II regions. Magenta coloured markers denote the spatially-resolved quantities of the regions of FOV excluding the four H II regions. The median error bars for the spatially-resolved quantities are shown in the right-hand corner.

Esteban, 2010; Vincenzo et al., 2016; Belfiore et al., 2017) and has been used to probe the origin of nitrogen in different metallicity regimes. Based on the analysis of 54 H II regions in BCDs, Izotov & Thuan (1999) proposed three metallicity regimes related to the origin of nitrogen. In the low-metallicity regime (12 + log(O/H) $<$ 7.6), nitrogen is thought to have a primary origin and is produced by massive stars only, which set the level of log(N/O) at ~ -1.6 with a very low scatter. However, since the mechanism of production of nitrogen in massive stars is not clearly understood, the behaviour of the relationship in the low-metallicity regime could also result due to effects related to stellar rotation (Meynet & Maeder, 2005), low SFR (Henry, Edmunds & Köppen, 2000), low number of WR stars (Izotov et al., 2006), or the production of nitrogen by low-and intermediate-mass stars (see e.g López-Sánchez & Esteban, 2010). In the intermediate-metallicity regime (7.6 $<$ 12 + log(O/H) $<$ 8.3), the value of log(N/O) increases above -1.6 and the origin of nitrogen is interpreted to be primary but produced by intermediate-mass stars, which evolve and release their nucleosynthesis products into the interstellar medium. The relation shows a large scatter ($\pm$0.3 dex). Berg et al. (2012) reports a positive slope between the log(N/O) and 12 + log(O/H) for the metallicity values 12 + log(O/H) $>$ 7.7, indicating a secondary origin of nitrogen even in the intermediate-metallicity regime. However, their analysis of H II regions in low-luminosity dwarf galaxies does show a large scatter. This scatter has been observed in several observational studies of systems with low and intermediate metallici-

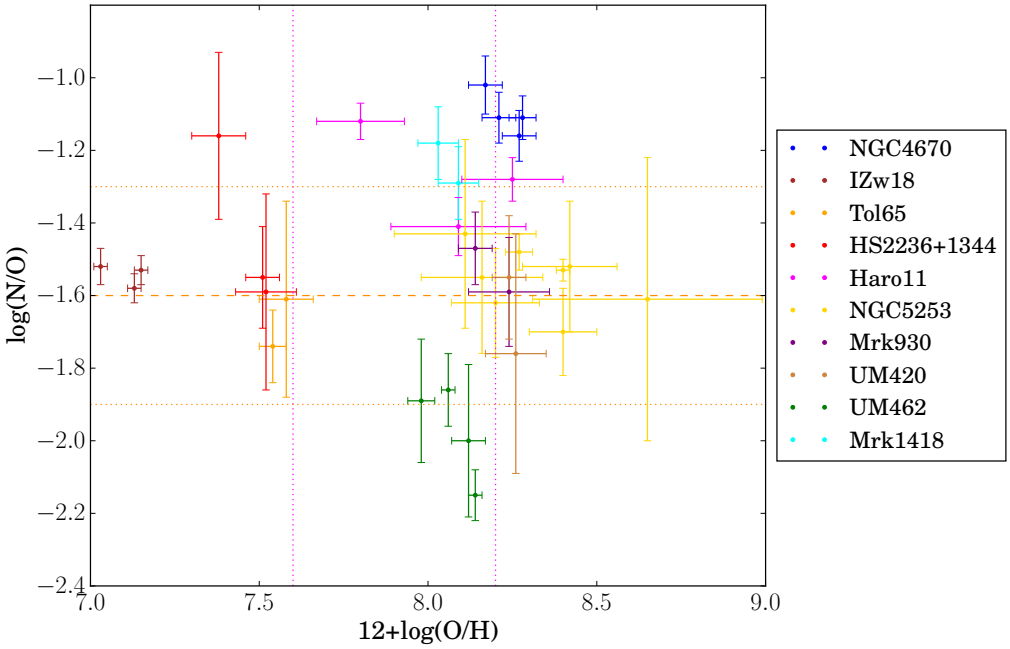

Figure 4.20 – log(N/O) versus 12 + log(O/H) of H II regions within BCDs, where data points in the same colour correspond to the H II regions from the same BCD. See Table 4.4 for the data reference. The orange dashed line indicates the plateau at log(N/O) $= -1.6$, and the orange dotted lines correspond to ± 0.3 dex enclosing the region of scatter found in the literature (e.g. Izotov & Thuan, 1999). The vertical pink dotted lines at metallicity 12 + log(O/H) = 7.6, define the transition from low- to intermediate-metallicity regime and the transition from the intermediate-metallicity regime to the high metallicity regime at 12 + log(O/H) = 8.2.

ties (e.g. van Zee & Haynes, 2006; Pérez-Montero & Contini, 2009; James et al., 2015, 2017), and has been attributed to factors such as, the time delay between the production of oxygen and secondary nitrogen (Garnett, 1990; Vila Costas & Edmunds, 1993; Pettini et al., 2008), variation in the star formation histories (Mollá et al., 2006; Mollá & Gavilán, 2010), the global gas flows in galaxies (Köppen & Hensler, 2005; Amorín et al., 2012b). At high metallicities (12 + log(O/H) $>$ 8.3), nitrogen is thought to have a secondary origin, and hence a positive slope is expected between log(N/O) and 12 + log(O/H). Interestingly, Kobulnicky & Skillman (1996) report a negative trend in the relation for H II regions within the irregular starburst galaxy NGC 4214, with strong WR features.

In Figure 4.19, I present the relationship between log(N/O) versus 12 + log(O/H) for the four H II regions as well as the whole FOV (on spaxel-by-spaxel basis). Caution here that given the spatial scale of the data ($\sim$9 pc), each spaxel may or may not host H II regions since the typical size of H II regions varies between a few to hundreds of pc (Kennicutt, 1984). The oxygen abundance and the nitrogen-to-oxygen ratio for the four H II regions are calculated from the direct T_e-method. However, O/H and N/O for the spatially-resolved data are estimated from the HII-CHI-mistry code. For the four H II regions, I compare these quantities calculated from the direct T_e-method and the HII-CHI-mistry that included the use of [O III] λ4363 line. I find that they agree with each other within 1σ, except for the metallicity of one H II region (region 4) that agrees within 2σ. As noted by Pérez-Montero (2014), there are dispersions of $\sim$0.2 dex in the HII-CHI-mistry model-based and direct T_e-method abundances. Such dispersions may also be due to the fact that these data show WR features but HII-CHI-MISTRY code uses POPSTAR evolutionary synthesis models which do not take into account the evolution within a binary system that affects the appearance of WR phase (Mollá, García-Vargas & Bressan, 2009). It is more difficult to account for such effects at low metallicities, where multiplicity fraction is poorly known (see e.g. Badenes et al., 2018). I expect no trend or a positive trend in these regimes as mentioned before. However, I find a hint of negative trend between N/O and O/H for the four H II regions, while the negative trend is more prominent for the spatially-resolved data (on spaxel-by-spaxel basis), covering 0.3 dex on y-axis and 0.6 dex on x-axis lying in the intermediate- and the high-metallicity regime. I find a correlation coefficient of $-$0.75 for the spatially-resolved data.

As a sanity test, I also estimated the log(N/O) from the N2S2 calibration (Pérez-Montero & Contini, 2009), and the metallicity from the N2 parameter (Pettini & Pagel, 2004), and studied the relation. Since calibrations for N/O and O/H based on nitrogen lines (such as N2S2 and N2, respectively) in principle assume a positive relation between N/O and metallicity, I expected to see a change in the trend found using the direct measurements. For example, from Pérez-Montero & Contini (2009), their Figures 5 and 6 show the existence of a strong correlation between the metallicity derived from the N2 parameter and the N/O ratio in such a way that the metallicity predicted by N2 is overestimated in objects with a high N/O. However, I find

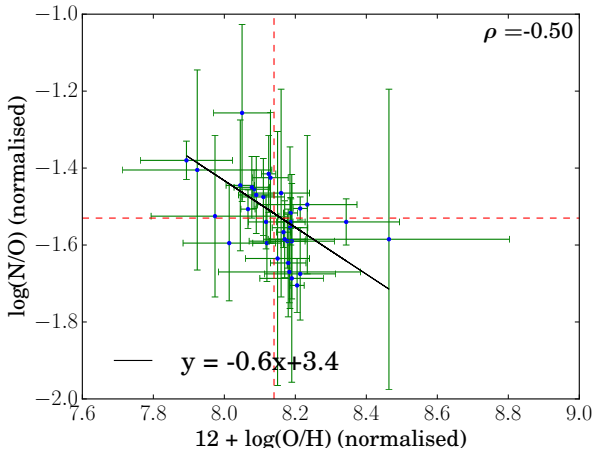

Figure 4.21 – Normalised log(N/O) versus 12 + log(O/H). Error bars are the same as on the original data points (as in Figure 4.20). Best-fit: y= (-0.6±0.16)x+(3.4±1.3). The red dashed straight lines correspond to the medians of the log(N/O) and 12 + log(O/H).

that the apparent anticorrelation between N/O and O/H in Figure 18 still holds, thereby adding confidence to the results. However, the slope (of the negative trend) in this case is steeper than that seen in the relation obtained using HII-CHI-mistry. This might be due to the intrinsic increasing trend of N/O with metallicity in the secondary regime, which will pull the slope to show a positive slope, and hence will result in a steeper negative trend. In Figure 4.19, I only show the spatially-resolved relation based on quantities obtained from the HII-CHI-mistry code rather than from indirect methods (N2 and N2S2), because the former is based on models that do not assume any relation between the metallicity and log(N/O). Moreover, the calibration uncertainty on indirect methods are very high (0.18 dex for (O/H)[N2] and 0.1 dex for (N/O)[N2S2] at 68% confidence level), compared to HII-CHI-mistry results. Given the spaxels are 0.1 arcsec, one may also argue about the effects of seeing. However, seeing will only smear out any pre-existing trend rather than producing a non-existent trend. The slope of the spatially-resolved data appears to be flatter than the slope of integrated data of the four H II regions. This is likely due to the limitations of the photoionisation models used in HII-CHI-mistry as described in Pérez-Montero (2014). High S/N data allowing the detection of the weak auroral line would help circumvent this problem. From the S/N of the faintest H II region (region 4), we estimate that we would need to stack around 20 spectra in order to achieve a S/N ([O III] 4363) $>$ 3.0 within this region. However, our tests on attempting to map this auroral line in the gaps between the H II regions were not successful due to lack of S/N, even after integrating over 100s of spaxels.

4.3.2 H II regions in other BCDs

I further explore the negative trend observed above by studying the relation for H II regions within other BCDs. Note here that all the observational studies mentioned in the beginning of Section 4.3.1, are based on the H II regions in different low-metallicity star-forming galaxies. None of those analyses involve the study of the relation at spatially-resolved scale in a single galaxy. Figure 4.20 shows this relation for star-forming regions in 10 BCDs, where data points in same colour correspond to the star-forming regions in the same BCD. I have compiled the data based on the following criteria: (1) All regional values are from the integrated spectra obtained from the IFS observations. (2) The regions are selected on the basis of Hα maps of BCDs. (3) The values of log(N/O) and 12 + log(O/H) are measured using the direct T_e-method. In Table 4.4 I specify a reference for each data set. Two separate IFU studies were performed for NGC 5253, but I analyse data from Westmoquette et al. (2013), which includes the star-forming regions studied in Monreal-Ibero, Walsh & Vílchez (2012).

In the sample of 10 galaxies, I first analyse six galaxies individually for which there are more than two data points. The values of the Pearson correlation coefficient ρ (Table 4.5) suggest a negative correlation for all the six galaxies. Taking error bars into account, I also fitted a constant model with and without any slope to perform a likelihood ratio test. In Appendix 4.5.3, I present the values of ρ and the details of the log likelihood ratio test for six galaxies in the sample. Amongst the six galaxies, IZw 18 and HS2236+1344 lie in the low-metallicity range where we would not expect a trend, which is also shown by the likelihood ratio test. For NGC 4670, $\rho = -0.83$, which suggests a strong anticorrelation. However, the likelihood ratio test does not favour a negative trend for the group of H II regions under study. Out of the remaining three galaxies, the likelihood ratio test shows that two BCDs in the sample Haro 11 and UM 462 exhibits a negative trend.

The above analysis cannot be performed on the remaining four galaxies (Mrk1418, Mrk930, UM420 and Tol 65) that have only two data points. However, for one of the two regions in Tol 65, Lagos et al. (2016) report high spatially-resolved log(N/O) values, preferentially in spaxels with lower oxygen abundance, which indicates a negative trend on spaxel-by-spaxel basis.

Though in the above analysis I have found hints of a negative trend in the log(N/O) versus log(O/H), it is difficult to say anything definite about the trend because of the few data points in each galaxy. To circumvent this problem, I put the data points corresponding to each galaxy on the same averaging scale of metallicity and log(N/O) by shifting them using the relative medians of the metallicities and log(N/O) for all H II regions in the 10 BCDs. Figure 4.21 shows the relation after normalisation. I find a negative correlation coefficient of $\rho = -0.50$. While the trend was not at all clear from the scatter plot of Figure 4.20, there is a strong hint of a negative trend in Figure 4.21. The likelihood ratio test also confirms the negative trend (see appendix 4.5.3). The negative slope (-0.6 ± 0.16) which I find here agrees within errors with

Table 4.4 – References and Distances of the BCDs shown in Figure 4.20

BCDs	References	Distance (Mpc)
NGC 4670	This study	18.6
IZw18	Kehrig et al. (2016)	18.2
Tol 65	Lagos et al. (2016)	42.7
HS2236+1344	Lagos et al. (2014)	79.7
Haro11	James et al. (2013b)	83.6
NGC 5253	Westmoquette et al. (2013)	3.8
Mrk930	Pérez-Montero et al. (2011)	83.2
UM420	James, Tsamis & Barlow (2010)	23.8
UM462	James, Tsamis & Barlow (2010)	14.4
Mrk1418	Cairós et al. (2009)	14.6

the slope (-0.798 ± 0.350) found for NGC 4214 (Kobulnicky & Skillman, 1996). This shows that it is quite possible that a negative trend between log(N/O) and metallicity might exist for H II regions within BCDs.

4.3.3 Possible causes for a negative relation between N/O and O/H

In this section, I discuss possible explanations for a negative trend between metallicity and log(N/O) in spatially resolved data. In order to understand the negative trend, the spatially-resolved data of NGC 4670 are required to put in a more global perspective. Figure 4.22 shows the spatially-resolved data from this study (brown points) along with the global data (grey points) of a galaxy sample drawn from the MPA-JHU catalogue of SDSS Data Release 7 including only objects classified as purely star-forming. They lie in the redshift range of $0.023 < z < 0.1$ and their stellar masses are restricted to $7 < log(M_\star/M_\odot) \leq 9$ because BCDs are dwarfs with a stellar mass $M_\star < 10^9$ $M_\odot$ (Lian et al., 2016). I compute the log(N/O) and log(O/H) for SDSS galaxies using the HII-CHI-mistry code. In Figure 4.22, I find that the higher metallicity and lower (N/O) end overlaps with the normal star-forming galaxies and therefore is experiencing the typical gas mixing observed within this metallicity range. The deviation occurs for the metallicity range 12+log(O/H) $\lesssim$ 8.2.

Relation to star-formation activity and localised N enrichment: To explain the deviation observed in Figure 4.22, I show in Figure 4.23 the spatially-resolved relation between log(N/O) versus 12 + log(O/H), obtained from the HII-CHI-mistry as explained in Section 4.2.4.2. The data points are colour-coded with respect to the intrinsic Hα fluxes in the corresponding spaxels. Since Hα traces the current (< 5 Myr) star-formation activity, I use the intrinsic Hα flux as a proxy for the on-going star-formation activity in the region of interest. I did not utilise the spatially-resolved star-formation rate maps created in Section 4.2.5.3 because the SFR recipes used to create these maps assume a certain metallicity (solar or sub-solar).

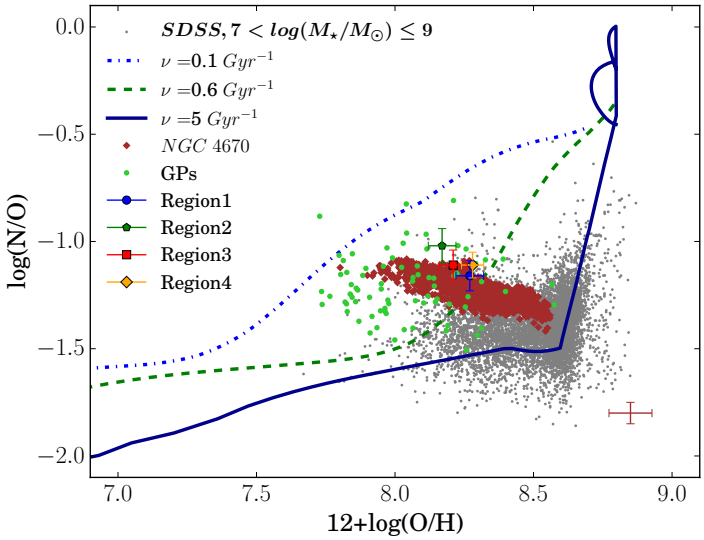

Figure 4.22 – Chemical evolution models from Vincenzo et al. (2016) on the log(N/O) versus log(O/H) plane. The three curves correspond to the three different SFEs, i.e. ν = 5 Gyr^{-1} (solid blue), ν = 0.6 Gyr^{-1} (dashed green) and ν = 0.1 Gyr^{-1}. These models are generated at the infall mass of 10^9 M$_\odot$, and Kroupa IMF. The data corresponding to the integrated spectra of the four star-forming regions are obtained from the direct T$_e$ method and are colour-coded as in the previous figures, region1: blue, region2: green, region3: red and region4: orange. The spatially-resolved data from this work are shown as brown points with the median error bars at the right-hand corner of the plot. The SDSS DR7 data for a sample of nearby star-forming galaxies are shown by grey dots, and the data for green peas are shown by light green points. The HII-CHI-mistry code has been used to generate the values of log(N/O) and log(O/H) for spatially-resolved data from this work, SDSS galaxies and the green peas.

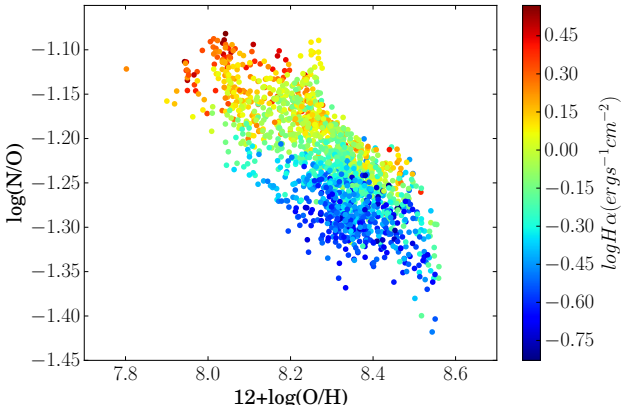

Figure 4.23 – Spatially-resolved relationship between log(N/O) and 12 + log(O/H), where data points are obtained from HII-CHI-mistry code and are colour-coded with respect to the intrinsic Hα fluxes in the corresponding spaxels. I find that the spaxels with lower metallicity and higher log(N/O) also show higher Hα fluxes, whereas the spaxels with higher metallicity and lower log(N/O) show lower Hα fluxes. Hα being a proxy for current ($<$ 5 Myr) star-formation, the negative trend in the log(N/O) versus metallicity is apparently dependent on the on-going star-formation.

Though the metallicity-dependence will only act as an additive constant in Figure 4.23, I prefer avoiding any circularity of argument in the analysis. In Figure 4.23, I find that the spaxels with higher metallicity and lower log(N/O) shows a lower intrinsic Hα flux whereas the spaxels with lower metallicity and higher log(N/O) shows a higher intrinsic Hα flux.

At the low metallicity end, the trend between low-metallicity and increased star-formation can be explained by a scenario in which metal-poor gas flows in, increasing the star-formation rate of the region and decreasing the metallicity. The velocity map of the FOV (Figure 4.7, left panel) shows a rotating structure, with no shock or turbulence that is typical of inflows/outflows. However, gas flows have been proposed/studied in galaxies with indication of rotation (Queyrel et al., 2012; Sánchez Almeida et al., 2014a, 2015; Olmo-García et al., 2017), which may be the case in NGC 4670. A possible cause of the high log(N/O) is a localised nitrogen enrichment of the interstellar medium from the ejecta of WR stars (Kobulnicky et al., 1997; Brinchmann, Kunth & Durret, 2008; López-Sánchez & Esteban, 2010). In support of this enrichment scenario, the log(N/O) map (Figure 4.11) also shows an increase in the region approximately coincident with the peak in WR emission (Figure 4.15). Note here that if metal-poor gas were inflowing, the level of nitrogen enrichment needed to produce an elevated log(N/O) for a given low log(O/H) would be significant. Note here that the inflow does not change N/O at all, only changes O/H. Even if the inflow dilutes the metallicity by say 0.2 dex, the N/O is still larger than the spaxels with that metallicity. Hence, pollution seems certainly more likely than inflow in this case because the N/O enhancement seems local.

Varying star-formation efficiency in different star-forming regions: In Figure 4.22, I

also show the chemical evolution models (three curves) taken from Vincenzo et al. (2016). Though these models have been originally tested on a global basis for galaxies (SDSS sample and low-metallicity dwarfs), they can be used for the spatially-resolved data. This is because in these models, it is assumed that a galaxy is made up of a single zone within which the chemical elements mix instantaneously and uniformly. This assumption is valid for individual star-forming regions as well. Note here that no chemical evolution models are available currently for studies inside galaxies at spatially-resolved scales, hence these models provide the best alternative for the spatially-resolved study presented here. Details on these models can be found in Vincenzo et al. (2016) and Matteucci (2012) including their specific parameters such as infall mass (M_{inf}), infall time-scale, star-formation efficiency (SFE denoted by ν), IMF, mass loading factor, differential galactic outflow.

While employing the chemical evolution models, I have assumed the reference values for all parameters given in Vincenzo et al. (2016), except M_{inf} and SFE. Since the BCDs are low-mass galaxies, I have assumed $M_{inf} = 10^9$ $M_\odot$. At the infall time scale of $\tau_{inf} = 0.1$ Gyr and Kroupa IMF (Kroupa, Tout & Gilmore, 1993), SFEs are varied from 0.1 Gyr^{-1} to 5 Gyr^{-1}, and are shown by three curves with the purpose of covering the region on the plot occupied by the spatially-resolved data of NGC 4670. I find that the spaxels with higher log(N/O) and lower metallicity lie on the region in the plot covered by the chemical evolution model with a relatively low SFE, i.e. $\nu \sim 0.1$ Gyr^{-1}. However, the spaxels with lower log(N/O) and higher metallicity lie in that region that is covered by the models with a relatively high SFE, i.e. $\nu \sim 5$ Gyr^{-1}. The curve corresponding to an intermediate value of SFE appears to go through the middle of the distribution of (N/O)-(O/H) values. Hence I find a gradient in SFE while going from one end [high (N/O)-low (O/H)] to the other end [low (N/O)-high (O/H)] of (N/O)-(O/H) plane. A higher SFE will result in an increased production of oxygen per unit time by massive stars increasing the metallicity of the corresponding regions. If there is a delay in the production of nitrogen, the ratio of nitrogen-to-oxygen will decrease. The same argument related to the delayed production of nitrogen can be applied to the regions with lower SFE, low-metallicity and high nitrogen-to-oxygen ratio. Hence, it appears that the SFE at small spatial scales plays an important role in maintaining the oxygen abundance and the nitrogen-to-oxygen ratio within galaxies. It is likely through its effect on the star-formation history and on the balance of the different stellar population that contribute to the oxygen and nitrogen abundance (Vincenzo et al., 2016).

However, this scenario does not tie in easily with the increased Hα at high log(N/O) and low metallicity. An increased Hα indicates a higher SFR, while the same regions are covered by lower SFE as seen in Figure 4.22. This indicates a higher SFR in a region with lower SFE. If SFE is defined as the ratio of SFR to the available gas for forming stars, then a high SFR for a region with lower SFE simply implies that a large amount of gas is available in the region that is not forming stars. To explore this hypothesis, a more complete analysis of the

spatial distribution of the relative abundance of neutral, molecular, and ionised gas are required. High SFR with low SFE may also point towards the fact that star-formation is a self-regulating process at local sub-galactic scales. Regions with high SFRs may have strong negative energetic feedback from the massive dying stars, which will result in a decreased SFE in the respective star-forming regions.

Alternative explanation: In Figure 4.22, I also show data corresponding to green pea galaxies that are low-redshift extreme emission-line galaxies with very high specific SFR, that are also thought to be excellent analogues of high-redshift star-forming galaxies (Cardamone et al., 2009). As can be seen in Figure 4.22, they exhibit relatively high log(N/O) at a given metallicity in the low-to-intermediate metallicity regime compared to the SDSS galaxies. As discussed in Amorín, Pérez-Montero & Vílchez (2010); Amorín et al. (2012a), the possible cause of such a behaviour could be the simultaneous inflow of metal-poor gas induced by interactions and the outflow of metal-rich gas driven by supernova remnants and stellar winds. The scenario involving gas dynamics was proposed by other observational (van Zee, Salzer & Haynes, 1998) and theoretical studies (Köppen & Hensler, 2005) as well. In this study, a relative increase in the He abundance is found in the region of NGC 4670 surrounding the WR bump, which suggests the local effect of a strong wind emanating from the WR stars. The age of the stellar population found in this work is 10–30 Myr, which are old enough for the existence of supernovae remnants and stellar winds from them. Further analysis is required to find the dynamical state of the ionised, molecular and neutral gas in this galaxy.

4.4 Summary

I have carried out a spatially-resolved study of four H II regions and the surrounding ionised gas located in the central region of the BCD NGC 4670 using the GMOS-N IFS data at the spatial scale of 9 pc. A summary of the main results is as follows:

1. The radial velocity map indicates a slow rotation of the ionised gas varying between ~ -10 and 30 km s^{-1} about an isovelocity S-shaped contour. The velocity dispersion varies between 40 and 104 km s^{-1}, with relatively lower dispersion in the H II regions. No signatures of shock or complex velocity structure is found. The classical [S II]/Hα and [N II]/Hα emission line ratio or BPT diagrams show that photoionisation by massive stars is the main source of ionisation.

2. In the integrated spectra of the four H II regions I could detect the auroral lines [O III] λ4363, [O III] $\lambda\lambda$7320, 7330 which I use to estimate T_e ([O III]), N_e ([S II]) and T_e ([O II]), and hence calculate 12 + log(O/H) varying between 8.17 and 8.28, log(N/O) varying between -1.02 and -1.16 and the helium abundance y^+(5876) varying between 0.086 and 0.093 for the four H II regions.

3. In the spatially-resolved data of the FOV, the auroral line [O III] λ4363 could not be detected with enough S/N (>3), which prevented the chemical abundance determination using the direct T_e-method. Hence I use the HII-CHI-mistry (v3.0) to map 12 + log(O/H) and log(N/O), which vary between 7.80 and 8.56, and between -1.4 and -1.08, respectively, across the FOV. I then use the 12+log(O/H) map to create T_e and N_e maps, with which I map helium abundance $y^+(5876)$ varying between 0.05 and 0.12.

4. The age map is created at a metallicity of $0.35 Z_\odot$ by comparing the observed EW(Hα) map with the modelled EW map using the STARBURST99 population synthesis model. The resultant age map varies between 10 and 30 Myr.

5. I also estimate the number of WR stars from the integrated spectrum of the WR region, which overlaps with three of four H II regions. The WR region contains approximately $\sim$125$\pm$4 WC4 stars, $\sim$60$\pm$20 WN7-9 stars and $\sim$480$\pm$50 WN2-4 stars. The estimate is done by using the LMC WR templates from Crowther & Hadfield (2006).

6. I map SFR of the FOV from the dereddened Hα luminosity at sub-solar metallicity of 0.35 $Z_\odot$ which varies between 0.02 and 0.49 $\times$ 10^{-3} $M_\odot$ yr^{-1}.

7. I revisit the N/O conundrum by studying the relation between the spatially-resolved 12 + log(O/H) and log(N/O) and the integrated data of the H II regions from 9 other BCDs from the literature, and find an unexpected negative trend. I also compare the spatially-resolved data with the low-mass SDSS galaxies and the green pea galaxies and explore various scenarios to explain the trend including nitrogen enrichment, and variations in SFE via chemical evolution models.

In summary, the present analysis shows that a negative trend between log(N/O) and 12+log(O/H) may exist at the spatially-resolved scales and H II regions within BCDs. It is possible that the negative trend that is observed in the spatially-resolved data is merely a manifestation of the large scatter that has been observed previously in other low-metallicity galaxies. To confirm the behaviour of log(N/O) with metallicity, these two properties and their relation need to be studied with high S/N data at spatially-resolved scales across a large sample of BCDs. Those data sets would allow us to map the distribution of metallicity and log(N/O) from robust direct methods and also analyse the WR population in the entire galaxy for a plausible effect of chemical pollution. Moreover such data sets would enable the study of variation of the above-mentioned observables not only within galaxies but also within H II regions, for example via radial profile analysis or a segmentation analysis of individual H II regions (López-Hernández et al., 2013). Those studies would be possible in the future with the current and upcoming IFS facilities like MUSE on Very Large Telescope, WEAVE on William Herschel Telescope and Keck Cosmic

Web Imager because of their large FOV and good spatial sampling, which will enable us to map chemical abundances of entire galaxies. Moreover, such studies could also investigate kinematic signatures to further probe the possible cause of the observations related to gas dynamics. The combination of chemical and kinematical analyses is essential in disentangling chemical evolution scenarios, and obtaining such information across a large sample of entire systems will be key in understanding the origin of nitrogen in these less chemically evolved star-forming systems. In so doing, we will enhance our understanding of chemical evolution scenarios in galaxies within the high-redshift Universe.

4.5 Appendix

4.5.1 Formulae

I present here some of the formulae used in this work, which are actually taken from Pérez-Montero (2017), but have some misprints in the published version. The correct expressions are as follows:

- Temperature of low-ionisation zone:

$$t([O\textsc{ii}])(10^4K) = a_0(n) + a_1(n)R_{O2} + \frac{a_2(n)}{R_{O2}} \tag{4.1}$$

  where

  n : electron density in units of cm^{-3}

$$R_{O2} = \frac{I(3726\mathring{A}) + I(3729\mathring{A})}{I(7319\mathring{A}) + I(7330\mathring{A})} \tag{4.2}$$

$$a_0(n) = 0.2526 - 0.000357n - \frac{0.43}{n} \tag{4.3}$$

$$a_1(n) = 0.00136 + 5.431 \times 10^{-6}n + \frac{0.00481}{n} \tag{4.4}$$

$$a_2(n) = 35.624 - 0.0172n + \frac{25.12}{n} \tag{4.5}$$

- The ratio N^+/O^+

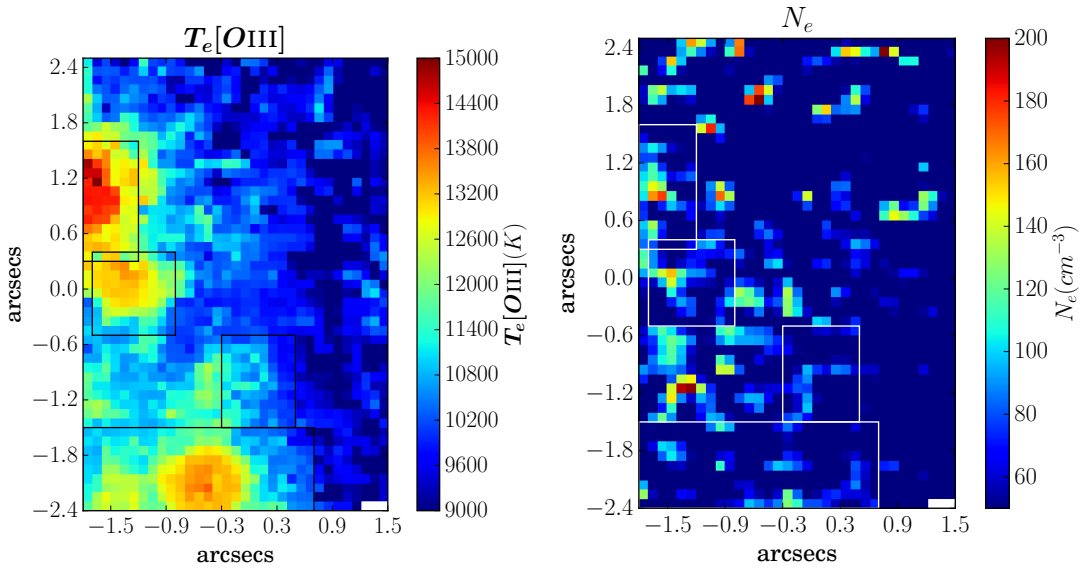

Figure 4.24 – Left panel: T_e([O III]) map obtained from the metallicity map (Figure 4.10). Right panel: N_e map using the [S II] doublet ratio map and T_e([O III] map on left. Majority of the spaxels have upper-density limit of 50 cm^{-3} in those spaxels. The four rectangular boxes in the two maps show the location of the four H II regions.

$$log(\frac{N^+}{O^+}) = log(\frac{I(6583)}{I(3726)+I(3729)}) + 0.493 - 0.025t_l - \frac{0.687}{t_l} + 0.1621log(t_l) \tag{4.6}$$

where t_l is the low-ionisation zone temperature in units of $10^4 K$.

4.5.2 Electron temperature and density derived from metallicity

Figure 4.24 (left panel) shows the T_e([O III]) map obtained from the metallicity map (Figure 4.10), which was itself derived from the HII-CHI-mistry code. Using this indirectly obtained T_e map and the [S II] doublet ratio, I derived the N_e map (Figure 4.24, right panel). I find that the majority of spaxels show 50 cm^{-3}, which is actually an upper-limit on the electron density. This shows that the region under study is a low-density region.

4.5.3 Analysis of log(N/O) versus 12 + log(O/H) for HII regions within BCDs

The correlation-coefficient for the six galaxies are given in Table 4.5.

I performed the likelihood ratio test (Neyman-Pearson test) for 6 out of 10 BCDs to find out if there exists a negative trend between log(N/O) and log(O/H) for H II regions within BCDs.

Table 4.5 – Pearson correlation coefficient for individual galaxies.

Galaxy	ρ
NGC4670	-0.83
IZw18	-0.50
HS2236+1344	-1.00
Haro11	-0.68
UM462	-0.79
NGC5253	-0.45

Table 4.6 – Likelihood ratio test fit for individual galaxies and all galaxies.

Galaxy	$\chi^2_{y=c}$	$\chi^2_{y=mx+c}$	$\chi^2_{y=c}$ - $\chi^2_{y=mx+c}$	$\frac{\chi^2_{y=c}-\chi^2_{y=mx+c}}{\sigma}$
NGC4670	1.758	0.713	1.045	0.7
IZw18	1.152	0.961	0.191	0.1
HS2236+1344	2.340	0.001	2.339	1.7
Haro11	10.592	5.381	5.211	3.7
UM462	6.517	1.560	4.957	3.5
NGC5253	3.554	3.122	0.432	0.3
10 galaxies	31.896	23.085	8.811	6.2

For each BCD, I fit two straight lines of the form: y = c and y = mx+c, where m is the negative slope and c is the constant. The individual straight line fits for the six galaxies are shown in Figure 4.25. All these fits take into account the error bars on the fitted data. The corresponding χ^2 values are tabulated in Table 4.6. $\chi^2_{y=c} - \chi^2_{y=mx+c}$ is known to follow a χ^2_1 distribution. Since for a χ^2 distribution, $variance(\chi^2) = \sigma^2 = 2\nu$, hence $\sigma = \sqrt{2}$. The results of the test are shown in Table 4.6. I find that a straight line of the form y = c, fits four out of six galaxies which includes NGC 4670. Only two galaxies Haro 11 and UM462 show a negative trend. The results of the likelihood ratio test on the normalised data for all H II regions (Figure 4.21) are shown in the last column, which show that a negative correlation exits between log(N/O) and log(O/H).

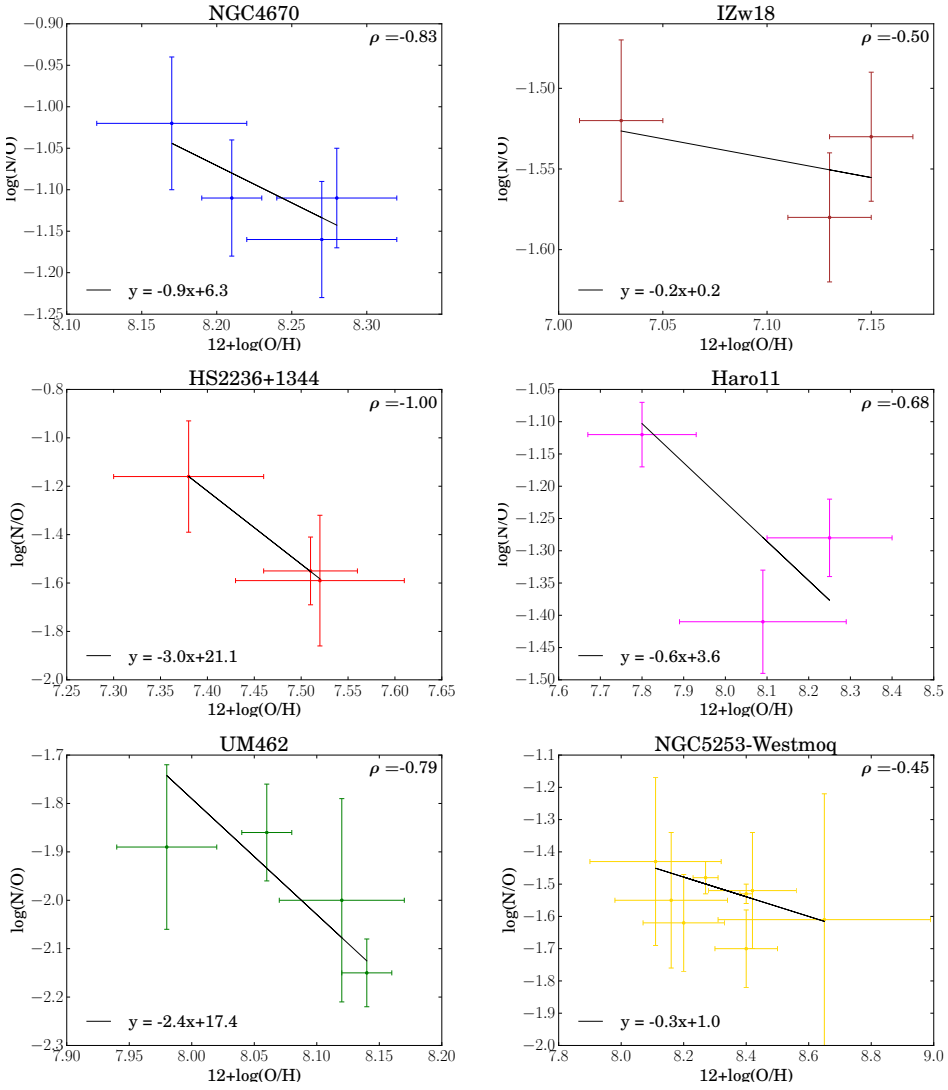

Figure 4.25 – The individual straight line fits for the six galaxies, which have more than 2 data points. The best-fit parameters is shown at the bottom-left corner in each panel, where y denotes log(N/O) and x denotes 12 + log(O/H). The Pearson correlation co-efficient is shown in the top-right corner of each panel, which is negative for six galaxies.

5

Chemical abundance mapping of SBS 1415+437

5.1 Introduction

Our understanding of the chemical evolution of the Universe relies on our knowledge of the origin and distribution of elements in the nearby and distant Universe. The study of abundance of oxygen (O) and its distribution is important because it is the third most abundant element in the Universe after hydrogen and helium, and hence acts as a good proxy to the total metal-content of a star-forming system. The abundances of other elements and their relative abundance with respect to oxygen tell us about the nucleosynthetic origin of these elements. For example, α-elements such as neon (Ne), sulphur (S) and argon (Ar) are thought to be produced in massive stars along with oxygen (see e.g. Woosley & Weaver, 1995). The case of nitrogen (N) is even more interesting as it is thought to form in massive, as well as intermediate mass stars, though there have been many debates on its origin (see e.g. Kumari et al., 2018, and references therein).

Various observational studies have been performed for studying the chemical distribution in stars and gas within star-forming and quiescent systems (see e.g. Vílchez & Iglesias-Páramo, 1998; Henry & Worthey, 1999; López-Sánchez et al., 2007; García-Benito et al., 2010; Monreal-Ibero et al., 2011; Lind et al., 2011; Berg et al., 2013; López-Hernández et al., 2013; Berg et al., 2015). These studies show that the distribution of chemical abundances may vary over both

Table 5.1 – General Properties of SBS 1415+437

Parameter	SBS 1415+437
Morphological Type	BCD
R.A. (J2000.0)	14h17m01.4s
DEC (J2000.0)	+43d30m05s
Redshift (z)[a]	0.002031 ± 0.000007
Distance (Mpc)[b]	13.6
Helio. Radial Velocity(km s^{-1})[a]	609 ± 2
E(B-V)[c]	0.0077 ± 0.0003
$M_{stellar}$ (10^7 $M_\odot$)[d]	17 ± 3
$M_{molecular}$ (10^7 $M_\odot$)[d]	7.6 ± 2.3
M_{HI} (10^7 $M_\odot$)[d]	6.8 ± 0.7

[a] Taken from NED
[b] Aloisi et al. (2005)
[c] Foreground galactic extinction (Schlafly & Finkbeiner, 2011)
[d] Lelli, Verheijen & Fraternali (2014)

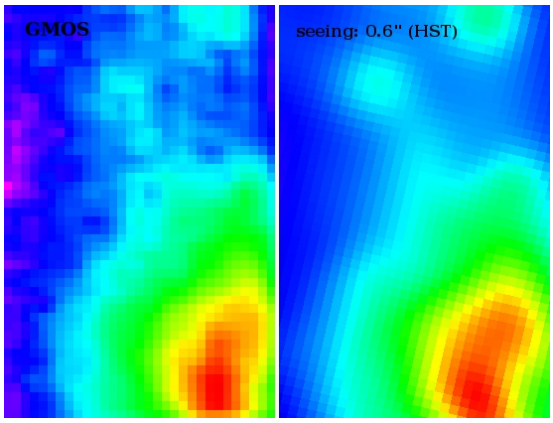

Figure 5.1 – Left: R-band continuum image from GMOS-IFU. Right: HST (F606W filter) image convolved by a bidimensionsal Gaussian corresponding to a seeing FWHM of 0.6 arcsec and binned to the GMOS pixel size of 0.1 arcsec.

small sub-galactic scales or large galactic scales within galaxies (see e.g. Henry & Worthey, 1999; Kewley et al., 2010; Pilkington et al., 2012; James et al., 2015). The abundance pattern tells us about various constituents of chemical evolutionary models such as star-formation history, chemical enrichment, merger events, gas dynamics and stellar-populations. Such studies of large and small-scale chemical variation have been revolutionised with the advent of integral field spectroscopy (IFS) which allows us to derive spatially-resolved spectroscopic properties of the star-forming systems (Pérez-Montero et al., 2011; Sánchez et al., 2012; Westmoquette et al., 2013; Kehrig et al., 2013; Ho et al., 2015; Belfiore et al., 2017). For example the spectrum of a star-forming galaxy, or an H II region, contains a plethora of emission lines. IFS enables us to map emission lines across the star-forming galaxy, or region within a galaxy, depending on the field-of-view (FOV) of instruments, and therefore map the physical properties encoded in those emission lines. This simultaneous observation in wavelength and space is key to an efficient study of the distribution of chemical abundances within a star-forming system (James et al., 2009; James, Tsamis & Barlow, 2010; James et al., 2013a,b; Lagos et al., 2012, 2014, 2016; Kumari et al., 2018).

In this Chapter, I explore small-scale chemical variation within a blue compact dwarf (BCD) galaxy SBS1415+437 by using IFS observations obtained from the integral field unit (IFU) installed on the Gemini Multi-Object Spectrograph (GMOS; Hook et al. (2004)). This is the first ever IFS study of SBS1415+437, whose general properties are tabulated in Table 5.1. SBS1415+437 is a suitable target to study the small-scale chemical abundance variation for several reasons. The oxygen abundance derived previously from long-slit observations of this galaxy show that its metallicity is $\sim Z_{\odot}/21$ (Guseva et al., 2003; Thuan, Izotov & Foltz, 1999). Such a low-metallicity ensures the detection of weak auroral line such as [O III] λ4363 with enough signal-to-noise (S/N) to allow us to map the chemical abundance of various elements and their ratios via the robust direct T_e-method. Moreover this galaxy is relatively nearby ($\sim$ 13.6 Mpc), which enables us to map the variation on scales as small as $\sim$ 6.5 pc with the high 0.1 arcsec angular-resolution of GMOS-IFU. Though this galaxy was initially thought to be quite young with the first burst of star-formation occuring in the last 100 Myr (Thuan, Izotov & Foltz, 1999), an analysis involving colour-magnitude diagrams has shown the presence of asymptotic giant branch and red giant branch stars which are at least $\sim$ 1 Gyr old (Aloisi et al., 2005). Being a BCD at low-metallicity, this galaxy is a local analogue of high-redshift galaxies despite hosting older stellar population, and hence a study of chemical distribution within this galaxy provides insight into the characteristic physical processes of the high-redshift Universe.

The aim of this Chapter is to better understand the physical and chemical properties of star-forming regions in BCDs at very small scales. I have done this analysis in the framework of the three questions regarding homogeneity, excitation mechanisms and stellar properties posed in Chapter 1. The observing log and steps of data-reduction for this galaxy SBS1415+437 are already presented in Chapter 2. I estimated the seeing FWHM of $\sim$0.6 arcsec by comparing the

R-band continuum image from GMOS-IFU with the convolved and binned image of this galaxy obtained from the Hubble Space Telescope in the equivalent V(F606W) filter (Figure 5.1).

The Chapter is structured as follows: Section 5.2 presents the results and a discussion of the maps of emission line fluxes, dust attenuation, gas kinematics, electron temperature and density, ionic and elemental abundances of various elements and the abundance ratios and stellar properties. In this section, I also perform a radial profile analysis on the elemental abundance maps and abundance ratio maps to investigate any systematic signatures of chemical inhomogeneities. Section 5.3 summarises the main results.

5.2 Results & Discussion

5.2.1 Observed and Intrinsic Fluxes

Figure 5.2 shows the HST image of SBS1415+437 taken in the filter F606W. The green rectangular box represents the GMOS aperture (3.5 arcsec $\times$ 5 arcsec). The upper-inset shows the Hα image obtained from GMOS IFU data where I mark Region 1 and Region 2 selected on the basis of an isophotal Hα emission. The blue parallel lines indicate the long-slit position of the Kitt Peak 4m Mayall Telescope observations used in the analysis of Guseva et al. (2003, hereafter G03). Figure 5.3 shows the GMOS-IFU integrated spectra of the entire FOV in the blue and red parts of the optical spectrum. I have overplotted the principal emission lines at their rest wavelengths in air.

I measure the emission line fluxes for the recombination and collisonally excited lines within the spectra by fitting Gaussian profiles after subtracting a linear continuum in the spectral region of interest. I give equal weight to flux in each spectral pixel while fitting Gaussians. The fitting uncertainties on the three Gaussian parameters (amplitude, centroid and FWHM) are propagated to estimate the uncertainty in fluxes. These uncertainty estimates are consistent with those calculated from Monte Carlo simulations. I have propagated these estimated uncertainties in the fluxes to other quantities using Monte Carlo simulations in the subsequent analysis.

Figure 5.4 shows the observed fluxes of R-band continuum, [O III] λ4363, [O III] λ5007, Hα, [N II] λ6584 and [SII] λ6717 over the FOV. I obtained the R-band continuum by integrating the red cube in the wavelength range of 5890–7270 Å (in the rest wavelength). In all maps, white spaxels correspond to spaxels in which emission lines have S/N $<$ 3. The [O III] λ4363 has S/N $>$ 3 for a region extending over 143 pc $\times$ 143 pc, though all pixels do not show detection (Figure 5.4, upper-right panel). Note here that the [O II] $\lambda\lambda$3727,3729 doublet was not detected because of the low sensitivity of the blue wavelength end of the GMOS-IFU. In all flux maps, there are two distinct regions with elevated fluxes, represented by a quarter-ellipse and a circle, which I refer as Region 1 and Region 2 in subsequent analysis (also see Figure 5.2). [O III] λ4363 is detected in the integrated spectrum of Region 1, but not in Region 2. The observed

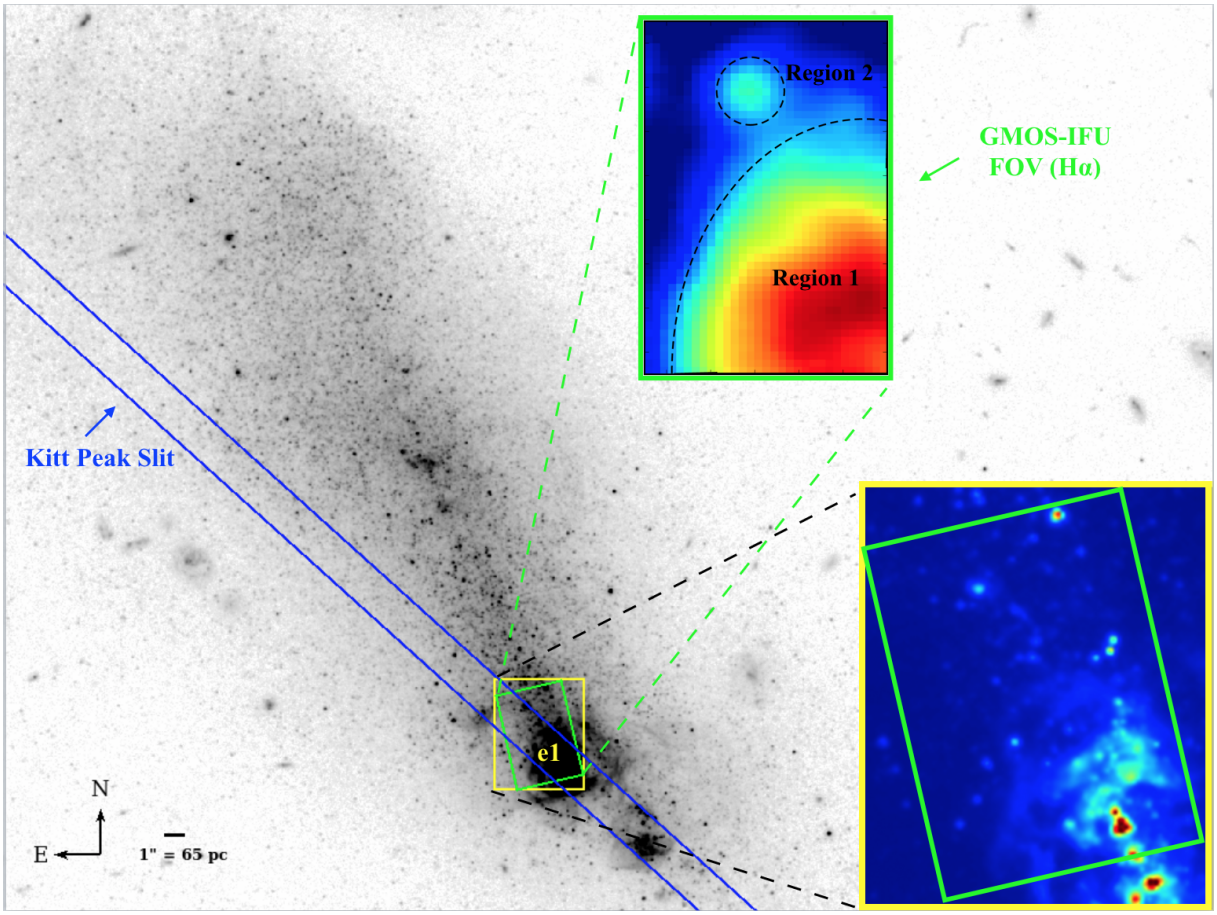

Figure 5.2 – HST/ACS 0.05 arcsec image of SBS1415+437 taken in the F606W(V) filter (Aloisi et al., 2005). The small green rectangular box inside the yellow rectangular box shows the GMOS aperture (3.5 arcsec × 5 arcsec) centered at (RA, Dec) : (214.2559958, 43.50158528). The lower-right inset denotes the zoomed-in version of the small yellow and green boxes. The upper inset is the Hα image created from GMOS-IFU data presented here, where I mark principal emission regions as Region 1 and Region 2. The colour scale and stretch of background and inset HST images are set to be different for better visibility. The blue parallel lines represent the long-slit position of spectroscopic observation with Kitt Peak 4m Mayall Telescope, used by Guseva et al. (2003) to study various regions, including "e1" which coincides with our GMOS data. The compass on the bottom-left of the figure shows north and east on the HST image. At the distance of this galaxy, 1 arcsec corresponds to 65 pc.

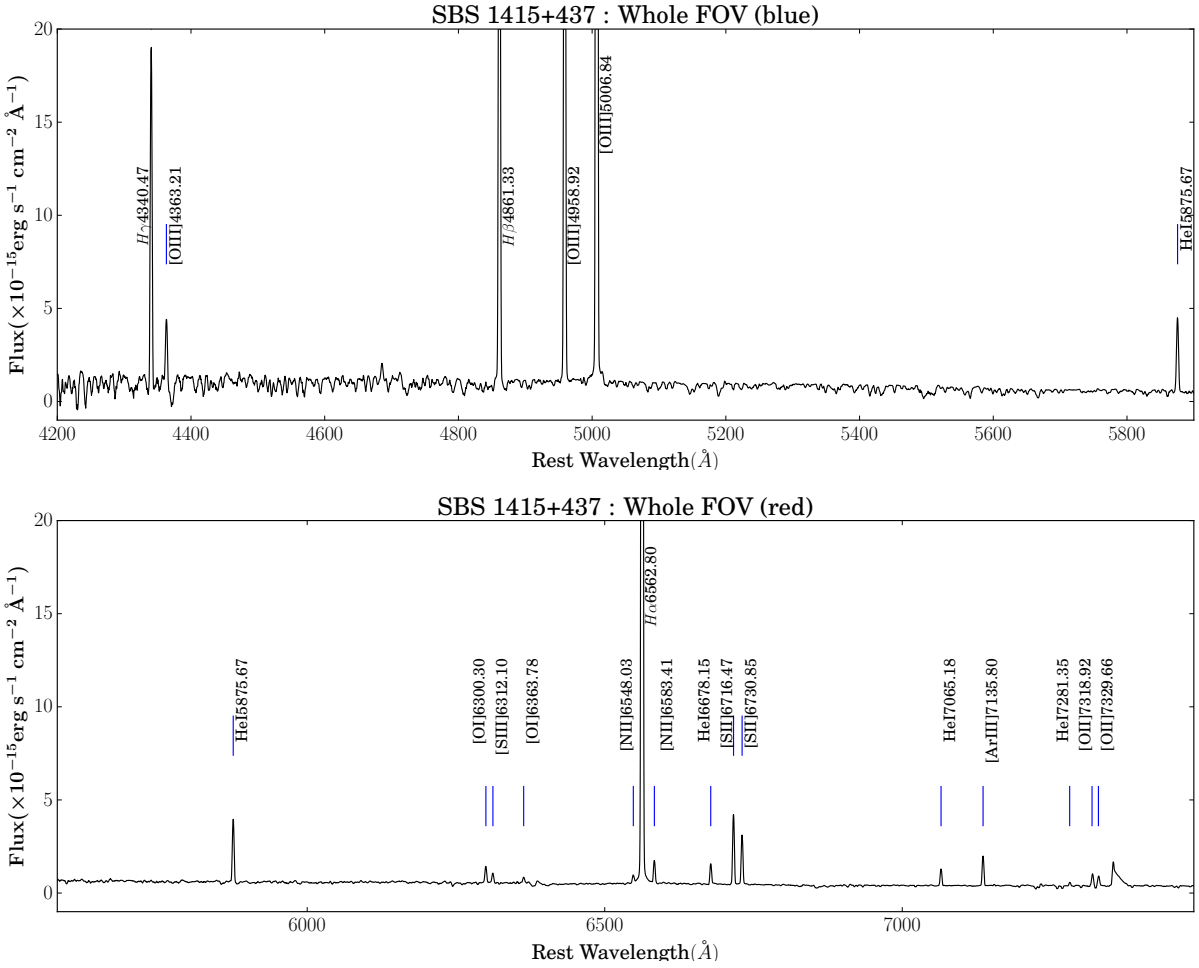

Figure 5.3 – GMOS-IFU integrated spectra of SBS1415+437 integrated over the entire FOV. The principal emission lines are marked as blue lines at their rest wavelengths. The spectra are smoothed using a one-dimensional box kernel with an effective smoothing of 7 pixels. The pixel scale before smoothing for blue and red spectra is ∼0.46 Åand ∼0.47 Å, respectively.

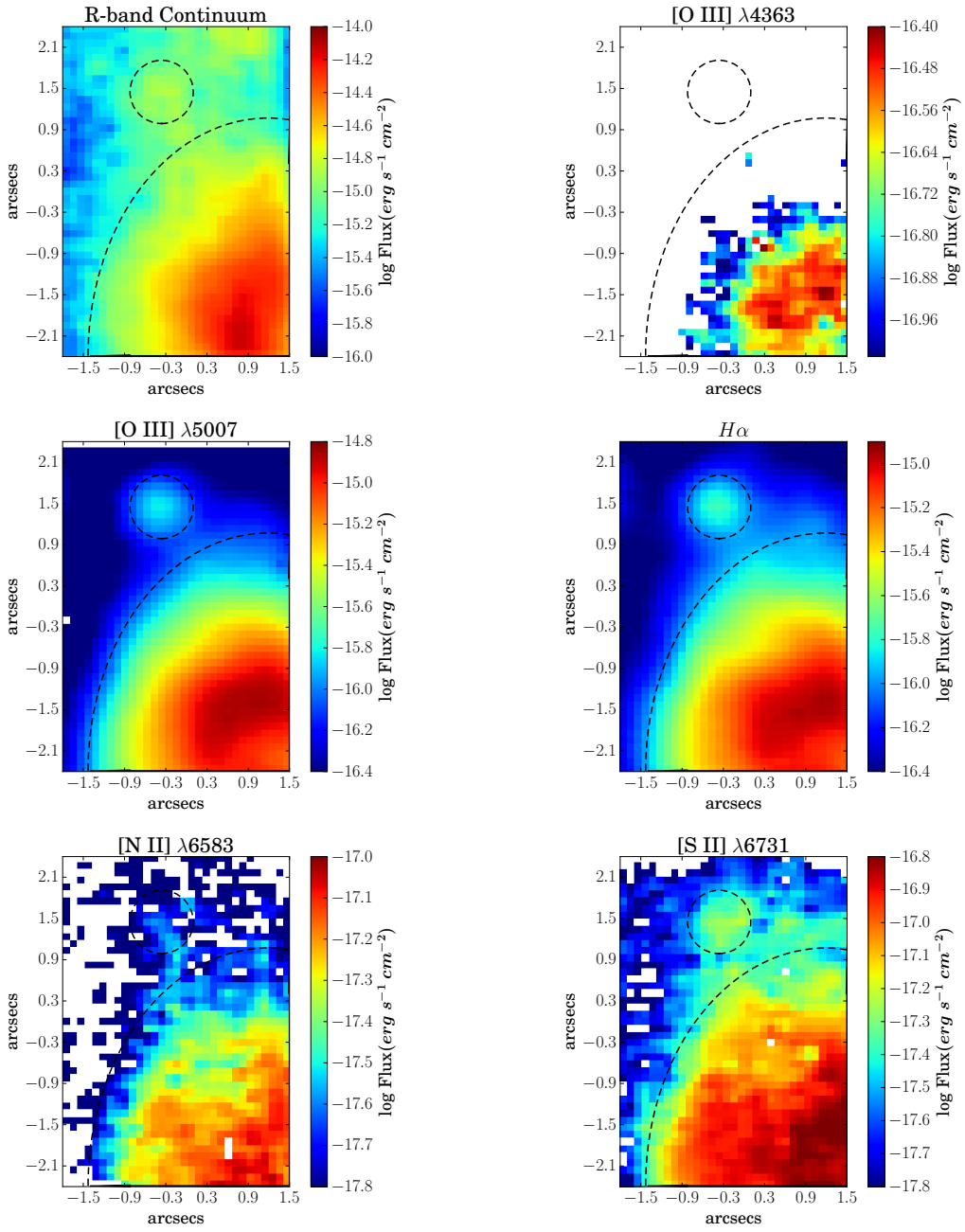

Figure 5.4 – Observed R-band continuum map and the emission line flux maps ([O III]λ4363, [O II]λ5007, Hα, [N II]λ6584 and [SII]λ6731) of SBS 1415+437. The dashed quarter ellipse and circle indicate the H II regions identified by a relatively higher flux values, and are referred as Region 1 and Region 2 in the rest of the Chapter. The spaxels in which emission line fluxes had S/N $<$ 3, are shown in white.

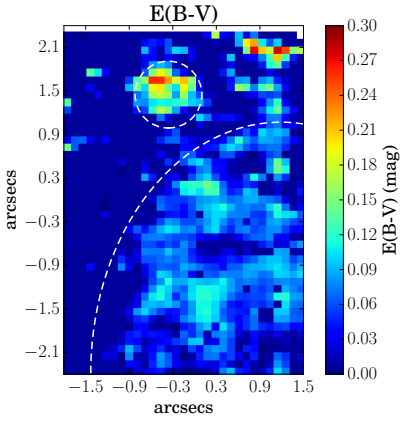

Figure 5.5 – E(B-V) map created assuming the LMC extinction curve. Spaxels with E(B-V) $<$ 0 are set to E(B-V) of the Milky Way. The spaxels in which emission line fluxes had S/N $<$ 3, are shown in white. The dashed quarter ellipse and circle indicate Region 1 and Region 2, respectively.

fluxes of the main emission lines in the integrated spectrum of Region 1 are presented in Table 5.2.

To estimate dust attenuation, I used the LMC (Large Magellanic Cloud) attenuation curve (Fitzpatrick, 1999) along with the observed Hα/Hβ ratio to first estimate the nebular emission line colour excess E(B–V), at an electron temperature and density of 10000 K and 100 cm^{-3}, respectively (Case B recombination). While mapping E(B-V), I found that some spaxels away from the bright star-forming regions have negative values of E(B–V) which is possibly due to stochastic error and shot noise (Hong et al., 2013). For such spaxels, I fixed E(B–V) to that of the Galactic Foreground (0.0077, Schlafly & Finkbeiner, 2011). Figure 5.5 shows the E(B-V) map of the FOV, which varies between 0.0077–0.30 mag. The increased value of E(B–V) in Region 1 and Region 2 shows that the star-forming regions are dustier than the rest of the FOV. The E(B–V) map obtained was used to deredden the observed flux maps as described in Chapter 3. From the integrated spectrum of Region 1, I obtain a value of E(B–V) = 0.055$\pm$0.005, which lies in the range of values found in the literature for this region (0.08 by Thuan, Izotov & Foltz (1999) and 0.00 by G03). The E(B–V) estimated here was used to deredden the observed emission line fluxes of Region 1. The dereddened/intrinsic fluxes for the main emission lines are shown in Table 5.2.

5.2.2 Gas Kinematics

Figure 5.6 shows the maps of radial velocity (left panel) and velocity dispersion (right panel) of the Hα emission line, obtained from the centroid and the FWHM of the Gaussian fit to the emission line. The radial velocity map is corrected for the systemic velocity of 609 kms^{-1}, and the barycentric velocity of $-$6.9 kms^{-1}. The velocity dispersion map is corrected for the

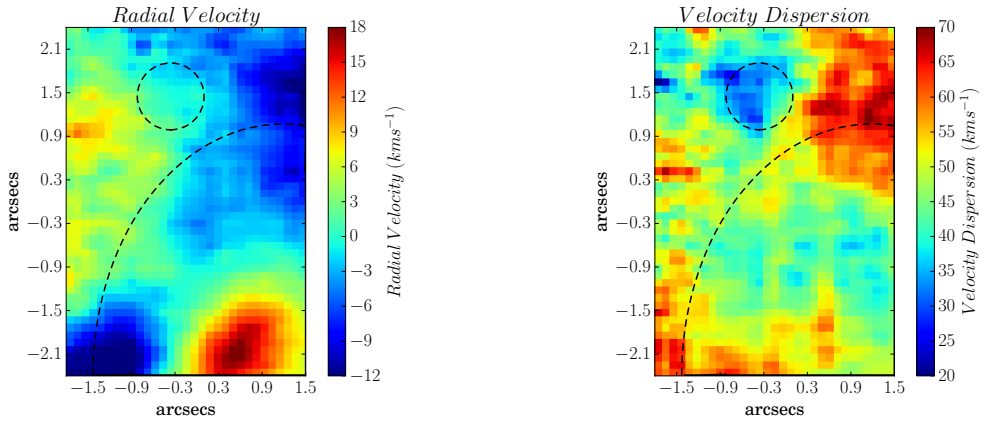

Figure 5.6 – Radial velocity (left panel) and velocity dispersion (right panel) maps of the ionised gas obtained from the Hα emission line. Radial velocity is corrected for systemic ($\sim$ 609 km s^{-1}) and barycentric ($\sim$ $-$6.90 km s^{-1}) velocities. Velocity dispersion is corrected for instrumental broadening. The dashed quarter ellipse and circle indicate Region 1 and Region 2, respectively.

Table 5.2 – Emission line measurements (relative to Hβ = 100) for the integrated spectrum of Region 1 (Quarter Ellipse) and Region 2 (Circular) (see Section 6.3.1). Line fluxes (F_λ) are extinction corrected using E(B-V) to calculate I_λ.

Line	λ_{air}	F_λ (Region 1)	I_λ (Region 1)	F_λ (Region 2)	I_λ (Region 2)
$H\gamma$	4340.47	47.15 ± 0.56	48.36 ± 1.37	44.98 ± 2.88	47.34 ± 4.64
$[OIII]$	4363.21	8.87 ± 0.60	9.09 ± 0.66	–	–
$H\beta$	4861.33	100.00 ± 0.47	100.00 ± 1.76	100.00 ± 1.52	100.00 ± 5.14
$[OIII]$	4958.92	119.89 ± 0.80	119.40 ± 2.94	93.94 ± 1.81	93.16 ± 6.65
$[OIII]$	5006.84	356.30 ± 2.29	354.03 ± 8.66	284.25 ± 4.63	280.62 ± 19.72
HeI	5875.67	10.72 ± 0.20	10.30 ± 0.29	11.86 ± 0.85	10.96 ± 1.04
$[OI]$	6300.3	2.09 ± 0.06	1.98 ± 0.07	3.55 ± 0.53	3.20 ± 0.51
$[SIII]$	6312.1	1.47 ± 0.05	1.39 ± 0.06	1.75 ± 0.37	1.57 ± 0.34
$H\alpha$	6562.8	303.55 ± 1.62	286.00 ± 6.08	322.39 ± 4.97	286.00 ± 17.61
$[NII]$	6583.41	2.92 ± 0.40	2.75 ± 0.38	4.86 ± 0.50	4.31 ± 0.51
HeI	6678.15	2.84 ± 0.05	2.67 ± 0.07	3.19 ± 0.44	2.81 ± 0.42
$[SII]$	6716.47	8.59 ± 0.08	8.06 ± 0.18	14.50 ± 0.47	12.76 ± 0.86
$[SII]$	6730.85	6.14 ± 0.07	5.76 ± 0.14	11.35 ± 0.47	9.97 ± 0.72
$[ArIII]$	7135.8	4.14 ± 0.05	3.84 ± 0.09	4.96 ± 0.36	4.28 ± 0.40
$[OII]$	7318.92	1.64 ± 0.10	1.51 ± 0.10	3.13 ± 0.42	2.67 ± 0.39
$[OII]$	7329.66	1.31 ± 0.09	1.22 ± 0.08	2.46 ± 0.36	2.10 ± 0.33
E(B-V)		0.057±0.005		0.115 ± 0.015	
F(Hβ)		117.42 ± 0.55		1.95 ± 0.03	

Notes: F(Hβ) in units of $\times$ 10^{-15} erg cm^{-2} s^{-1}

For Region 2, [O III] λ 4363 is not detected with S/N $>$ 3, so analysis involving this emission line is not performed for Region 2.

instrumental broadening of 1.7Å.

Figure 5.6 (left panel) shows that the radial velocity of the ionised gas in the region of study varies between ~ -14 and 19 kms^{-1}. Thuan, Izotov & Foltz (1999) reports a solid body rotation for this BCD across $\sim$ 30 arcsec. Though the velocity map clearly shows blueshift and redshift at different locations of the FOV, there is no definite axis of rotation. This could be because the GMOS-FOV is comparatively small (3.5 arcsec $\times$ 5 arcsec).

Figure 5.6 (right panel) shows that the velocity dispersion of the ionised gas in the region of study varies between $\sim$20 and 70 kms^{-1}. Region 1 shows a range of values, whereas Region 2 has a relatively low velocity dispersion, The ionised gas to the north-west of Region 1 and west of Region 2 shows the highest values of velocity dispersion.

5.2.3 Emission line ratio diagnostics

In Figure 5.7, I show the classical emission line ratio diagnostic diagrams ([O III]λ5007/Hβ versus [S II]$\lambda\lambda$6717,6731/Hα (left panel) and [O III]λ5007/Hβ versus [N II]λ6584/Hα (right panel)), which are commonly known as BPT diagrams (Baldwin, Phillips & Terlevich, 1981). In both panels, I show the maximum starburst line also known as the "Kewley line" as the solid black curve, which presents a classification based on ionisation/excitation mechanism. On the [N II] diagnostic diagram (Figure 5.7, right panel), the dashed black curve represents the empirical line derived by Kauffmann et al. (2003) using SDSS spectra of 55 757 galaxies. The spatially-resolved line ratios are shown by blue, green and magenta markers which correspond to the spaxels of Region 1, Region 2 and the rest of the FOV, respectively. I also show the line ratios obtained from the integrated spectra of Region 1 and Region 2 using larger markers (black contour). I find that both spatially-resolved and integrated data lie well below and to the left of the Kewley line, as well as the empirical line of Kauffmann et al. (2003). This shows that the ionised gas in the region under study is predominantly ionised by the photons from the massive stars.

Figure 5.8 shows the line ratio maps of the region under study, which I use to study the ionisation structure of the ionised gas. As expected, I find that the peak of emission shows the lowest values of of [N II]λ6584/Hα (upper-left panel) and [S II]$\lambda\lambda$6717,6731/Hα (upper-right panel), and highest values of [O II]λ5007/Hβ (lower panel). This indicates that the more luminous regions (on Hα map) have relatively high excitation, which is due to the presence of young and massive stars producing harder ionising radiation. Note here that the peak of Hα map is offset by $\sim$ 58 pc with respect to the peak of the R-band continuum indicative of the region containing an older stellar population.

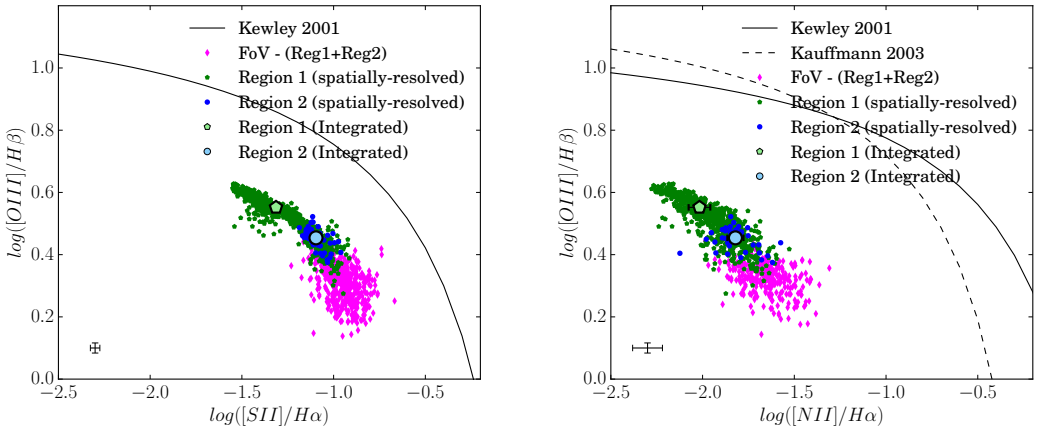

Figure 5.7 – Emission line ratio diagnostic diagrams: [O III]/Hβ versus [S II]/Hα (left), and [O III]/Hβ versus [N II]/Hα (right). Black solid curve and dashed curve represent the theoretical maximum starburst line from Kewley et al. (2001) and Kauffmann et al. (2003), respectively, showing a classification based on excitation/ionisation mechanisms. The line ratios of the two H II regions are colour-coded as follows: Region 1: green pentagon, Region 2: blue circle. Smaller markers denote the spatially-resolved (spaxel-by-spaxel) line-ratios and the bigger markers (black contours) denote the line-ratios obtained from the integrated spectrum of the corresponding regions. Magenta coloured markers denote the spatially-resolved line-ratios of the regions of FOV excluding the two H II regions. The size of errorbars varies for line ratios and the median error bars are shown in left corner of each panel.

5.2.4 Electron temperature and density

To estimate electron temperature T_e([O III]), I use the dereddened [O III] line ratio, [O III] (λ5007 +λ4959)/[O III]λ4363 and the calibration from Pérez-Montero (2017, hereafter P17), which is derived assuming a five-level atom, using collision strengths from Aggarwal & Keenan (1999). Figure 5.9 (left panel) shows the derived T_e([O III]) map, which shows a variation of 12000–24000 K. The median uncertainty on T_e([O III]) map is $\sim$ 1700 K. From the integrated spectrum of Region 1, I find T_e([O III]) = 17100 $\pm$ 700 K, in agreement with the value found by G03 (16490 $\pm$ 140 K). The derived temperature is higher than that of typical H II region (T_e([O III]) $\sim$ 7000–14000; Osterbrock & Ferland, 2006a), which indicates that this region is metal-poor compared to typical H II regions.

To derive the electron density N_e, I use [S II] doublet ratio and T_e([O III]) derived above, along with the theoretical curves of the [S II] doublet ratio versus N_e at given temperatures. Figure 5.9 shows the N_e map, where I find that majority of the spaxels have $N_e < 50$ cm^{-3}, indicating that the region under study lies in the low-density regime. From the integrated spectrum of Region 1, I find $N_e < 50$ cm^{-3} which is in agreement with the value (60 $\pm$ 30 cm^{-3}) found by G03. The derived electron densities correspond to typical H II regions ($N_e \approx 10^2$ cm^{-3}; Osterbrock & Ferland, 2006a).

The temperature of low-ionisation zone T_e([O II]) is estimated by using N_e and T_e calcu-

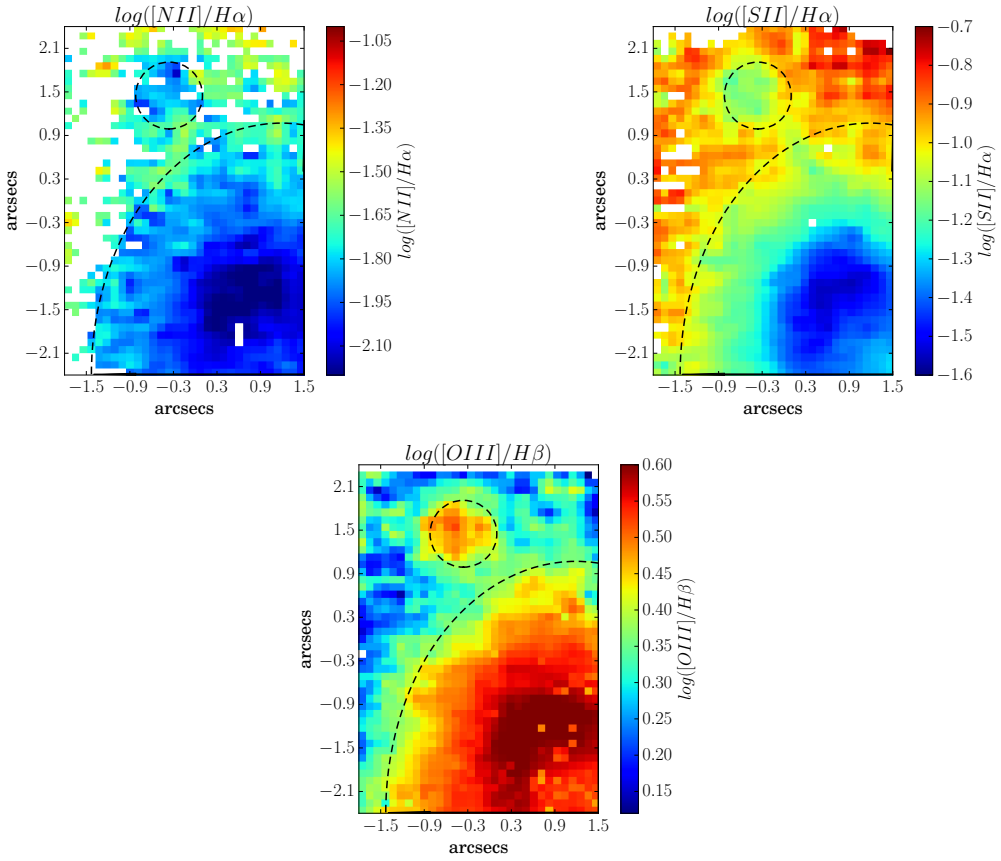

Figure 5.8 – Emission line ratio maps of [N II]λ6583/Hα, [S II]$\lambda\lambda$6717,6731/Hα and [O III]λ5007/Hβ. The dashed quarter ellipse and circle indicate Region 1 and Region 2, respectively. The spaxels in which emission line fluxes had S/N $<$ 3, are shown in white in above line ratio maps.

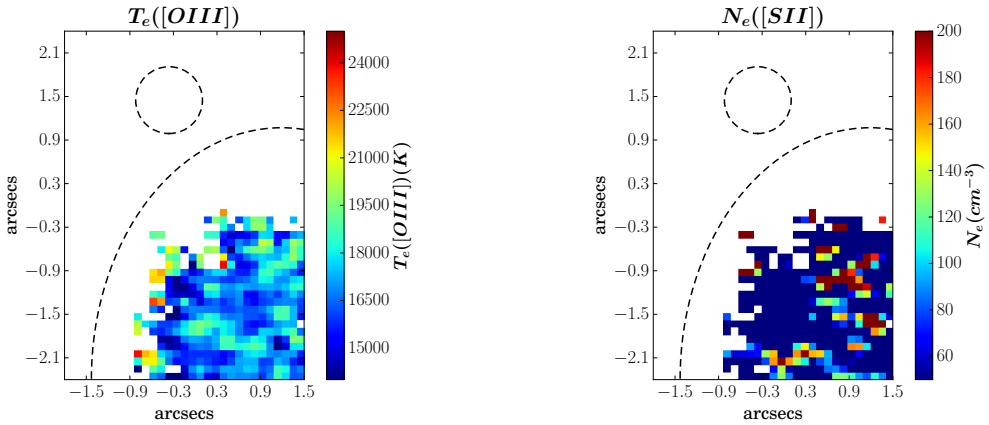

Figure 5.9 – Left panel: Map of electron temperature of high-ionisation zone (T$_e$ ([O III])). Right panel: Electron density (N$_e$(S[II])) map obtained from the [S II] doublet ratio and T$_e$ ([O III]) map. The dashed quarter ellipse indicate Region 1. The spaxels in which emission line fluxes had S/N $<$ 3, are shown in white. Single pixel features or few-pixel features should be interpreted with caution since the seeing FWHM (0.6 arcsec) extends over 6 pixels.

lated above and the density-dependent calibration given in P17. The T_e([O II]) map shows a mean and standard deviation of ∼15000 K and ∼1600 K, respectively. I calculated T_e([O II]) ∼16000 ± 400 for the integrated spectrum of Region 1, which is higher than the value found by G03 (14430 ± 110 K). The main difference is that G03 have used the expression from Izotov, Thuan & Lipovetsky (1994), which is independent of density. Using their expression, I find the value to be ∼14600 ± 300 K for Region 1, which is in good agreement with their value. The electron density should be taken into account in determining T_e([O II]) because of only a weak correlation between T_e([O II]) and T_e([O III]) (Hägele et al., 2006, 2008; López-Hernández et al., 2013).

I map T_e([N II]) by using the T_e([O III]) map in the calibration of Pérez-Montero & Contini (2009), which is based on photoionisation models. The map shows a variation of 11900–16300 K. For Region 1, I followed same procedure involving the T_e([O III]) estimated above and calculated T_e([N II]) = 14200 ± 200 K.

I map the temperature of the intermediate-ionization zone T_e([S III]) by using the empirical fitting between T_e([O III]) and T_e([S III]) given by Hägele et al. (2006), and has a calibration uncertainty of the order of 12%. The T_e([S III]) map shows a mean and standard deviation of 17000 K and 2000 K, respectively. Following the same procedure for the integrated spectrum of Region 1, I estimated T_e(S [III]) = 17100±900 K, which is higher than reported by G03 (15380 ± 110 K), but is in agreement with their value if I consider the large calibration uncertainty from Hägele et al. (2006). G03 have followed the procedure of Garnett (1992), who assumed that T_e([S III]) = T_e([Ar III]) and estimated T_e([Ar III]) from T_e([O III]). Using their recipe, I get a value of T_e([S III]) = 15900 ± 600 which is in good agreement with G03.

Table 5.3 summarizes the above results for the integrated spectrum of Region 1 and the spatially-resolved data. In this table, I have reported the median and the uncertainty on the median of the values on the entire map and take into account the correlation between pixels due to resampling in forming data cube. I do not show maps of T_e([O II]), T_e([N II]) and T_e([S III]) as they are obtained from the T_e([O III]) map (Figure 5.9, upper panel), and not directly from the auroral emission lines originating from the respective ionic species.

5.2.5 Chemical Abundances

5.2.5.1 Ionic and Elemental Abundance

For both spatially-resolved data and the integrated spectrum of Region 1, I estimate the ionic abundances (O^+/H^+, O^{2+}/H^+, N^+/H^+, S^+/H^+, S^{2+}/H^+, Ne^{2+}/H^+ and Ar^{2+}/H^+). I calculate the corresponding ionisation correction factor (ICF) for each elemental species using the prescription described below and hence estimate the elemental abundances of oxygen, nitrogen, sulphur, neon and argon. Table 5.3 presents the ionic and elemental abundances obtained from

Table 5.3 – Summary of nebular diagnostics, ionic abundances, elemental abundances and abundance ratios obtained from the integrated spectrum (Value ± Uncertainty), and the spatially-resolved maps (Median ± Uncertainty) of Region 1. The uncertainty on the median takes into account the correlation between pixels due to resampling in forming data cube.

Parameter	Integrated spectrum Value ± Uncertainty	Spatially-resolved Map Median ± Uncertainty
Te([O III]) ($\times 10^4$)	1.71 ± 0.07	1.72 ± 0.02
Te([O II]) ($\times 10^4$)	1.59 ± 0.05	1.53 ± 0.02
Te([N II]) ($\times 10^4$)	1.42 ± 0.03	1.42 ± 0.01
Te([S III]) ($\times 10^4$)	1.71 ± 0.09	1.72 ± 0.03
Ne([SII]) (cm^{-3})	< 50	50 ± 9
12 + log(O^+/H^+)	7.15 ± 0.06	7.21 ± 0.03
12 + log(O^{2+}/H^+)	7.46 ± 0.04	7.48 ± 0.01
12+ log(O/H)	7.63 ± 0.03	7.67 ± 0.02
12 + log(N^+/H^+)	5.41 ± 0.05	5.39 ± 0.01
ICF(N^+)	3.03 ± 0.47	2.79 ± 0.09
12 + log(N/H)	5.89 ± 0.08	5.84 ± 0.02
N/O	-1.74 ± 0.09	-1.82 ± 0.02
S^+/H^+ ($\times 10^7$)	1.31 ± 0.06	1.27 ± 0.06
S^{2+}/H^+ ($\times 10^7$)	4.95 ± 0.69	5.02 ± 0.33
ICF ($S^+ + S^{2+}$)	1.10 ± 0.02	1.08 ± 0.01
12 + log(S/H)	5.84 ± 0.05	5.83 ± 0.02
log(S/O)	-1.79 ± 0.06	-1.83 ± 0.02
Ne^{2+}/H^+ ($\times 10^5$)	0.49 ± 0.08	0.55 ± 0.03
ICF (Ne^{2+})	1.10 ± 0.01	1.11 ± 0.03
12 + log(Ne/H)	6.73 ± 0.07	6.80 ± 0.02
log(Ne/O)	-0.90 ± 0.08	-0.90 ± 0.02
Ar^{2+}/H^+ ($\times 10^7$)	1.23 ± 0.09	1.23 ± 0.03
ICF (Ar^{2+})	1.15 ± 0.01	1.16 ± 0.01
12 + log(Ar/H)	5.15 ± 0.03	5.16 ± 0.01
log(Ar/O)	-2.48 ± 0.04	-2.50 ± 0.01

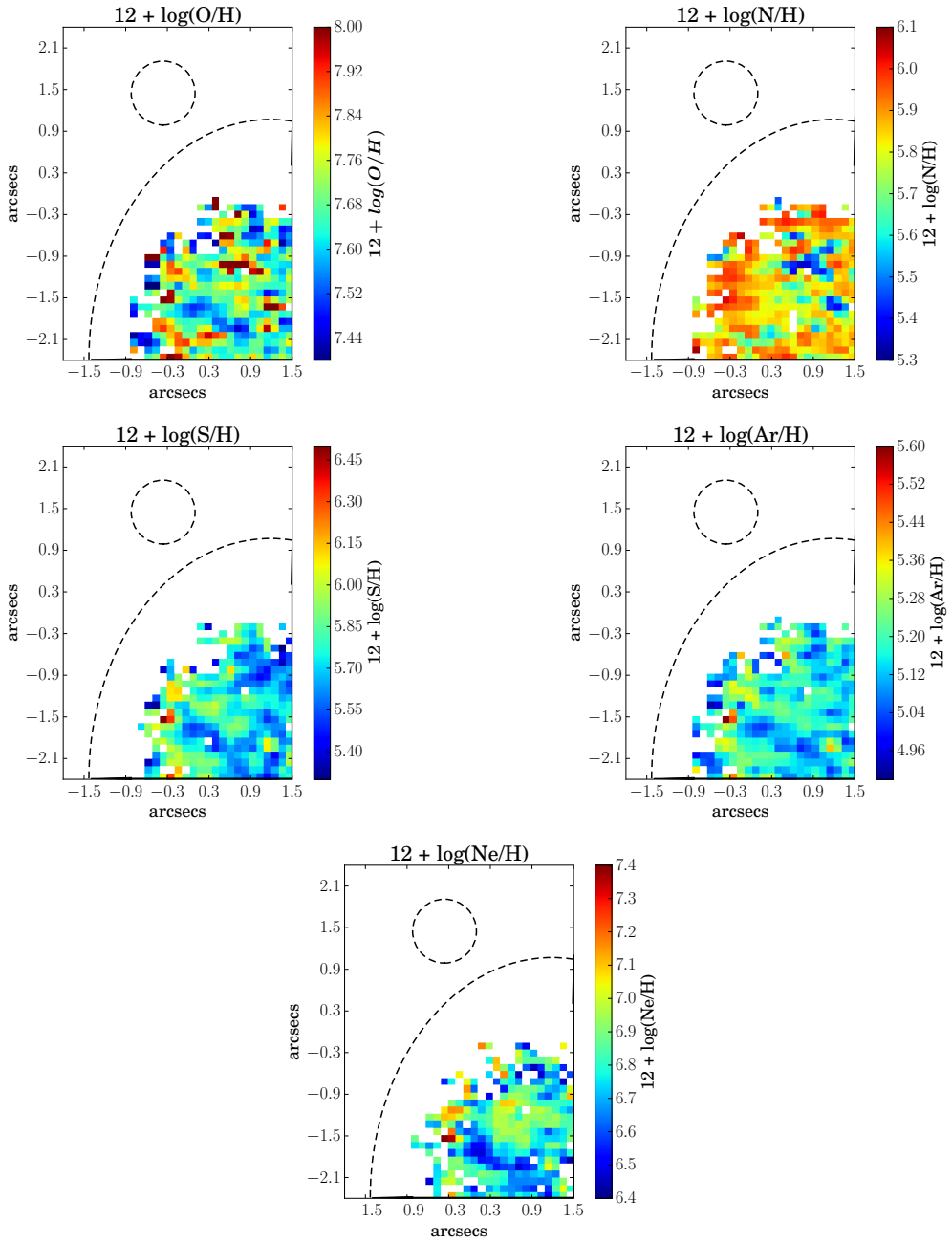

Figure 5.10 – Maps of elemental abundances of oxygen, nitrogen, sulphur, argon and neon. They are obtained by first estimating the ionic abundances and then applying the ICF on a pixel-by-pixel basis. The dashed quarter ellipse and circle indicate Region 1 and Region 2, respectively. Single pixel features or few-pixel features should be interpreted with caution since the seeing FWHM (0.6 arcsec) extends over 6 pixels. The median uncertainties on elemental abundance maps of oxygen, nitrogen, sulphur, argon and neon are 0.08 dex, 0.18 dex, 0.3 dex, 0.3 dex and 0.3 dex, respectively.

the integrated spectrum of Region 1 and also the spatially-resolved maps for which I give the median and the uncertainty of all valid data. I find that the inferred values of the quantities for the integrated spectrum and spatially-resolved data are in reasonable agreement with each other. In the following points, I describe the methodology used to derive the chemical abundance maps shown in Figure 5.10.

- *Oxygen abundance:* The metallicity of the ionised gas is expressed as the oxygen abundance as oxygen is the most prominent heavy element observed in the optical spectrum. The total oxygen abundance (12 + log(O/H)) is calculated from the sum of O^+/H^+ and O^{++}/H^+. Generally, O^+/H^+ is estimated from the oxygen doublets of [O II] $\lambda\lambda$3727,3729. However, these doublets could not be detected in the GMOS data due to the low sensitivity of GMOS-N IFU in the blue end of the optical spectrum (see Chapter 2). Instead, I use [O II] $\lambda\lambda$7320,7330 to estimate O^+/H^+ at the low-ionisation zone temperature T_e([O II]) by employing the formulation of Kniazev et al. (2003). I estimated O^{++}/H^+ using the [O III] $\lambda\lambda$4959, 5007 at the high ionisation zone temperature T_e([O III]) using the formulation of P17. Finally I combined O^+/H^+ and O^{++}/H^+, and obtained the total metallicity. Map is shown in Figure 5.10 (upper-left panel).

- *Nitrogen abundance:* [N II] λ6548 is not detected with enough S/N $>$ 3, but [N II] λ6584 is detected at sufficient S/N. Assuming an intrinsic emission line ratio between the two nitrogen lines [N II] λ6548 = (1/2.9)[N II] λ6584, I estimated the dereddened [N II] λ 6548 from the dereddened flux of [N II]λ6584. Using the dereddened flux of [N II] and T_e ([N II]) estimated in Section 5.2.4, I employed the formula given in P17 to map 12 + log(N^+/H^+). I estimated ICF(N^+) from the abundance maps of total oxygen and singly-ionised oxygen, and finally mapped 12 + log(N/H) (Figure 5.10, upper-right panel).

- *Sulphur abundance:* I estimated singly-ionised sulphur abundance (S^+/H^+) by using the dereddened [S II] $\lambda\lambda$6717, 6731 and T_e ([O II]). The auroral line [S III] λ6312 was used along with T_e ([S III]) to estimate S^{2+}/H^+. All of these estimates were derived by using the corresponding expressions given in P17. I estimated ICF(S^+ + S^{2+}) using the classical formula from Stasińska (1978), but using α = 3.27 derived by Dors et al. (2016). I finally combined the ionic abundance with the ICF correction to derive the elemental sulphur abundance, 12 + log(S/H). Corresponding map is shown in Figure 5.10 (middle-left panel).

- *Neon abundance:* I estimated doubly-ionised neon abundance (Ne^{2+}/H^{+}) by using the dereddened [Ne III] λ3869 and T_e ([O III]), and derived ICF(Ne^{2+}) using the expressions from Pérez-Montero et al. (2007). Combining the ionic-abundance with the ICF, I derived the elemental neon abundance, 12 + log(Ne/H). The map is shown in Figure 5.10 (lower panel).

- *Argon abundance:* I estimated doubly-ionised argon abundance (Ar^{2+}/H^{+}) by using the dereddened [Ar III] λ7135 and T_e ([S III]) the temperature of intermediate-ionisation zone, in the expression given in P17. I estimated ICF(Ar^{2+}) using expression given in Pérez-Montero et al. (2007) to derive the elemental argon abundance, 12 + log(Ar/H). The map is shown in Figure 5.10 (middle-right panel).

The abundance maps of 12 + log(O/H) and 12 + log(N/H) shows relatively high and low values, respectively in the north of the peak Hα flux exactly at the same location where I find high electron density (Figure 5.9, bottom panel). I estimated electron densities from the integrated spectra of two different regions within this over-density region. Though their electron densities are high, the associated uncertainties are also large, which indicates that the region may well have the same electron density as the majority of the pixels, i.e. $N_e < 50$ cm^{-3}. So it is suspected that the abundance patterns on the maps of 12 + log(O/H) and 12 + log(N/H) are not real variation.

The derived values of 12 + log(O/H), 12 + log(O^{2+}/H^{+}), 12 + log(N^{+}/H^{+}) and Ne^{2+}/H^{+} (from maps and the integrated spectrum) are in excellent agreement with those obtained by G03. However, the values of 12 + log(O^{+}/H^{+}), S^{+}/H^{+}, S^{2+}/H^{+} and Ar^{2+}/H^{+} do not agree with those from G03, since these abundance estimates depend on the low-ionisation zone temperature (T_e ([O II])) and the intermediate zone temperature (T_e ([S III])), and these temperature estimates in this work are different from those obtained by G03 for the reasons described in section 5.2.4.

Different ICF recipes exist which may or may not depend on metallicity, depending on the assumptions of photoionisation models used for deriving ICF expressions (see e.g. Izotov et al., 2006; Pérez-Montero et al., 2007). The recipes of ICF(Ne^{2+}) and ICF(Ar^{2+}) used here are independent of metallicity based on the work of Pérez-Montero et al. (2007) who do not find any notable dependence of ICFs on metallicity. The derived ICFs in this work do not match those of G03. So, I estimated the ICFs for data from G03 using my adopted recipes for ICF calculation, which now exactly match my results. The total elemental abundances of nitrogen, sulphur, neon and argon do not match those derived from G03 because of the differences in the ionic abundances and ICFs as described above. This results in obvious differences in the abundances ratios between this work and G03.

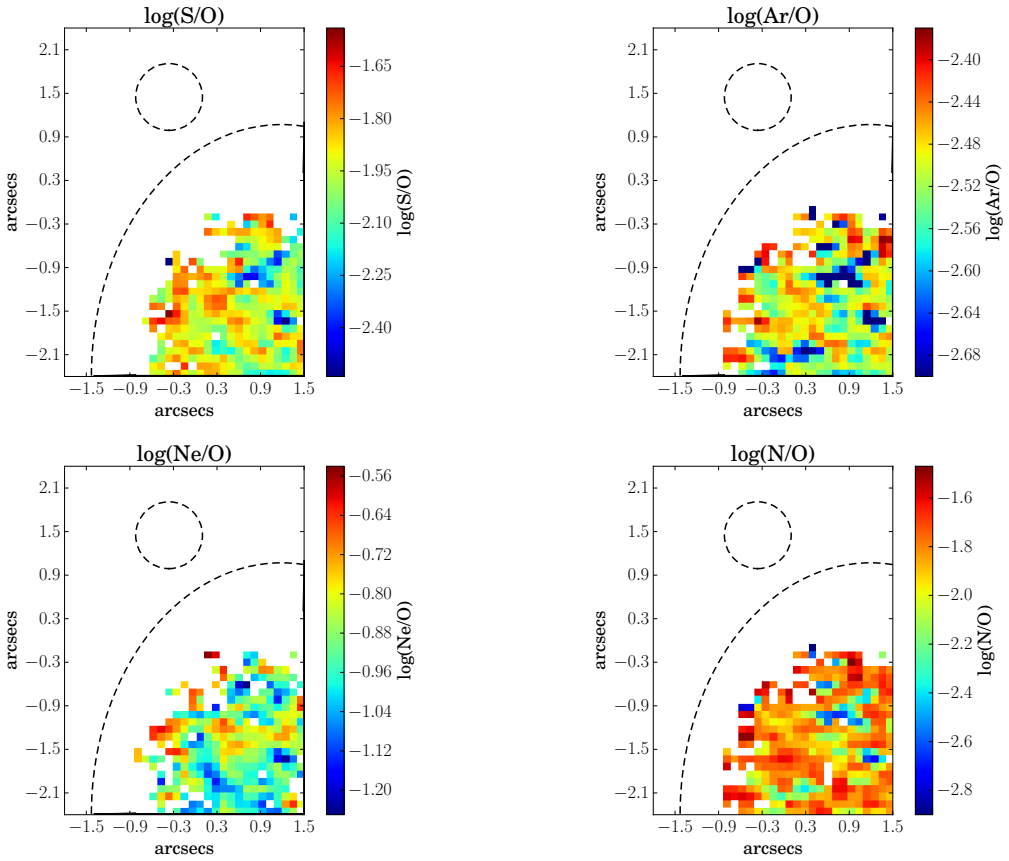

Figure 5.11 – Abundance ratios of S/O, Ar/O, Ne/O and N^+/O^+. The dashed quarter ellipse and circle indicate Region 1 and Region 2, respectively. Single pixel features or few-pixel features should be interpreted with caution since the seeing FWHM (0.6 arcsec) extends over 6 pixels. The median uncertainties on maps of S/O, Ar/O, Ne/O and N/O are 0.3 dex, 0.3 dex, 0.3 dex, 0.17, respectively.

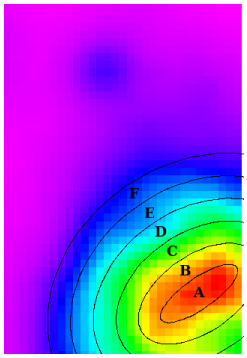

Figure 5.12 – Hα flux map is used to separate the H II region into six equally-spaced segments (A, B, C, D, E, F), roughly separated by a seeing disc such that each of them have similar overall flux within each annulus. These annuli are used for the chemical inhomogeneity investigation described in Section 5.2.5.3.

5.2.5.2 Abundance Ratios

Figure 5.11 shows the maps of abundances ratios. I find an abundance pattern in the northern region in the maps of S/O, Ar/O and N/O similar to that of electron density map and may not be real as discussed in Section 5.2.5.1. The abundance ratios for the integrated spectrum and spatially-resolved maps of Region 1 agree with each other within error bars as tabulated in Table 5.3. The abundance ratio estimates in this work are systematically lower than those of a sample of 40 BCDs analysed by Izotov & Thuan (1999). However such low values have been reported in several IFU studies of BCDs. One of such BCDs is the interaction-induced starburst UM 462 (James, Tsamis & Barlow, 2010) where abundance ratios of N/O, S/O and Ar/O are found to be in agreement with SBS 1415+437 in this study. Likewise, the values of N/O, Ne/O and Ar/O in the BCD SBS 1415+437 are in agreement with those of the main body of another metal-poor BCD Tol 65 (Lagos et al., 2016) where tidal interaction has also been proposed.

5.2.5.3 Variation of abundances

The high-resolution HST image shows distinct structure throughout the region of study (Figure 5.2). However, the observed Hα emission line flux map of Region 1 shows approximately an elliptical distribution (Figure 5.4). No elliptical distribution is obvious in any abundance maps (Figure 5.10) or abundance ratio maps (Figure 5.11), though it is noted that an over-density is observed in Ne abundance map (Figure 5.10, bottom panel) in the region north of the peak of Hα emission. In this Section, I explore the small scale abundance variation to investigate how well-mixed the gas is within the region of study.

I perform this analysis via three different methods, though I show results from only two methods. The first two methods are based on the segmentation of Region 1 in six elliptical annuli of equal widths selected on the basis of Hα flux distribution such that each of the annuli have roughly similar level of flux within a given annulus. The position of the chosen elliptical

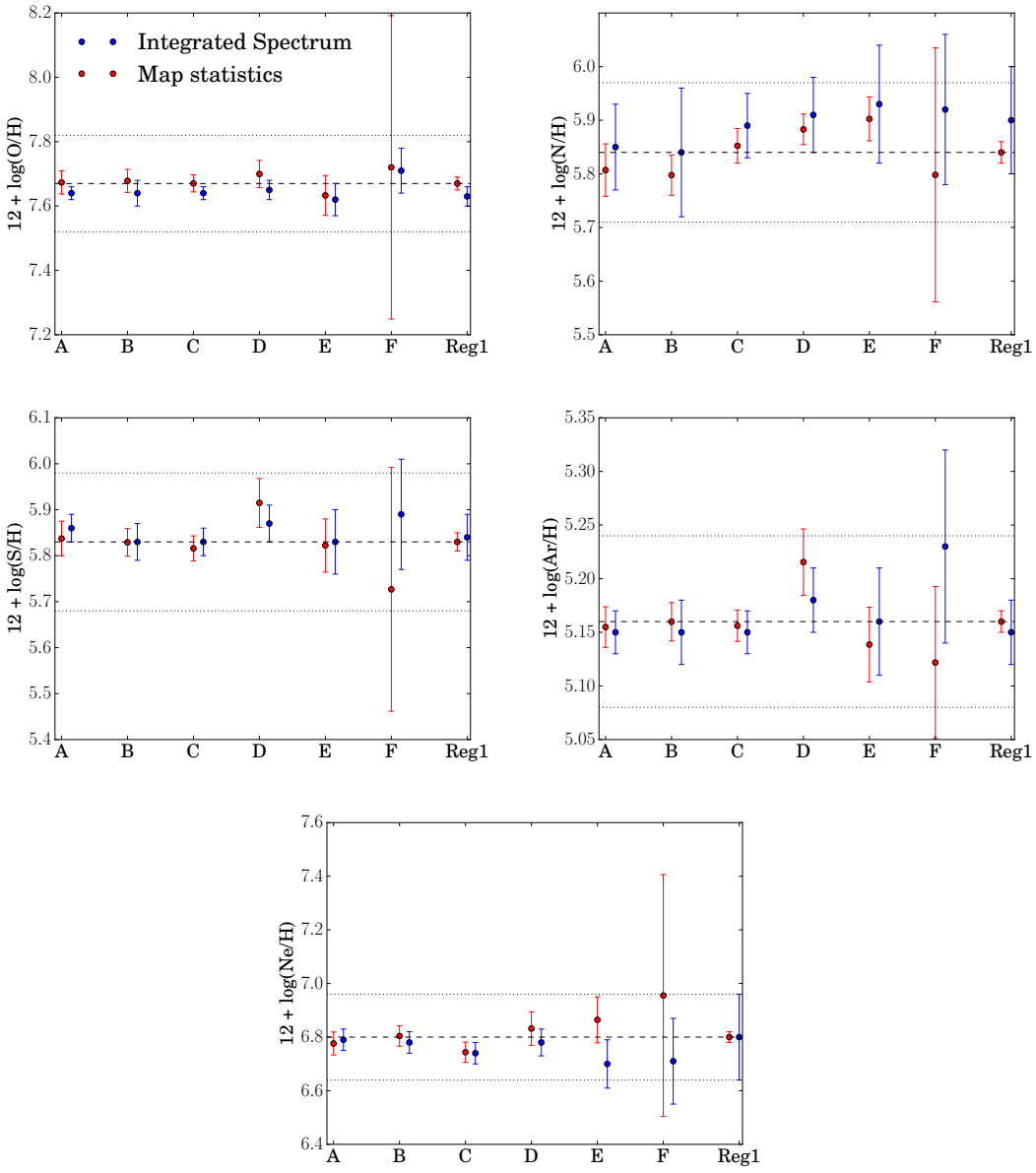

Figure 5.13 – Variation of elemental abundances across Region 1. In all panels, red points with vertical bars corresponds to the median of data and the associated uncertainty within annuli A, B, C, D, E, F (shown in Figure 5.12) of a given chemical abundance map. The error bar corresponding to annulus F is large because of the paucity of data points in this annulus. Blue points are the observables derived from the integrated spectra of each annulus. I also present the corresponding values of entire Region 1 (marked as "Reg1"). The black dashed line corresponds to the median of all data on an abundance map. The dotted black lines indicate the $\pm 1\sigma$ as determined from the standard deviation of all valid data in a map.

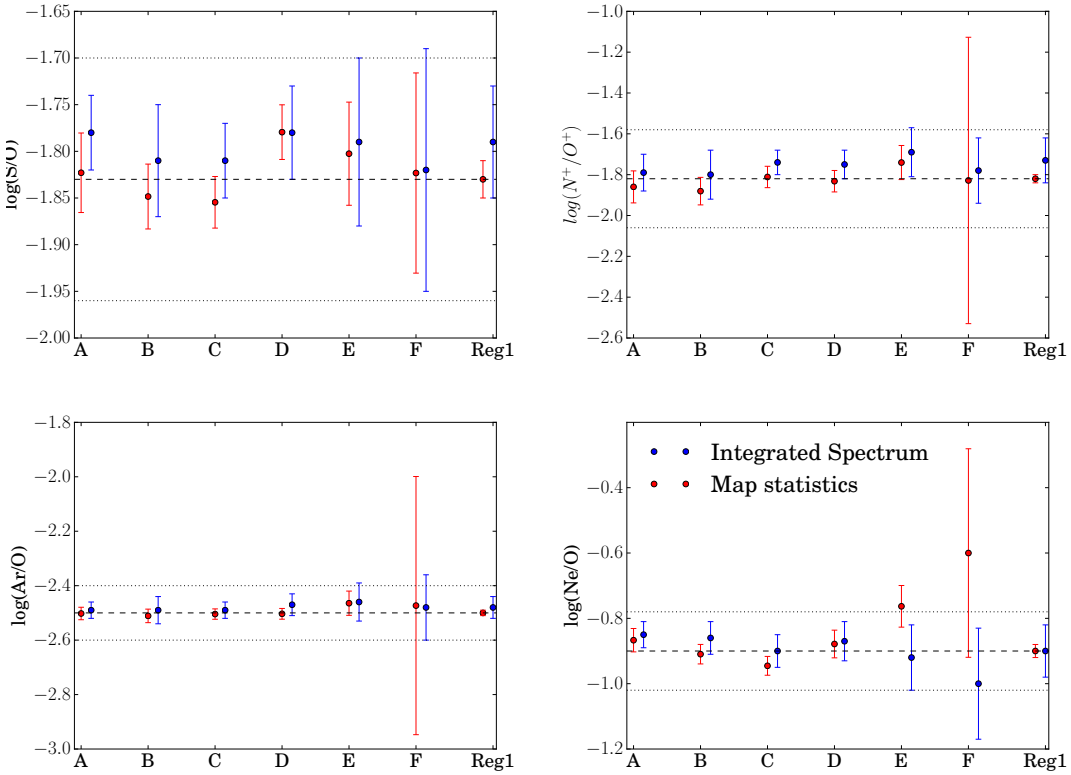

Figure 5.14 – Variation of abundance ratios across Region 1 - see caption of figure 5.13 for details on legends.

annuli are shown in Figure 5.12, and are marked as A, B, C, D, E and F. In the first method, I estimated abundances and abundance ratios from the emission line fluxes from integrated spectra within each annulus, which are reported in Tables 5.4 and 5.5. In the second method, I estimate abundances and abundance ratios within each annulus from their maps instead of integrated spectra. I study the variation of estimated observable from the two methods from one annulus to another as described later. In the third method, I simply study the variation of abundances in a pixel with respect to its physical distance from the pixel of peak Hα flux. This last method was performed to check if the method of segmentation could affect any observed trend.

Figures 5.13 and 5.14 show the variation of elemental abundances and abundance ratios from one elliptical annulus to another. The observables from the integrated spectra of each annulus is shown as blue dots. For all maps of abundances and abundance ratios, I estimate median and uncertainty on the median within each annulus, and are shown as red dots and vertical bars, respectively. The uncertainties on the median values for each sample point take into account the spatial correlation between adjacent spaxels arising from the resampling used in generating the data cubes. The overall average level of the correlation was estimated using an autocorrelation analysis of selected regions from the spaxel map after first removing larger scale gradients. In practice this provides an estimate of the factor (in this case ≈ 4) by which the number of apparently independent spaxels in each elliptical annulus region should be reduced to allow for the induced spatial correlation. The abundance and abundance ratios of Region 1 are also shown on the panels in Figures 5.13 and 5.14, as estimated from the integrated spectrum (blue dots) and the maps (red dots) for a better visual comparison, and should not be considered for abundance variation analysis. In each panel, the dashed black horizontal line indicates the median (μ) of the abundances or abundance ratio distribution of entire maps, while the two dotted black horizontal lines indicate $\mu \pm \sigma$, where σ denoted the standard deviation of entire maps.

Inspecting all panels in Figures 5.13 and 5.14, I find that the integrated spectra values and mapped values in each annulus are in reasonable agreement with each other. Results of annulus F should be interpreted with caution where uncertainties on each observable are comparatively large because of a few valid data points ($\sim$ 2–3 depending on the map) in this annulus (see maps in Figures 5.10 and 5.11). Though results of annulus F are not very informative, I have included them in this analysis as I do not wish to discard any detection.

No variation is found in 12 + log(O/H). There appears to be a variation in abundances and abundance ratios around annuli C and D, though these variations are < 0.1 dex for each observable. Given that there exists a region of over-density in the Ne abundance map (Figure 5.10), it is possible that the physical conditions are different within the region of study and is supported by the HST image which shows structures throughout this region. The absence of radial variation is probably because averaging over a considerable number of pixels with

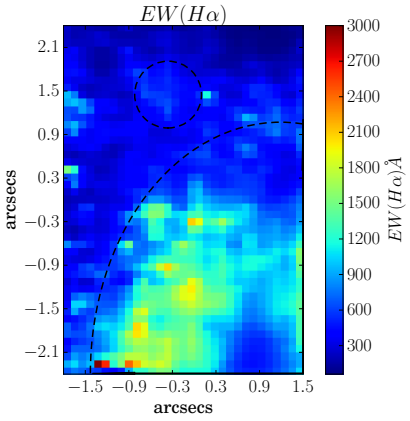

Figure 5.15 – Map of the equivalent width of Hα (in Å). The dashed quarter ellipse and circle indicate Region 1 and Region 2, respectively.

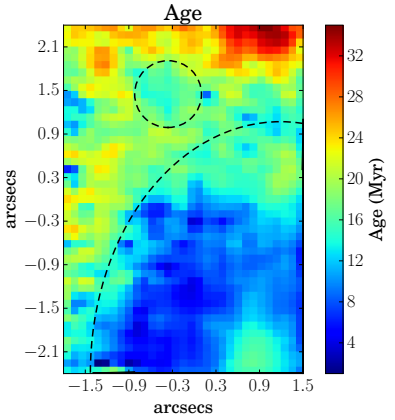

Figure 5.16 – Age map in Myr estimated from Starburst99 models at a constant metallicity of Z = 0.1 $Z_{\odot}$ (mean of the metallicity map in Figure 5.10, upper-left panel). The dashed quarter ellipse and circle indicate Region 1 and Region 2, respectively.

mixture of abundances in annuli A, B and C have suppressed signatures of over-abundance. This experiment shows that such segmentation analysis may not be a good tool to find localised abundance variation, which results in averaging out such local effects. The current analysis also shows the power of IFS with good spatial-resolution, without which over-abundance in the Ne abundance map would only have appeared as noise. However, the effects of seeing must also be considered which may have washed out any such variation in other abundance maps. I will address this issue further in an upcoming paper on chemical inhomogeneities in BCDs (Kumari et al. in prep).

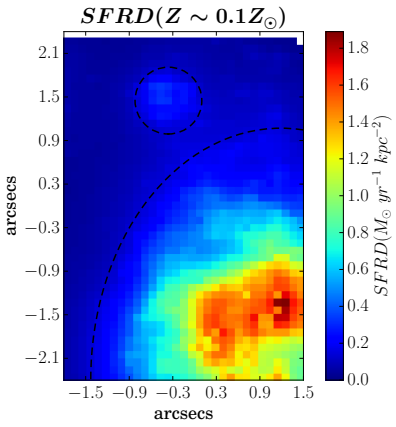

Figure 5.17 – SFRD map at a constant metallicity of Z = 0.1 $Z_\odot$ (mean of the metallicity map in Figure 5.10, upper-left panel). The dashed quarter ellipse and circle indicate Region 1 and Region 2, respectively.

5.2.6 Stellar Properties

5.2.6.1 Age of stellar population

The integrated spectrum of the FOV (Figure 5.3) show Balmer emission lines indicating the presence of young, hot and massive O and B stars embedded in gas. I do not find any Balmer absorption lines showing that the region is mostly composed of younger stellar populations. No Wolf-Rayet features are found in the integrated or spatially-resolved spectra of SBS 1415+437, in agreement with the results of López-Sánchez & Esteban (2010).

For age-dating the current ionising population, I first map the equivalent width (EW) of Hα recombination line (Figure 5.15). This map shows a variation of ∼55-3120 Å across the FOV, with a mean of ∼696 Å and standard deviation of ∼440 Å. I find that only 2% of the pixels have EW(Hα) higher than 1700 Å , which is known to be the highest EW found in the literature, i.e in the high redshift galaxy sample by (Shim et al., 2011). From the integrated spectrum of Region 1, I find an equivalent width of ∼940 ± 10 Å, which is in reasonable agreement with the value found by G03 (997.9 ± 1.7 Å).

Next, I calculate the EW(Hα) from the evolutionary synthesis models of STARBURST99. The parameters have been described in detail in Chapter 3. The only difference here is on the assumption of metallicity, which is the mean of the metallicity map (Figure 5.10, upper-left panel), i.e. Z = 0.1$Z_\odot$. Note here that instead of assuming a constant metallicity for the entire FOV, I could use the metallicity map where metallicity varies from spaxel to spaxel. Howeover, the minimum metallicity of the spectra output by STARBURST99 is 0.05$Z_\odot$, whereas the metallicity map shows values $< 0.05Z_\odot$. Moreover, the metallicity grid used by STARBURST99 is far too coarse to correctly reflect the pixel-to-pixel variation seen in the metallicity map. Hence, with the current set of models, it is not possible to create an age map varying as a function of

metallicity. By comparing the modelled EW from the evolutionary synthesis models with the observed EW(Hα), I obtain the age map (Figure 5.16) which shows a variation of $\sim$0.1–36 Myr across the FOV with a mean and standard deviation of 15 Myr and 6 Myr, respectively. I find the age of $\sim$ 10 Myr for Region 1 obtained from its integrated spectrum. These results are in agreement with that of Thuan, Izotov & Foltz (1999), who reports the presence of young stellar population ($\sim$ 5 Myr) along with stars as old as 100 Myr in Region 1. G03 estimated an age of 4 Myr for Region 1 from the galactic evolution code PEGASE, which is lower than the value of $\sim$ 10 Myr obtained in this work for two reasons. Firstly, the metallicity assumed by G03 is 0.05 $Z_{\odot}$ compared to the metallicity assumption of 0.1 $Z_{\odot}$ in this work. Secondly, the modelling in this analysis does not take into account the nebular continuum or dust-extinction which will lead to systematic uncertainties in the estimated age (Cantin et al., 2010; Pérez-Montero et al., 2007). These age estimates should be further interpreted with caution as suggested by Aloisi et al. (2005), who report the presence of stars older than $\sim$ 1.3 Gyr via a photometric analysis involving colour-magnitude diagrams.

5.2.6.2 Star Formation Rate

I estimated the star-formation rate (SFR) from the dereddened Hα luminosity assuming solar and sub-solar metallicity by using the recipes of Ly et al. (2016) and Kennicutt (1998a), respectively, assuming a Chabrier IMF. I normalise the SFR map by the area of each pixel to obtain the SFR density (SFRD) map. The SFRD map created assuming sub-solar metallicity (Figure 5.17) shows a variation of 0.03–1.89 $M_{\odot}$ yr^{-1} kpc^{-2}. SFR values on pixel-by-pixel basis should be interpreted with caution because of the failure of SFR recipes due to the stochastic sampling of the IMF at such small spatial scales. For Region 1, I find a SFR of $\sim 21.9 \pm 0.3 \times 10^{-3}$ $M_{\odot}$ yr^{-1} assuming metallicity of 12 + log(O/H) = 7.63 , and $\sim 44.7 \pm 0.5 \times 10^{-3}$ $M_{\odot}$ yr^{-1} assuming solar metallicity. The SFR estimates are in agreement with those of other BCDs, which might span a range of 10^{-3} to 10^{2} $M_{\odot}$ yr^{-1}, with the mean SFR varying from 0.1 $M_{\odot}$ yr^{-1} to 10 $M_{\odot}$ yr^{-1} (Fanelli, O'Connell & Thuan, 1988; Sage et al., 1992; Hopkins, Schulte-Ladbeck & Drozdovsky, 2002). For Region 1, I estimate a SFRD $\sim$ 0.7 $M_{\odot}$ yr^{-1} kpc^{-2} from GMOS data. For comparison, if we were to use the MMT spectroscopic observation of Thuan, Izotov & Foltz (1999) extracted over a region of 1.5 arcsec $\times$ 5 arcsec, I estimate a SFRD $\sim$ 0.5 $M_{\odot}$ yr^{-1} kpc^{-2}. The value of SFRD in this study agrees with that of Thuan, Izotov & Foltz (1999) within a factor of 2. From the Hα flux value of G03, I estimate a SFRD $\sim$ 0.17 $M_{\odot}$ yr^{-1} kpc^{-2} over a region of 2 arcsec $\times$ 4.6 arcsec. The low value of SFRD obtained from the data of G03 is due to their estimate of c(Hβ) = log(F(Hβ)/I(Hβ)) = 0.00, which results in a lower value of dereddened Hα flux.

5.3 Summary & Conclusion

Using GMOS-N IFS data, I carried out a spatially-resolved analysis of the ionised gas in a star-forming region within the BCD SBS 1415+437 at scales of ∼6.5 pc (i.e. per pixel of 0.1 arcsec). What follows is a summary of the main results.

1. The radial velocity of the ionised gas varies between -12 and 18 km s^{-1}, with no particular axis of rotation. The velocity dispersion varies between 20 and 70 km s^{-1}. The gas is predominantly photoionised as inferred from the emission line ratio diagnostic diagrams.

2. The IFS data enables the mapping of the weak auroral line [O III] λ4363 across a region of 143 pc $\times$ 143 pc. Hence I map the electron temperature T_e([O III]) and density N_e ([S II]) in this region. This allows to use the direct T_e method to map the ionic and elemental abundances of various elements.

3. I map the ionic and elemental abundances of O, N, Ne, Ar and S, and also the abundance ratios, N/O, Ne/O, S/O and Ar/O. I also estimate these observables from the integrated spectrum of the main emission region, which are in reasonable agreement with the mean of corresponding values in the maps. The oxygen abundance from the IFS data is in agreement with that obtained from the long-slit spectroscopy, i.e. 12 + log(O/H) = 7.63 $\pm$ 0.03.

4. The region under study contain a range of stellar population (0.1–36 Myr), as inferred from a comparison of the Hα EW map to the values determined from the STARBURST99 models at a uniform metallicity of 0.1 $Z_\odot$. The SFRD is found to vary between 0.03–1.89 $M_\odot$ yr^{-1} kpc^{-2} across the region of study.

5. I performed a radial profile analysis on the maps of chemical abundances and their ratios, where I chose elliptical annuli of equal widths following the Hα flux distribution in the FOV. No significant radial variation is found in either elemental abundance maps or the abundance ratio maps, despite the map of Ne/H exhibiting signatures of chemical inhomogeneity.

In conclusion, this study not only answers questions related to kinematics, ionisation conditions, chemical variations and stellar properties of SBS 1415+437 posed in the Chapter 1, but also pose further questions as how we can properly study chemical variations at small scales from IFS studies. I found that the radial profile analysis does not show significant chemical variation despite local enhancements in the neon abundance map. As such I will dedicate a study (Kumari et al. in prep.) to this problem given that an understanding of chemical inhomogeneities is essential to understand the chemical evolution of galaxies and therefore of

the Universe. In the current study, seeing prevented us from studying such variations at spatial scales exploitable at the high resolution of GMOS-IFU. There will not be such a problem with the implementation of adaptive optics in the current IFS instruments, e.g. MUSE on the Very Large Telescope, and space-based IFUs, e.g. the Near-Infrared Spectrograph on the James Webb Space Telescope. From this study, we learnt that the abundances estimated from the integrated spectrum of a star-forming region is in reasonable agreement with the average value derived from the abundance maps across the star-forming region. This consistency adds confidence to our chemical abundance measurements of star-forming systems in the high-redshift Universe, where no spatial resolution is available. This further adds confidence to the comparison of abundances between local star-forming systems and systems in the distant Universe, and hence to the study of the chemical evolution across different star-forming epochs. With the long-awaited James Webb Space Telescope, we will be able to detect the distant and hence faint star-forming systems and study the chemical evolution of Universe with relatively less biases.

5.4 Appendix

Table 5.4 presents the observed and intrinsic flux values from integrated spectra of each annulus described in Section 5.2.5.3. The abundances and abundance ratios within each annulus are presented in Table 5.5.

Table 5.4 – Emission line measurements (relative to Hβ = 100) for the integrated spectrum of each annulus shown in Figure 5.12. Line fluxes (F_λ) are extinction corrected using E(B-V) to calculate F_λ.

Line	λ_{air}	$F(A)_\lambda$	$I(A)_\lambda$	$F(B)_\lambda$	$I(B)_\lambda$	$F(C)_\lambda$	$I(C)_\lambda$	$F(D)_\lambda$	$I(D)_\lambda$	$F(E)_\lambda$	$I(E)_\lambda$	$F(F)_\lambda$	$I(F)_\lambda$
[NIII]	3868.76	27.11 ± 1.75	28.82 ± 2.04	26.63 ± 1.23	28.18 ± 1.52	24.13 ± 1.50	25.55 ± 1.72	26.22 ± 1.88	27.34 ± 2.09	23.62 ± 2.74	24.94 ± 3.01	19.29 ± 4.12	19.98 ± 4.32
$H\gamma$	4340.47	44.05 ± 0.56	45.42 ± 1.36	44.79 ± 0.55	46.07 ± 1.34	44.50 ± 0.58	45.78 ± 1.27	45.53 ± 0.76	46.48 ± 1.40	46.47 ± 0.85	47.75 ± 1.71	47.81 ± 1.04	48.65 ± 1.94
$[OIII]$	4363.21	9.38 ± 0.30	9.66 ± 0.40	9.46 ± 0.44	9.72 ± 0.52	9.21 ± 0.31	9.46 ± 0.40	8.53 ± 0.41	8.70 ± 0.48	8.58 ± 0.86	8.81 ± 0.93	6.71 ± 1.17	6.82 ± 1.22
$H\beta$	4861.33	100.00 ± 0.49	100.00 ± 1.86	100.00 ± 0.48	100.00 ± 1.81	100.00 ± 0.43	100.00 ± 1.67	100.00 ± 0.47	100.00 ± 1.72	100.00 ± 0.58	100.00 ± 2.11	100.00 ± 0.65	100.00 ± 2.31
$[OIII]$	4958.92	130.21 ± 0.95	129.57 ± 3.38	129.92 ± 0.90	129.32 ± 3.29	126.28 ± 0.83	125.70 ± 2.96	118.76 ± 0.74	118.36 ± 2.85	111.56 ± 0.87	111.07 ± 3.27	100.63 ± 0.83	100.34 ± 3.22
$[OIII]$	5006.84	388.09 ± 2.75	385.12 ± 9.97	385.75 ± 2.64	383.02 ± 9.68	374.54 ± 2.35	371.88 ± 8.68	353.61 ± 2.30	351.76 ± 8.43	330.75 ± 2.41	328.50 ± 9.57	300.52 ± 2.35	299.20 ± 9.50
HeI	5875.67	10.67 ± 0.17	10.18 ± 0.28	10.78 ± 0.15	10.32 ± 0.27	10.64 ± 0.18	10.19 ± 0.27	10.67 ± 0.20	10.33 ± 0.29	10.65 ± 0.23	10.21 ± 0.35	10.40 ± 0.30	10.12 ± 0.41
$[OI]$	6300.3	1.44 ± 0.07	1.36 ± 0.07	1.36 ± 0.05	1.28 ± 0.05	1.74 ± 0.06	1.64 ± 0.06	2.09 ± 0.08	2.00 ± 0.09	2.77 ± 0.10	2.62 ± 0.12	3.35 ± 0.16	3.23 ± 0.18
$[SIII]$	6312.1	1.54 ± 0.07	1.45 ± 0.08	1.47 ± 0.05	1.39 ± 0.06	1.43 ± 0.05	1.35 ± 0.06	1.51 ± 0.07	1.45 ± 0.07	1.51 ± 0.07	1.42 ± 0.08	1.25 ± 0.10	1.20 ± 0.11
$[NII]$	6548.03	0.81 ± 0.45	0.76 ± 0.42	0.90 ± 0.44	0.84 ± 0.42	1.04 ± 0.43	0.98 ± 0.40	1.07 ± 0.37	1.02 ± 0.36	1.20 ± 0.41	1.13 ± 0.39	1.58 ± 0.37	1.51 ± 0.36
$H\alpha$	6562.8	307.16 ± 1.73	286.00 ± 6.42	305.53 ± 1.68	286.00 ± 6.27	305.63 ± 1.55	286.00 ± 5.79	300.28 ± 1.56	286.00 ± 5.94	304.73 ± 1.94	286.00 ± 7.27	297.93 ± 2.07	286.00 ± 7.93
$[NII]$	6583.41	2.14 ± 0.45	1.99 ± 0.42	2.23 ± 0.44	2.08 ± 0.42	2.62 ± 0.43	2.45 ± 0.40	2.99 ± 0.37	2.85 ± 0.36	3.82 ± 0.41	3.59 ± 0.40	3.95 ± 0.37	3.79 ± 0.37
HeI	6678.15	2.92 ± 0.07	2.71 ± 0.08	2.87 ± 0.05	2.68 ± 0.07	2.88 ± 0.06	2.69 ± 0.08	2.87 ± 0.07	2.73 ± 0.09	2.85 ± 0.09	2.66 ± 0.10	2.76 ± 0.15	2.64 ± 0.16
$[SII]$	6716.47	6.05 ± 0.09	5.61 ± 0.15	6.13 ± 0.07	5.71 ± 0.14	7.21 ± 0.07	6.72 ± 0.15	8.82 ± 0.10	8.38 ± 0.19	11.04 ± 0.12	10.32 ± 0.28	12.79 ± 0.17	12.25 ± 0.36
$[SII]$	6730.85	4.42 ± 0.09	4.09 ± 0.12	4.57 ± 0.07	4.25 ± 0.11	5.15 ± 0.07	4.79 ± 0.11	6.11 ± 0.09	5.80 ± 0.15	7.79 ± 0.11	7.27 ± 0.21	9.12 ± 0.16	8.72 ± 0.28
$[ArIII]$	7135.8	4.11 ± 0.07	3.76 ± 0.10	4.11 ± 0.05	3.79 ± 0.09	4.09 ± 0.09	3.77 ± 0.11	4.16 ± 0.07	3.91 ± 0.10	4.32 ± 0.08	3.99 ± 0.12	4.13 ± 0.11	3.92 ± 0.15
$[OII]$	7318.92	1.31 ± 0.07	1.19 ± 0.07	1.31 ± 0.08	1.20 ± 0.07	1.49 ± 0.08	1.36 ± 0.08	1.66 ± 0.10	1.56 ± 0.09	2.01 ± 0.12	1.85 ± 0.12	2.18 ± 0.19	2.06 ± 0.18
$[OII]$	7329.66	1.11 ± 0.07	1.01 ± 0.06	1.10 ± 0.07	1.01 ± 0.07	1.17 ± 0.07	1.08 ± 0.07	1.31 ± 0.08	1.22 ± 0.08	1.63 ± 0.11	1.50 ± 0.11	1.74 ± 0.17	1.65 ± 0.16
E(B-V)		0.069 ± 0.005		0.063 ± 0.005		0.064 ± 0.005		0.047 ± 0.005		0.061 ± 0.006		0.039 ± 0.007	
F(Hβ)		12.61 ± 0.06	15.83 ± 0.29	28.6 ± 0.14	35.25 ± 0.64	26.83 ± 0.12	33.14 ± 0.57	17.07 ± 0.08	19.94 ± 0.34	13.50 ± 0.08	16.53 ± 0.35	10.26 ± 0.07	11.68 ± 0.27

Table 5.5 – Summary of nebular diagnostics, ionic abundances, elemental abundances and abundance ratios obtained from the integrated spectra of annuli (A, B, C, D, E, F) shown in Figure 5.12.

Parameter	A	B	C	D	E	F
Te([OIII]) (X 10^4 K)	1.69 ± 0.04	1.70 ± 0.04	1.70 ± 0.04	1.67 ± 0.05	1.75 ± 0.11	1.60 ± 0.15
Te([OII]) (X 10^4 K)	1.58 ± 0.02	1.57 ± 0.09	1.59 ± 0.03	1.58 ± 0.04	1.62 ± 0.07	1.53 ± 0.09
Te([NII]) (X 10^4 K)	1.41 ± 0.01	1.41 ± 0.02	1.41 ± 0.01	1.40 ± 0.02	1.43 ± 0.04	1.38 ± 0.06
Te([SIII]) (X 10^4 K)	1.69 ± 0.04	1.70 ± 0.05	1.70 ± 0.05	1.67 ± 0.06	1.76 ± 0.13	1.59 ± 0.19
Ne([SII]) (cm^{-3})	< 50	60 ± 14	< 50	< 50	< 50	< 50
12 + log(O^+/H^+)	7.07 ± 0.03	7.10 ± 0.11	7.11 ± 0.04	7.18 ± 0.05	7.21 ± 0.08	7.36 ± 0.11
12 + log(O^{2+}/H^+)	7.51 ± 0.02	7.50 ± 0.03	7.49 ± 0.03	7.48 ± 0.03	7.40 ± 0.06	7.45 ± 0.10
12 + log(O/H)	7.64 ± 0.02	7.64 ± 0.04	7.64 ± 0.02	7.65 ± 0.03	7.62 ± 0.05	7.71 ± 0.07
12 + log(N+/H+)	5.28 ± 0.08	5.29 ± 0.04	5.36 ± 0.04	5.44 ± 0.04	5.52 ± 0.04	5.58 ± 0.04
ICF (N^+)	3.73 ± 0.34	3.53 ± 0.94	3.39 ± 0.33	2.96 ± 0.36	2.56 ± 0.57	2.22 ± 0.67
12 + log(N/H)	5.85 ± 0.08	5.84 ± 0.12	5.89 ± 0.06	5.91 ± 0.07	5.93 ± 0.11	5.92 ± 0.14
log(N/O)	-1.79 ± 0.09	-1.80 ± 0.12	-1.74 ± 0.06	-1.75 ± 0.07	-1.69 ± 0.12	-1.78 ± 0.16
S^+/H^+ (X 10^7)	0.93 ± 0.03	0.97 ± 0.10	1.10 ± 0.04	1.37 ± 0.06	1.62 ± 0.13	2.14 ± 0.23
S^{2+}/H^+ (X 10^7)	5.33 ± 0.49	5.02 ± 0.51	4.84 ± 0.42	5.45 ± 0.62	4.66 ± 0.97	5.24 ± 1.89
ICF (S^+ + S^{2+})	1.15 ± 0.01	1.13 ± 0.04	1.13 ± 0.02	1.10 ± 0.02	1.07 ± 0.02	1.05 ± 0.03
12 + log(S/H)	5.86 ± 0.03	5.83 ± 0.04	5.83 ± 0.03	5.87 ± 0.04	5.83 ± 0.07	5.89 ± 0.12
log(S/O)	-1.78 ± 0.04	-1.81 ± 0.06	-1.81 ± 0.04	-1.78 ± 0.05	-1.79 ± 0.09	-1.82 ± 0.13
Ne^{2+}/H^+ (X 10^5)	0.57 ± 0.05	0.55 ± 0.05	0.50 ± 0.05	0.55 ± 0.06	0.45 ± 0.09	0.45 ± 0.15
ICF (Ne^{2+})	1.09 ± 0.00	1.09 ± 0.01	1.10 ± 0.00	1.10 ± 0.01	1.12 ± 0.02	1.14 ± 0.04
12 + log(Ne/H)	6.79 ± 0.04	6.78 ± 0.04	6.74 ± 0.04	6.78 ± 0.05	6.70 ± 0.09	6.71 ± 0.16
log(Ne/O)	-0.85 ± 0.04	-0.86 ± 0.05	-0.90 ± 0.05	-0.87 ± 0.06	-0.92 ± 0.10	-1.00 ± 0.17
Ar^{2+}/H^+ (X 10^7)	1.24 ± 0.06	1.23 ± 0.07	1.23 ± 0.06	1.31 ± 0.08	1.23 ± 0.14	1.43 ± 0.30
ICF (Ar^{2+})	1.14 ± 0.00	1.14 ± 0.01	1.14 ± 0.00	1.15 ± 0.01	1.17 ± 0.03	1.20 ± 0.05
12 + log(Ar/H)	5.15 ± 0.02	5.15 ± 0.03	5.15 ± 0.02	5.18 ± 0.03	5.16 ± 0.05	5.23 ± 0.09
log(Ar/O)	-2.49 ± 0.03	-2.49 ± 0.05	-2.49 ± 0.03	-2.47 ± 0.04	-2.46 ± 0.07	-2.48 ± 0.12

6

Metallicity calibrations for diffuse ionised gas

6.1 Introduction

Knowledge of the gas-phase metallicity of galaxies is essential to study various topics related to the chemical evolution of the Universe. A robust measure of gas-phase metallicity within galaxies is imperative for studying the physical correlations between the gas-phase metallicity of galaxies and physical properties associated with the history of chemical enrichment of galaxies such as stellar mass (i.e. mass-metallicity relation, MZR, see e.g. Tremonti et al. (2004)) and star-formation rate (i.e. fundamental metallicity relation, FMR, see e.g Mannucci et al. (2010)), or to explore the abundance gradients within galaxies (see e.g. Sánchez Almeida et al., 2013). As described in Chapter 1, the so-called direct T_e-method is based on fundamental knowledge of atomic physics and hence is deemed to provide a robust estimate of gas-phase metallicity. However, the direct T_e method requires the detection of weak auroral emission lines (e.g. [O III] λ4363, [N II] λ5755), which are difficult to observe even in low-metallicity environments. Hence, correct metallicity estimates using the direct T_e method become impossible in high metallicity environments unless very sensitive, high S/N spectra are available (Garnett, Kennicutt & Bresolin, 2004; Kewley & Ellison, 2008). To circumvent this problem, many indirect methods have been devised which involve the use of relatively strong emission lines (see

Table 6.1 – Properties of galaxy sample

Galaxy	RA(J2000)	Dec(J2000)	Type	z	Distance (Mpc)	Spaxel spatial scale (pc)
NGC289	00 52 42.365	-31 12 20.99	SBbc	0.005434	18.6	18.0
NGC1042	02 40 23.976	-08 26 01.13	SABcd	0.004573	15.7	15.2
NGC1309	03 22 06.557	-15 24 00.26	SA(s)bc	0.007125	27.0	26.2
NGC1483	03 52 47.608	-47 28 39.06	SB(s)bc	0.003833	15.0	14.5
NGC3256	10 27 51.284	-43 54 13.55	Sb	0.009354	41.9	40.6
NGC3783	11 39 01.721	-37 44 18.60	SBab	0.009730	38.5	37.3
NGC4030	12 00 23.643	-01 05 59.87	SAbc	0.004887	24.8	24.0
NGC4592	12 39 18.779	-00 31 54.64	Sd	0.003566	11.6	11.2
NGC4603	12 40 55.195	-40 58 35.05	Sc	0.008647	39.0	37.8
NGC4790	12 54 51.932	-10 14 52.16	SB(rs)c?	0.004483	22.8	22.1
NGC4900	13 00 39.148	+02 30 05.27	SBc	0.003201	17.5	17.0
NGC4941	13 04 13.143	-05 33 05.83	(R)SAB(r)ab	0.003696	19.6	19.0
NGC4980	13 09 10.082	-28 38 30.44	Sa	0.004767	23.6	22.9
NGC5334	13 52 54.470	-01 06 53.12	SBcd	0.004623	22.7	22.0
NGC5584	14 22 23.811	-00 23 14.82	SABc	0.005464	25.7	24.9
NGC5643	14 32 40.778	-44 10 28.60	Sc	0.003999	22.7	22.0
NGC5806	15 00 00.432	+01 53 28.56	SABb	0.004533	10.6	10.2
NGC7162	21 59 39.053	-43 18 22.41	Sa	0.007720	28.4	27.5
NGC7421	22 56 54.316	-37 20 49.91	Sbc	0.005979	20.8	20.2
NGC7496	23 09 47.292	-43 25 40.87	Sc	0.005500	19.2	18.6
NGC7552	23 16 10.767	-42 35 05.39	SB(s)ab	0.005365	18.6	18.0
PGC3853	01 05 04.877	-06 12 44.57	SAB(rs)d^n	0.003652	10.6	10.3
ESO 498-G5	09 24 40.671	-25 05 33.78	Sb	0.008049	37.0	35.9
ESO 499-G37	10 03 41.840	-27 01 40.12	Sb	0.003186	17.6	17.1

Notes: Column 1: Name of galaxies in the sample, Columns 2, 3: ICRS coordinates (Equinox J2000) from Simbad, Column 4: Morphological Type taken from Simbad except for PGC 3853 which is taken from NED, Column 5: redshift from NASA extragalactic Database (NED), Column 6: Distances. Column7: Spatial scale corresponding to the spaxel of 0.2 arcsec. Required maximum seeing for each of the targets is 0.8 arcsec.

Chapter 1 and references therein).

The indirect metallicity diagnostics have either been calibrated empirically against the direct method metallicity estimates of H II regions or theoretically by using photoionisation models of H II regions such as MAPPINGS (Sutherland & Dopita, 1993) and CLOUDY (Ferland et al., 2013). Other ways to determine metallicity are to make use of codes such as HII-CHI-MISTRY (Pérez-Montero, 2014), IZI (Blanc et al., 2015) and BOND (Vale Asari et al., 2016), which utilise grids from the photoionisation models mentioned above. These theoretical models suffer from problems such as limitations related to the geometry of H II regions, poorly constrained out-of-gas phase metal depletion and no implementation of the clumpiness of the density distribution of gas and dust (Kewley & Ellison, 2008). Moreover, the photoionization models also depend on the spectrum of the incident light (i.e. the emitted integrated spectrum of the stellar population) which is also strongly dependent on the stellar atmosphere and evolution models used. However, another overlooked problem with using indirect metallicity calibrators is that both empirical and theoretical indirect diagnostics are calibrated for H II regions, and do not consider the possible contamination of the observed fluxes by the more diffuse component of the ionised gas: diffuse ionised gas (DIG).

DIG, also known as the warm ionised medium (WIM) is an important ionised gas component of the interstellar medium (ISM) in galaxies, along with the denser H II regions. It is found in the Milky Way (Reynolds, 1984, 1990), and also in the discs and halos of other spiral galaxies (see, e.g. Rossa & Dettmar, 2003a,b; Oey et al., 2007; Belfiore et al., 2016). The fraction of DIG increases with a decrease in the Hα surface brightness of galaxies, in contrast to H II regions (Oey et al., 2007). Moreover, the emission line ratios of DIG and H II regions are significantly different. For example, the line ratios [O I] λ6300/Hα, [O II] λ3727/Hβ, [N II] λ6584/Hα and [S II] $\lambda\lambda$6717,6731/Hα are known to increase in DIG regions compared to H II regions (see e.g. Haffner, Reynolds & Tufte, 1999; Voges & Walterbos, 2006; Madsen, Reynolds & Haffner, 2006; Blanc et al., 2009; Zhang et al., 2017). These emission line ratios resemble those of the low-ionisation (nuclear) emission line regions (LI[N]ERs Belfiore et al., 2016) on the classical emission line ratio diagnostic diagrams (the so-called BPT diagrams, Baldwin, Phillips & Terlevich, 1981). Since metallicity diagnostics are dependent on the use of emission line ratios, the metallicity estimated for a DIG region is in fact determined assuming the physical conditions of an H II region, and is not necessarily indicative of the true metallicity estimate of the DIG region.

The impact of DIG on metallicity measurements has been recently studied at global and spatially-resolved scales. For example, Sanders et al. (2017) find that the contamination of the global galaxy spectrum by DIG results in an increase in the strength of low-ionisation lines and a decrease in the temperature of the low-ionisation zone, hence resulting in a higher metallicity estimate than the true value. Their study also shows that combining DIG contamination with flux weighting effects may bias metallicity estimates by more than 0.3 dex in some cases. Con-

sidering local scales, Zhang et al. (2017) made use of integral field spectroscopic data from the Mapping Nearby Galaxies at APO (MaNGA) survey to study the effect of the DIG. They demonstrated via a radial profile analysis that the biases in metallicities derived by strong line metallicity calibrators [R_{23} (see e.g. McGaugh, 1991; Kewley & Ellison, 2008, and references therein), O3N2, N2 (Pettini & Pagel, 2004) and N2S2Ha (Dopita et al., 2016)] may be as large as the metallicity gradients exhibited in spiral galaxies.

The aim of this Chapter is to devise strong line metallicity calibrations which correct for the biases introduced in the determination of metallicity of DIG-dominated regions within galaxies. I make use of the publicly available IFS data of nearby spiral galaxies obtained from the Multi Unit Spectroscopic Explorer (MUSE) instrument on the Very Large Telescope for studying the biases mentioned above. The high spatial resolution of MUSE allows us to separate regions in galaxies dominated by the properties of H II regions and DIG at scales of tens of parsec. By comparison, the previous study of Zhang et al. (2017) exploring the impact of the DIG, used IFS data from Mapping Nearby Galaxies at APO (MaNGA) survey, could only resolve at kiloparsec scales. Given the size of a typical H II region may vary between a few and hundreds of parsecs (e.g. Kennicutt, 1984), each MANGA spaxel will always contain a mixture of emission from the H II regions and the surrounding DIG. However, these mixing effects are reduced in the MUSE data because of its higher spatial resolution.

The Chapter is organised as follows. Section 6.2 describes the galaxy sample and MUSE observation. Section 6.3 presents the methodology regarding spectral fitting, flux extraction, mapping metallicities using existing metallicity calibrators and identifying H II and DIG-dominated regions with similar metallicities. Section 6.4 presents the main results of the analysis, a discussion concerning the biases involved in using existing metallicity calibrations, and introduces new methods to mitigate such biases. Section 6.5 summaries the main results. Throughout this Chapter, I use Z to denote 12 + log(O/H) and the following shorthand notation for the strong line ratios for a compact presentation in equations and figures:

$$O3 = log([O\textsc{iii}]\lambda5007/H\beta) \tag{6.1}$$

$$N2 = log([N\textsc{ii}]\lambda6584/H\alpha) \tag{6.2}$$

$$S2 = log([S\textsc{ii}]\lambda\lambda6717,6731/H\alpha) \tag{6.3}$$

$$O3N2 = log\frac{[O\textsc{iii}]\lambda5007/H\beta}{[N\textsc{ii}]\lambda6584/H\alpha} \tag{6.4}$$

6.2 Observations

This work utilises the publicly available data of 24 nearby spiral galaxies observed by MUSE on the Very Large Telescope. Table 6.1 presents the celestial coordinates of each galaxy in the

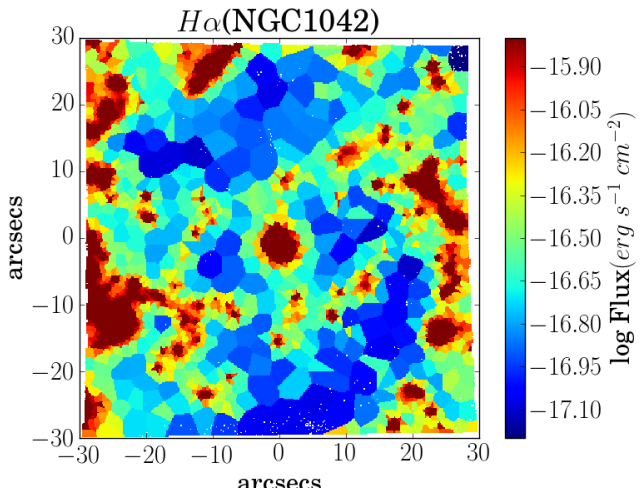

Figure 6.1 – Hα emission line map of NGC 1042. White spaxels denote the bins with S/N of emission line < 5.

sample along with redshift and distance. The IFS observations of these galaxies were taken from June – August 2014, and from October 2014 – September 2015 (i.e. ESO P95, P96 and P97) in the wide field mode and were reduced using MUSE pipeline version muse-1.4 and higher (Freudling et al., 2013), which included removal of instrumental signature, astrometric calibration, sky-subtraction, wavelength calibration and flux calibration. The final reduced data cube of each galaxy covers a field of view (FOV) of $\sim$1 arcmin $\times$ 1 arcmin sampled by $\sim$ 100,000 individual spectra and a spatial resolution 0.2 arcsec per spatial pixel. The wavelength range covered for each data cube is $\sim$ 4800–9300 Å with a spectral sampling of 1.25Å per spectral pixel.

6.3 Methodology

6.3.1 Spectral fitting & Flux extraction

The emission line fluxes are measured after subtracting the stellar continuum using a customized spectral-fitting IDL-based routine. The procedure essentially involves the following steps. An initial Voronoi binning (Cappellari & Copin, 2003) is first performed on the data cubes to optimise the S/N in the continuum. A set of simple stellar population templates from the MUISCAT library (Vazdekis et al., 2012; Ricciardelli et al., 2012) are then used to fit the continuum within each Voronoi bin using the penalised pixel fitting (pPXF) routine (Cappellari & Emsellem, 2004)[1]. For each data cube, the best-fit continuum within each Voronoi bin is now scaled to the continuum level (6000-6200 Å) of each spectrum of the bin and subtracted from the observed

[1]The pPXF routine fits the line-of-sight velocity distribution (LOSVD) of stars in a galaxy, expanded as a Gauss-Hermite series. The fit is Gaussian when the S/N is low, while the actual profile of LOSVD is reproduced in the case where S/N is high.

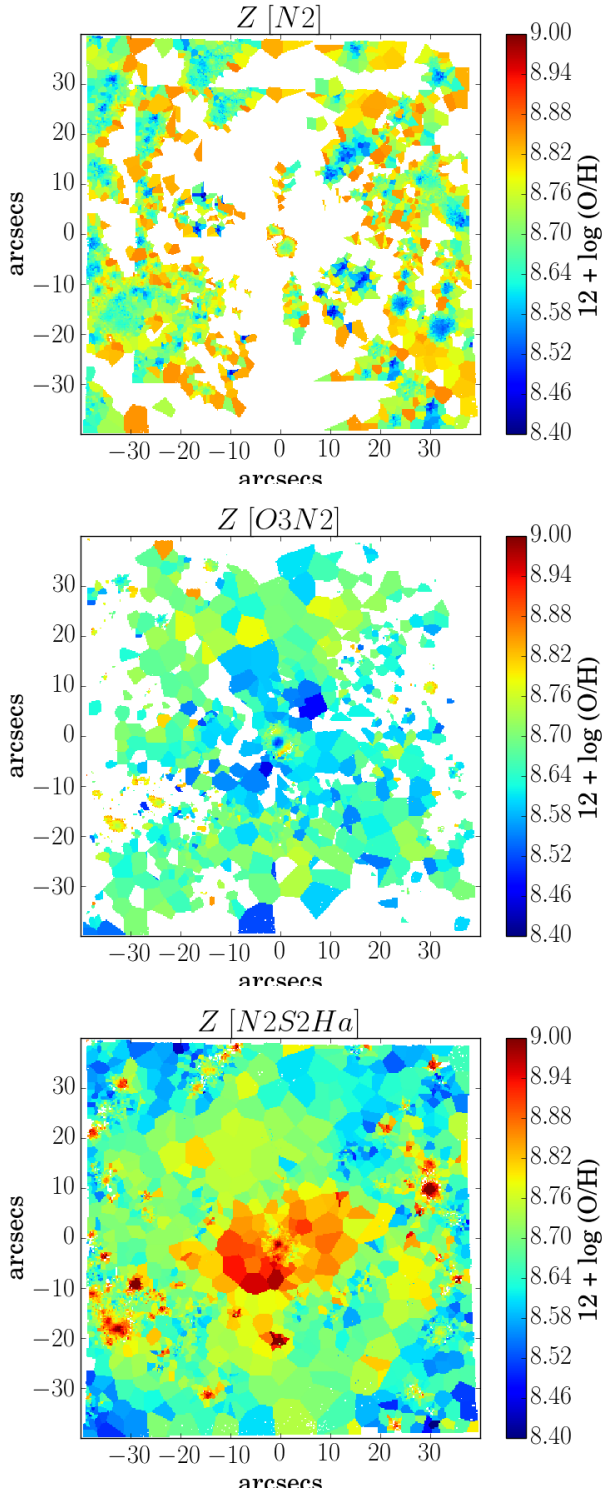

Figure 6.2 – Metallicity maps of NGC 1042 obtained using the metallicity calibrators Z[N2], Z[O3N2] and Z[N2S2Hα]. White spaxels denote the bins with S/N of emission lines $<$ 5 or spaxels whose emission line ratios do not permit the use of a particular metallicity calibrator. Note here that the metallicity maps determined from different calibrators show no apparent correlation at all, demonstrating the inherent discrepancies between the strong line metallicity calibrators mentioned in Chapter 1.

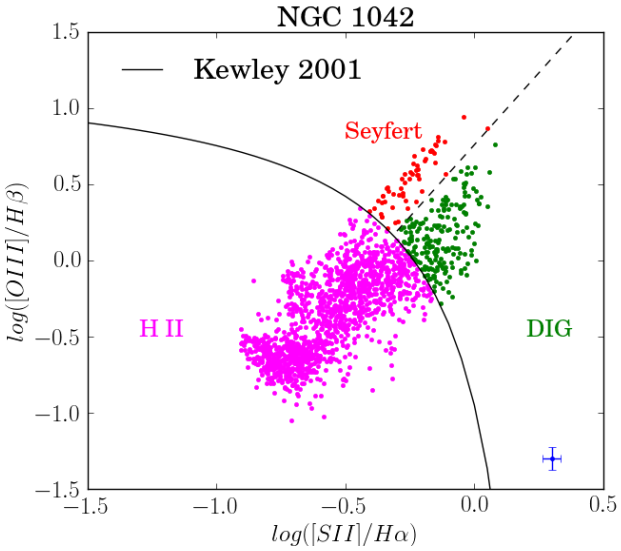

Figure 6.3 – Emission line ratio diagnostic of NGC 1042. Each point corresponds to a Voronoi bin, black solid curve represents the theoretical maximum starburst line from Kewley et al. (2001), providing a demarcation between the bins with H II regions and DIG-dominated regions. In the DIG-dominated regime on the BPT diagnostic diagram, the dashed line shows the demarcation between the DIG and Seyfert regions. The median error bars (in blue) on the emission line ratios are shown in the bottom right-hand corner.

spectrum to obtain a continuum-subtracted data cube containing only the emission lines. A second Voronoi binning is now performed for optimising the S/N in the Hα emission lines. The emission line flux maps are created by fitting a Gaussian profile to each emission line of interest within each bin. For more details of the fitting procedure, see Belfiore et al. (2016). A S/N cut of 5 is performed on the emission line flux maps before carrying out further analysis. The Hα emission line map of NGC 1042 is shown in Fig 6.1. Note that the Voronoi-binned maps are used as it allows us to preserve the initial spatial resolution of high S/N regions and also allows us to analyse the regions which have low S/N at the original sampling.

6.3.2 Metallicity Maps

Metallicity maps are created for each galaxy using the observed flux maps (an example for NGC 1042 is shown in Fig 6.2), and three indirect metallicity calibrators Z[N2], Z[O3N2] and Z[N2S2Hα]. Each of the three diagnostics use the ratio of emission lines which are very close in wavelength space and hence do not require any reddening correction. The frequently used R_{23} (= ([O II] $\lambda\lambda 3727, 3729$ + [O III] $\lambda\lambda 4959, 5007$)/H$\beta$) parameter or N2O2 (= [N II]/[O II]) could not be used for mapping metallicity because the spectral range of MUSE does not cover the [O II] $\lambda\lambda 3727, 3729$ doublet.

1. **N2 parameter:** The following non-linear calibration involving the N2 parameter from

Pettini & Pagel (2004) was used to map metallicity, which provides a better estimate than the linear calibration:

$$Z[N2] = 9.37 + 2.03 \times N2 + 1.26 \times N2^2 + 0.32 \times N2^3 \quad (6.5)$$

The calibration is valid in the range $-2.5 <$ N2 < -0.3, which results in discarding a large number of spaxels that have line ratios corresponding to DIG.

2. **O3N2 parameter:** Metallicity maps from the O3N2 parameter were created using the following linear calibration

$$Z[O3N2] = 8.73 - 0.32 \times O3N2 \quad (6.6)$$

given by Pettini & Pagel (2004) which is valid in the range $-1 <$ O3N2 < 1.9.

The calibration uncertainty associated with the N2 and O3N2 parameters is ± 0.18 and ± 0.14 dex, respectively at 68% confidence interval, which dominates the measurement error.

3. **The N2S2Hα** metallicity diagnostic presents the relation between metallicity and the emission line ratios [N II] λ6584/Hα and [N II] λ6584/[S II] $\lambda\lambda$6717,6731 via the following linear relation devised by Dopita et al. (2016):

$$Z[N2S2H\alpha] = 8.77 + log([N\textsc{ii}]/[S\textsc{ii}]) + 0.264log([N\textsc{ii}]/H\alpha) \quad (6.7)$$

This calibration is derived by constructing a grid of photoionisation model of H II regions implemented in MAPPINGS (Sutherland & Dopita, 1993), in contrast to the previous two empirically-calibrated diagnostics (N2 and O3N2).

6.3.3 Selecting HII-DIG pairs

As explained in Section 6.1, the aim of this work is to determine the abundance of DIG-dominated regions, for which no metallicity calibrator exists. However, the metallicity of the diffuse medium surrounding an H II region is expected to be the same as that of the H II region itself. This expectation is supported by the observational studies which explored azimuthal variations of the metallicity in galactic discs both by using the direct T_e method (Li, Bresolin & Kennicutt, 2013; Berg et al., 2015) and the strong line method (Zinchenko et al., 2016). With the exception for a few individual H II regions, these studies have not found evidence of significant azimuthal variation of the metallicity in galactic discs. The similarity of metallicity in H II regions and the surrounding DIG region is due to the fact the dynamical timescale internal to these small regions is shorter than the supernovae burst time scale responsible for ejecting metals into the ISM, or the cooling timescales. With this simple idea in mind, I approach this problem of

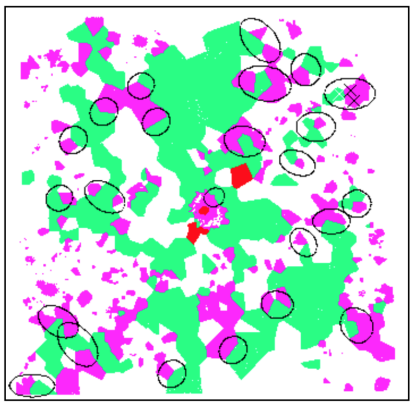

Figure 6.4 – Resolved [S II]-BPT map of NGC 1042. White spaxels denote the bins with S/N <5 (for the involved emission lines, i.e. Hβ, [O III] λ5007, [S II] $\lambda\lambda$6717, 6731). Magenta represents H II regions, green represents DIG and red represents Seyfert regions. Each ellipse denotes the selected H II-DIG pair.

determining the metallicity of DIG-dominated region by first comparing their metallicity to that of a nearby H II region, when determined naively by the standard metallicity calibrators.

For such a comparison, we need to select the pairs of adjacent H II and DIG-dominated regions, whose metallicity is expected to be same. To establish the maximum distance between an HII region and the corresponding DIG region in pair, I used the catalogue of H II regions in NGC 0628 from Berg et al. (2013), which provided the metallicities of H II regions derived from direct method and the coordinates of all H II regions. I estimated the metallicity difference and distances between all possible pairs of H II regions in the catalogue. I plotted the metallicity difference versus distance, which showed that the metallicity difference is more than 0.1 dex when H II regions are located about 500 parsec apart. The assumption of a maximum distance of 500 parsec can be further justified by a comparison of the involved timescales. For example, at a typical ISM velocity of 100 km s^{-1}, time taken to traverse a distance of 500 pc is about 5 Myr, which is much smaller than the supernova timescale of $\sim$ 100 Myr (i.e. the main mechanism responsible for ejecting metals into the ISM). Hence, in the following analysis, selected HII and DIG-dominated regions in a pair are within 500 parsec distance.

The emission line ratios are used here to separate H II regions from DIG, in contrast to the previous studies which have used Hα surface-brightness for this separation. The classical BPT diagnostic diagrams are used to create the spatially-resolved [S II]-BPT maps of all galaxies in the sample. Figs 6.3 and 6.4 show the [S II]-BPT diagnostic diagram and map, respectively, for galaxy NGC 1042, where magenta, green and red coloured data points correspond to H II, DIG and Seyfert regions, respectively. Using these maps as reference, it is possible to manually select the adjacent bins [2] with S2 emission line ratios corresponding to H II and DIG-dominated

[2]While selecting bins, it was made sure that they contained at least four pixels corresponding 0.8 arcsec, which is the maximum targeted seeing of data.

Table 6.2 – Mean and standard deviation of the distribution of differential metallicities between H II and DIG-dominated regions as determined from original metallicity calibrators.

Calibrator	Mean ΔZ	Standard deviation ΔZ	Minimum Z	Maximum Z
Z[N2S2Ha]	0.01	0.13	7.58	9.27
Z[N2]	0.06	0.07	8.17	8.86
Z[O3N2]	−0.06	0.09	8.24	9.04

regions. Figure 6.4 presents ellipses showing some of the selected H II -DIG pairs. At first, ∼50 such ellipses were placed randomly on the resolved [S II]-BPT maps and histogram of differential metallicities were plotted (see Figure 6.10 in Appendix). To explore the entire range of DIG, maps of N2, O3, Z[N2], Z[O3N2] and Z[N2S2Hα] were examined simultaneously and ∼285 more H II-DIG pairs were selected. For doing so, the range of values for each of the five maps were divided into nine equal bins[3], and the H II-DIG pairs with variations larger than the binsize were included in the sample. Such a procedure is adopted for minimal bias in sample selection The pairs with variation in metallicity of more than 0.1 dex were also included in the sample. Note here that selecting on metallicity difference will also bias the results. I will address this issue by selecting all possible pairs in the follow-up work. The method was followed for each of the 24 galaxies. However, because of the rigour of this method, not all H II-DIG pairs were selected, which might be the source of potential biases. As mentioned in Section 6.5, I will explore this issue further as a follow-up work.

For DIG-dominated regions surrounded by multiple H II regions, the mean of metallicity and emission line ratios of all of those adjacent H II region bins is used as a representative value. Using Voronoi bins for HII-DIG region selection results in the selection of low S/N regions. However, for high S/N region, minimum size of feature resulting from Voronoi tessellation may be a pixel. Hence, H II-DIG pairs in high S/N regions are selected using a slightly different method but based on the same underlying idea. Adjacent H II-DIG regions are identified where circular apertures of 1 arcsec radii with their centres separated by roughly 500 pc are placed, such that there are no other H II region in the close vicinity of the DIG dominated region which could affect its metal-content. The mean of the unique values of metallicities and line ratios within each circular aperture are taken as a representative metallicity and line ratios, for consistency with the Voronoi-bin selection method. Even though not all H II-DIG pairs were selected in the sample, note here that similar biases (i.e. offsets in the differential Z[N2] and Z[O3N2], and large dispersion in the differential Z[N2S2Hα]) in metallicity estimates, discussed in the following Section 6.4, are observed in each sub-sample (either Voronoi-bin selection or circular-aperture selection) as well as their combined sample.

[3]This bin number (9) is a default value for colour bar in ds9 and has been chosen purely for convenience.

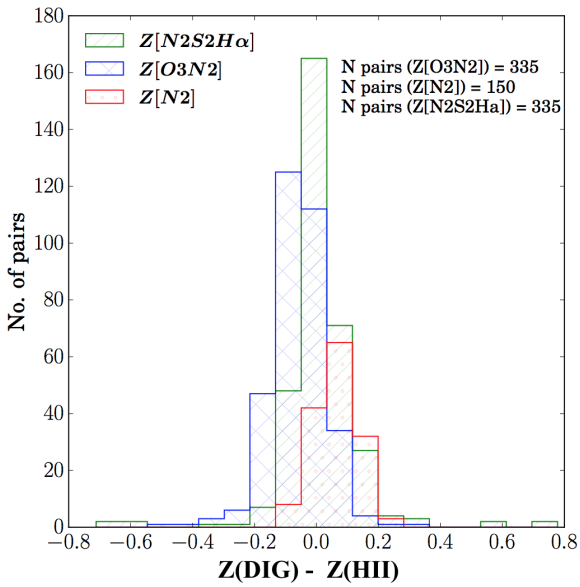

Figure 6.5 – Distribution of differential metallicity (ΔZ) of the pairs of star-forming and DIG-dominated regions, as obtained from three standard metallicity calibrators, Z[N2] (red), Z[O3N2] (blue), and Z[N2S2Hα] (green) given by equations 6.5, 6.6 and 6.7, respectively. "N pairs" denote the total number of pairs of H II and DIG-dominated regions involved in the analysis of each metallicity calibrator.

6.4 Results and Discussion

6.4.1 Biases in metallicity estimates of DIG-dominated regions

Fig 6.5 shows the distribution of the differential metallicities (ΔZ) of the pairs of H II-DIG regions, as determined from the three metallicity calibrators given in Section 6.3. Table 6.2 tabulates the mean and standard deviation of the distribution of ΔZ, along with the metallicity range of H II regions spanned by each calibrator. I find that the N2 parameter overestimates the metallicity of the DIG-dominated regions whereas the O3N2 parameter underestimates their metallicities by $\sim$0.06 dex on average when compared to the surrounding H II regions. The N2S2Hα appears to produce a negligible positive ($\sim$0.01 dex) mean offset with a standard deviation of 0.13 dex, though the offset may be as large as $\pm$ 0.8 dex for some pairs. Note here that the Z[N2S2Hα] calibration is linear up to 9.05, though the metallicity range of H II regions in this sample spans up to 9.27. Ignoring all values of Z[N2S2Hα] $>$ 9.05 for both DIG and H II regions, I obtain a negligible mean offset of $-$0.004 and a standard deviation of 0.11 dex comparable to that of the full sample.

The systematic overestimate of metallicity in DIG-dominated regions by the N2 parameter is most likely due to the expected enhancement of the N2 emission line ratio in those regions. Let us now compare these results to those of Zhang et al. (2017) who studied the impact of DIG on metallicity measurements by analysing the normalised metallicity with the normalised

Table 6.3 – Best-fit parameters of equation 6.8 (i.e. ΔZ = aO3 + bN2 + cS2 + d) for each line ratio and all possible combinations. The uncertainty on each best-fit parameter is the standard error. σ represents the standard deviation of ΔZ_{corr}.

C	ΔZ	a (O3)	b (N2)	c (S2)	d	σ
C1*	Z[O3N2]	-0.244±0.018			-0.029±0.005	0.073
C2	Z[O3N2]		-0.007±0.018		-0.062±0.008	0.091
C3	Z[O3N2]			0.182±0.052	-0.031±0.009	0.09
C4	Z[O3N2]	-0.245±0.018	-0.017±0.015		-0.034±0.006	0.073
C5	Z[O3N2]	-0.239±0.019		0.047±0.044	-0.022±0.008	0.073
C6	Z[O3N2]		-0.046±0.02	0.244±0.058	-0.036±0.01	0.089
C7	Z[N2]	-0.052±0.026			0.07±0.007	0.068
C8	Z[N2]		0.116±0.022		0.126±0.013	0.064
C9	Z[N2]			0.385±0.061	0.136±0.013	0.061
C10	Z[N2]	-0.034±0.024	0.112±0.022		0.129±0.013	0.063
C11	Z[N2]	0.032±0.027		0.427±0.07	0.139±0.013	0.061
C12*	Z[N2]		0.084±0.021	0.317±0.06	0.169±0.015	0.058
C13	Z[N2S2Ha]	0.036±0.032			-0.017±0.008	0.129
C14	Z[N2S2Ha]		0.157±0.024		0.037±0.01	0.121
C15	Z[N2S2Ha]			0.13±0.074	0.008±0.014	0.128
C16	Z[N2S2Ha]	0.046±0.03	0.159±0.024		0.032±0.011	0.121
C17	Z[N2S2Ha]	0.053±0.033		0.16±0.076	0.006±0.014	0.128
C18	Z[N2S2Ha]		0.175±0.027	-0.108±0.079	0.026±0.013	0.121
C19	Z[O3N2]	-0.236±0.019	-0.031±0.017	0.09±0.049	-0.025±0.008	0.073
C20	Z[N2]	0.032±0.026	0.084±0.021	0.359±0.069	0.172±0.015	0.058
C21	Z[N2S2Ha]	0.039±0.031	0.172±0.027	-0.082±0.082	0.024±0.013	0.121

Notes: * are the best of all calibrator corrections.

Hα surface brightness (ΔZ-$\Delta log\Sigma_{H\alpha}$) for three galaxy samples grouped according to their stellar masses. For Z[N2], they report a negative slope for ΔZ-$\Delta log\Sigma_{H\alpha}$ for all the galaxy sample, which indicates that DIG biases towards a higher metallicity in agreement with our results. Zhang et al. (2017) did not find a fixed correlation between the variation of Z[O3N2] and the fraction of ionised gas having DIG properties in individual galaxies. However, their ΔZ[O3N2]-$\Delta log\Sigma_{H\alpha}$ relation for the one-third most massive galaxies ($> 10^{10.08}$ $M_{\odot}$) in their sample shows a positive slope indicating that the DIG biases towards a lower metallicity. Given that my sample consists of mostly massive Sa and Sb galaxies (see Table 6.1), current results are in reasonable agreement with those of results Zhang et al. (2017). For Z[N2S2Hα], Zhang et al. (2017) found no slope for the ΔZ-$\Delta log\Sigma_{H\alpha}$ relation but a large dispersion, in agreement with the results of this work.

6.4.2 New calibrations

A scatter matrix plot of all ratios and ΔZ[O3N2] is shown in Fig 6.6. ΔZ[O3N2] shows a clear correlation with O3. Corresponding bottom panels of this scatter plot for ΔZ[N2] and ΔZ[N2S2Hα] are presented in Fig 6.7. No correlation between ΔZ[N2S2Hα] and emission line ratios is found (Fig 6.7 lower panel). I explore the relation of ΔZ obtained from different metallicity calibrators with respect to the emission line ratios of the DIG-dominated regions in

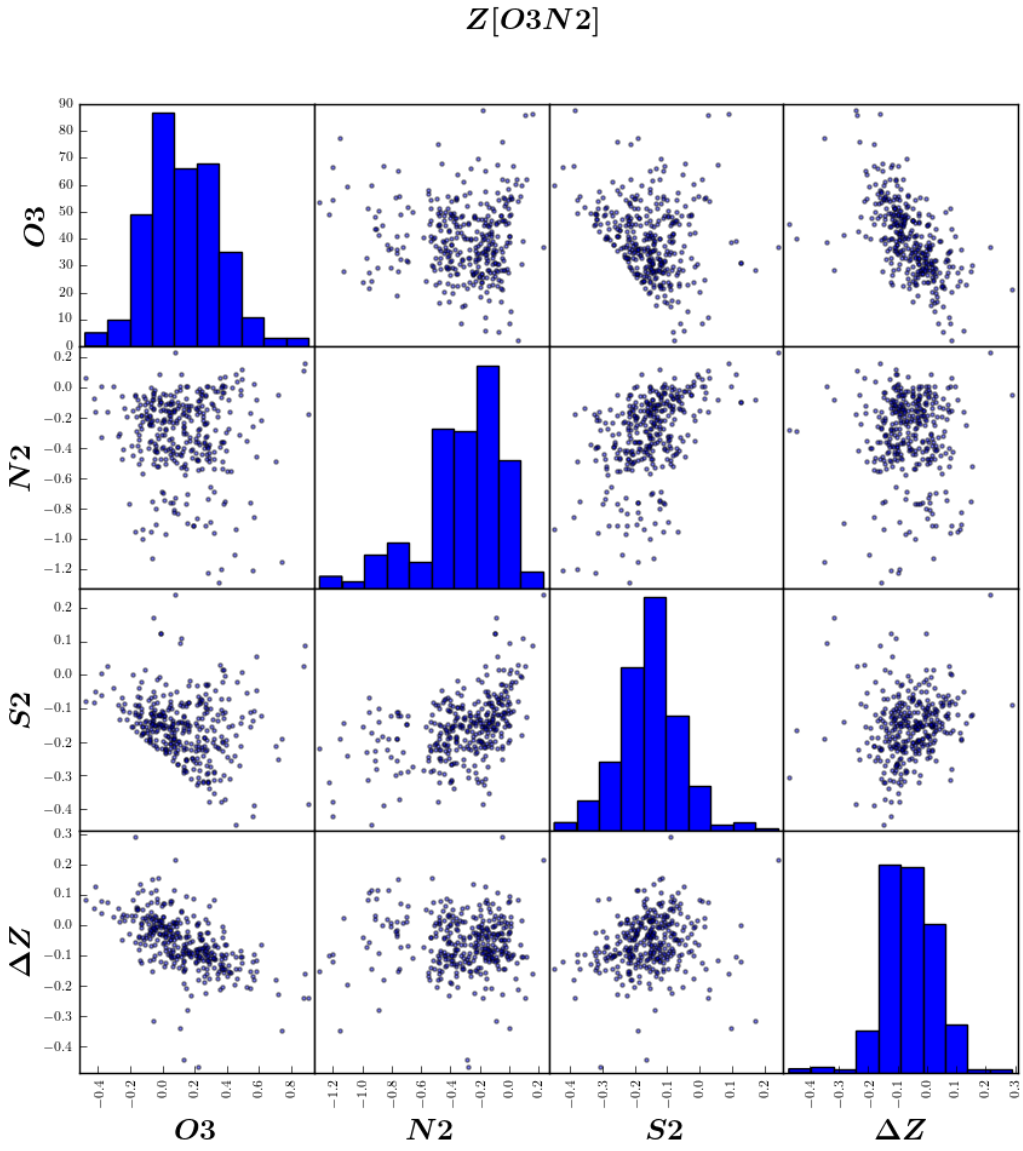

Figure 6.6 – Scatter Matrix plot for evaluating the dependence of ΔZ[O3N2] on the three line ratios, O3, N2 and S2.

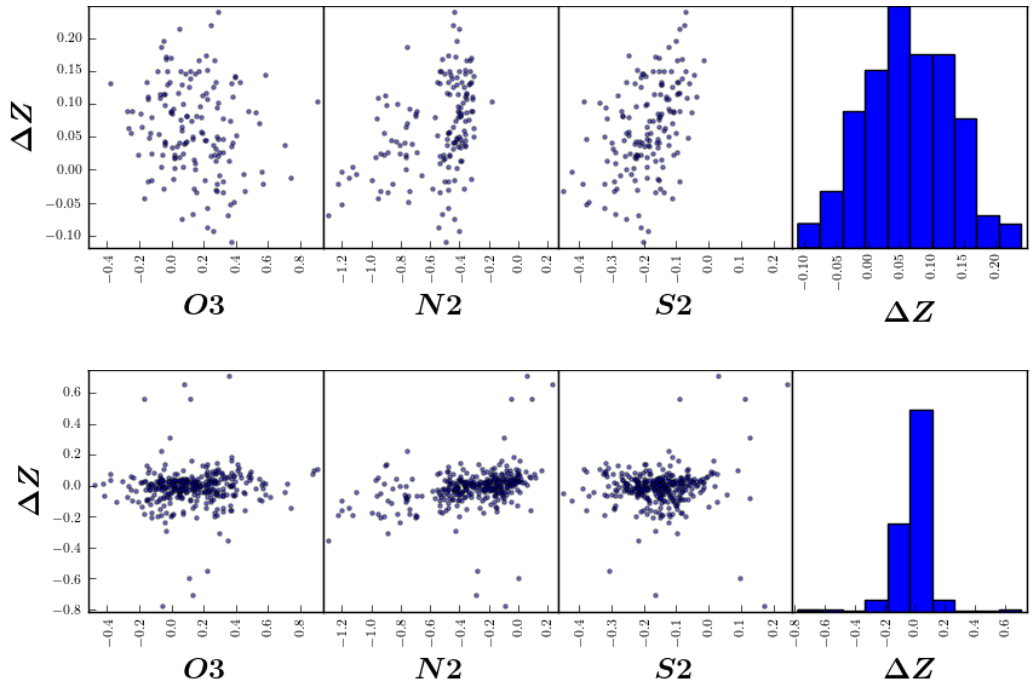

Figure 6.7 – Variation of differential metallicity (upper panel: ΔZ[N2] and lower panel: ΔZ[N2S2Ha]) with respect to the three line ratios, O3, N2 and S2.

order to mitigate the biases found above. ΔZ for each metallicity calibrator is fit as a multi-linear function of the emission line ratios O3, N2 and S2 of the form:

$$\Delta Z = aO3 + bN2 + cS2 + d. \tag{6.8}$$

Beside solving this equation for all ratios, separate solutions for all possible combinations of different line ratios were generated. The aim is to find the coefficients a, b, c and d which gives the best-fit ΔZ prediction for a DIG dominated region, so that the true metallicity is given by Z(DIG)$_{true}$ = Z(DIG)$_{orig}$ − ΔZ. Evidently, ΔZ after correction ΔZ$_{corr}$ = Z(DIG)$_{true}$ - Z(H II) should be zero, and the best calibrator should have the least scatter for the entire sample. Given that the calibration uncertainties of Z[O3N2] and Z[N2] are large, the error on ΔZ will always be larger than those on any of the emission line ratios. Hence, I solve for the coefficients (a, b, c and d) in the above equation using an ordinary least squares method, which minimises the scatter between the data points and the best-fit line. For Z[N2S2Hα], uncertainties on ΔZ are comparable to those on the emission line ratios. However, achieving the least scatter for Z[N2S2Hα] using a correction term based on O3, N2 and S2 is unlikely due to a lack of correlation between ΔZ[N2S2Hα] and the line ratios.

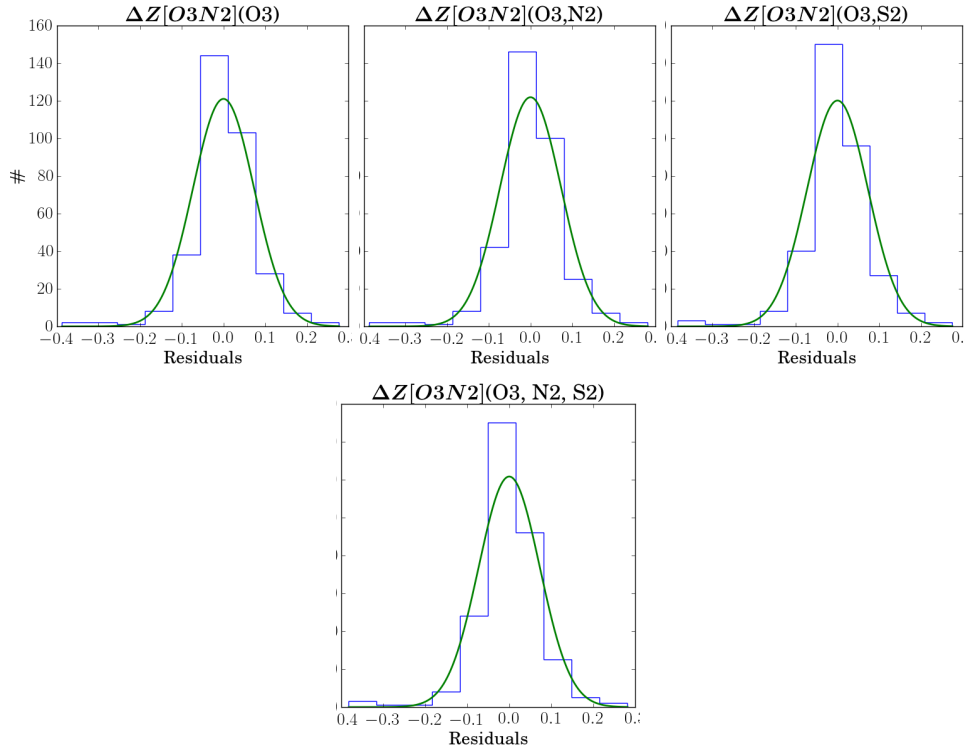

Figure 6.8 – Histograms of the residuals of four fits to ΔZ[O3N2]: C1 (upper-left panel), C4 (upper-middle) C5 (upper-right panel) and C19 (lower panel).

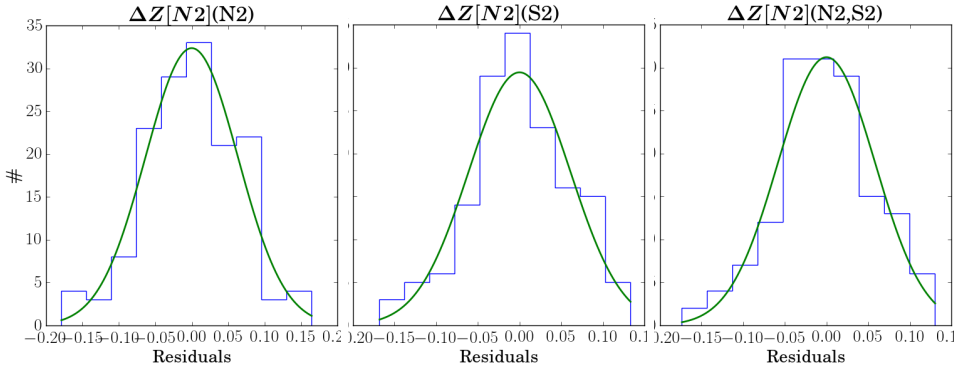

Figure 6.9 – Histograms of the residuals of three fits to ΔZ[N2]: C8 (left panel), C9 (middle panel) and C12 (right panel).

6.4.3 Which calibration is the most suitable?

Table 6.3 provides the best-fit parameters of equation 6.8 for each line ratio and all possible combinations. The uncertainty on each coefficient is the standard error obtained from the fit. σ denotes the standard deviation of ΔZ_{corr}. By design, the mean of ΔZ_{corr} is zero for each fit. Comparing with the initial scatter, the correction terms results in a decrease in scatter by at most $\sim$0.02 dex for Z[O3N2] and Z[N2] and no decrease in scatter for Z[N2S2Hα]. However, the scatter in ΔZ[N2] and ΔZ[O3N2] is lower by a factor of 2 compared to ΔZ[N2S2Hα]. Hence, I discard any correction related to ΔZ[N2S2Hα] and concentrate on ΔZ[N2] and ΔZ[O3N2].

Fig 6.8 shows a comparison of the residuals of fits of ΔZ[O3N2] obtained from C1, C4, C5 and C19 (Table 6.3), discarding other ΔZ[O3N2] fits which do not show any change in scatter. There is no significant change in the distribution of residuals from different fits, showing that no fit is better than the other. However, the coefficients of N2 and S2 in C4 and C5, respectively are close to zero within 1σ (standard error). Hence, I conclude that ΔZ[O3N2] obtained from O3 (C1 in Table 6.3) is the best of all ΔZ[O3N2] corrections since ΔZ[O3N2] including all emission line ratios (C19) will likely reduce the precision of coefficient estimates.

All ΔZ[N2] corrections involving O3 show that the value of the corresponding O3 coefficient (a) is close to zero within 2σ (standard error). Discarding these correction fits, Fig 6.9 compares the residuals of fits of ΔZ[N2] obtained from C8, C9 and C12 (Table 6.3). Since the distribution of all residuals is well reproduced by Gaussians, I compared the adjusted R-squared values for each fit, and found that ΔZ[N2] from N2 and S2 (C12) is the best of all ΔZ[N2] corrections.

The scatter in ΔZ[N2](C12) is lower than ΔZ[O3N2](C1) by $\sim$ 0.02 dex, which is not significant. So the two corrections can be used interchangeably. However, the initial condition of Z[N2] being valid for $-2.5 <$ N2 < -0.3 constrains the use of this calibrator. Comparing the metallicity of H II regions in our selected sample, Z[N2] varies between 8.17 and 8.86 while Z[O3N2] varies between 8.24 and 9.04. Since the strength of [O III] decreases, in contrast to the saturation of [N II] or [S II] (Sanders et al., 2017) with increasing metallicity, O3N2 is particularly useful in the high-metallicity regime (Pettini & Pagel, 2004). Though revised Z[O3N2] appears to be a useful calibrator, I will further explore the other two calibrators in the follow-up work. For example, it is possible that low scatter in Δ Z[N2] is simply due to lower number of data points; and the initial negligible offset in Δ Z[N2S2Hα] has resulted from the inclusion of both emission lines [N II] and [S II]. Further details of future work are presented in conclusion.

6.5 Summary & Future Work

In this Chapter, I utilise the integral field spectroscopic data of 24 nearby spiral galaxies from MUSE to study the biases in the metallicities of DIG-dominated regions when strong line calibrators Z[N2], Z[O3N2] (Pettini & Pagel, 2004) and Z[N2S2Hα] (Dopita et al., 2016) are used. I also prescribe suitable methods to correct the observed biases. The main findings are summarised below:

1. On the basis of S2 line ratio, I separate the H II regions from the surrounding DIG-dominated region. I find that the metallicity calibrator N2 overestimates the metallicity of the DIG dominated region compared to the surrounding H II region by 0.06 dex on average, with a standard deviation of 0.07 dex. The metallicity diagnostic O3N2 underestimates the metallicity of the DIG, with respect to the adjacent H II region by 0.06 dex on average, with a standard deviation of 0.09 dex.The N2S2Hα does not introduce any significant biases, though the spread in differential metallicity is the worst of all metallicity diagnostics, with a standard deviation of 0.13 dex.

2. I revisit all the three metallicity calibrators Z[O3N2], Z[N2] and Z[N2S2Hα] to correct for the observed offsets in terms of the emission line ratios O3, N2 and S2. I propose the following corrections for estimating metallicity of DIG dominated regions using Z[N2] and Z[O3N2]:

$$\Delta \mathrm{Z[N2]} = (0.084 \pm 0.021)\mathrm{N2} + (0.317 \pm 0.06)\mathrm{S2} + (0.169 \pm 0.015) \tag{6.9}$$

$$\Delta \mathrm{Z[O3N2]} = (-0.244 \pm 0.018)\mathrm{O3} + (-0.029 \pm 0.005) \tag{6.10}$$

   After correcting Z(DIG) with the above terms, the differential metallicity [i.e. Z(DIG)$_{true}$ - Z(H II)] shows a scatter which is about a factor of 2 lower than that observed in the original Z[N2S2Hα].

This Chapter is a work in progress, and I plan to carry this further as one of my future projects. Firstly, I aim to improve the proposed correction terms further by extending the range of their applicability. For example, two of three metallicity diagnostics used here (Z[N2] and Z[O3N2] from Pettini & Pagel (2004)) are only suitable for a given range of line ratios (see 6.3.2), which results in excluding a majority of DIG-dominated regions. Moreover, calibrations of the two diagnostics involved the use of only few data at high metallicities, which is the range span by spiral galaxies. To overcome the two problems, I will use calibrations from Curti et al. (2017) based on same line ratios (N2 and O3N2) which include high metallicity data points and are not restricted to certain line ratios. Secondly, I aim to replace the manual selection of H II -DIG pairs with a more robust automated selection method which allows us to select all

H II -DIG pairs, and check how it affects the correction terms in equations 6.9 and 6.10. The observed metallicity biases from the standard metallicity calibrators will affect all spatially-resolved studies which include DIG-dominated regions. Zhang et al. (2017) showed that the biases might be as large as the gradient found in spiral galaxies, which is typically ~ -0.1 dex R_e^{-1} (Sánchez et al., 2014; Ho et al., 2015). Further work is required to find out how the average offsets of $\sim$0.06 dex in the metallicities of DIG from Z[N2] and Z[O3N2] found in this Chapter will influence metallicity gradients. It is also possible that the offsets are larger when a wider range of DIG are included, which I will explore further using the calibrations of Curti et al. (2017). The correction terms from the follow-up of this work will hopefully allow to correct for such biases in future and, hence will enable consistent studies of metallicity gradients and their correlation with other spatially-resolved properties of galaxies, such as star-formation and stellar mass, which will further our understanding of galaxy formation and evolution.

6.6 Appendix

Figure 6.10 shows the distribution of differential metallicity on an initial random sample of 50 H II-DIG pairs. This sample shows that Z[N2] overestimates the metallicity of DIG regions, while Z[O3N2] underestimates the metallicity of DIG regions by $\sim$0.06 dex on average compared to the surrounding H II region counterpart. Z[N2S2Ha] does not introduce any such offset, though the scatter is large. All these observations agree with the entire sample analysed in Section 6.4. The number of H II-DIG pairs for Z[N2] is less than for the other two calibrators because Z[N2] calibrator is valid for a certain range of N2 ratio (see Section 6.3.2).

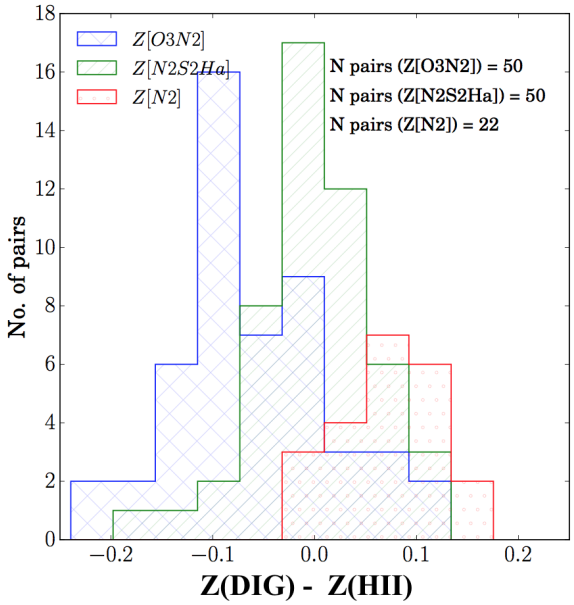

Figure 6.10 – Distribution of differential metallicities on an initial sample of 50 H II-DIG pairs. See caption of Figure 6.5 for details.

7

Local Schmidt-Kennicutt relation in nearby spiral galaxies

7.1 Introduction

The physics of star-formation is one of the most explored topics of contemporary astrophysics. Though both theorists and observers, have worked on different aspects of star-formation (see reviews by Shu, Adams & Lizano, 1987; Kennicutt, 1998a; Evans, 1999; Massey, 2003; Bromm & Larson, 2004; Mac Low & Klessen, 2004; Glover, 2005; Zinnecker & Yorke, 2007; McKee & Ostriker, 2007; Kennicutt & Evans, 2012; Krumholz, 2014), there are many missing links and we still lack a complete theory. This is mainly because the formation of stars is not a single process but involves a wide range of physical and chemical processes: self-gravity (Goodman et al., 2009); magnetic fields (Li et al., 2014); turbulence (Kritsuk, Ustyugov & Norman, 2011); formation and destruction of molecules; and ionisation from local and background sources (Ward-Thompson, Fraser & Rawlings, 2002). We are familiar with different conditions involved in the processing of the intergalactic and interstellar medium (ISM) which result in star-formation but we still have to understand the primary mechanism which drives and also dominates the formation of stars.

As described in Chapter 1, the Kennicutt-Schmidt Law is the widely accepted star-formation law, which is a power-law relation between the surface densities of SFR (Σ_{SFR}) and total gas

(Σ_{gas}), i.e. both atomic and molecular, where the value of power-law index N = 1.5 $\pm$ 0.15. However, this disk-averaged law might not follow from a fundamental and causal relationship. Hence, to understand the underlying physical processes and consequently the physics of star-formation, a spatially-resolved analysis of star-formation is required. Thanks to the technical advances resulting in an explosion of spatially-resolved multiwavelength data for nearby galaxies, the Schmidt relation has been studied at sub-galactic scales extensively. Various approaches have been adopted for such analyses, which can be grouped into two main categories: radial profiles (i.e. comparing azimuthally averaged values) of Σ_{SFR} and Σ_{gas} and point-by-point analysis (either pixel-by-pixel analysis or aperture photometry). Depending on the approach and data used, different observers have found different values of the power-law index (slope) in the Schmidt relation (see for example, Wong & Blitz, 2002; Boissier et al., 2003; Heyer et al., 2004; Komugi et al., 2005; Schuster et al., 2007; Kennicutt et al., 2007; Bigiel et al., 2008; Blanc et al., 2009; Liu et al., 2011; Rahman et al., 2011, 2012; Leroy et al., 2013; Momose et al., 2013; Shetty et al., 2014; Casasola et al., 2015; Roychowdhury et al., 2015; Azeez et al., 2016; Morokuma-Matsui & Muraoka, 2017).

A common observation in all these studies is that the molecular gas is more correlated with the SFR than the atomic gas. Wong & Blitz (2002) analysed radial profiles of seven CO-bright spiral galaxies and found that the Σ_{SFR} is directly proportional to the molecular gas density, while Boissier et al. (2003) used the same technique on a sample of 16 galaxies and found a range (0.6 – 1.3) of power-law slopes. Kennicutt et al. (2007) used aperture photometry of the star-forming regions in M51a and obtained a slope of 1.37$\pm$0.03 between the Σ_{SFR} and the molecular gas density at a spatial resolution of 520 pc. In contrast, Bigiel et al. (2008) found a linear molecular law (power-index = 1) from their pixel-by-pixel analysis on seven spiral galaxies. Bigiel et al. (2008) suggested that the slope found by Kennicutt et al. (2007) was steeper because of the subtraction of a local background in the SFR tracers, performed as a step in the aperture photometry. Liu et al. (2011) investigated this issue through a pixel-by-pixel analysis on two nearby spiral galaxies where they subtracted a diffuse/local background using the software $HIIphot$ (Thilker, Braun & Walterbos, 2000), and reproduced the results of Kennicutt et al. (2007) and Bigiel et al. (2008). See Liu et al. (2011) and Rahman et al. (2011) for a detailed discussion on the astrophysical significance of diffuse background in SFR tracers (Hα, far-ultraviolet (FUV), 24 μm hereafter in this Chapter) described as an emission unrelated to the current star-formation.

As discussed in various studies (Lonsdale Persson & Helou, 1987; Leroy et al., 2012; Crocker et al., 2013; Johnson et al., 2013; Boquien, Buat & Perret, 2014; Boquien et al., 2016), the observed stellar flux and the dust-emission in a star-forming region not only contains the contribution from the young stars and the related dust component, but also an underlying diffuse component of stellar/dust emission unassociated with current star-formation. For example, the FUV continuum contains a considerable amount of diffuse emission from evolving or al-

ready evolved stars (Tremonti et al., 2001) as FUV emission from an instantaneous-burst takes about 100 Myr to diminish by two orders of magnitude (Leitherer et al., 1999) compared to the 10 Myr for Hα emission. In addition stars migrate away from their birth-site (Chandar et al., 2005). Similarly, dust in the star-forming regions possibly contains ultra-small grains or large molecules which are unassociated with the current star-formation and are likely to substitute for the effects produced by polyaromatic hydrocarbon (PAH) e.g single-photon heating (Draine & Li, 2007). Thus, the mid-infrared emission may not only be produced by PAH heated by young stars but also dust grains/molecules with vibrational properties of PAH and small/large enough to be heated by older stellar population through single-photon heating. Emission at higher infrared wavelength contains contribution from diffuse dust "cirrus" and traces increasingly cooler components. Thus, diffuse component unrelated to the "current star-formation" are likely to be present in all SFR tracers.

In this Chapter, I also investigate the possibility of diffuse background in the atomic gas. Most of the spatially-resolved observational studies have found no correlation between the surface densities of SFR and atomic gas and hence concluded that molecular gas is the sole driver of star-formation. However, some studies (Boissier et al., 2003) also suggest that star-formation may be considered as a result of dynamical processes where total gas density is important, rather than as a purely sequential process where stars form from molecular gas which is initially formed from atomic gas. Moreover, some theoretical works also suggest that the stars can form as easily in atomic gas as in molecular gas (Glover & Clark, 2012; Krumholz, 2012). The most commonly used atomic gas tracer, the H I 21 cm emission line, traces cool H I, warm H I and diffuse molecular gas (Draine, 2011). Among these components of the ISM, I aim to identify that component of H I 21 cm emission which may contribute to star-formation, and study its effect on spatially-resolved Schmidt relation, in case that component is present in the atomic gas.

Hence, the goal of this Chapter is to extend the previous analyses (e.g. Kennicutt et al., 2007; Liu et al., 2011) by performing a spatially-resolved study on a larger sample of galaxies, and study the effect of inclusion and removal of a diffuse component not only in the SFR tracers but also in the atomic gas. The Chapter is organised as follows: Section 7.2 describes the galaxies in the sample and the multiwavelength data used in this work. Section 7.3 describes the essentials of aperture photometry, the SFR and gas density measurements and the novel method adopted to subtract diffuse background in SFR tracers and atomic gas. Section 7.4 presents the main results and Section 7.5 present a comparison of my results to those in the literature, a comparison with the global Kennicutt-Schmidt relation and possible implications of the results of this work.

Table 7.1 – Properties of sample galaxies

Name	Hubble[1] Type	Distance[2] (Mpc)	i[3,6] (deg)	P.A.[3,6] (deg)	$r_{25}^{3,6}$ (arcmin)	E(B–V)[4]	log(Hα+NII)[2] ($ergs^{-1}cm^{-2}$)	[NII]/Hα [2]
NGC 0628	Sc	7.3	7	20	4.89	0.0600 ± 0.0012	-10.84 ± 0.04	0.345 ± 0.046
NGC 3184	SABc	11.1	16	179	3.71	0.0144 ± 0.0001	-11.12 ± 0.05	0.523 ± 0.052
NGC 3351	SBb	9.33	41	192	3.60	0.0239 ± 0.0001	-11.42 ± 0.08	0.655 ± 0.027
NGC 3521	SABb	8.03	73	165	4.16	0.0496 ± 0.0014	-10.85 ± 0.04	0.558 ± 0.008
NGC 4736	SAab	5.20	41	296	3.88	0.0155 ± 0.0004	-10.72 ± 0.06	0.711 ± 0.006
NGC 5194	Sbc	8.2	20	172	3.88	0.0350 ± 0.0017	-10.45 ± 0.04	0.590 ± 0.006
NGC 5055	Sbc	7.8	59	102	5.93	0.0153 ± 0.0003	-10.80 ± 0.07	0.486±0.019
NGC 5457	Sbc	6.7	18	39	11.99	0.0074 ± 0.0001	-10.22[5]	0.54[5]
NGC 6946	SABc	6.8	33	243	5.74	0.2942 ± 0.0028	-10.42 ± 0.06	0.448 ± 0.087

[1]Values from NASA/IPAC Extragalactic Database (NED), [2]Values from Kennicutt et al. (2009), [3]Values from Bigiel et al. (2008), [4]Values from Schlafly & Finkbeiner (2011), [5]Values from Leroy et al. (2013) - no error was given in the paper, [6]Values from Schruba et al. (2011), Column 4 (i): inclination angle, Column 5 (P.A.): position angle, Other columns are self-explanatory.

7.2 Sample & Data

7.2.1 Sample galaxies

I study a sample of nine nearby spiral galaxies shown in Figure 7.1. The criteria for sample selection are as follows: (1) the centres of the galaxies are principally dominated by molecular gas as inferred from CO(2–1) images; (2) the maximum distance of the galaxies in the sample is 11.1 Mpc, beyond which the spatial scale is too compact for detailed spatial studies ; (3) the highest inclination angle of the galaxies studied here is 72.7°. The criteria (2) and (3) are adopted considering the aperture sizes described in Section 7.3.1.

Table 7.1 presents the galaxies in the sample along with their relevant properties: galaxy type, distance, inclination angle, position angle and r_{25}. This table also contains the values of Galactic E(B–V) (Schlafly & Finkbeiner, 2011), which are used to correct foreground Galactic extinction for optical (Hα) and FUV data; log(Hα + N II) and [N II]/Hα to calibrate the Hα images. Details related to the multiwavelength data and the respective instruments are given in Table 7.2. All data have been obtained in a reduced form from archival sources associated with ongoing large local galaxy surveys, which are mentioned in the following sections.

7.2.2 Hα Emission-line Images

Narrowband images centered at Hα and continuum R-band images are taken either with the 1.5 m telescope at Cerro Tololo Inter-American Observatory (CTIO) or the 2.1 m telescope at Kitt Peak National Observatory (KPNO). They are either part of the *Spitzer* Infrared Nearby Galaxies Survey (SINGS; Kennicutt et al., 2003) or of the "Key Insights on Nearby Galaxies: A Far-Infrared Survey with Herschel" (KINGFISH; Kennicutt et al., 2011).

To obtain an emission line only image of Hα for each galaxy, the corresponding R-band

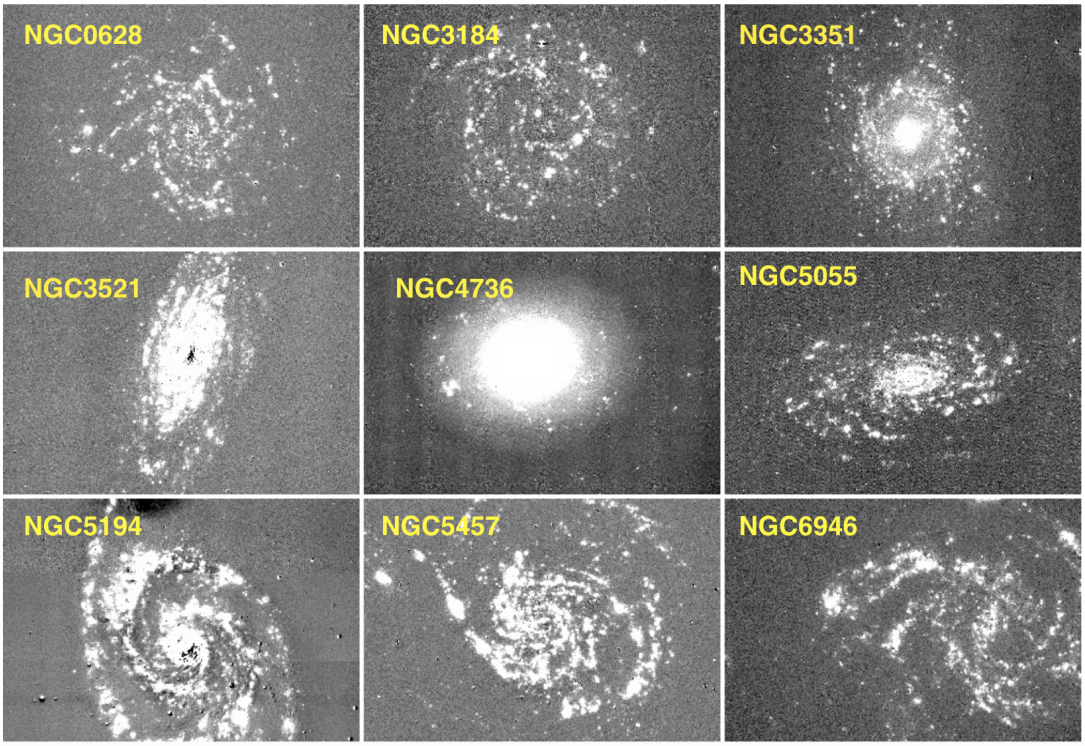

Figure 7.1 – Hα images of spiral galaxies in the sample. They are obtained either from SINGS survey or KINGFISH survey.

image is rescaled and subtracted from the narrow-band image. The Hα image is corrected for the foreground galactic extinction using $F(H\alpha)_{corr} = F(H\alpha)_{obs} \times 10^{0.4\times2.535\times E(B-V)}$. A constant ratio of [N II]/Hα for each galaxy is adopted to correct for the contamination from the neighbouring [N II] $\lambda\lambda$6548, 6584 in the narrowband Hα filter. The Hα image is finally calibrated using the total flux (Hα + N II). The flux calibration error is $\sim$ 5% and the point spread function (PSF) is typically $\sim$ 2 arcsec.

7.2.3 GALEX FUV Images

FUV images are taken from the Galaxy Explorer (GALEX) and form part of KINGFISH except NGC 5194 which is from the GALEX NGS Survey (Gil de Paz et al., 2007). Technical details are described in Morrissey et al. (2005). The FUV images are corrected for foreground galactic extinction using $FUV_{corr} = FUV_{obs} \times 10^{0.4\times8.02\times E(B-V)}$, and are calibrated assuming an AB magnitude system. The calibration uncertainty is $\sim$ 0.15 mag. The images obtained from KINGFISH were already corrected for obvious artefacts and the bright foreground galactic stars were entirely removed.

7.2.4 Spitzer MIPS 24 μm Images

The 24 μm infrared (IR) data are used to estimate and correct for the Hα and FUV radiation obscured by dust (details in Section 7.3.3). The 24 μm images are taken with the Multiband Imaging Photometer (MIPS) installed on the *Spitzer Space Telescope* and are obtained either from the KINGFISH or SINGS survey. The calibration error is 5%. For details on the observing strategy and data reduction procedures of the MIPS Instrument, see Kennicutt et al. (2003) and Gordon et al. (2005), respectively.

7.2.5 HERACLES CO (J=2–1) Images

CO (J= 2–1) images from "The HERA CO-Line Extragalactic Survey" (HERACLES) are used for estimating the molecular gas content of the galaxies in the sample. These maps are obtained using the IRAM 30 m telescope; details of observation and data reduction are given in Leroy et al. (2009). The angular resolution of these maps is 11arcsec (Bigiel et al., 2008) and the flux calibration error is 20% (Leroy et al., 2009). For all galaxies, I adopt a constant standard value of X(CO) = 2×10^{20} cm^{-2} (K km s^{-1})$^{-1}$ as established for the Milky Way (Dame, Hartmann & Thaddeus, 2001) and ratio CO(2-1)/CO(1-0) = 0.8 (Leroy et al., 2009), for converting the CO intensity maps to the mass maps of molecular hydrogen, noting that uncertainties in the X(CO) factor contribute to the overall calibration error.

7.2.6 VLA H I Images

The neutral atomic hydrogen gas content in the galaxies is estimated from the moment 0 maps (integrated H I map from "robust" weighting) obtained from "The H I Nearby Galaxy Survey" (THINGS; Walter et al., 2008). These maps are obtained by using the National Radio Astronomy Observatory (NRAO) Very Large Array (VLA). The typical beam size for robust weighted maps is $\sim$ 6 arcsec. The atomic mass maps are created by using the formulae given in Walter et al. (2008). The calibration error for the H I is 5%.

Note here that neither H I nor H_2 is corrected for the presence of helium and other metals. Equation (4) from Leroy et al. (2009) used for calculating H_2 surface density includes the multiplicative factor of 1.36 to account for helium and other elements in the galaxies, which is dependent on metallicity and other environmental factors. This factor is not included for comparison and consistency with other published works.

Table 7.2 – Details and properties of multiwavelength data

Data (1)	Instrument (2)	Central Wavelength (3)	PSF (4)	Surveys (5)
Hα	CTIO/KPNO	6563 Å	$\sim$1.9"	KINGFISH/SINGS
FUV	GALEX	1528 Å	$\sim$5.5"	KINGFISH/GALEX NGS
24 μm	Spitzer/MIPS	24 μm	$\sim$6"	KINGFISH/SINGS
H I	VLA	21 cm	$\sim$6"	THINGS
CO(2-1)	IRAM	1.3 mm	$\sim$11"	HERACLES

NOTES: Column 1: data name; Column 2: telescope, instrument, and filter; Column 3: filters' central wavelength; Column 4: FWHM of the PSF; Column 5: Associated surveys.

7.3 Methodology

7.3.1 Aperture photometry: apertures sizes and aperture correction

I employ aperture photometry for this spatially-resolved analysis. The galaxies in the sample lie at distances ranging from 3.13–11.10 Mpc, with inclination angles varying between 7–72.7°. In practice this drives us toward adopting a range of physical aperture sizes to accomodate the different angular resolution available. The SFR calibration combining observed Hα and 24 μm (see equations 7.4 and 7.6, which are also presented as footnote here[1]) is valid for regions larger than the H II complexes ($\sim$0.8–5.1 kpc) which produce the ionizing radiation (Calzetti et al., 2007). The proportionality coefficient in equation 7.4 varies by only $\sim$20% (within 1σ uncertainty) when derived for NGC 5194 (Kennicutt et al., 2007) on regions of physical diameter 520 pc. Hence for this study, a minimum physical diameter of $>$ 500 pc is adopted. However, this physical diameter can not be used for the galaxies with high inclination angles and large distances (NGC 3351, NGC 3521 and NGC 5055) as this physical size corresponds to radii of 1–2 pixels and results in undersampling for the aperture. To determine a viable maximum aperture size, I performed an experiment described in Appendix 7.7.1, and hence decided to use aperture sizes varying between $\sim$0.5–2.0 kpc depending on the distance and inclination angle of individual galaxy.

For flux extraction, images in all wavelengths in each galaxy are aligned and registered on the astrometric grid of the CO image which has the coarsest pixel size ($\sim$ 2 arcsec). This ensures that flux is extracted in all image apertures over the same region. Potential star-forming regions are selected by visual inspection of the Hα images. Fluxes are measured in the apertures placed over the potential star-forming regions in all images using the "phot" task available in IRAF.

[1]

$$L(H\alpha)_{corr} = L(H\alpha)_{obs} + 0.031L(24) \quad (7.1)$$

$$SFR(H\alpha)(M_{\odot}yr^{-1}) = 5.3 \times 10^{-42} L(H\alpha)_{corr}(ergs^{-1}) \quad (7.2)$$

Given that the star-forming regions in all galaxies are extended sources, a fixed-size circular aperture for a galaxy may or may not enclose entire H II regions. However, it was made sure that no two apertures overlapped in the analysis, so that apertures were independent of each other. Beside choosing bright star-forming knots, apertures were also placed on faint regions with diffuse Hα emission as the aim of this work is to find out the effect of diffuse background in Schmidt relation studies. However, a S/N cut of 3 was applied on the aperture-extracted flux while studying any relation. The same procedure is applied on images where the diffuse background has been subtracted using *Nebulosity Filter (Nebuliser)* described later in section 7.3.4. As a check, I estimate an overall clipped median value for the background in each image though note here that the $Nebuliser$ reduces the background in the corrected maps to negligible levels.

Since the H II regions in the sample galaxies are extended sources, or are composed of overlapping point sources, an aperture correction is required to obtain total fluxes. I use synthetic PSFs for 24 μm and FUV, and Gaussian PSFs of 2 arcsec, 6 arcsec and 11 arcsec for Hα, H I and CO, respectively[2], to create a curve-of-growth by calculating flux in successive apertures centred on the PSF and hence calculate aperture correction as a function of radius for each wavelength. Though a standard procedure is followed here to apply aperture correction, one should bear in mind that the aperture correction thus derived is mainly applicable to point sources and not the extended sources, and affects all such studies including the current one.

7.3.2 Uncertainty calculation

Three main sources of uncertainty (variance) are present in the derived fluxes: systematic offsets in estimates of the local background σ^2_{sys}; *rms* errors in the summed flux σ^2_{rms}; and the systematic uncertainty from physical calibration of the source images during data reduction σ^2_{cal}. The dominant pixel-level *rms* error σ_b is estimated by placing several apertures in the outer regions of the galaxies for each image and analysing the pixel-level flux variation. The main random error in each aperture pixel is then given by $\sqrt{n}\,\sigma_b$, where n is the number of pixels in the aperture. The systematic uncertainty due to large scale variations in the background is smaller than the random error because of the large number of effective pixels m used in tracking the background variation. All uncertainties are added in quadrature to calculate the final uncertainties in the fluxes in different wavebands following equation 7.3,

$$\sigma^2_{flux} = \sigma^2_{rms} + \sigma^2_{sys} + \sigma^2_{cal} \simeq n\sigma^2_b + n^2\sigma^2_b/m + \sigma^2_{cal} \tag{7.3}$$

These errors are then propagated to errors in Σ_{SFR} and gas surface densities (Σ_{H1}, Σ_{H_2} and Σ_{H1+H_2}).

[2]http://www.astro.princeton.edu/ ganiano/Kernels.html

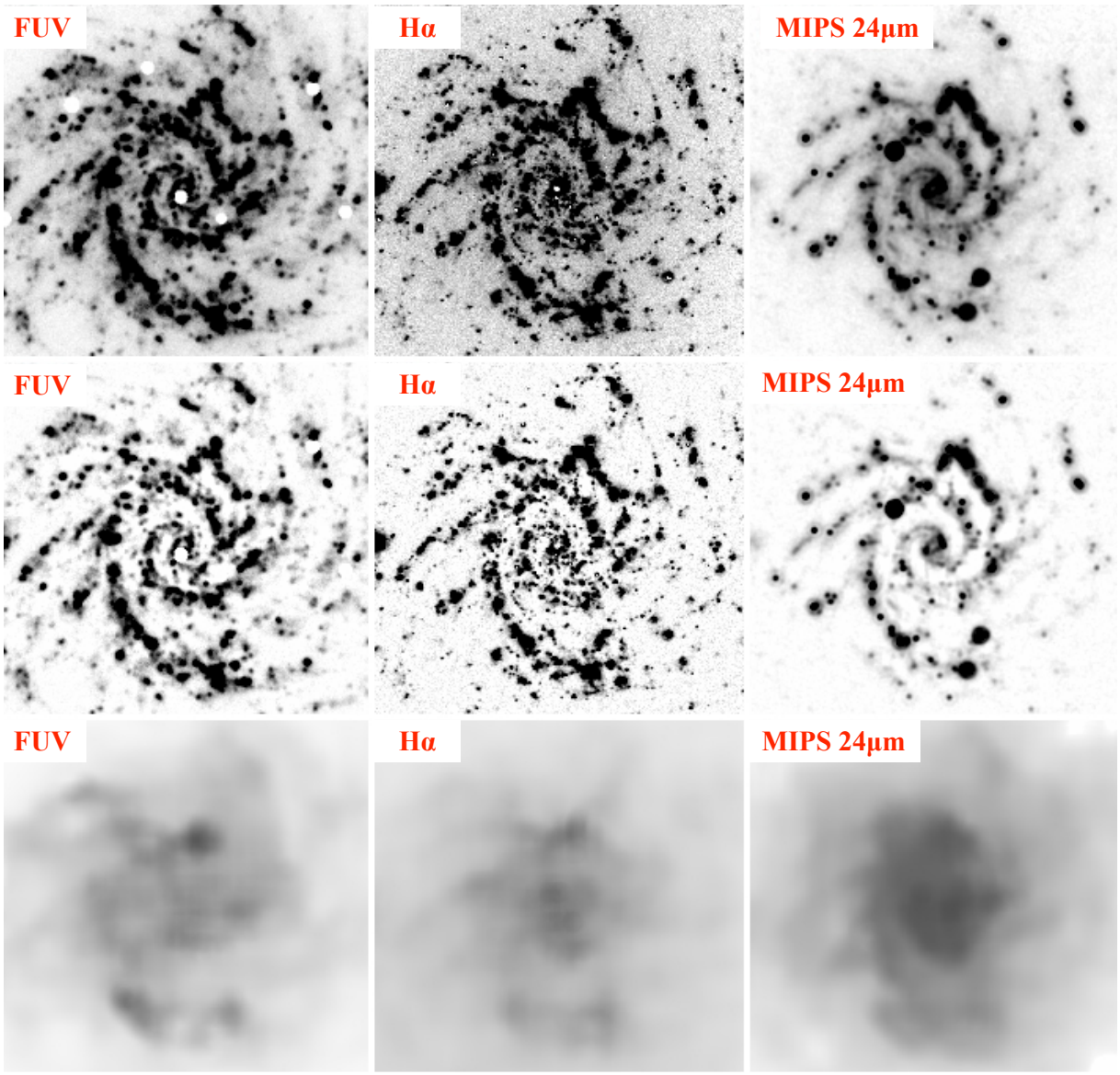

Figure 7.2 – Upper panel: Original images of the galaxy NGC 0628 before subtraction of the diffuse background, middle panel: images after subtraction of diffuse background, which show likely current star-forming regions, lower panel: images of the estimated diffuse background, showing its complex spatially-varying nature. The images in a particular wavelength have the same flux scale limits.

7.3.3 Conversion of luminosity into SFR

Before converting optical (Hα) or FUV luminosity to SFR, they need to be corrected for internal dust-attenuation. This makes use of a simple energy-balance argument (Gordon et al., 2000; Kennicutt et al., 2007; Calzetti et al., 2007) involving the use of IR luminosities (here MIPS 24 μm) to estimate the attenuation of Hα and FUV luminosities. This method allows both dust-obscured and dust-unobscured fluxes to be taken into consideration. The reason behind using MIPS 24 μm is the strong correlation between Hα and 24 μm emission in H II regions as found by Calzetti et al. (2005).

The attenuation-correction coefficients of Hα are taken from Calzetti et al. (2007) and FUV from Leroy et al. (2008)

$$L(H\alpha)_{corr} = L(H\alpha)_{obs} + 0.031L(24) \tag{7.4}$$

$$L(FUV)_{corr} = L(FUV)_{obs} + 6L(24) \tag{7.5}$$

where the subscripts obs and $corr$ denote the observed and attenuation-corrected luminosities, respectively.

The conversion of attenuation-corrected luminosity into SFR requires assumptions on the initial mass function (IMF) related to its form and sampling. Two forms of IMF are widely used - Salpeter IMF (Salpeter, 1955) and Kroupa IMF (Kroupa, 2001). Adopting the more realistic Kroupa IMF and applying the dust-attenuation correction as described above, the following formulae (Liu et al., 2011) are used to calculate the SFR:

$$SFR(H\alpha)(M_{\odot}yr^{-1}) = 5.3 \times 10^{-42} L(H\alpha)_{corr}(ergs^{-1}) \tag{7.6}$$

$$SFR(FUV)(M_{\odot}yr^{-1}) = 3.4 \times 10^{-44} L(FUV)_{corr}(ergs^{-1}) \tag{7.7}$$

If required, conversion from a Kroupa IMF to a Salpeter IMF can be easily done by multiplying the calibration constant by 1.6. The two SFR calibrations noted here are generally used in spatially-resolved star-formation studies, though Kennicutt et al. (2007) applied the global conversion (derived in Kennicutt (1998b)) for the spatially-resolved study of NGC 5194. As pointed out by Kennicutt et al. (2007), using the global conversion to calculate the SFR for an individual H II region, has limited physical meaning because stars are younger and the region under study go through an instantaneous event compared to any galactic evolutionary or dynamical timescale. The purpose of using the global conversion in Kennicutt et al. (2007) was to make a comparison of the slope and zero-point of the spatially-resolved Schmidt relation with the global Kennicutt-Schmidt relation (Kennicutt, 1998b). While comparing the spatially-resolved results with the global relation in Section 7.5.2, I take into account the change of IMF. As Calzetti et al. (2007) notes, the choice of IMF contributes more significantly (59%) to the $\sim$50% difference between the global SFR recipe (Kennicutt, 1998b) and the spatially-resolved calibration used here (equation 7.6), derived by Calzetti et al. (2007). Other factors such as assumptions on the stellar populations (100 Myr in Calzetti et al. (2007) versus infinite age in

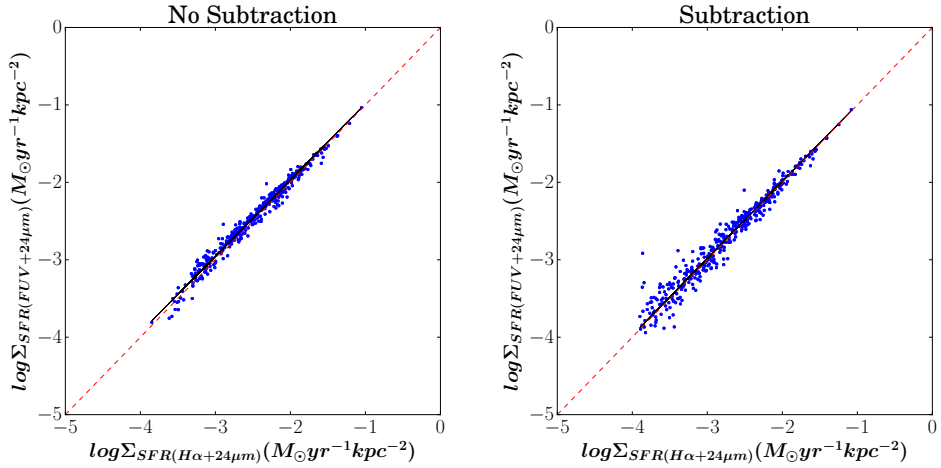

Figure 7.3 – Comparison of attenuation-corrected Σ_{SFR} calculated from Hα and FUV before (left panel) and after subtraction (right panel) of diffuse background in SFR tracers for NGC 0628. The solid black line shows the best-fit to the data and the dashed red line is the one-to-one relation between the two recipes of Σ_{SFR}. The scaling relation does not change significantly which shows that the subtraction of diffuse background is done consistently in all SFR tracers.

Kennicutt (1998b)) gives only a 6% decrease in the discrepancy given by the different IMFs. The contribution of the above-mentioned factors should be taken into account while making comparisons between different star-formation studies.

Since the eventual aim of this analysis is to study the spatially-resolved Schmidt relation, the SFRs are converted to SFR surface densities (Σ_{SFR}) by normalising the SFRs by the area of the aperture and dividing by an additional factor of $\sim$ 1/cos i to correct for the inclination of the galaxies given in Table 7.1.

7.3.4 Subtraction of Diffuse Background

Various methods have been devised and employed to subtract the underlying diffuse component of stellar and dust emission (Calzetti et al., 2005; Kennicutt et al., 2007; Prescott et al., 2007; Blanc et al., 2009; Liu et al., 2011). The methods based on statistics of the regions in galaxies seem to work better than a method with an astrophysical approach (Liu et al., 2011), in terms of the estimated fraction of diffuse component. This might be because the nature of diffuse background is not fully understood in all wavelengths. In this work, a novel statistical approach is adopted which makes use of the *Nebulosity Filter*[3] software to subtract the diffuse background. This nebulosity filtering algorithm uses an iteratively clipped non-linear filter to separate different spatial scales in an image, in this case the diffuse background from the more compact H II regions. The algorithm works by forming successive estimates of the diffuse background using

[3] http://casu.ast.cam.ac.uk/publications/nebulosity-filter

Table 7.3 – Percentage of diffuse background in each of the SFR tracers and atomic gas in the star-forming regions in the sample galaxies

Galaxy	Diffuse Background			
	Hα	FUV	24 μm	H I
NGC 0628	25	28	37	59
NGC 3184	25	20	32	53
NGC 3351	45	33	25	73
NGC 3521	22	45	17	80
NGC 4736	26	15	16	74
NGC 5055	26	38	43	71
NGC 5194	2	25	20	58
NGC 5457	5	14	23	37
NGC 6946	19	28	17	61

clipped two-dimensional median filters. The difference between the smoothed image and the original is used to define regions for masking for subsequent application of the median filter. The size of the median filter defines the scale. For the analysed galaxies, this scale was adopted as 50 arcsec or more, which is larger than the angular resolution of any dataset on which background subtraction is performed. After the final iteration, the diffuse background estimate is further smoothed using a conventional boxcar two-dimension linear filter 1/3 of the scale of the median filter. This final step ensures that the diffuse background image is free of the discrete steps that median filters are prone to delivering while maintaining the desired overall scale. The number of iterations is determined by the convergence of the number of rejected pixels. I tested the results of using this software on a modelled galaxy (see Appendix 7.7.2 for further details) to assess possible systematic biases.

Fig. 7.2 shows an example of this process for the two split components of the FUV (left panel), Hα (middle panel) and 24 μm (right panel) images of NGC 0628. As found in Fig. 3 of Liu et al. (2011), the background images in this analysis also show higher diffuse background in star-forming regions than elsewhere; however, the relative effect is stronger in fainter regions (Section 7.4.1). These images highlight the complex spatially-varying nature of the diffuse background and the variation of this component in the different wavelength regions. To investigate the efficacy of background subtraction, I check the scaling relations between attenuation-corrected Σ_{SFR} estimated from Hα and FUV before and after subtraction of the diffuse background (Fig. 7.3). The slope of the scaling relation changes by typically ± 0.01 after the subtraction of the diffuse background, which is an insignificant change and indicates that the background subtraction has been done consistently in all the SFR tracers. This test has been done for each galaxy in the sample. A slight increase in scatter (0.08 to 0.13) is observed because the background subtraction decreases the signal-to-noise (S/N) due to loss of signal

from the removal of the diffuse background, whereas the noise remains essentially the same. The scale-free scatter in the log-log domain when applied to the linear signal, decreases by more than a factor of three on average, hence decreasing the scatter in the linear difference in the derived SFRs. Adopting the same filtering scale length in the *Nebulosity Filter* as found for the SFR tracers, I also experimented with removing a diffuse background component from the H I map.

The aperture-corrected fluxes (section 7.3.1) from the original and subtracted images are used to calculate the fraction of diffuse background in the H II regions in Hα, FUV, MIPS 24 μm and H I. The combined results for each galaxy in the sample are tabulated in Table 7.3. Since our aim is to remove the diffuse background in order to trace $current$ star-formation, the fraction of diffuse background in the star-forming regions is a more relevant quantity than the diffuse background in the entire galaxy. Over the entire images of the galaxies, the mean diffuse fraction is $\sim$34% in Hα, $\sim$43% in FUV, $\sim$37% in 24μm, and $\sim$75% in atomic gas. The diffuse fraction in SFR tracers is in agreement with previous studies ($\sim$30–50% diffuse ionised gas (DIG) related to Hα (Ferguson et al., 1996); 30–40% related to 24μm in galactic centres and 20% in disks (Verley et al., 2009); at least a 40% diffuse UV (Liu et al., 2011)). The diffuse FUV fraction of 46% for NGC 5194 and 58% for NGC 3521 found in this work, are comparable to that (44% for NGC 5194 and 56% for NGC 3521) found by Liu et al. (2011). The diffuse fraction of 36% in the 24μm image of NGC 5194, is close to the range (15–34%) given in Kennicutt et al. (2007). The Hα diffuse fraction of $\sim$17% in the central region of NGC 5194, is within the range of values calculated by Blanc et al. (2009, 11%) and Liu et al. (2011, 32%). Note here that the diffuse fraction of Hα is more difficult to estimate accurately because of the necessity of scaling and subtracting the appropriate R-band continuum image from the Hα image. In all cases, the fraction of diffuse background in the SFR tracers is significantly less than that in the atomic gas.

7.4 Results

7.4.1 Radial profiles

The spatial variation of diffuse background in SFR tracers in individual galaxies is studied through their radial profiles, which are created by averaging over the pixels of the Σ_{SFR} maps in elliptical annuli of constant width 12 arcsec centred on the galaxies. Σ_{SFR} maps are created by combining the optical/FUV and IR using formulae 7.6 & 7.7 and normalised by the de-projected area of each pixel. Fig.7.4 presents radial profiles of Σ_{SFR} of the diffuse-background-subtracted data and Σ_{SFR} of diffuse-background, showing the relative contribution of the two components (potential currently star-forming regions and diffuse background) in the star-forming galaxies. The effect of the diffuse background in the faint outer star-forming regions is more significant

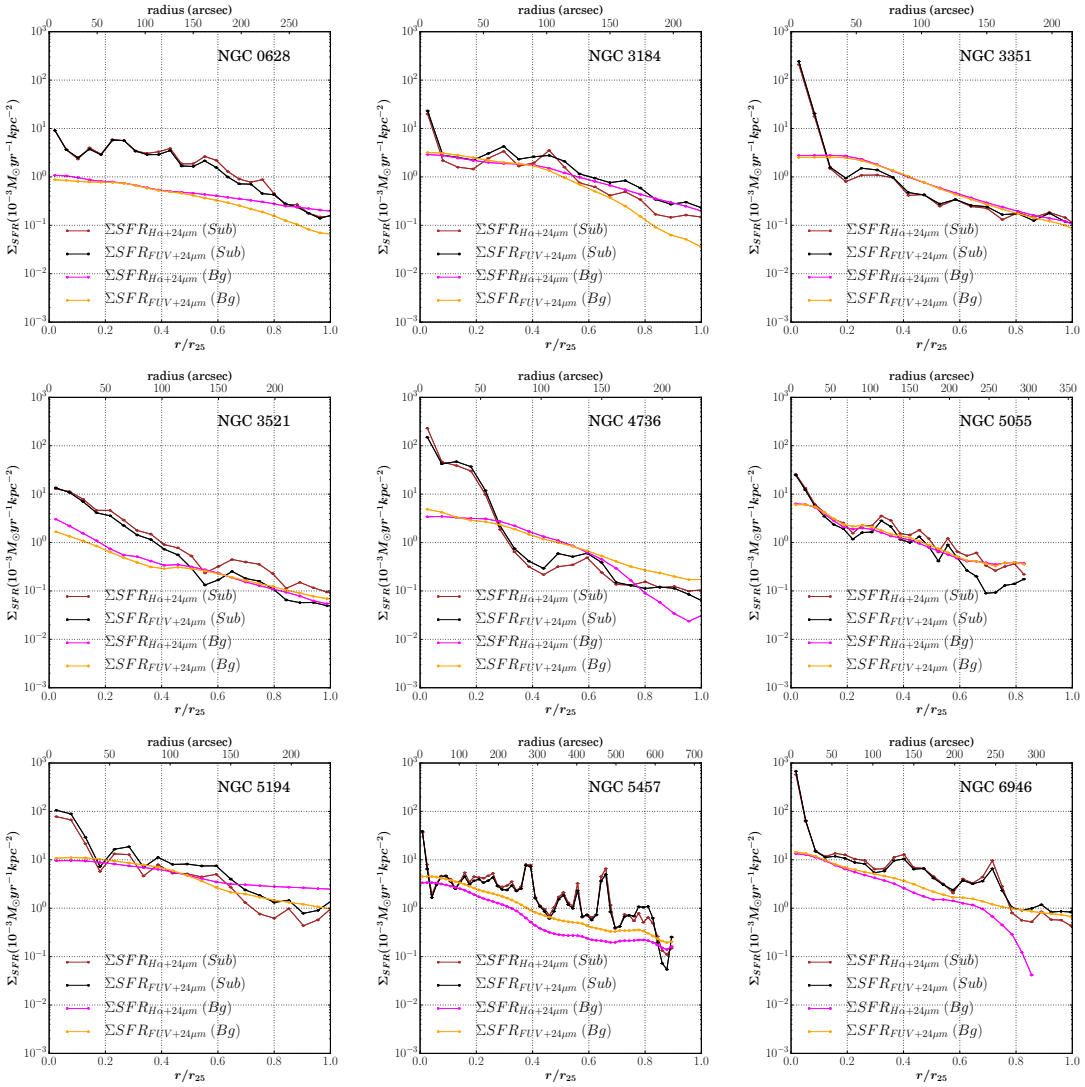

Figure 7.4 – Radial profiles of Σ_{SFR} for all nine galaxies in the sample after removal of the diffuse background. The x-axis presents the galactocentric radius normalised by r_{25} (bottom) and in arcsecs (top). The y-axis presents Σ_{SFR} in units of 10^{-3} $M_{\odot}$ yr^{-1} kpc^{-2} (the scaling is performed for comparison with radial plots from original unsubtracted data in Fig. 7.13). The brown and black curves denote $\Sigma_{SFR}(H\alpha+24\mu m)$ and $\Sigma_{SFR}(FUV+24\mu m)$, respectively, obtained from the data where diffuse background is subtracted from the SFR tracers. The magenta and orange curves denote $\Sigma_{SFR}(H\alpha+24\mu m)$ and $\Sigma_{SFR}(FUV+24\mu m)$, respectively, obtained from the diffuse background maps of the SFR tracers.

than in the bright central star-forming region. For comparison, radial profiles for the original unsubtracted SFR and gas data presented in Appendix 7.7.3. This comparison shows that Σ_{SFR} even after subtraction of the diffuse background, follows a similar pattern to the molecular gas profile, highlighting the importance of molecular gas in star-formation in the central regions of galaxies.

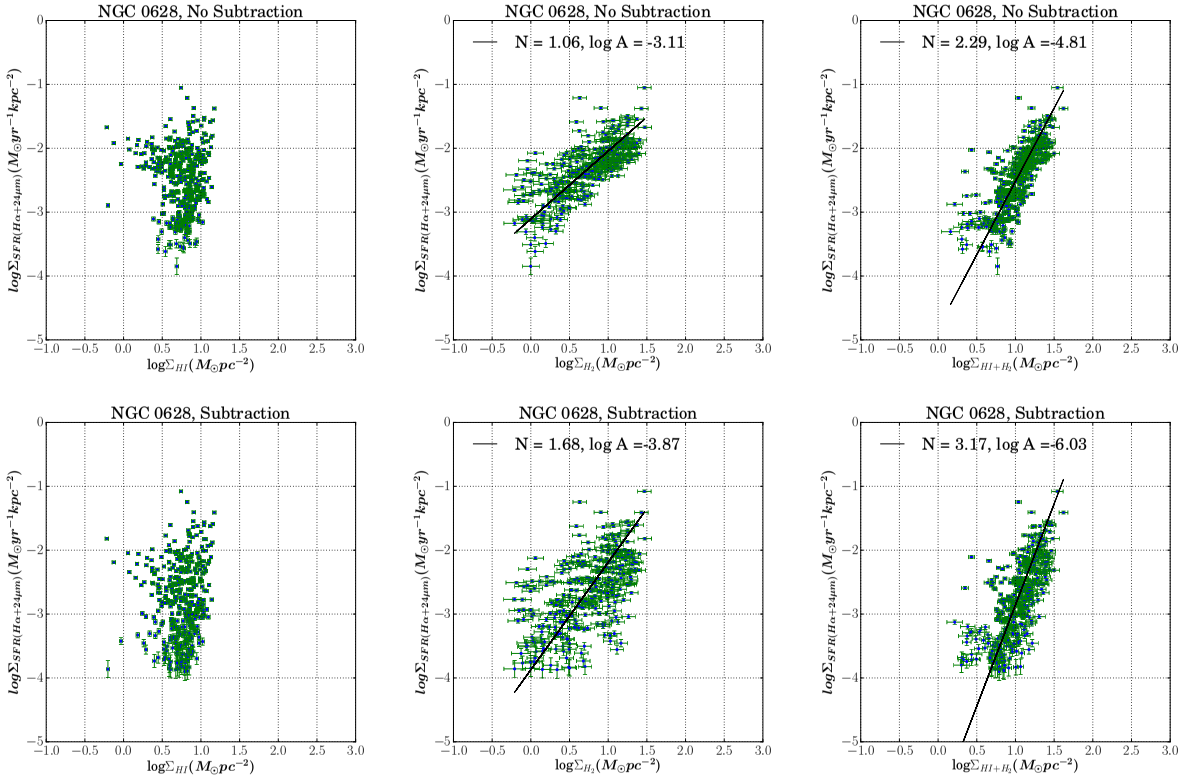

Figure 7.5 – Effect of subtraction of diffuse background in SFR tracers on spatially-resolved (∼560 pc) Schmidt relations in NGC 0628. Upper panel: analysis on the images with diffuse background (no subtraction), Lower panel: analysis on the images where diffuse background is subtracted. Left panel: Σ_{SFR} versus $\Sigma_{H\textsc{i}}$, middle panel: Σ_{SFR} versus Σ_{H_2}, right panel: Σ_{SFR} versus $\Sigma_{H\textsc{i}+H_2}$. The error bars include the random error and systematic error on the flux measurements. The solid black line in each plot denotes the best-fit line to the data where equal weight is given to each data point on both axes. N and A denote the power-law index and the star-formation efficiency. The slope of the $\Sigma_{SFR} - vs - \Sigma_{H_2}$ and $\Sigma_{SFR} - vs - \Sigma_{H\textsc{i}+H_2}$ increases after subtraction of diffuse background. Note the saturation of H I at ∼10 $M_{\odot}pc^{-2}$. Here, I assumed a Kroupa IMF and adopted a constant X(CO) factor = 2.0×10^{20} cm^{-2} (K km s^{-1})$^{-1}$.

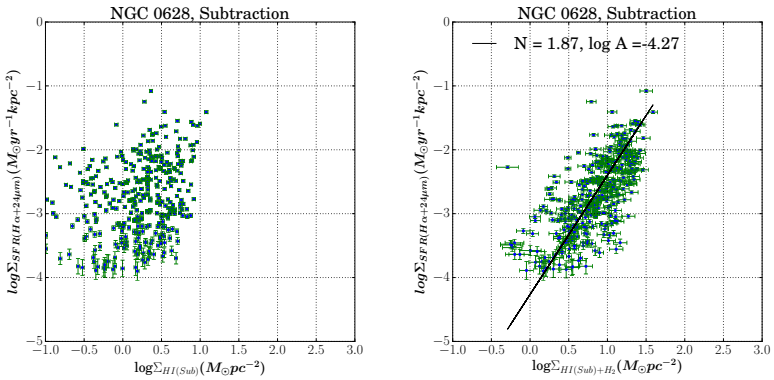

Figure 7.6 – Effect of subtraction of diffuse background in atomic gas and SFR tracers on spatially-resolved Schmidt relations in NGC 0628. Left panel: Σ_{SFR} versus Σ_{H1}, Right panel: Σ_{SFR} versus Σ_{H1+H_2}. See caption of Fig. 7.5 for details on legends.

7.4.2 Effect of subtraction of diffuse background in spatially-resolved Schmidt relations

I fit Σ_{SFR} versus Σ_{gas} in logarithmic space: $log(\Sigma_{SFR}) = Nlog(\Sigma_{gas}) + logA$, using the orthogonal distance regression (ODR) algorithm (Boggs et al., 1992), where maximum likelihood estimation of parameters is performed assuming that the distribution of errors on both axes is Gaussian. A S/N-cut of 3 was performed on all fits. In what follows, I make use of unweighted fits for analysing the Schmidt relation variation. Using unweighted fits is standard practice in Schmidt relation studies (see for example Bigiel et al., 2008; Liu et al., 2011). Systematic uncertainties as large as 30-50% are present on both axes related to SFR calibration and CO-to-H_2 conversion (Leroy et al., 2013), which explains the adoption of unweighted fits giving equal weight to each point on both axes. Problems with fitting power-laws in star-formation studies is a well-known issue (Blanc et al., 2009; Leroy et al., 2013; Casasola et al., 2015). In Appendix 7.7.4, I revisit this problem by comparing different fits including unweighted fits and maximum likelihood fits weighted by uncertainties calculated in section 7.3.2. Including systematic calibrations errors of 20% on both axes is necessary to yield data models with reduced χ^2 values of order unity. With this additional calibration error the difference between weighted fit and unweighted fit parameters lies witin the measurement error.

To study the effect of inclusion and removal of diffuse background, I explored the spatially-resolved Schmidt relation on the original and diffuse-background-subtracted data for each individual galaxy. Fig. 7.5 and Fig. 7.6 show this analysis for NGC 0628. The study on rest of the galaxies are shown in Appendix 7.7.5. I have performed the entire analysis using both SFR(Hα+24μm) and SFR(FUV+24μm), though for space considerations only the Schmidt relations where SFR is determined using Hα are shown. The use of Hα is justified by its ability to trace the current SFR due to its short age sensitivity ($\sim$ 5 Myr), which is thus more relevant for

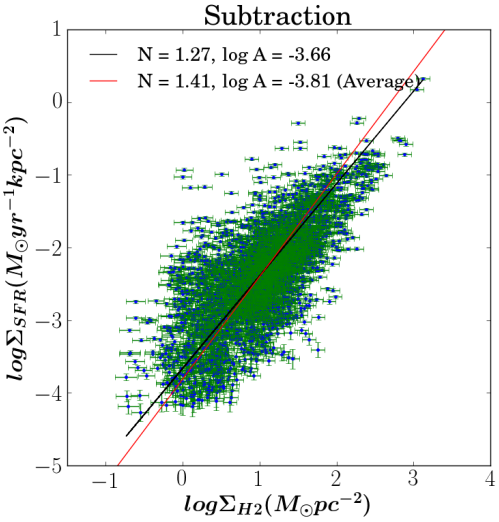

Figure 7.7 – Spatially-resolved molecular gas Schmidt relation (Σ_{SFR} vs Σ_{H_2}) for all sample galaxies, where the diffuse background has been subtracted from the SFR tracers. The red line is the fit obtained by averaging N (power-law indices) and log A (star-formation efficiencies) from individual galaxies (Table 7.4). The solid black line shows the best-fit to the spatially-resolved data for all galaxies. A Kroupa IMF and a constant X(CO) factor = 2.0×10^{20} cm^{-2} (K km s^{-1})$^{-1}$ have been assumed.

the present analysis. However, I also give the slope of the Schmidt relation obtained by using FUV as the SFR tracer, in Section 7.4.2.1 for a comparison with another relevant study. Table 7.4 presents the best fit parameters (N, log A) for the original and subtracted data individually for each galaxy.

Table 7.4 – Summary of best-fit parameters of Schmidt relation for each galaxy in the sample

Galaxy	No subtraction				Subtraction (SFR only)				Subtraction (SFR & H I)	
	H_2		H I+H_2		H_2		H I+H_2		H I+H_2	
	log A	N	log A	N	log A	N	log A	N	log A	N
NGC 0628	-3.11	1.06	-4.49	2.08	-3.87	1.68	-5.62	2.91	-4.36	1.96
NGC 3184	-3.18	0.85	-3.99	1.36	-3.93	1.32	-4.99	1.97	-4.33	1.56
NGC 3351	-3.36	1.29	-4.12	1.94	-4.13	1.80	-5.15	2.66	-4.39	2.03
NGC 3521	-2.89	0.84	-5.16	2.48	-3.22	1.10	-6.02	3.1	-3.9	1.66
NGC 4736	-2.99	0.99	-3.37	1.16	-4.13	1.70	-4.89	2.07	-4.26	1.75
NGC 5055	-3.10	0.85	-3.81	1.27	-3.90	1.25	-4.85	1.81	-4.15	1.40
NGC 5194	-3.18	0.97	-3.70	1.21	-4.32	1.52	-5.17	1.92	-4.63	1.66
NGC 5457	-2.64	0.66	-3.98	1.63	-3.24	1.16	-4.79	2.21	-4.03	1.70
NGC 6946	-2.95	0.86	-3.62	1.21	-3.55	1.15	-4.46	1.61	-3.77	1.28

7.4.2.1 Molecular gas and star-formation

I find that the scaling relation between Σ_{SFR} and Σ_{H_2} is approximately linear where no subtraction of diffuse background is done whereas the relation is super-linear when diffuse background is subtracted from the SFR tracers. Considering the individual galaxies, NGC 5457 is worth mentioning. For this galaxy, the slope of the molecular gas Schmidt relation before subtraction of the diffuse background is very low at 0.66 (Fig. 7.21, top-middle panel), which falls in the sub-linear regime (Shetty, Kelly & Bigiel, 2013) and has been explained by bright diffuse CO emission (Shetty, Clark & Klessen, 2014; Shetty et al., 2014). However, after subtraction of the diffuse background from the SFR tracers the Schmidt relation slope lies within the range found for the rest of the sample.

Taking the average of slopes found for each of the galaxies in the sample (Table 7.4), the slope is 0.93 $\pm$ 0.06 before subtraction and 1.41 $\pm$ 0.09[4] after subtraction of diffuse background. Note that Σ_{SFR} is estimated using Hα and 24 μm (equation 7.6) in the above analysis. If instead the combination of FUV and 24 μm (equation 7.7) are used to estimate Σ_{SFR}, the slope is 0.91 $\pm$ 0.07 before subtraction and 1.37 $\pm$ 0.11 after subtraction of diffuse background.

Fig. 7.7 shows the spatially-resolved Schmidt relation between $\Sigma_{SFR(H\alpha+24\mu m)}$ and Σ_{H_2} for all galaxies in the sample on a single plot. The red line denotes the fit obtained above by averaging the slopes and intercepts from individual galaxies (Table 7.4) which gives equal weight to each galaxy. This method was adopted for a comparison with the pixel-by-pixel analysis of Bigiel et al. (2008). Each galaxy in principle should be weighted by the number of star-forming regions used in each galaxy. This can also be achieved by deriving parameters directly from the best-fit line to the spatially-resolved data of all galaxies (solid black line in Fig. 7.7). The best-fit slope is now 1.27 $\pm$ 0.1 (cf. 1.41) with a large *rms* scatter (0.34 dex). The formal fitting error in the slope is however small due to the large number of points (n$\sim$3000) used in the fit. Note here that owing to the large systematic uncertainties on the determination of quantities on each axes, the formal fitting error can not reflect the true error on the estimated best-fit parameters. Hence, the uncertainties are estimated from the dispersion in the best-fit parameters (N and log A) obtained for each galaxy.

7.4.2.2 H I Saturation in all galaxies

I do not find any correlation between Σ_{SFR} and $\Sigma_{H\,I}$ before or after subtraction of the diffuse background in the SFR tracers. Prior to subtraction of the diffuse H I background, saturation of H I is observed around $\sim 10^{1.5}$ M$_\odot$ pc^{-2} (leftmost panels in Figs. 7.5 and 7.15–7.22). After subtraction, the saturation of $\Sigma_{H\,I}$ is still observed but at a lower value of $\sim$10 M$_\odot$ pc^{-2} (Fig 7.6, left panel and Fig. 7.23).

[4]error = standard deviation/$\sqrt{N-1}$ where N is the total number of galaxies.

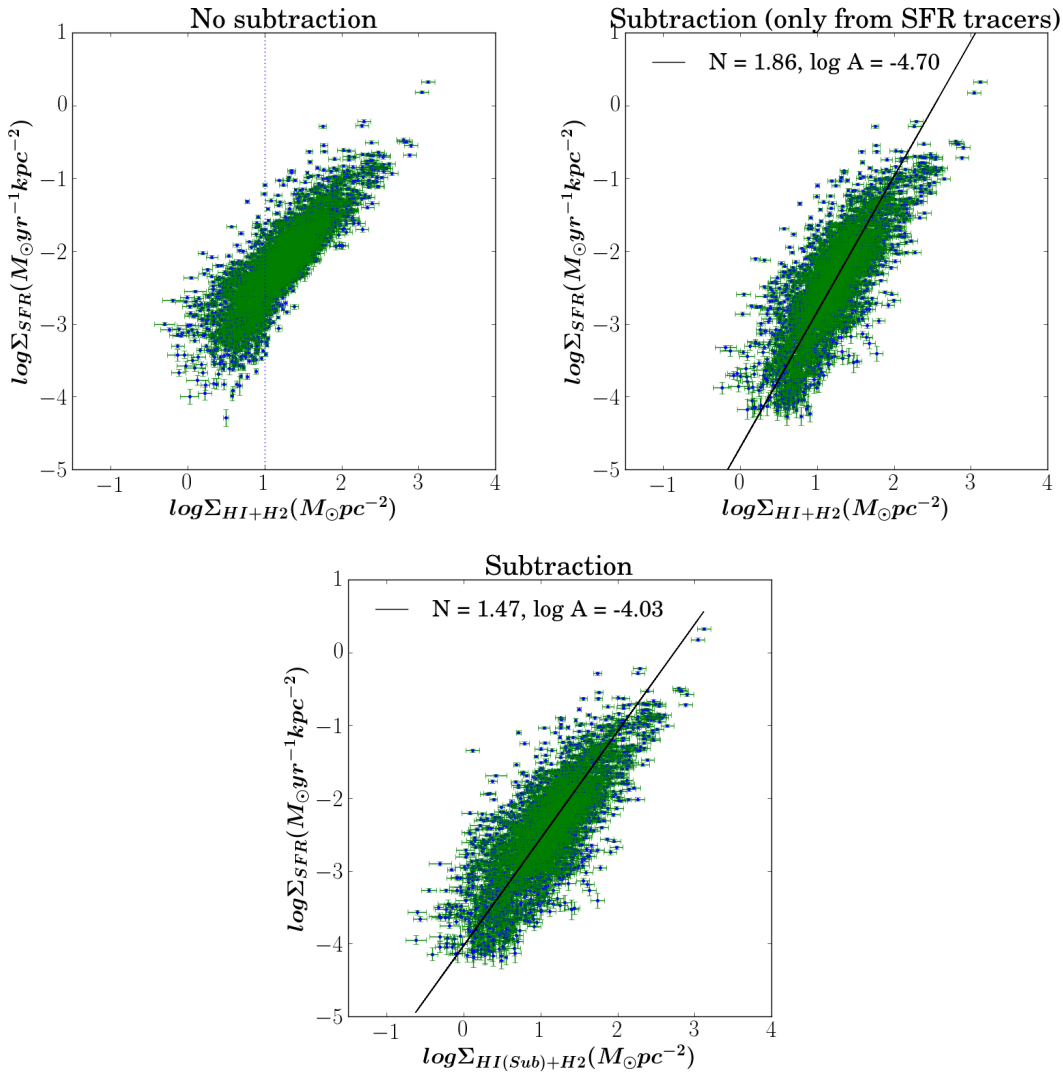

Figure 7.8 – Spatially-resolved total gas Schmidt relation (Σ_{SFR} and Σ_{H1+H_2}). In each panel, blue dots with green error bars are the spatially-resolved data. Upper left panel: No subtraction of diffuse background is done. Upper right panel: The diffuse background is subtracted from the SFR tracers. Lower panel: The diffuse background is subtracted from the SFR tracers as well as from the atomic gas. The solid black line shows the best-fit to the spatially-resolved data for all galaxies, using a Kroupa IMF and a constant X(CO) factor = 2.0×10^{20} cm^{-2} (K km s^{-1})$^{-1}$.

7.4.2.3 Total gas and star-formation

The relation between Σ_{SFR} and Σ_{H1+H_2} is always super-linear irrespective of the background subtraction in SFR tracers (rightmost panels in Figs. 7.5, 7.15–7.22). When diffuse background is removed from the SFR tracers , the slope steepens and varies from ∼1.5–3 depending on the relative quantity of Σ_{H1} and Σ_{H_2} (bottom-right panels in Figs. 7.5, 7.15–7.22). In galaxies like NGC 3184 (Fig. 7.15) & NGC 6946 (Fig. 7.22), molecular gas surface density dominates extending to 2 orders of magnitude higher than the atomic gas whose surface density is concentrated around 10 $M_{\odot}pc^{-2}$. This dominance of molecular gas leads to a flatter slope compared to a galaxy like NGC 0628 (Fig 7.5) where neither of the components dominates.

When diffuse background is removed from SFR tracers as well as atomic gas data, the slope of Σ_{SFR} and Σ_{H1+H_2} varies from ∼1.3–2.0 depending on the galaxy (Figs. 7.6, right panel and 7.24). The range of slope is significantly lower than the case with no background subtraction (∼1.16–2.5) or the case where the background is subtracted only from SFR tracers (∼1.6–3).

Fig. 7.8 presents the spatially-resolved total gas Schmidt relation for all galaxies in the sample. Upper-left panel shows the original data where diffuse background is not subtracted, a bimodal relation is observed. Upper-right panel shows the Schmidt relation where diffuse background is subtracted from SFR tracers only, and the slope is super-linear. Lower panel shows data where diffuse background is subtracted from SFR tracers as well as atomic gas data. Here, the best-fit line (solid black) to the spatially-resolved data (blue dots with green error bars) for all galaxies results in a slope of $\sim 1.47 \pm 0.08$ with a scatter of 0.27. The reported error on the slope is the dispersion in slopes obtained for each galaxy in the sample. Thus comparing these panels, I find that the removal of the diffuse background from the SFR tracers and the atomic gas results in a continuous relation which might indicate the increased importance of atomic gas in the faint star-forming regions.

7.5 Discussion

7.5.1 Comparison with Literature

The current work is a spatially-resolved star-formation study where diffuse background has been taken into account in both the SFR tracers as well as the atomic gas while studying the Schmidt relations. Earlier spatially-resolved star-formation studies have either been through radial-profile analysis (Wong & Blitz, 2002) or through point-by-point analysis (e.g. Bigiel et al., 2008; Kennicutt et al., 2007; Liu et al., 2011), where either diffuse background is not considered at all (e.g. Bigiel et al., 2008; Wong & Blitz, 2002) or it is accounted for in the SFR tracers (e.g. Kennicutt et al., 2007; Liu et al., 2011; Momose et al., 2013; Morokuma-Matsui & Muraoka, 2017) or in the molecular gas (Rahman et al., 2011) but not in the atomic gas.

H I saturation is a common result found in all works. From the aperture photometry analysis, I find the mean saturation value to be 16 $\pm$ 8 $M_{\odot}$ pc^{-2} when diffuse background is not subtracted, which is consistent with the value of $\sim$ 25 $M_{\odot}$ pc^{-2} derived by aperture photometry analysis of Kennicutt et al. (2007) on NGC 5194. The radial profile analysis in this work (Figure 7.13) also shows a saturation below 10 $M_{\odot}$ pc^{-2} in agreement with $\sim$ 9–10 $M_{\odot}$ pc^{-2} derived by earlier radial profile analyses (Wong & Blitz, 2002; Bigiel et al., 2008). The difference in results can be attributed to the different approaches adopted in these studies. Unlike aperture photometry, pixel-by-pixel analysis or radial profile analysis does not take into account the flux lost in the adjacent pixels, which might be the cause of the lower level of saturation for H I in these analyses.

Comparison of the power-law index of the molecular gas Schmidt relation found by pixel-pixel analysis (Bigiel et al., 2008) and aperture photometry (upper panels in Figs. 7.5 and 7.15–7.22) for individual galaxies in the sample shows a large variation in the case where diffuse background is not subtracted. However, results from the two works agree with each other statistically as found in Section 7.4.2.1. The slope of the molecular gas Schmidt relation reported by Bigiel et al. (2008) (0.96 $\pm$ 0.07) agrees within error with the slope found here obtained by averaging the slopes of individual galaxies (i.e. 0.93 $\pm$ 0.06 using Hα and 0.91 $\pm$ 0.07 derived using FUV). Hence, both of these works show that before background subtraction, Σ_{SFR} scales linearly with molecular gas surface density statistically, in agreement with various other studies (e.g. Liu et al., 2011; Schruba et al., 2011; Leroy et al., 2013). The total gas Schmidt relation before subtraction of diffuse background shows a knee at 10 $M_{\odot}$pc^{-2}, which is in agreement with the results of Bigiel et al. (2008). Compared to the bimodal relation of Bigiel et al. (2008), I find a higher dispersion at the lower end of the total gas Schmidt relation. This is simply because Bigiel et al. (2008) only include the molecular gas data in the regime where $\Sigma_{H_2} > 3\ M_{\odot}$ pc^{-2} for HERACLES data and $\Sigma_{H_2} > 10\ M_{\odot}$ pc^{-2} for BIMA SONG data. Since H I saturates around this cut-off value for all the galaxies, the total gas Schmidt relation at the lower end is basically the atomic gas Schmidt relation. In this work, by using forced aperture photometry based on positions derived from the Hα map, I can legitimately include regions with minimal ab-initio detection of molecular gas, particularly in the outer regions of galaxies. These results are supported by those of Schruba et al. (2011), whose stacking analysis allow them to trace the molecular gas surface density even in the outskirts of the galaxy. They report marginal CO detections which are as low as 0.1 $M_{\odot}$ pc^{-2} equivalent to the S/N $>$ 3 cut in this work. Hence this analysis shows that the Schmidt relations on sub-galactic scales do not depend on the method adopted - aperture photometry or pixel-by-pixel analysis.

Some studies (Heyer et al., 2004; Komugi et al., 2005; Momose et al., 2013) have found a super-linear molecular Schmidt relation even using data where diffuse background was not subtracted from the SFR tracers. However, all of these studies have used CO(1–0) data to trace the molecular gas, instead of CO(2–1) used in this work. The excitation for CO(2–1)

is significantly affected by a slight change in the kinetic temperature and volume density of molecular gas, which in turn affects the power-law index of the Schmidt relation (Momose et al., 2013). The change of the power-law index resulting from using a different molecular gas tracer (for example, CO(1–0), CO(3–2), HCN(1–0)) has been observed before by other studies as well (Narayanan et al., 2008; Bayet et al., 2009; Iono et al., 2009).

Subtraction of the diffuse background in SFR tracers naturally leads to an increase in the slope of the molecular gas Schmidt relation in all galaxies in the sample. This result is in agreement with Liu et al. (2011), who reports that the subtraction of diffuse background in SFR tracers leads to a super-linear slope of the molecular gas Schmidt relation from their analysis on two galaxies (NGC 5194 and NGC 3521). Adopting the same method of subtraction as Liu et al. (2011), Momose et al. (2013) and Morokuma-Matsui & Muraoka (2017) found the steepening of slope in agreement with this study. Rahman et al. (2011) also shows that the spatially-resolved molecular Schmidt relation can be non-linear if SFR tracers contain a significant fraction of diffuse emission. Leroy et al. (2013) subtracted diffuse background only in the 24 μm data before combining it to Hα and found subtle effects in the molecular gas Schmidt relation. This is likely due to the presence of diffuse background in Hα as well, which should also be taken into account while studying the current star-formation rate. However, their results are consistent with this work, in the sense of increase in scatter of the relation after removal of diffuse background. After subtraction of the diffuse background in SFR tracers, the best-fit line to our spatially-resolved data gives a slope of 1.26 ± 0.10 for the molecular gas Schmidt relation. This result is in agreement with previous works (Kennicutt et al., 2007; Liu et al., 2011). Using integral field spectroscopic data (IFS) for NGC 5194, Blanc et al. (2009) determined the diffuse emission in Hα using the [S II]/Hα line ratio and found the slope of the molecular gas Schmidt relation to be 0.84 in this galaxy. However, a direct comparison between their work and ours is complicated by the large differences in the methodology adopted, particularly the difference in data (photometric versus IFS), physical scale of study (0.5–2 kpc versus $\sim$170 pc) and diffuse background estimation.

For both molecular and total gas Schmidt relations of individual galaxies, I find that the *rms* scatter increases after subtraction of diffuse background (Figs. 7.5, 7.15-7.22). This result is consistent with previous works (Liu et al., 2011; Leroy et al., 2013; Morokuma-Matsui & Muraoka, 2017), which have employed different techniques for diffuse background subtraction. This consistency in the increase in scatter in the Schmidt relation in a log-log domain may point toward an astrophysical origin but is quite likely a result of removal of diffuse signal whilst minimally changing the underlying noise.

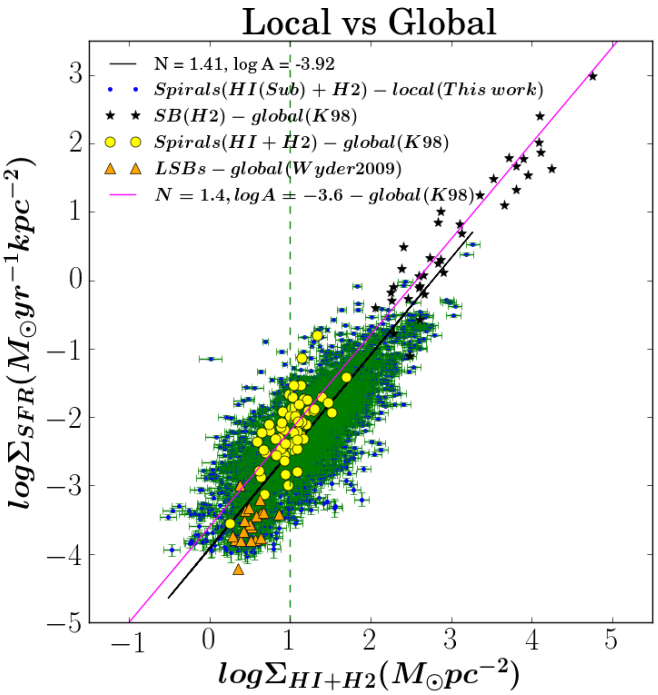

Figure 7.9 – Comparison of the spatially-resolved total gas Schmidt relation for nine spiral galaxies in this work with the global Kennicutt-Schmidt relation of the starbursts (black stars) and spirals (yellow dots) taken from Kennicutt (1998b). The diffuse background has been subtracted from the SFR tracers as well as from the atomic gas for the spatially-resolved data. These local measurements assume a Salpeter IMF and an X(CO) factor of 2.8×10^{20} cm^{-2} (K km s^{-1})$^{-1}$ to match the parameters adopted in Kennicutt (1998b). The pink line represents the global Kennicutt-Schmidt relation from Kennicutt (1998b) while the solid black line is the best-fit line to the spatially-resolved data from all galaxies in this work.

7.5.2 Comparison with the global Kennicutt-Schmidt relation

Fig. 7.9 presents a summary of the Schmidt relation with all the star-forming regions from our galaxy sample together with the integrated measurements of starburst and spiral galaxies taken from Kennicutt (1998b). For the spatially-resolved data, the diffuse background has been subtracted from the SFR tracers and the atomic gas, and the IMF and X(CO) factor of the spatially-resolved data are adjusted to those of integrated data (i.e. a Salpeter IMF and an X(CO) factor of 2.8×10^{20} cm^{-2} (K km s^{-1})$^{-1}$), yielding the following best-fit line:

$$\Sigma_{SFR} = 10^{-3.9\pm0.1}\Sigma_{gas}^{1.4\pm0.1} \tag{7.8}$$

The slope of the global and local best-fit lines is identical within the errors. However, there is an offset in the zeropoints, i.e. -3.9 in this study versus -3.6 in the global relation. A Kolmogorov-Smirnov test on the global and spatially-resolved data shows that the observed offset in the zeropoints of the global and local results is significant enough to affect the overall interpretation of the star-formation relation. There are several possible reasons for this difference in zero-points. In local sample selection, the chosen sub-regions of star-formation in any spatially-resolved study will be biased by the selection criteria. For example, in this study I used Hα luminous regions but given our understanding of the formation of stars from molecular gas clouds, I could also have selected star-forming regions on the basis of molecular gas peaks. There is no such sampling effect in global studies. In addition, Kennicutt et al. (2007) describes the filling factor of star-forming regions in the disc of galaxies as a potential cause of the observed offset. Other reasons which can contribute to the observed offset are the different SFR calibration recipes at local and global scale. Note here that the non-negligible uncertainties due to age and the IMF are present in the conversion factor of luminosity to SFR. While comparing the spatially-resolved Schmidt relation with the global Kennicutt-Schmidt Law, I took into account the IMF which contributes significantly to the differences in SFR calibration at global and local scale (in section 7.3.3) but I did not take into account for example, the age of the H II regions. Hence it not surprising to see differences in the global-vs-local total gas Schmidt relations.

7.6 Conclusion

In summary, I have studied the spatially-resolved molecular and total gas Schmidt relation individually for nine galaxies, and also the overall combined fit for all galaxies for both molecular and total gas (Figures 7.7 and 7.8). Though the slope of the combined total gas spatially-resolved Schmidt relation matches the global Schmidt-Kennicutt relation, there is considerable variation in slopes from galaxy to galaxy. Such variation has been observed before in previous studies, even without the subtraction of diffuse background (see e.g. Wong & Blitz, 2002; Boissier et al., 2003; Bigiel et al., 2008) though note here the subtraction of diffuse background

from H I gas has led to a decrease in the variation of slopes. To explore the variation in the background subtracted data, I examined the variation of slope with respect to the ratio of the molecular-to-atomic gas surface density (within the analysis apertures) for all galaxies, however I did not find any trend. The variation of X(CO) factor may be another cause of the observed variation, for example, by using a radially-varying metallicity-dependent X(CO) factor, Boissier et al. (2003) derived a steeper slope ($\sim$2). Sandstrom et al. (2013) reports a radial variation of X(CO) in eight out of nine galaxies in the sample, with an overall decrease of 0.3 dex in the centre of galaxies. Since in this work, a constant X(CO) factor was assumed (for comparison with other works), it is likely that the reported molecular gas surface densities are underestimated in the centres. It is possible that the variation of slope from galaxy-to-galaxy will further reduce if a radially-varying X(CO) factor is adopted in conjunction with diffuse background subtraction in SFR tracers and atomic gas. Another possible source of systematics affecting the derived slopes are selection effects and sample biases from using the Hα maps for picking out the star-forming regions. Ideally, to check this one should use the peaks of molecular gas (from CO maps), as indicators of star-forming regions. However, to check the effect of such systematics, one would need high resolution molecular gas maps, where the peaks can be readily resolved. Large variation in slope from galaxy to galaxy may also result from the aperture corrections applied to extended sources as if they were point sources.

Though I find the slopes of the global and local total gas Schmidt relation to be similar, it is difficult to draw conclusions from this similarity especially when a large variation in slopes has been observed from galaxy to galaxy. The smaller scatter in log-log space in the total gas Schmidt relation compared to the molecular gas Schmidt relation may simply be the result of having more signal with respect to the noise contributions from the combination of H I and H_2. However, it may also indicate that atomic gas may be contributing to the star-formation. In the spatially-resolved total gas Schmidt relation, I obtain a slope of 1.4 when diffuse background is subtracted from SFR tracers and the atomic gas. I find that the fraction of diffuse atomic gas in all galaxies is higher than the fraction of diffuse background in the SFR tracers (Table 7.3) at the same spatial scale. It constitutes $\sim$ 37–80% depending on the galaxy. Excluding NGC 5457, diffuse atomic gas is $>$ 50% in all galaxies. This indicates that at the local scale in projection, a vast amount of atomic gas (i.e. diffuse background) in the ISM is not relevant for star-formation. However, about 20–50% of this atomic gas is available locally for star-formation and hence its role can not be neglected. It is probably the cold component of the atomic gas i.e. cold neutral medium rather than the warm neutral medium, which contributes to star-formation. Since no diffuse background is detected or subtracted from the molecular gas data, this work still shows that molecular gas is the prime driver of star-formation. However, the role of atomic gas in star-formation especially in the outskirts of galaxies should not be neglected, where there is an abundance of atomic gas with no detection of molecular gas. Moreover, in the nearby Universe, atomic gas forms a large fraction of the cold gas reservoir in galaxies. The molecular gas which

directly feeds star-formation, constitutes only $\sim$ 30% of the cold gas (Catinella et al., 2010; Saintonge et al., 2011; Boselli et al., 2014). A recent study by Cortese, Catinella & Janowiecki (2017) also shows that the gas reservoirs of star-forming disks at z $\sim$ 0.2 are not predominantly molecular. So in such systems, atomic gas seem to be the source of star-formation. Though from the current study it is difficult to infer the relative importance of atomic and molecular gas in star-formation, we may say that both of the components (atomic and molecular) of the ISM may be collectively important for forming stars. Furthermore, a super-linear Schmidt relation would imply the dominant role of non-linear processes in driving star-formation at spatially-resolved scales, and a non-constant star-formation efficiency or time scale for different gas surface densities.

To explore the above hypotheses, we need to study the distribution of different phases of the ISM at the scales of H II regions, their spatial correlation, and also study these star-forming regions in different evolutionary stages. This will allow us to understand the relative importance of the different components of the ISM responsible for star-formation and the nature of diffuse emission in SFR tracers, for example warm ionised medium (DIG) traced by Hα. It is now possible to study in great detail the characteristic properties of DIG in the nearby star-forming regions, with the advent of IFS facilities like the Multi-Unit Spectroscopic Explorer (MUSE) and the Keck Cosmic Web Imager (KCWI). Moreover, the IFS technique allows us to correct the internal dust-attenuation in the galaxies directly from the Balmer-decrement (Hα:Hβ:Hγ), bypassing the use of the infrared (24μm) images, which means that we can reduce the uncertainties related to the diffuse component in infrared images. Similarly, observational facilities like the Atacama Large Millimeter/submillimeter Array (ALMA), the Submillimeter Array (SMA), the Robert C. Byrd Green Bank Telescope (GBT) are apt to characterise the neutral gas (both atomic and molecular) in the nearby star-forming regions. Thus, these combined analyses will help us better understand the intricacies of star-formation.

7.7 Appendix

7.7.1 Maximum aperture-size

To determine a viable maximum aperture size I experimented on NGC 0628 which is at an intermediate distance ($\sim$ 7.3 Mpc) and is almost-face-on (inclination angle $\sim$ 7°), mitigating any effect due to inclination angle. Figure 7.10 shows the results of this experiment where in each panel, the y-axis shows the flux (for SFR tracers), or mass for gas data, in successive apertures of size varying from 0.6–2.0 kpc, normalised by the flux, or mass, in the smallest aperture ($\sim$ 500 pc). The x-axes shows the average flux/mass in the corresponding apertures. In the first four panels, we find that for each tracer (Hα, FUV, 24 μm and CO) the normalised flux/mass (solid

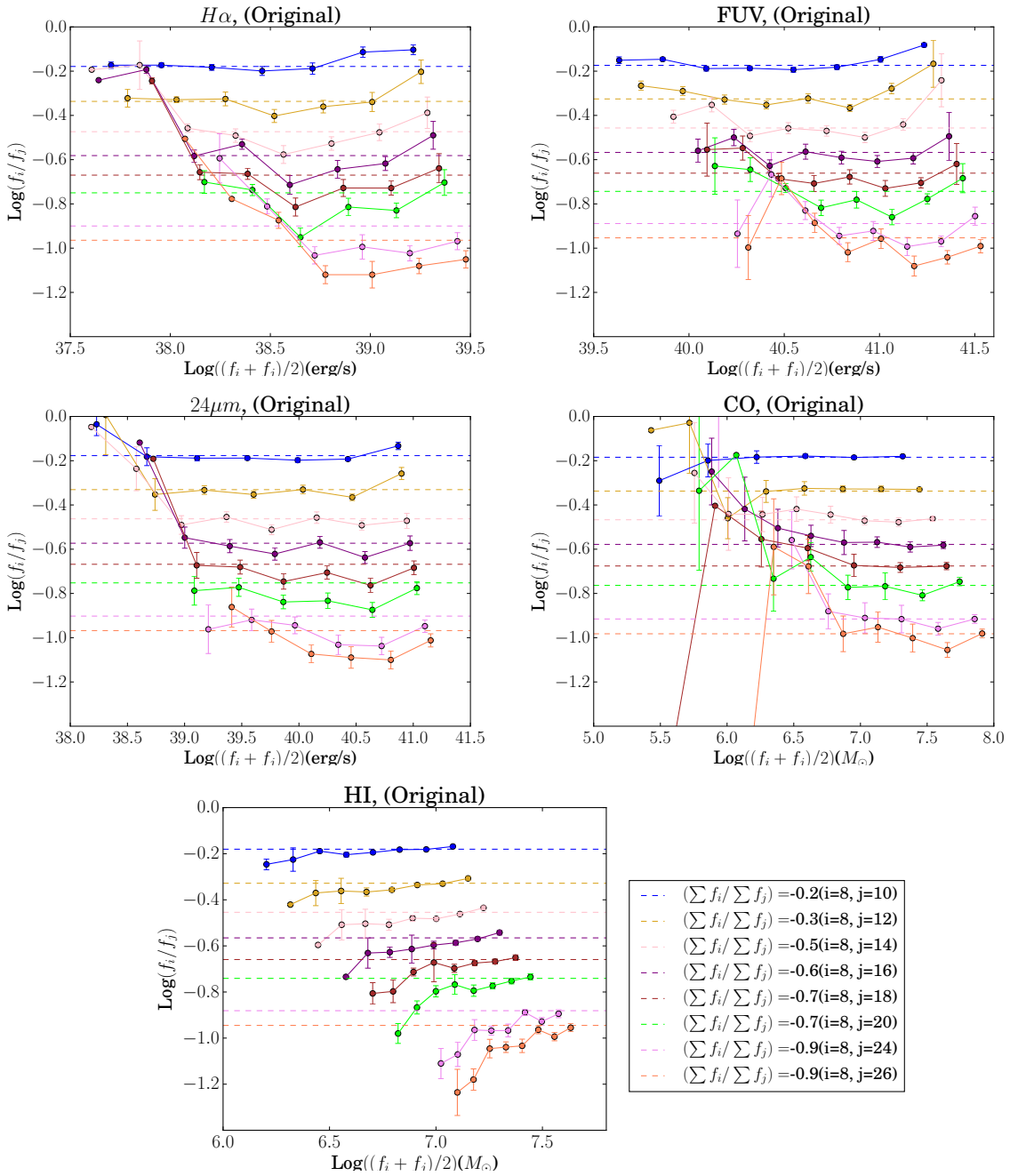

Figure 7.10 – The flux (mass) in apertures of size varying from 0.6–2.0 kpc normalised by the flux (mass) in an aperture of size ∼500 pc compared to the average flux (mass) in the corresponding apertures. The solid color lines show the normalised flux (mass) while the dashed color lines show the ratio of the total flux in the apertures under study, where i & j denote the aperture radii in arcsec. These figures correspond to analysis of the galaxy NGC 0628, for which the minimum radius (8 arcsec) and maximum radius (26 arcsec) correspond to physical sizes of ∼ 600 pc and 2 kpc, respectively.

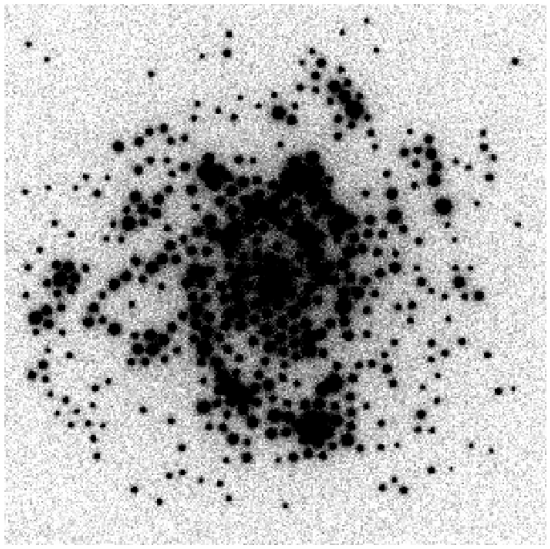

Figure 7.11 – Mock galaxy where H II regions are modelled as Moffat profiles with β = 1.5. For more details on the modelling see the text in Appendix 7.7.2.

color line) shows the same trend, following closely the ratio of the total flux or mass (dashed color line) for all apertures varying from 0.6–2.0 kpc. However, the corresponding plot for H I (bottom panel), shows a deviation in the trend at an aperture radius of ∼14 arcsec (solid pink line) which corresponds to physical size of ∼1 kpc. This deviation becomes significant at physical sizes greater than ∼2 kpc. A physical size of 1.0 kpc was found suitable for two galaxies (NGC 3351 and NGC 5055) in the sample owing to their distances and inclination angles. Due to the high inclination angle of NGC 3521, a physical size of 1.0 kpc still leads to problems of under-sampling the enclosed pixels in apertures. Hence for a comparison with Liu et al. (2011) who studied Schmidt relation for this galaxy at 2.0 kpc scale, I set the aperture size for NGC 3521 to correspond to a physical size of ∼2.0 kpc. The individual results for this galaxy should be interpreted with caution due to the potential deviation in trend of H I beyond 1 kpc.

7.7.2 Background subtraction on a mock galaxy

I modelled the mock galaxy (Fig. 7.11) as a combination of star-forming regions, a disky exponential profile and used similar noise model properties to the real data. For simulating H II regions, I used Moffat profiles defined by $I(r) = I_o[1+(r/\alpha)^2]^{-\beta}$ where I_o is the peak intensity at the centre, and α and β are related to FWHM as: $FWHM = 2\alpha\sqrt{2^{1/\beta}-1}$. The FWHM was set to be 2 arcsec similar to the real data. The intensity enclosed in an aperture of radius R is given by $I(< R) = \frac{\pi\alpha^2}{\beta-1} I_o[1-[1+(R/\alpha)^2]^{-\beta+1}]$ from which aperture corrections can be readily computed. In this modelling, I experimented with two values of β = 1.5, 2.5. A Moffat profile with β=2.5 produces a more Gaussian-like profile, while a Moffat profile with β=1.5 produces extended outer wings, providing a better representation of the H II regions. Model flux values for the H II regions were taken from the original unsubtracted Hα image of

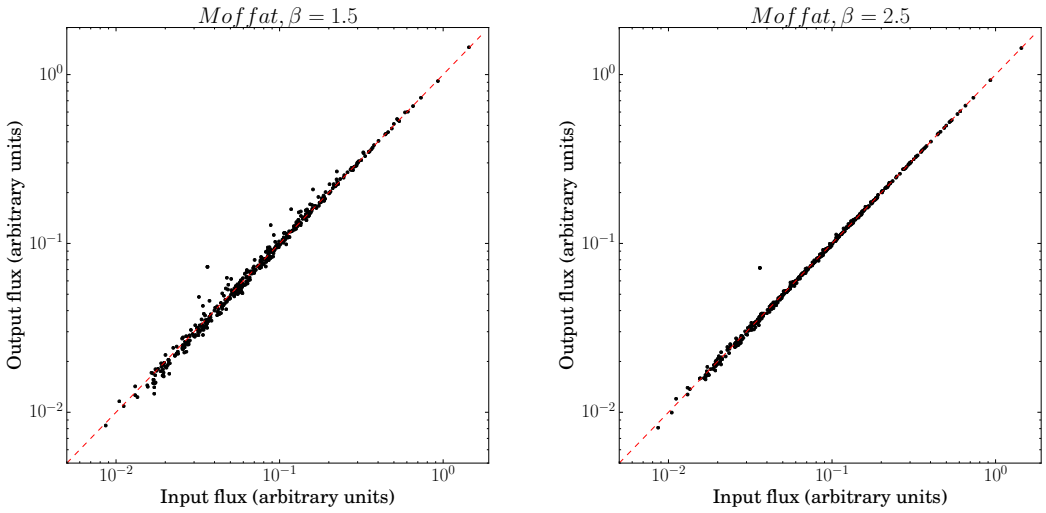

Figure 7.12 – In both panels, x-axis shows the input fluxes to model H II regions in a mock galaxy with an underlying diffuse component and y-axis shows the fluxes in H II regions after diffuse background subtraction. In both panels, the dashed red line is the one-to-one line. H II regions are modelled as the Moffat profiles with β = 1.5 (upper panel) and β = 2.5 (lower panel).

the galaxy NGC 0628. The diffuse background exponential disk was modelled based on the effective radius of the galaxy and scaled to yield a diffuse background component of 25%. On the modelled galaxy images (β = 1.5, 2.5), as for the real data, the Nebulosity Filter software was used to estimate ab-initio the diffuse background component. I then performed aperture photometry with apertures of radii of 8 arcsec (the same as adopted for NGC 0628) to extract fluxes in the background subtracted modelled H II regions. Aperture corrections corresponding to the two Moffat profiles were applied on the extracted fluxes, and aperture-corrected fluxes were compared with the input fluxes used to model H II regions. Figure 7.12 shows comparisons of the input and output fluxes for the modelled galaxies with $\beta = 1.5$ (left panel) and β = 2.5 (right panel). The input and output fluxes lie on the expected one-to-one line (red-dashed line) expanding over two order of magnitudes.

7.7.3 Radial profiles on unsubtracted data

Fig. 7.13 presents radial profiles of Σ_{SFR} (brown curve: Hα and black curve: FUV), $\Sigma_{H\textsc{i}}$ (blue curve), Σ_{H_2} (red curve), $\Sigma_{H\textsc{i}+H_2}$ (green curve) for all nine galaxies in the sample before subtraction of diffuse background. I do not show radial profiles of Σ_{H_2} for r > 0.7 r$_{25}$ because the radial profiles of CO intensity are found to fall below 3σ approximately after this radius (Leroy et al., 2009). The radial profiles Σ_{H_2} (red curves) are decreasing strongly with radius in all galaxies and are closely correlated with the Σ_{SFR} radial profiles (brown and black curves).

The radial profiles of $\Sigma_{H\textsc{i}}$ (blue curves) on the other hand show a well-defined upper limit of

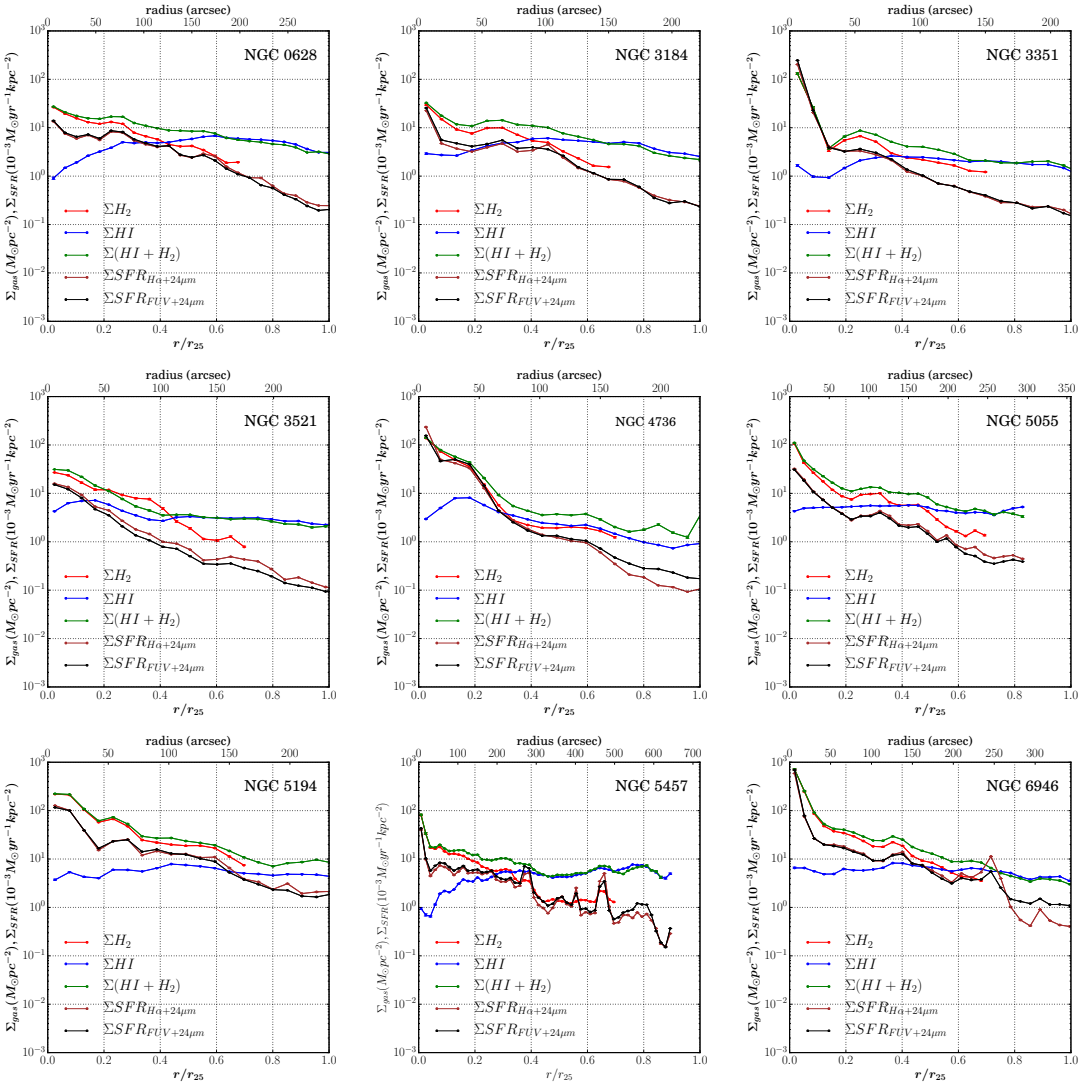

Figure 7.13 – Radial profiles of Σ_{SFR} (original unsubtracted data), Σ_{HI}, Σ_{H_2} and Σ_{HI+H_2} for all nine galaxies in the sample. The x-axis presents the galactocentric radius normalized by r_{25} (bottom) and in arcsecs (top). The y-axis presents Σ_{gas} in units of $M_\odot$ pc^{-2} and Σ_{SFR} in units of 10^{-3} $M_\odot$ yr^{-1} kpc^{-2} (the scale range is the same for all galaxies). Σ_{H_2} (red curves) and Σ_{SFR} (brown and black curves) show a similar radial falloff for all galaxies. Σ_{HI} (blue curves) have a relatively flat radial profile, usually a deficit toward the centre and show an upper limit of $\sim$10 $M_\odot$pc^{-2}

$\sim$10 $M_{\odot}pc^{-2}$ and in general a strong depletion towards the galaxy centres. There is a relatively high surface density of molecular gas compared to atomic gas in the centre of all galaxies ($r < 0.2\ r_{25}$), while in the outer parts Σ_{H_2} decreases in the regions where H I saturates. Clearly the formation and destruction of H I and H_2 are interdependent and these trends presumably follow naturally from the interplay of H I, H_2 and star formation. In the centres of these galaxies most of the H I is presumably in the form of H_2 which is itself being used to form stars. In the outer regions, either molecular gas dissociates back to form atomic gas which suppresses star-formation, or formation of molecular gas is itself low because of the lower amount of dust[5] needed for molecule formation, and sufficient provision of energetic FUV photons in the extended arms of galaxies leading to further dissociation of molecular gas into atomic gas.

Note that the radial profiles of the original unsubtracted data for these galaxies have been published before by Bigiel et al. (2008), Leroy et al. (2008) and Schruba et al. (2011), though the methods adopted are slightly different in each analysis. I present them here to compare with the profiles obtained from the subtracted data presented in Fig. 7.4.

7.7.4 Power-law fit: weighted versus unweighted

Different methods were tested for fitting the total gas Schmidt relation to the spatially-resolved data of NGC 0628, where no diffuse background was subtracted. These fitting methods include a standard unweighted regression, inverse unweighted regression, and maximum likelihood fits (both weighted and unweighted). The results of all the fits are shown in Fig. 7.14. Previous studies have shown that calibration errors as large as 30–50% may exist on both axes owing to uncertainties on the SFR calibration and the CO-to-H_2 conversion. Hence in the weighted maximum likelihood fit (solid blue line), a 20% calibration error is included on both axes in addition to the uncertainties estimated in section 7.3.2. The goodness of fit is tested from the value of the reduced-χ^2 obtained. The reduced-χ^2 is found to be close to unity (0.98 in this case) when additional calibration uncertainties are included in the maximum likelihood fit. Without this additional uncertainty the reduced-χ^2 is much larger than 1 indicative of an incorrect data model. The parameters obtained from the weighted fit are similar to those derived from a maximum likelihood fit where equal weight is given to each point on both axes (solid black line). Hence based on these experiments, I decided to estimate the best-fit parameters using an equal weight maximum likelihood fit in all the analysis.

7.7.5 Schmidt Law fits to individual galaxies

Figs. 7.15–7.22 show the effect of inclusion and removal of diffuse background from the SFR tracers for each individual galaxy, except NGC 0628 for which the plots are shown in Fig. 7.5.

[5]Infrared maps of galaxies are brighter in the inner regions of galaxies compared to the outer regions

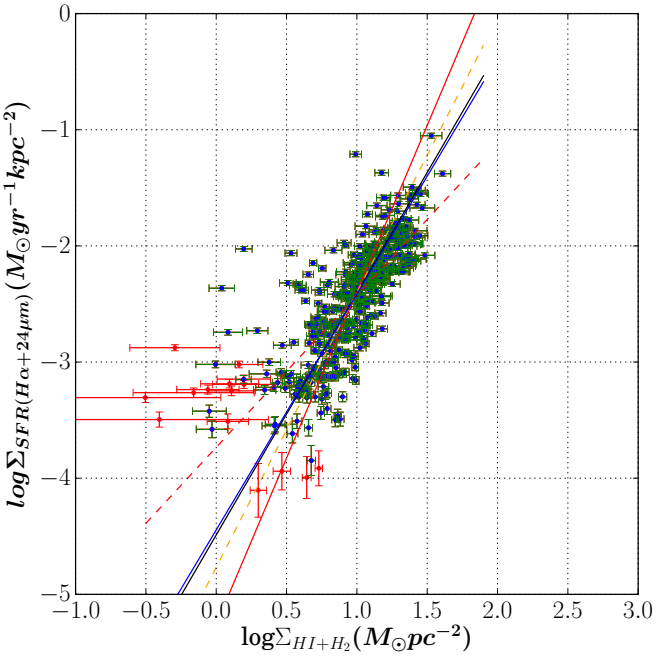

Figure 7.14 – Different fits to the spatially-resolved total Schmidt relation for NGC 0628. Only blue points with green error bars are used for fitting. The red data points with errorbars correspond to points with S/N<3, and have not been included in the fits. The error bars shown here include the random error and systematic error on flux measurements as explained in Section 7.3.2, but not the additional calibration error. Dashed red line: standard unweighted regression, dashed orange line: inverse weighted regression. solid black line: maximum likelihood estimate where each point on both axes is given equal weight, solid blue line: maximum likelihood estimate where 20% calibration error has been included on both axes in addition to the uncertainties estimated in Section 7.3.2, solid red line: maximum likelihood estimate where points have been weighted solely with respect to the uncertainties estimated in Section 7.3.2.

The caption of Fig. 7.5 holds true for all the eight figures. Fig. 7.23 shows the Schmidt relation between Σ_{SFR} and $\Sigma_{H\,I}$ after the diffuse background is subtracted from the SFR tracers as well as from the H I, individually for all the sample galaxies, except NGC 0628. Fig. 7.24 shows the total gas Schmidt relation after subtraction of diffuse background from SFR tracers and atomic gas for all galaxies except NGC 0628. See Fig. 7.8 for the corresponding plots of NGC 0628.

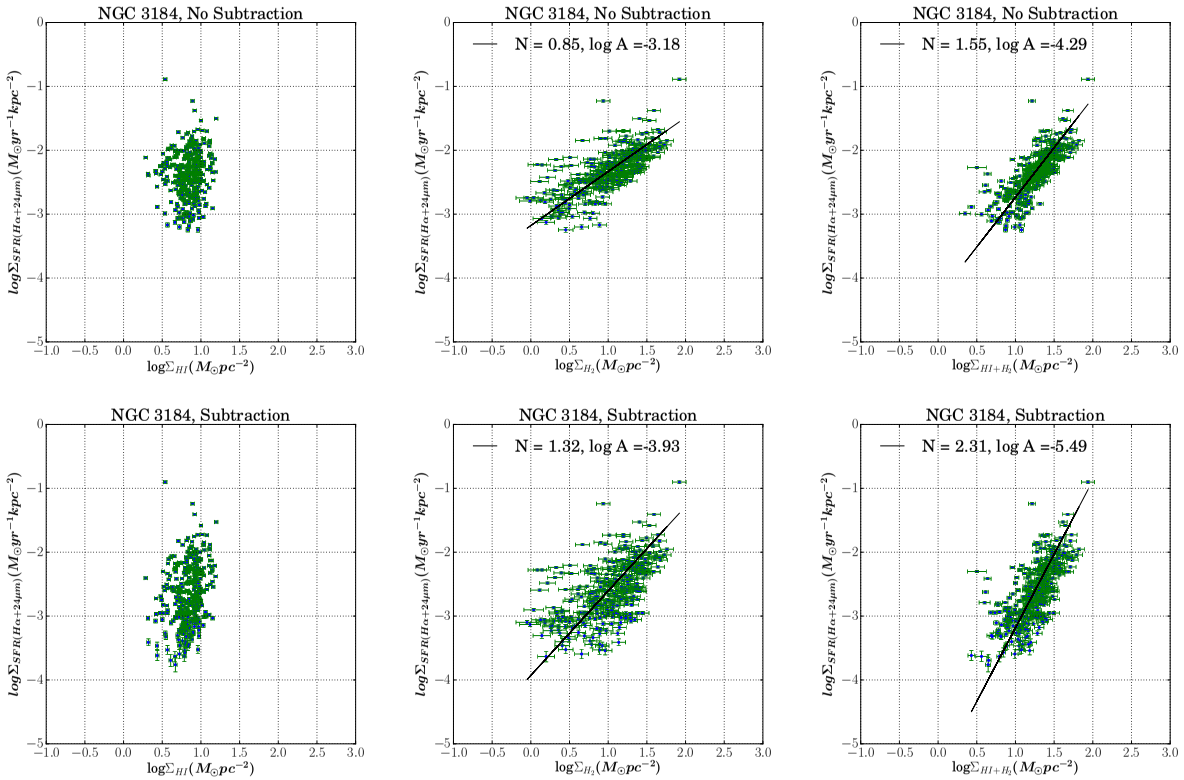

Figure 7.15 – NGC 3184: an aperture size of 10 arcsec is adopted, which corresponds to a physical diameter of $\sim$ 520 pc for NGC 3184, at a distance of 11.1 Mpc and inclination angle of 18°. See caption of Fig. 7.5 for details.

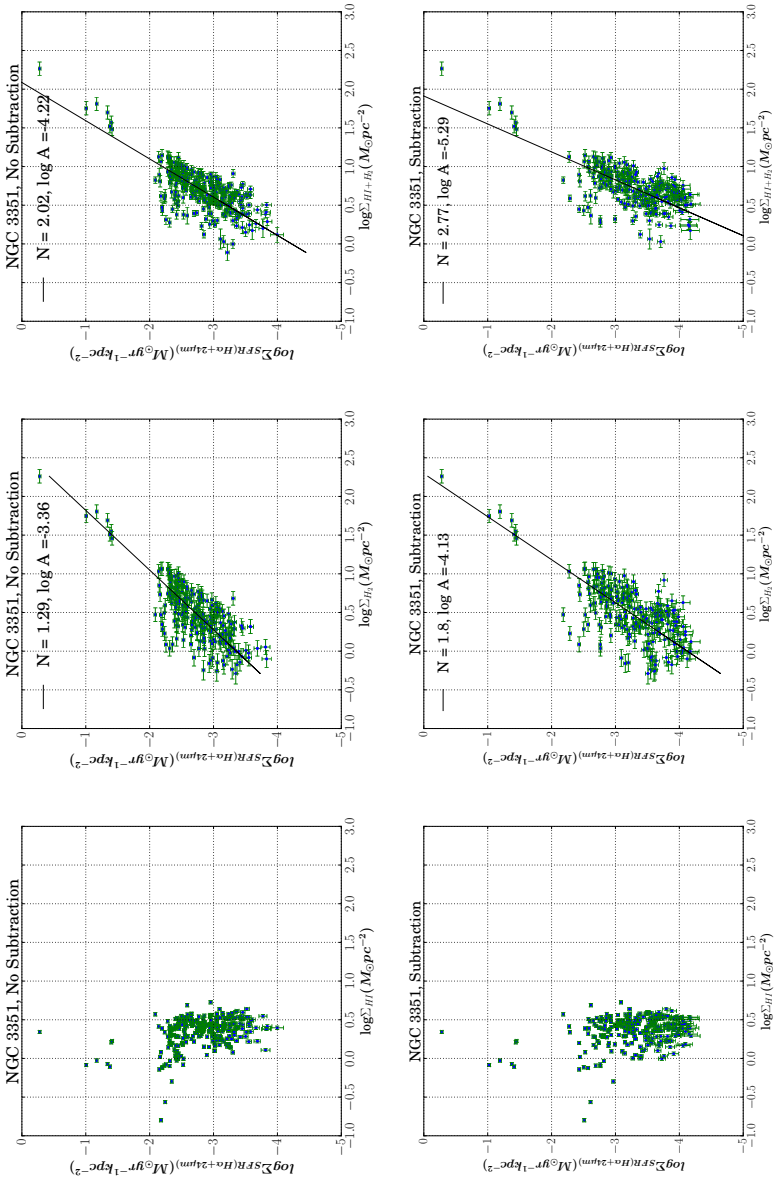

Figure 7.16 – NGC 3351: an aperture size of 16 arcsec is adopted, which corresponds to the physical diameter of $\sim$ 1.0 kpc at a distance of 9.33 Mpc and inclination angle of 41°. See caption of Fig. 7.5 for details.

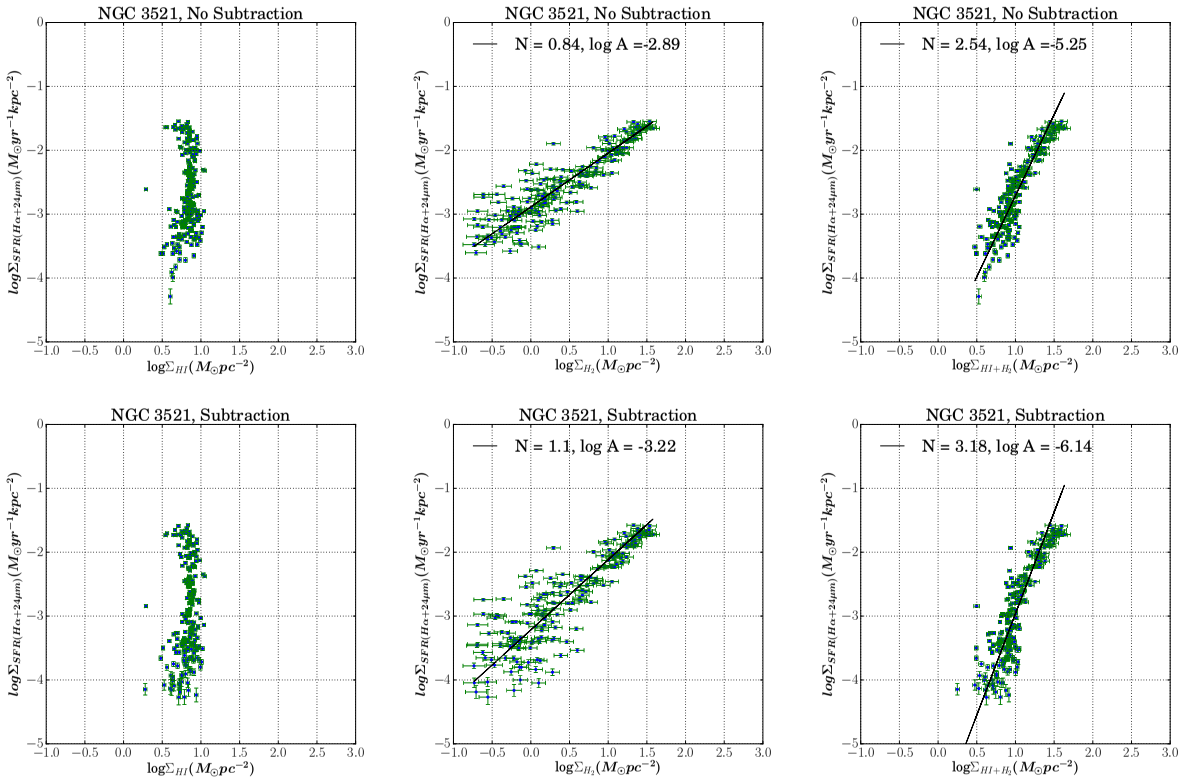

Figure 7.17 – NGC 3521: an aperture size of 18 arcsec is adopted, which corresponds to the physical diameter of $\sim$ 2.0 kpc at a distance of 8.03 Mpc and inclination angle of 73°. See caption of Fig. 7.5 for details.

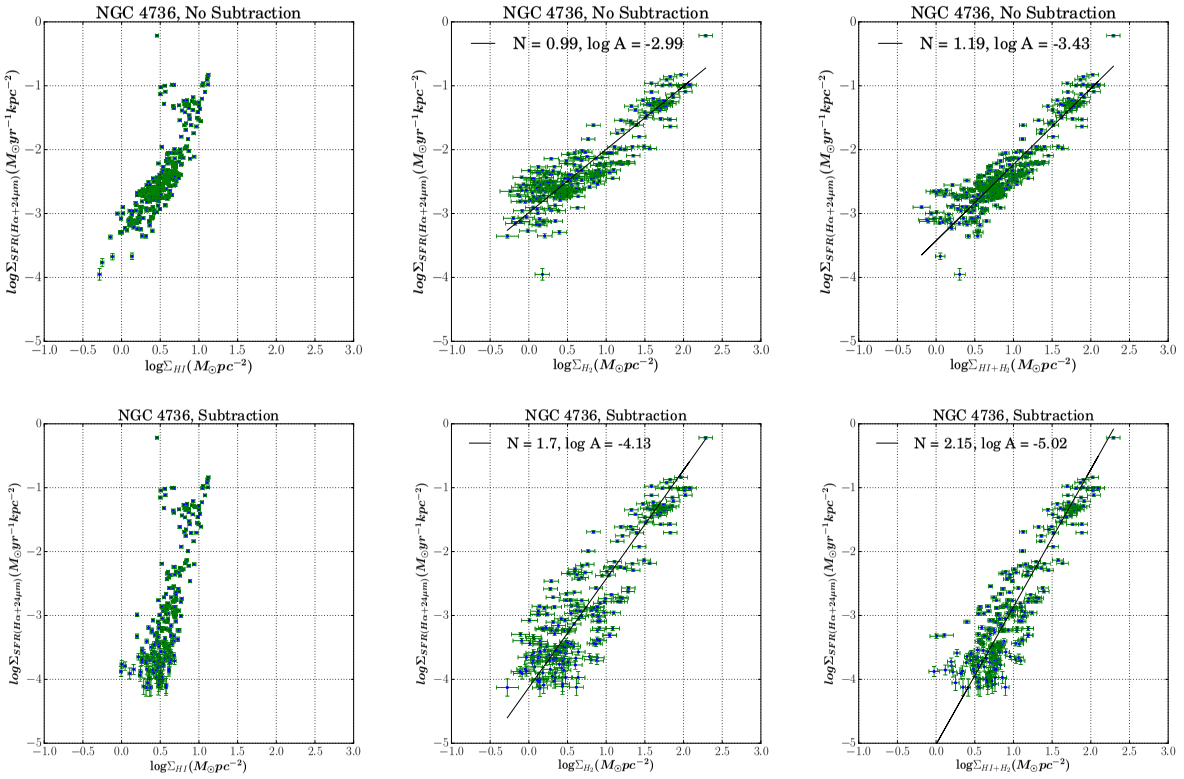

Figure 7.18 – NGC 4736: an aperture size of 15 arcsec is adopted, which corresponds to the physical diameter of $\sim$ 500 pc at a distance of 5.20 Mpc and inclination angle of 41°. See caption of Fig. 7.5 for details.

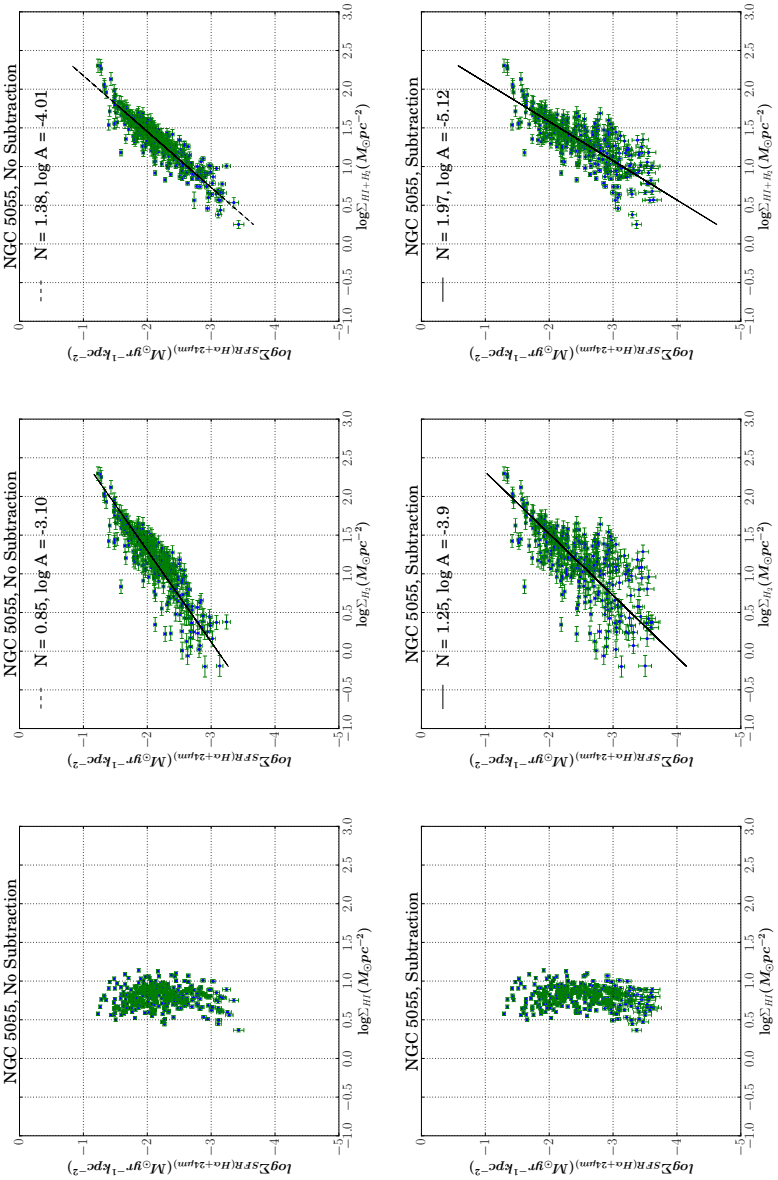

Figure 7.19 – NGC 5055: an aperture size of 12 arcsec is adopted, which corresponds to the physical diameter of $\sim$ 1 kpc at a distance of 7.8 Mpc and inclination angle of 59°. See caption of Fig. 7.5 for details.

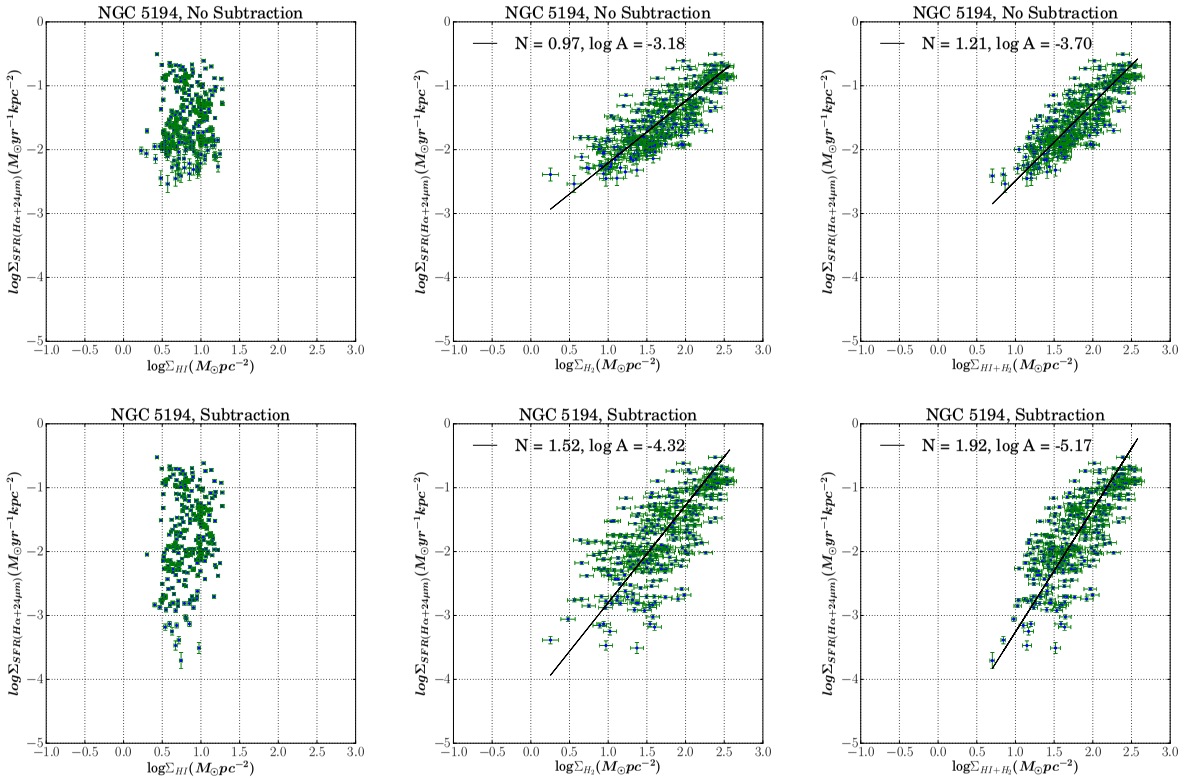

Figure 7.20 – NGC 5194: an aperture size of 13 arcsec is adopted, which corresponds to the physical diameter of $\sim$ 520 pc at a distance of 8.2 Mpc and inclination angle of 20°. See caption of Fig. 7.5 for details.

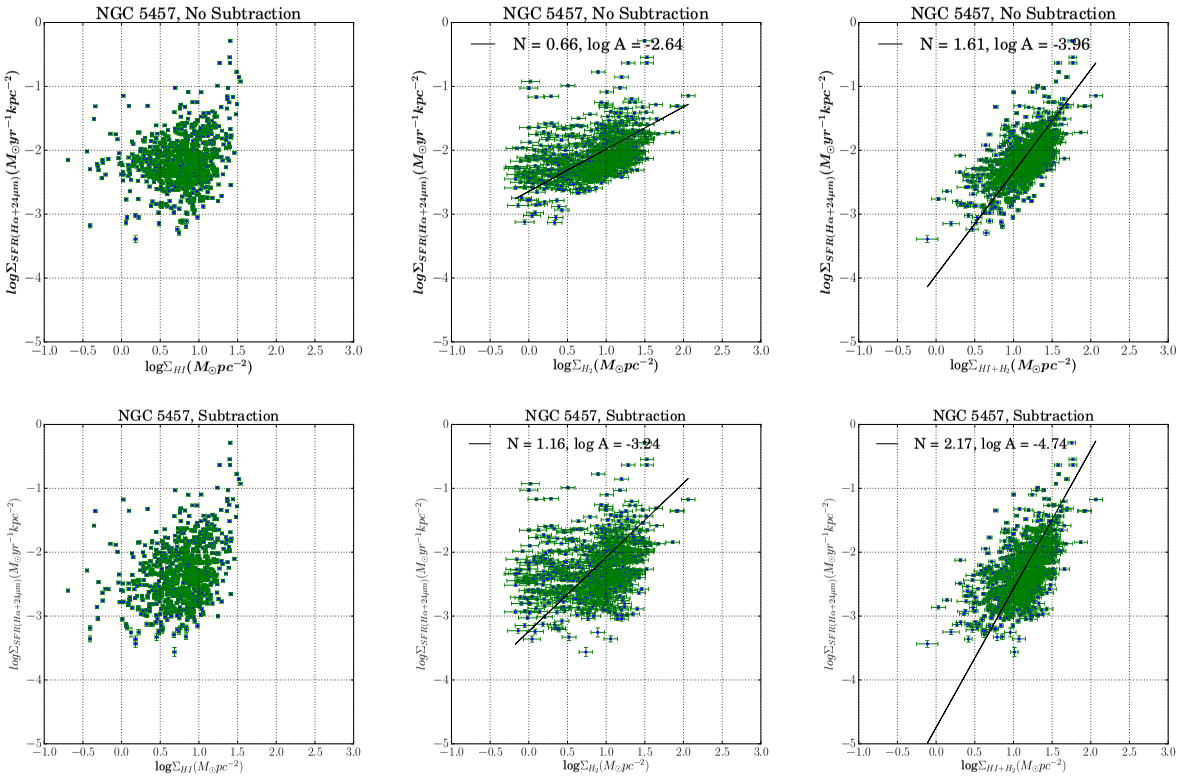

Figure 7.21 – NGC 5457: an aperture size of 14 arcsec is adopted, which corresponds to the physical diameter of $\sim$ 500 pc at a distance of 6.7 Mpc and inclination angle of 18°. See caption of Fig. 7.5 for details.

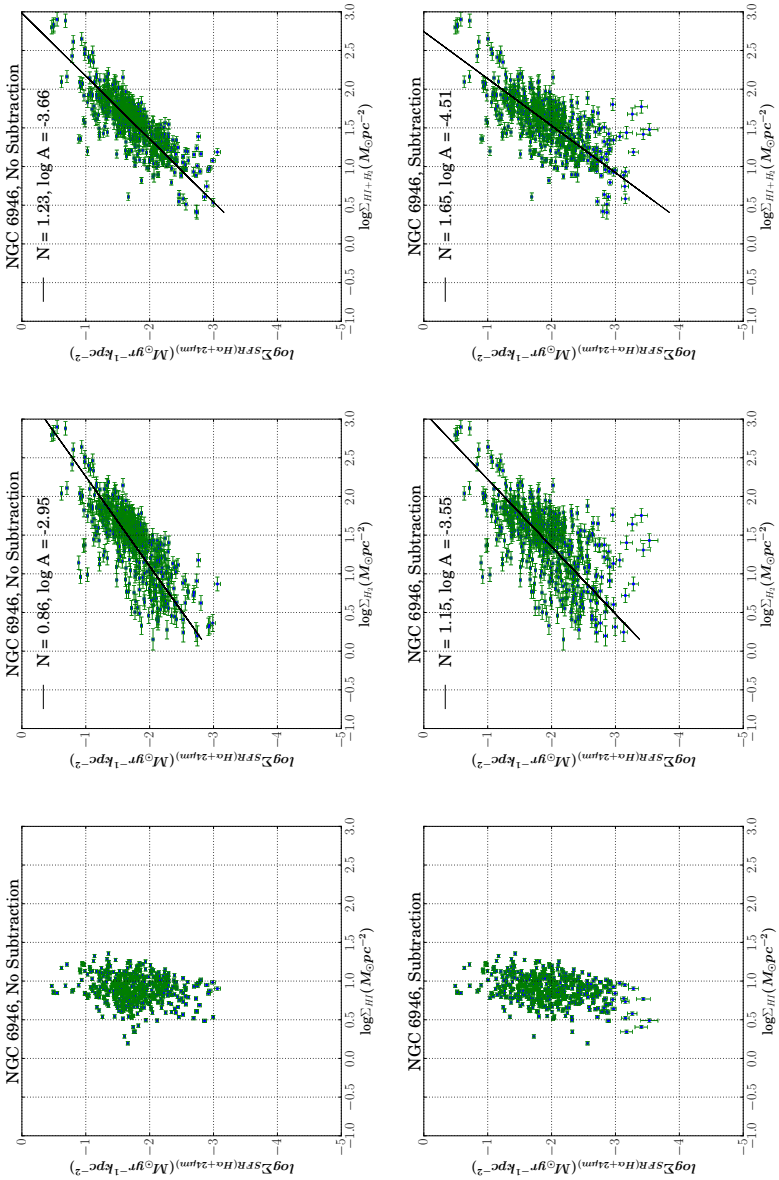

Figure 7.22 – NGC 6946: an aperture size of 12 arcsec is adopted, which corresponds to the physical diameter of $\sim$ 596 pc at a distance of 6.8 Mpc and inclination angle of 33°. See caption of Fig. 7.5 for details.

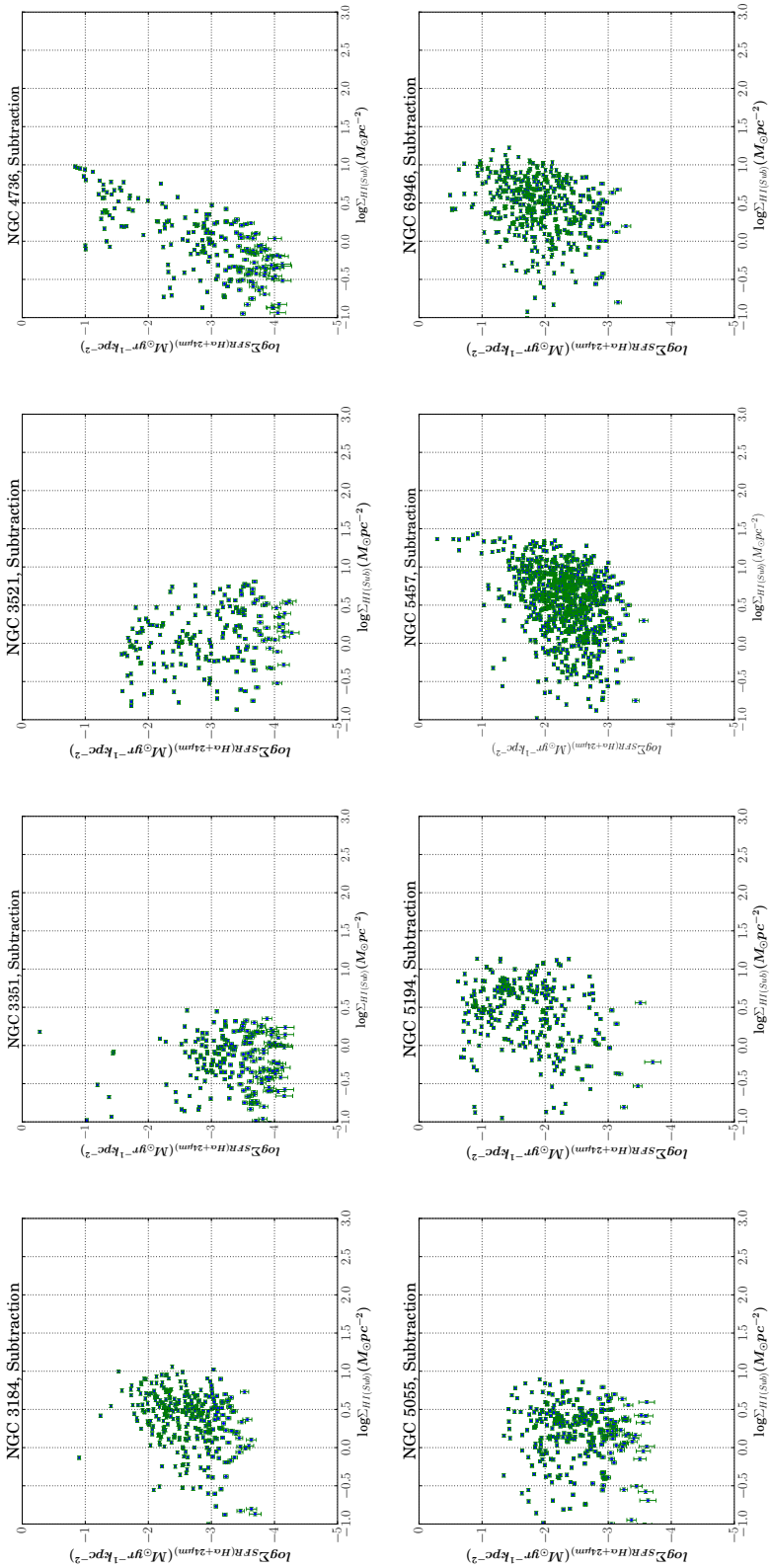

Figure 7.23 – Spatially-resolved atomic gas Schmidt relation (Σ_{SFR} and $\Sigma_{HI(sub)}$). The diffuse background has been subtracted from both SFR tracers and atomic gas.

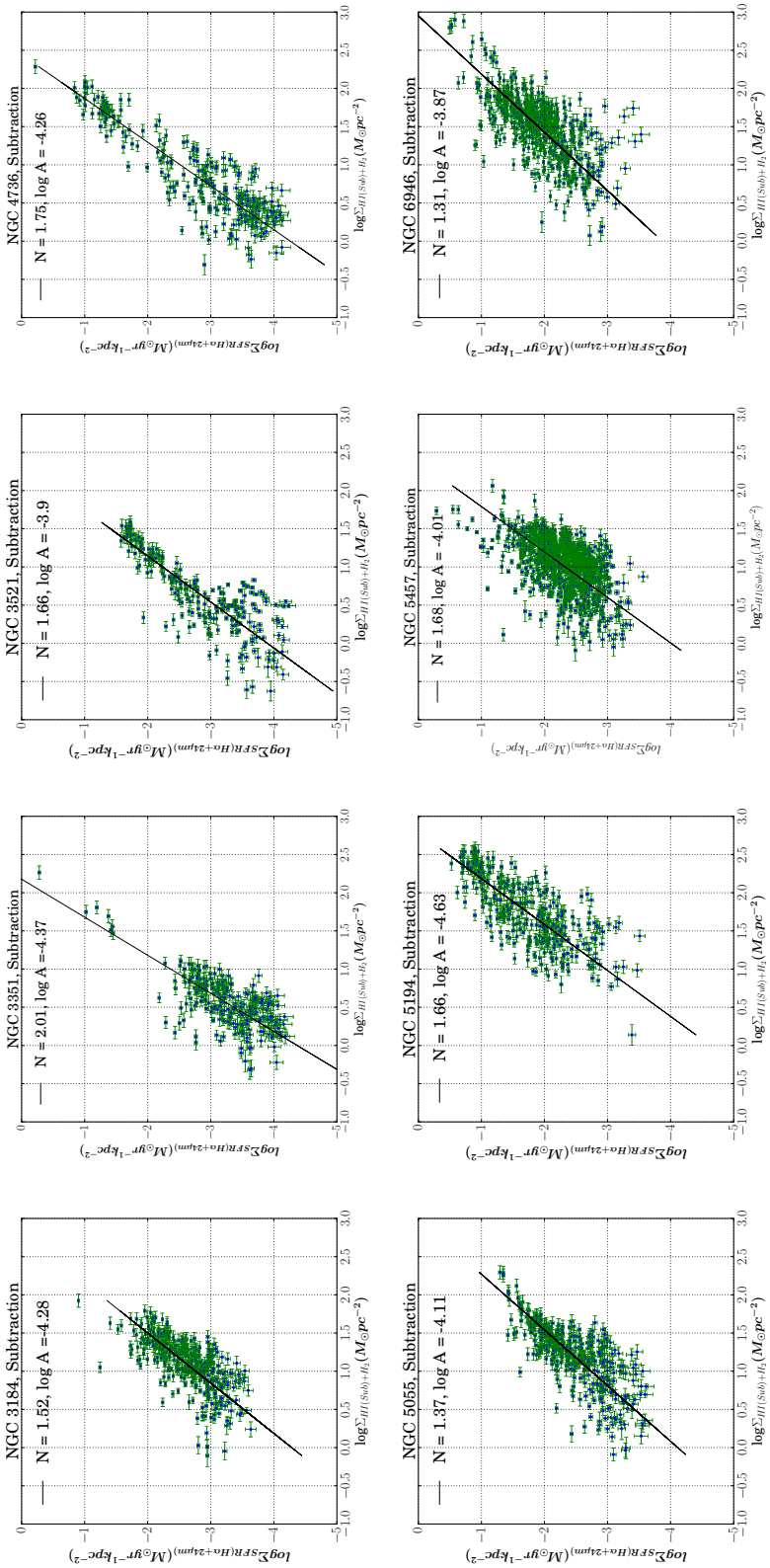

Figure 7.24 – Spatially-resolved total gas Schmidt relation (i.e. Σ_{SFR} and $\Sigma_{H1(sub)+H_2}$) for individual galaxies. The diffuse background has been subtracted from both SFR tracers and atomic gas. A Kroupa IMF and a constant X(CO) factor = 2.0×10^{20} cm^{-2} (K km s^{-1})$^{-1}$) have been assumed.

8

Conclusions and Future Prospects

8.1 Summary

In this thesis, I have performed spatially-resolved analyses of nearby star-forming galaxies - blue compact dwarf galaxies and spiral galaxies - using high-quality integral field spectroscopic (IFS) and photometric data. Through my analysis, I have explored the broad field of galaxy formation and evolution, and contributed to its sub-fields particularly stellar nucleosynthesis, chemical abundances, star-formation and gas-dynamics.

In what follows, I summarise the main findings of my thesis in terms of the questions which were introduced in Chapter 1.

- In Chapters 3 to 5, I worked at spatial scales smaller than or comparable to the size of typical H II regions. For this purpose I used the optical GMOS-N IFS data of regions within three BCDs (NGC 4449, NGC 4670 and SBS 1415+437). In Chapter 2, I presented the details of the data reduction for two modes of data acquisition in GMOS-IFU, for which I developed codes whenever the standard pipeline did not provide satisfactory results. I reduced the one-slit mode GMOS-IFS data of the three BCDs presented in this thesis, and also reduced the two slit-mode GMOS-IFS data of another BCD, Mrk 71, for collaborative work (Oey et al. in prep). I analysed IFS data of the three BCDs in the framework of answering the following questions in Chapters 3, 4 and 5:

  1. *Do chemical inhomogeneities exist in the ionised gas within BCDs?*

In my work, I have addressed this question by exploring chemical variation within BCDs at parsec as well as kiloparsec scales. In the central star-forming region of the BCD NGC 4449, the ionised gas is likely to be chemically homogeneous as inferred from the metallicity maps obtained by the direct T_e method and indirect methods. At kiloparsec scales, NGC 4449 shows signatures of an inverse metallicity gradient. This discovery is interesting because star-forming galaxies in the nearby Universe usually show a negative metallicity gradient, while at higher redshifts, abundance gradients have been found to be flat, negative (Swinbank et al., 2012; Jones et al., 2013) as well as positive (Cresci et al., 2010; Queyrel et al., 2012; Stott et al., 2014).

The IFS analysis of a nearby BCD, NGC 4670, reveals the presence of four H II regions within this galaxy which had remained hidden even from the sharp eye of HST. The chemical maps (including O/H and N/O) of the region under study show signatures of inhomogeneities.

The IFS data of another BCD, SBS 1415+437, enabled "direct" mapping of the chemical abundances of not only the third most abundant element, oxygen, but also nitrogen, argon, sulphur and neon. A radial profile analysis following the distribution of Hα within the region of study does not show any significant trend, despite chemical abundance maps showing some variation.

Further analysis to confirm the signatures of chemical variation in these BCDs, is discussed later in Section 8.2.1.

2. *What is the main physical mechanism responsible for ionisation in the star-forming regions and surrounding gas?*

   By using emission line ratio diagnostic (BPT) diagrams, I found that photoionisation by young and massive stars in H II regions is the main physical mechanism responsible for ionisation in the star-forming regions and surrounding gas in two out of three analysed BCDs. There have been numerous studies on BCDs which report photoionisation as the dominant ionisation mechanism (see, e.g. James et al., 2009; James, Tsamis & Barlow, 2010; James et al., 2013a,b). In NGC 4449, some of the points lie above the maximum starburst line devised by Kewley et al. (2001) on the [S II]/Hα-BPT diagram, though no study reports the presence of AGN in this BCD. The spatially-resolved velocity structure in NGC 4449 shows the existence of internal kinematic disturbance, which indicates that shocks may also ionise the gas in BCDs.

3. *What is the age of the stellar population currently ionising the gas?*

   BCDs were initially thought to be young star-forming systems going through the first burst of star-formation. However, subsequent studies have shown the presence of older stellar populations (e.g. Aloisi et al., 2005). The age of the stellar

population can be determined using different methods including the use of colour-magnitude diagrams, Balmer absorption and emission lines. In this thesis, I used the evolutionary population synthesis models of STARBURST99 to map the age of the regions of study within BCDs. The central star-forming region of NGC 4449 hosts stellar populations (20–60 Myr) older than the other two BCDs ($\sim$ 10 Myr).

The identification of Wolf-Rayet (WR) features is also an indication of the young stellar population ($<$ 7 Myr). In NGC 4670, the IFS data revealed a WR region non-coincident with the four H II regions indicating the propagation of star-formation within this BCD. Both red and blue WR bumps were obviously visible in the spectrum of this region, which I modelled using a χ^2 minimisation method to find the number of different types of WR stars in this region. The number density of WR stars in the identified region is within the range reported for BCDs in the literature. No WR features were evident in the other two BCDs.

The answers to the above questions not only enhanced our knowledge of the physical properties specific to the analysed BCDs but also led to further inquests related to the physical phenomena which might be at play in these systems in particular or in star-forming systems in general.

- Chapter 3: The discovery of an inverse metallicity gradient in NGC 4449 suggests an interplay between star-formation, metallicity and gas dynamics - the three fundamental elements of galaxy formation and evolution. Though I discuss several scenarios which may explain the existence of such a gradient, the most plausible one is the accretion of metal-poor gas in the centre of this galaxy which will not only increase the star-formation but also decrease the metallicity of the ionised gas.
- Chapter 4: Using IFS data for NGC 4670, I studied the relationship between N/O versus O/H. It is an intensely debated topic as the relation behaves differently in different metallicity regimes because of the primary and secondary origins of nitrogen, unlike other elements. I discovered an unexpected negative trend in this relationship at the spatially-resolved scale for NGC 4670. I further analysed this relation by combining the IFS data of NGC 4670 with nine other BCDs, SDSS data of low-mass star-forming galaxies and the green pea galaxies. I proposed various scenarios including localised chemical enrichment, star-formation rate, varying star-formation efficiencies and hydrodynamical effects to explain the observed trend.
- Chapter 5: The IFS analysis of SBS 1415+437 shows that the spatially-resolved chemical abundances are in agreement with those obtained from the integrated spectrum of a star-forming system. This finding will allow for a direct comparison of

spatially-resolved, low-redshift analyses with high-redshift observations that lack spatial detail.

- Chapter 6 concerns the derivation of new metallicity calibrators for the diffuse ionised gas (DIG). For this purpose, I analysed the emission line maps of 24 nearby spiral galaxies obtained by processing MUSE data to answer the following questions:

  1. *How does the metallicity of DIG region compare with that of an adjacent HII region when estimated with standard strong line metallicity calibrator?*

     Using the emission line ratio diagnostic diagrams, I identified pairs of star-forming regions and associated DIG regions and studied the differential metallicities (Z_{DIG} - $Z_{H II}$) from widely-used calibrators Z[N2], Z[O3N2] and Z[N2S2Hα]. In this work, I demonstrate that Z[N2] overestimates the metallicity of a DIG-dominated region while Z[O3N2] underestimates it by $\sim$ 0.06 dex systematically compared to that of an H II region near the DIG-dominated region. Z[N2S2Hα] does not show any systematic offset. However, the standard deviation of differential metallicity is significant (i.e. $\sim$ 0.13) and the offset may be as high as $\pm$0.8 dex.

  2. *How can we robustly measure the metal-content of DIG-dominated regions within galaxies?*

     I studied the differential metallicity as a function of combinations of line ratios of DIG-dominated regions. Through a multi-regression analysis, I quantified the corrections needed to robustly estimate the metallicities of DIG-dominated region from Z[N2] and Z[O3N2]. After applying these corrections, there is no offset between the H II regions and DIG-dominated regions, and the dispersion observed in the differential metallicity in these calibrations is about a factor of 2 lower than that observed while using Z[N2S2Hα].

- Chapter 7 is solely dedicated to a study of the widely-accepted Schmidt Law of star-formation at sub-galactic scales of $\sim$0.5–2 kpcs. I studied nine nearby spiral galaxies using data from imaging surveys, which included KINGFISH and SINGS for optical, FUV and infrared data, THINGS for the atomic gas data and HERACLES for the molecular gas data. This work has been built upon the previous works of Kennicutt et al. (2007); Bigiel et al. (2008) and Liu et al. (2011) to answer the following questions:

  1. *How does the inclusion and removal of a diffuse background in the SFR tracers and atomic gas affect the spatially-resolved Schmidt relation?*

     This work has confirmed the hypothesis of Bigiel et al. (2008) that the inclusion of a diffuse background in SFR tracers results in a linear relation between the surface

densities of SFR and molecular gas, and its removal leads to a super-linear relation - a result which was found for a sample of two galaxies by Liu et al. (2011).

Though molecular gas has been considered the sole driver of star-formation at local sub-galactic scales, the role of atomic gas has been pointed to in both theoretical and observational studies. Hence, I also explore the total gas Schmidt relation, which is always super-linear irrespective of the removal of diffuse background. The striking discovery is the similarity of the slope of the Schmidt relation at global scales and the local scales when a diffuse background is subtracted from the atomic gas. Further studies need to be performed to confirm/discard this coincidence.

2. *Does the slope of the spatially-resolved Schmidt relation depend on the adopted methodology, pixel-by-pixel analysis or aperture photometry?*

   The general conclusions of my work using aperture photometry are in line with that from the pixel-by-pixel analyses of Bigiel et al. (2008) and Liu et al. (2011). This agreement shows that the slope of the spatially-resolved Schmidt relation is independent of the methodology employed. Though it might appear a simple question with a simple answer, it has important implications for the further analysis of this work. Aperture photometry is a rigorous analysis and cannot match the simplicity and time-saving capacity of pixel-by-pixel analysis. Hence, any further study can now be done via pixel-by-pixel analysis.

8.2 Future Prospects

8.2.1 Chemical inhomogeneities in BCDs

"Are BCDs chemically homogeneous?" – it is a long-standing question, and no single study has answered it entirely. As shown in Chapter 5, a radial profile analysis may average out the small scale variations. Hence a spaxel-by-spaxel analysis of chemical variation is required to explore chemical inhomogeneities. I am carrying out such a study on eight blue compact dwarfs listed in Table 8.1. Each of these BCDs or regions within them have been studied in detail in previous works, which will be helpful in finding the cause and effects of chemical inhomogeneity or otherwise.

As discussed in Chapter 3, the large-scale chemical variation within BCDs may be due to various factors, such as the accretion of metal-poor gas from a merger event or even from the cosmic web, loss of metal-rich gas via supernovae-driven blow-out or galactic winds, or accretion of metal-rich gas during tidal interactions. At small scales, chemical variation within BCDs may be caused by local pollution from the winds emanating from the WR stars as explained in Chapter 4. Thus the motion of gas regulates the metal distribution within BCDs.

Table 8.1 – Galaxy sample for inhomogeneity study

	BCD	RA(J2000)	Dec(J2000)	z	IFS instrument	Reference
1	Haro 11	00 36 52.489	-33 33 17.23	0.020598	VLT/FLAMES	James et al. (2013a)
2	Mrk 996	01 27 35.5	-06 19 36	0.005410	VLT/VIMOS	James et al. (2009)
3	UM 420	02 20 54.530	+00 33 24.46	0.058420	VLT/VIMOS	James, Tsamis & Barlow (2010)
4	UM 462	11 52 37.19	-02 28 09.9	0.003527	VLT/VIMOS	James, Tsamis & Barlow (2010)
5	UM 448	11 42 12.253	+00 20 03.68	0.018559	VLT/FLAMES	James et al. (2013b)
6	NGC 4449	12 28 11.118	+44 05 36.81	0.000690	GMOS	Kumari, James & Irwin (2017)
7	NGC 4670	12 45 17.150	+27 07 31.76	0.003566	GMOS	Kumari et al. (2018)
8	SBS 1415 + 437	14 17 01.4	+43 30 05	0.002031	GMOS	Kumari et al. 2018 (in prep.)

Hence, along with an IFS analysis of chemical variation in BCDs, it will be useful to study the neutral gas distribution and dynamics in and around BCDs. Though there have been detailed analyses of the H I gas content of BCDs (Hunter, van Woerden & Gallagher, 1996; Hunter et al., 1998; Thuan, Hibbard & Lévrier, 2004), these studies lack information related to the metallicity distribution and star formation, available through the optical IFS analyses. The Square Kilometer Array (SKA) will enable observations of H I 21 cm at a resolution of 0.2 arcsec (Huynh & Lazio, 2013, SKA1-Mid), which is comparable to that of current state-of-the-art integral field spectrograph MUSE. On the other hand, few studies report the detection of molecular gas in BCDs (Barone et al., 2000) despite the arguments about the significance of molecular gas in star-formation. Since BCDs are actively forming stars, it will be useful to probe the CO content of BCDs with the highly sensitive Atacama Large Millimeter Array (ALMA), which also allows observations at high angular resolution. A comprehensive investigation involving both neutral gas and ionised gas observations at comparable spatial scales in a large sample of BCDs would help us understand the interplay of gas dynamics, star-formation and metallicity in BCDs.

8.2.2 Negative trend of N/O versus O/H

One of the most important results of my thesis is the discovery of an unusual negative trend between N/O and O/H at the spatially-resolved scales in the BCD NGC 4670 (Chapter 4). The reason is that this discovery provides new avenues to explore the nucleosynthetic origin of nitrogen, both theoretically and observationally. For example, existing chemical evolution models are designed to consider galaxies rather than star-forming regions within BCDs. The IFS studies will benefit from the revised chemical evolution models, which include the detailed spatially-resolved astrophysical processes at play. Similarly, a study of this relationship is limited when direct method abundances are not available due to the lack of high S/N data. In that case, one can use indirect methods, most of which employ the use of nitrogen, except for recipes using R_{23}. Beside being degenerate, R_{23} is not useful when the [O II] $\lambda\lambda$3727,3729 doublet is beyond the spectral coverage of the IFS instrument (e.g. MUSE). So in such cases, one needs to rely on photoionisation models or the recipes involving the use of such models. Though sophis-

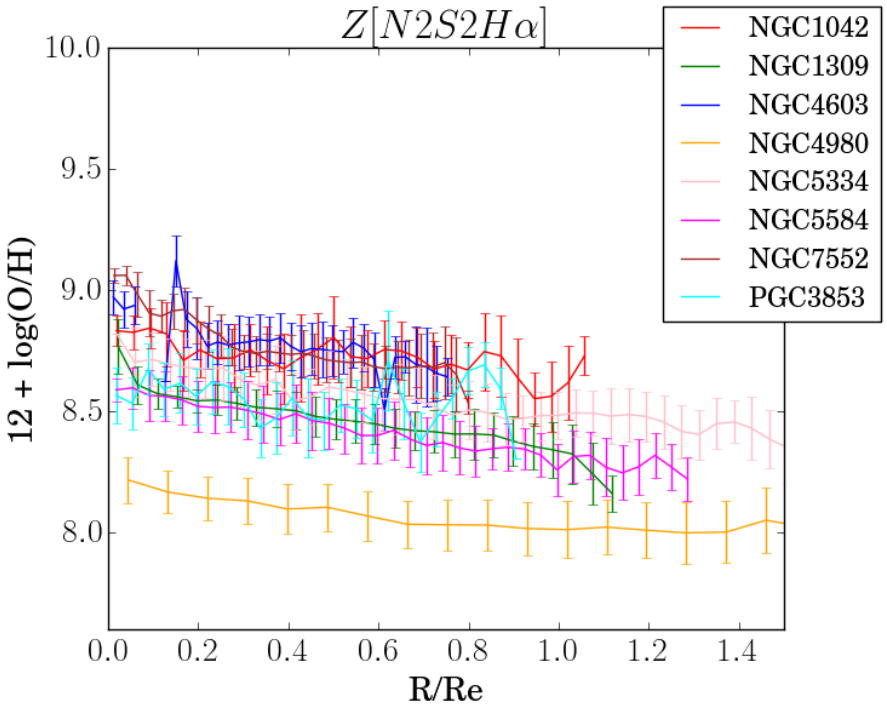

Figure 8.1 – Variation of metallicity determined from N2S2Hα with respect to radius normalised by the effective radius of each galaxy. These profiles are created by taking the median metallicity in radial bins of 2 arcsec (10 pixels on MUSE maps). Each colour represents a galaxy mentioned in the top-right box. The vertical bars denote the standard deviation of metallicites within a radial bin. The error bars on the medians are negligible by comparison, and therefore not shown here.

ticated photoionisation models (e.g. MOCASSIN) exist, their correct implementation depends on a proper characterization of the source under study, which may bias the derived quantities such as abundances or nitrogen-to-oxygen ratio. Lastly, further observational studies like the work on NGC 4670 in this thesis, are required for more BCDs and other low-mass star-forming galaxies. I will investigate a large sample of star-forming galaxies from the Mapping Nearby Galaxies at Apache Point Observatory (MaNGA) survey to find out if the unusual relation in NGC 4670 is specific to this BCD, or a common phenomenon at the spatially-resolved scale in BCDs, or if it can also be extended to other types of star-forming galaxies as well.

8.2.3 Metallicity gradients in star-forming galaxies

My overall work can be extended to study the metallicity gradients in star-forming galaxies, where chemical abundance maps are corrected for DIG content using the recipes presented in Chapter 6. Radial gradients in galaxies have been ascribed to various scenarios. For example, positive gradients suggest the inflow of metal-poor gas to the centre of galaxies triggered by mergers or cold-flows, while a negative radial gradient in non-interacting galaxies can be

explained by a scenario where galaxies form and grow inside-out (Pilkington et al., 2012). An azimuthal variation of metallicity may also exist in disc galaxies, since the time scale for oxygen production and mixing at sub-kiloparsec scales (<100 Myr, Roy & Kunth, 1995) is shorter than the time scale for differential rotation and therefore chemical mixing in the azimuthal direction ($\lesssim$1 Gyr, Ho et al., 2017).

To investigate the above-mentioned gradients, I have created emission line maps of eight galaxies on a spaxel-by-spaxel basis out of 24 spiral galaxies analysed in Chapter 6. Note that this mapping scheme is different from the Voronoi-binning done in Chapter 6. Figure 8.1 shows the radial metallicity profile of these galaxies, for which metallicity maps are created using the recipe N2S2Hα. I will utilise my correction recipes presented in Chapter 6, and redo these profiles using corrected Z[N2] and Z[O3N2] to find out the impact of the DIG correction term on the metal-distribution in spirals.

8.2.4 Star formation in atomic gas-dominated galaxies

In the Schmidt relation analysis in Chapter 7, the sample only included galaxies whose centres were dominated by molecular gas. However, a high star-formation rate has been observed in many galaxies which are mostly dominated by atomic gas (for example, the nearby spiral galaxy NGC 2403). The principal problem in studying the Schmidt relation in such galaxies is the insignificant detection of CO, which raises the question of whether these galaxies are devoid of molecular gas or if CO is not a good-enough tracer of the molecular gas present in these galaxies. To circumvent this problem, one can use dust as the tracer of the total gas column (see, e.g. Leroy et al., 2011; Sandstrom et al., 2013). Assuming that total gas is mainly composed of atomic and molecular gas and has a negligible contribution from ionised gas, dust emission (Σ_D) can be expressed as the sum of the atomic gas (Σ_{HI}) and molecular gas (Σ_{H2}) in the form of the equation: $\Sigma_D/DGR = \Sigma_{HI} + \Sigma_{H2}$, where DGR is the dust-to-gas ratio. Thus molecular gas surface density can be derived from dust maps of galaxies and their DGRs. The effect of a diffuse background can then be studied on the molecular gas and total gas Schmidt relations following the same procedure as Chapter 7.

8.3 Closing Remarks

This thesis has presented detailed analyses of nearby star-forming galaxies on spatial extents ranging from parsec to kiloparsec scales. These spatially-resolved studies have led to exciting discoveries, which will contribute to both observational and theoretical research in various sub-fields of astronomy, particularly stellar nucleosynthesis, the distribution and evolution of metals within galaxies, and star-formation.

Such findings will be very impactful given the technological advancements on the horizon.

The next decade will be marked by the commissioning of advanced IFS instruments such as WEAVE on William Herschel Telescope (WHT), the Keck Cosmic Web Imager (KCWI), and the largest space and ground-based telescopes ever made in history – the James Webb Space Telescope (JWST) and the European Extremely Large Telescope (EELT), respectively. Instruments such as WEAVE and KCWI have large field-of-view, which will enable mapping of the ionised gas content of an entire galaxy in a single pointing and will answer questions raised in this thesis on the distribution of elements within galaxies. Telescopes like JWST and EELT will provide an unprecedented view of the early Universe probing the first stars and galaxies, which will allow for a direct comparison of the properties of high-redshift star-forming galaxies and their local analogues. Instruments such as ALMA and SKA will prove to be complementary to the above facilities by probing the neutral gas content of star-forming galaxies. Thus, the wealth of information from these instruments will build upon the conclusions presented within this thesis and continue to further our understanding of galaxy formation and evolution.

Bibliography

Aggarwal K. M., Keenan F. P., 1999, ApJS, 123, 311

Allen D. A., 1976, MNRAS, 174, 29P

Allington-Smith J. et al., 2002, PASP, 114, 892

Allington-Smith J. R., Content R., Haynes R., Lewis I. J., 1997, in Proc. SPIE, Vol. 2871, Optical Telescopes of Today and Tomorrow, Ardeberg A. L., ed., pp. 1284–1294

Alloin D., Collin-Souffrin S., Joly M., Vigroux L., 1979, A&A, 78, 200

Aloisi A., van der Marel R. P., Mack J., Leitherer C., Sirianni M., Tosi M., 2005, ApJLett, 631, L45

Amorín R., Aguerri J. A. L., Muñoz-Tuñón C., Cairós L. M., 2009, A&A, 501, 75

Amorín R. et al., 2015, A&A, 578, A105

Amorín R., Pérez-Montero E., Vílchez J. M., Papaderos P., 2012a, ApJ, 749, 185

Amorín R., Vílchez J. M., Hägele G. F., Firpo V., Pérez-Montero E., Papaderos P., 2012b, ApJLett, 754, L22

Amorín R. O., Pérez-Montero E., Vílchez J. M., 2010, ApJLett, 715, L128

Ann H. B., Seo M., Ha D. K., 2015, ApJS, 217, 27

Annibali F., Aloisi A., Mack J., Tosi M., van der Marel R. P., Angeretti L., Leitherer C., Sirianni M., 2008, AJ, 135, 1900

Annibali F., Tosi M., Aloisi A., van der Marel R. P., 2011, AJ, 142, 129

Asplund M., Grevesse N., Sauval A. J., Scott P., 2009, ARA&A, 47, 481

Azeez J. H., Hwang C.-Y., Abidin Z. Z., Ibrahim Z. A., 2016, Scientific Reports, 6, 26896

Bacon R. et al., 1995, A&AS, 113, 347

Badenes C. et al., 2018, ApJ, 854, 147

Bajaja E., Huchtmeier W. K., Klein U., 1994, A&A, 285, 385

Baldwin J. A., Phillips M. M., Terlevich R., 1981, PASP, 93, 5

Barden S. C., Wade R. A., 1988, in Astronomical Society of the Pacific Conference Series, Vol. 3, Fiber Optics in Astronomy, Barden S. C., ed., pp. 113–124

Barone L. T., Heithausen A., Hüttemeister S., Fritz T., Klein U., 2000, MNRAS, 317, 649

Bayet E., Gerin M., Phillips T. G., Contursi A., 2009, MNRAS, 399, 264

Bekki K., 2008, MNRAS, 388, L10

Belfiore F. et al., 2016, MNRAS, 461, 3111
Belfiore F. et al., 2017, MNRAS, 469, 151
Bell E. F., de Jong R. S., 2000, MNRAS, 312, 497
Berg D. A., Skillman E. D., Croxall K. V., Pogge R. W., Moustakas J., Johnson-Groh M., 2015, ApJ, 806, 16
Berg D. A., Skillman E. D., Garnett D. R., Croxall K. V., Marble A. R., Smith J. D., Gordon K., Kennicutt, Jr. R. C., 2013, ApJ, 775, 128
Berg D. A. et al., 2012, ApJ, 754, 98
Bergvall N., Östlin G., 2002, A&A, 390, 891
Bigiel F., Leroy A., Walter F., Blitz L., Brinks E., de Blok W. J. G., Madore B., 2010, AJ, 140, 1194
Bigiel F., Leroy A., Walter F., Brinks E., de Blok W. J. G., Madore B., Thornley M. D., 2008, AJ, 136, 2846
Blanc G. A., Heiderman A., Gebhardt K., Evans, II N. J., Adams J., 2009, ApJ, 704, 842
Blanc G. A., Kewley L., Vogt F. P. A., Dopita M. A., 2015, ApJ, 798, 99
Boggs P. T., Byrd R. H., Rogers J. E., Schnabel R. B., 1992
Boissier S., Prantzos N., Boselli A., Gavazzi G., 2003, MNRAS, 346, 1215
Böker T., van der Marel R. P., Mazzuca L., Rix H.-W., Rudnick G., Ho L. C., Shields J. C., 2001, AJ, 121, 1473
Bolatto A. D., Wolfire M., Leroy A. K., 2013, ARA&A, 51, 207
Bomans D. J., Weis K., 2014, Astronomische Nachrichten, 335, 99
Boquien M., Buat V., Perret V., 2014, A&A, 571, A72
Boquien M. et al., 2016, A&A, 591, A6
Boselli A., Cortese L., Boquien M., Boissier S., Catinella B., Lagos C., Saintonge A., 2014, A&A, 564, A66
Brinchmann J., Kunth D., Durret F., 2008, A&A, 485, 657
Bromm V., Larson R. B., 2004, ARA&A, 42, 79
Buckalew B. A., Kobulnicky H. A., Dufour R. J., 2005, ApJS, 157, 30
Bundy K. et al., 2015, ApJ, 798, 7
Cairós L. M., Caon N., García Lorenzo B., Kelz A., Roth M., Papaderos P., Streicher O., 2012, A&A, 547, A24
Cairós L. M., Caon N., García-Lorenzo B., Monreal-Ibero A., Amorín R., Weilbacher P., Papaderos P., 2007, ApJ, 669, 251
Cairós L. M., Caon N., Vílchez J. M., González-Pérez J. N., Muñoz-Tuñón C., 2001a, ApJS, 136, 393
Cairós L. M., Caon N., Zurita C., Kehrig C., Weilbacher P., Roth M., 2009, A&A, 507, 1291
Cairós L. M., Vílchez J. M., González Pérez J. N., Iglesias-Páramo J., Caon N., 2001b, ApJS, 133, 321

Calzetti D., 2013, Star Formation Rate Indicators, Falcón-Barroso J., Knapen J. H., eds., p. 419
Calzetti D., Armus L., Bohlin R. C., Kinney A. L., Koornneef J., Storchi-Bergmann T., 2000, ApJ, 533, 682
Calzetti D. et al., 2007, ApJ, 666, 870
Calzetti D. et al., 2005, ApJ, 633, 871
Cantin S., Robert C., Mollá M., Pellerin A., 2010, MNRAS, 404, 811
Cappellari M., Copin Y., 2003, MNRAS, 342, 345
Cappellari M., Emsellem E., 2004, PASP, 116, 138
Cardamone C. et al., 2009, MNRAS, 399, 1191
Casasola V., Hunt L., Combes F., García-Burillo S., 2015, A&A, 577, A135
Catinella B. et al., 2010, MNRAS, 403, 683
Ceverino D., Sánchez Almeida J., Muñoz Tuñón C., Dekel A., Elmegreen B. G., Elmegreen D. M., Primack J., 2016, MNRAS, 457, 2605
Chabrier G., 2003, PASP, 115, 763
Chandar R., Leitherer C., Tremonti C. A., Calzetti D., Aloisi A., Meurer G. R., de Mello D., 2005, ApJ, 628, 210
Content R., 1997, in Proc. SPIE, Vol. 2871, Optical Telescopes of Today and Tomorrow, Ardeberg A. L., ed., pp. 1295–1305
Cortese L., Catinella B., Janowiecki S., 2017, ApJLett, 848, L7
Cox D. P., Smith B. W., 1974, ApJLett, 189, L105
Cresci G., Mannucci F., Maiolino R., Marconi A., Gnerucci A., Magrini L., 2010, Nature, 467, 811
Crocker A. F. et al., 2013, ApJ, 762, 79
Crowther P. A., Hadfield L. J., 2006, A&A, 449, 711
Curti M., Cresci G., Mannucci F., Marconi A., Maiolino R., Esposito S., 2017, MNRAS, 465, 1384
Dame T. M., Hartmann D., Thaddeus P., 2001, ApJ, 547, 792
Davé R., Finlator K., Oppenheimer B. D., 2011, MNRAS, 416, 1354
Davé R., Finlator K., Oppenheimer B. D., 2012, MNRAS, 421, 98
Davé R., Katz N., Oppenheimer B. D., Kollmeier J. A., Weinberg D. H., 2013, MNRAS, 434, 2645
Dekel A. et al., 2009, Nature, 457, 451
Denicoló G., Terlevich R., Terlevich E., 2002, MNRAS, 330, 69
Dopita M. A., Kewley L. J., Heisler C. A., Sutherland R. S., 2000, ApJ, 542, 224
Dopita M. A., Kewley L. J., Sutherland R. S., Nicholls D. C., 2016, Ap&SS, 361, 61
Dors O. L., Pérez-Montero E., Hägele G. F., Cardaci M. V., Krabbe A. C., 2016, MNRAS, 456, 4407
Draine B. T., 2011, Physics of the Interstellar and Intergalactic Medium

Draine B. T., Li A., 2007, ApJ, 657, 810
Edmunds M. G., 1990, MNRAS, 246, 678
Elmegreen B. G., 1994, ApJLett, 425, L73
Elmegreen D. M. et al., 2016, ApJ, 825, 145
Erb D. K., Shapley A. E., Pettini M., Steidel C. C., Reddy N. A., Adelberger K. L., 2006, ApJ, 644, 813
Evans, II N. J., 1999, ARA&A, 37, 311
Fanelli M. N., O'Connell R. W., Thuan T. X., 1988, ApJ, 334, 665
Ferguson A. M. N., Wyse R. F. G., Gallagher, III J. S., Hunter D. A., 1996, AJ, 111, 2265
Ferland G. J., Korista K. T., Verner D. A., Ferguson J. W., Kingdon J. B., Verner E. M., 1998, PASP, 110, 761
Ferland G. J. et al., 2013, Revista Mexicana de Astronoma y Astrofsica, 49, 137
Field G. B., Goldsmith D. W., Habing H. J., 1969, ApJLett, 155, L149
Fitzpatrick E. L., 1986, AJ, 92, 1068
Fitzpatrick E. L., 1999, PASP, 111, 63
Freeman K., Bland-Hawthorn J., 2002, ARA&A, 40, 487
Freudling W., Romaniello M., Bramich D. M., Ballester P., Forchi V., García-Dabló C. E., Moehler S., Neeser M. J., 2013, A&A, 559, A96
García-Benito R. et al., 2010, MNRAS, 408, 2234
Garnett D. R., 1990, ApJ, 363, 142
Garnett D. R., 1992, AJ, 103, 1330
Garnett D. R., Kennicutt, Jr. R. C., Bresolin F., 2004, ApJLett, 607, L21
Gelatt A. E., Hunter D. A., Gallagher J. S., 2001, PASP, 113, 142
Gil de Paz A. et al., 2007, ApJS, 173, 185
Gil de Paz A., Madore B. F., Pevunova O., 2003, ApJS, 147, 29
Glover S., 2005, Space Sci. Rev., 117, 445
Glover S. C. O., Clark P. C., 2012, MNRAS, 421, 9
Goodman A. A., Rosolowsky E. W., Borkin M. A., Foster J. B., Halle M., Kauffmann J., Pineda J. E., 2009, Nature, 457, 63
Gordon K. D., Clayton G. C., Witt A. N., Misselt K. A., 2000, ApJ, 533, 236
Gordon K. D. et al., 2005, PASP, 117, 503
Green A. W. et al., 2017, ArXiv e-prints
Guseva N. G., Izotov Y. I., Stasińska G., Fricke K. J., Henkel C., Papaderos P., 2011, A&A, 529, A149
Guseva N. G., Papaderos P., Izotov Y. I., Green R. F., Fricke K. J., Thuan T. X., Noeske K. G., 2003, A&A, 407, 105
Haffner L. M., Reynolds R. J., Tufte S. L., 1999, ApJ, 523, 223
Hägele G. F., Díaz Á. I., Terlevich E., Terlevich R., Pérez-Montero E., Cardaci M. V., 2008,

MNRAS, 383, 209
Hägele G. F., Firpo V., Bosch G., Díaz Á. I., Morrell N., 2012, MNRAS, 422, 3475
Hägele G. F., Pérez-Montero E., Díaz Á. I., Terlevich E., Terlevich R., 2006, MNRAS, 372, 293
Henry R. B. C., Edmunds M. G., Köppen J., 2000, ApJ, 541, 660
Henry R. B. C., Worthey G., 1999, PASP, 111, 919
Heyer M. H., Corbelli E., Schneider S. E., Young J. S., 2004, ApJ, 602, 723
Hill R. S. et al., 1998, ApJ, 507, 179
Hirashita H., Tajiri Y. Y., Kamaya H., 2002, A&A, 388, 439
Ho I.-T., Kudritzki R.-P., Kewley L. J., Zahid H. J., Dopita M. A., Bresolin F., Rupke D. S. N., 2015, MNRAS, 448, 2030
Ho I.-T. et al., 2017, ApJ, 846, 39
Hong S., Calzetti D., Gallagher, III J. S., Martin C. L., Conselice C. J., Pellerin A., 2013, ApJ, 777, 63
Hook I. M., Jørgensen I., Allington-Smith J. R., Davies R. L., Metcalfe N., Murowinski R. G., Crampton D., 2004, PASP, 116, 425
Hopkins A. M., Schulte-Ladbeck R. E., Drozdovsky I. O., 2002, AJ, 124, 862
Hubble E. P., 1936, Realm of the Nebulae
Huchra J. P., Geller M. J., Gallagher J., Hunter D., Hartmann L., Fabbiano G., Aaronson M., 1983, ApJ, 274, 125
Hunter D. A., Gallagher, III J. S., 1997, ApJ, 475, 65
Hunter D. A., Thronson, Jr. H. A., 1995, ApJ, 452, 238
Hunter D. A., van Woerden H., Gallagher, III J. S., 1996, ApJS, 107, 739
Hunter D. A., Wilcots E. M., van Woerden H., Gallagher J. S., Kohle S., 1998, ApJLett, 495, L47
Huynh M., Lazio J., 2013, ArXiv e-prints
Iono D. et al., 2009, ApJ, 695, 1537
Izotov Y. I., Guseva N. G., Fricke K. J., Papaderos P., 2009, A&A, 503, 61
Izotov Y. I., Stasińska G., Meynet G., Guseva N. G., Thuan T. X., 2006, A&A, 448, 955
Izotov Y. I., Thuan T. X., 1998, ApJ, 500, 188
Izotov Y. I., Thuan T. X., 1999, ApJ, 511, 639
Izotov Y. I., Thuan T. X., 2004, ApJ, 602, 200
Izotov Y. I., Thuan T. X., 2016, MNRAS, 457, 64
Izotov Y. I., Thuan T. X., Lipovetsky V. A., 1994, ApJ, 435, 647
James B. L., Aloisi A., Heckman T., Sohn S. T., Wolfe M. A., 2014, ApJ, 795, 109
James B. L., Auger M., Aloisi A., Calzetti D., Kewley L., 2016, ApJ, 816, 40
James B. L., Koposov S., Stark D. P., Belokurov V., Pettini M., Olszewski E. W., 2015, MNRAS, 448, 2687
James B. L., Koposov S. E., Stark D. P., Belokurov V., Pettini M., Olszewski E. W., McQuinn

K. B. W., 2017, MNRAS, 465, 3977
James B. L., Tsamis Y. G., Barlow M. J., 2010, MNRAS, 401, 759
James B. L., Tsamis Y. G., Barlow M. J., Walsh J. R., Westmoquette M. S., 2013a, MNRAS, 428, 86
James B. L., Tsamis Y. G., Barlow M. J., Westmoquette M. S., Walsh J. R., Cuisinier F., Exter K. M., 2009, MNRAS, 398, 2
James B. L., Tsamis Y. G., Walsh J. R., Barlow M. J., Westmoquette M. S., 2013b, MNRAS, 430, 2097
Janowiecki S., Salzer J. J., 2014, ApJ, 793, 109
Jaskot A. E., Oey M. S., 2013, ApJ, 766, 91
Johnson B. D. et al., 2013, ApJ, 772, 8
Jones T., Ellis R. S., Richard J., Jullo E., 2013, ApJ, 765, 48
Kaplan K. F. et al., 2016, MNRAS, 462, 1642
Karczewski O. Ł. et al., 2013, MNRAS, 431, 2493
Kauffmann G. et al., 2003, MNRAS, 346, 1055
Kay S. T., Pearce F. R., Frenk C. S., Jenkins A., 2002, MNRAS, 330, 113
Kehrig C. et al., 2013, MNRAS, 432, 2731
Kehrig C. et al., 2016, MNRAS, 459, 2992
Kehrig C., Vílchez J. M., Sánchez S. F., Telles E., Pérez-Montero E., Martín-Gordón D., 2008, A&A, 477, 813
Kennicutt R. C. et al., 2011, PASP, 123, 1347
Kennicutt R. C., Evans N. J., 2012, ARA&A, 50, 531
Kennicutt, Jr. R. C., 1984, ApJ, 287, 116
Kennicutt, Jr. R. C., 1998a, ARA&A, 36, 189
Kennicutt, Jr. R. C., 1998b, ApJ, 498, 541
Kennicutt, Jr. R. C., 2008, in Astronomical Society of the Pacific Conference Series, Vol. 390, Pathways Through an Eclectic Universe, Knapen J. H., Mahoney T. J., Vazdekis A., eds., p. 149
Kennicutt, Jr. R. C. et al., 2003, PASP, 115, 928
Kennicutt, Jr. R. C. et al., 2007, ApJ, 671, 333
Kennicutt, Jr. R. C. et al., 2009, ApJ, 703, 1672
Kewley L. J., Dopita M. A., 2002, ApJS, 142, 35
Kewley L. J., Dopita M. A., Sutherland R. S., Heisler C. A., Trevena J., 2001, ApJ, 556, 121
Kewley L. J., Ellison S. L., 2008, ApJ, 681, 1183
Kewley L. J., Groves B., Kauffmann G., Heckman T., 2006, MNRAS, 372, 961
Kewley L. J., Rupke D., Zahid H. J., Geller M. J., Barton E. J., 2010, ApJLett, 721, L48
Kingsburgh R. L., Barlow M. J., 1994, MNRAS, 271, 257
Kirshner R. P., Blair W. P., 1980, ApJ, 236, 135

Kniazev A. Y., Grebel E. K., Hao L., Strauss M. A., Brinkmann J., Fukugita M., 2003, ApJLett, 593, L73
Kobulnicky H. A., Kennicutt, Jr. R. C., Pizagno J. L., 1999, ApJ, 514, 544
Kobulnicky H. A., Kewley L. J., 2004, ApJ, 617, 240
Kobulnicky H. A., Skillman E. D., 1996, ApJ, 471, 211
Kobulnicky H. A., Skillman E. D., Roy J.-R., Walsh J. R., Rosa M. R., 1997, ApJ, 477, 679
Komugi S., Sofue Y., Nakanishi H., Onodera S., Egusa F., 2005, PASJ, 57, 733
Köppen J., Hensler G., 2005, A&A, 434, 531
Kritsuk A. G., Ustyugov S. D., Norman M. L., 2011, in IAU Symposium, Vol. 270, Computational Star Formation, Alves J., Elmegreen B. G., Girart J. M., Trimble V., eds., pp. 179–186
Kroupa P., 2001, in Astronomical Society of the Pacific Conference Series, Vol. 228, Dynamics of Star Clusters and the Milky Way, Deiters S., Fuchs B., Just A., Spurzem R., Wielen R., eds., p. 187
Kroupa P., Tout C. A., Gilmore G., 1993, MNRAS, 262, 545
Krumholz M. R., 2012, ApJ, 759, 9
Krumholz M. R., 2014, Phys. Rep., 539, 49
Kumari N., James B. L., Irwin M. J., 2017, MNRAS, 470, 4618
Kumari N., James B. L., Irwin M. J., Amorín R., Pérez-Montero E., 2018, MNRAS, 476, 3793
Kunth D., Östlin G., 2000, A&A Rev., 10, 1
Lagos P., Demarco R., Papaderos P., Telles E., Nigoche-Netro A., Humphrey A., Roche N., Gomes J. M., 2016, MNRAS, 456, 1549
Lagos P., Papaderos P., Gomes J. M., Smith Castelli A. V., Vega L. R., 2014, A&A, 569, A110
Lagos P., Telles E., Nigoche Netro A., Carrasco E. R., 2012, MNRAS, 427, 740
Leitherer C., Heckman T. M., 1995, ApJS, 96, 9
Leitherer C., Ortiz Otálvaro P. A., Bresolin F., Kudritzki R.-P., Lo Faro B., Pauldrach A. W. A., Pettini M., Rix S. A., 2010, ApJS, 189, 309
Leitherer C. et al., 1999, ApJS, 123, 3
Lelli F., Verheijen M., Fraternali F., 2014, A&A, 566, A71
Lequeux J., Peimbert M., Rayo J. F., Serrano A., Torres-Peimbert S., 1979, A&A, 80, 155
Leroy A. K. et al., 2012, AJ, 144, 3
Leroy A. K. et al., 2011, ApJ, 737, 12
Leroy A. K. et al., 2009, AJ, 137, 4670
Leroy A. K., Walter F., Brinks E., Bigiel F., de Blok W. J. G., Madore B., Thornley M. D., 2008, AJ, 136, 2782
Leroy A. K. et al., 2013, AJ, 146, 19
Levesque E. M., Leitherer C., 2013, ApJ, 779, 170
Li H.-B., Goodman A., Sridharan T. K., Houde M., Li Z.-Y., Novak G., Tang K. S., 2014, Protostars and Planets VI, 101

Li Y., Bresolin F., Kennicutt, Jr. R. C., 2013, ApJ, 766, 17
Lian J., Hu N., Fang G., Ye C., Kong X., 2016, ApJ, 819, 73
Lilly S. J., Carollo C. M., Pipino A., Renzini A., Peng Y., 2013, ApJ, 772, 119
Lind K., Charbonnel C., Decressin T., Primas F., Grundahl F., Asplund M., 2011, A&A, 527, A148
Liu G., Koda J., Calzetti D., Fukuhara M., Momose R., 2011, ApJ, 735, 63
Liu X.-W., Danziger J., 1993, MNRAS, 263, 256
Lonsdale Persson C. J., Helou G., 1987, ApJ, 314, 513
López-Hernández J., Terlevich E., Terlevich R., Rosa-González D., Díaz Á., García-Benito R., Vílchez J., Hägele G., 2013, MNRAS, 430, 472
López-Sánchez Á. R., Dopita M. A., Kewley L. J., Zahid H. J., Nicholls D. C., Scharwächter J., 2012a, MNRAS, 426, 2630
López-Sánchez Á. R., Esteban C., 2010, A&A, 517, A85
López-Sánchez Á. R., Esteban C., García-Rojas J., Peimbert M., Rodríguez M., 2007, ApJ, 656, 168
López-Sánchez Á. R., Koribalski B. S., van Eymeren J., Esteban C., Kirby E., Jerjen H., Lonsdale N., 2012b, MNRAS, 419, 1051
López-Sánchez Á. R., Mesa-Delgado A., López-Martín L., Esteban C., 2011, MNRAS, 411, 2076
Ly C., Malhotra S., Malkan M. A., Rigby J. R., Kashikawa N., de los Reyes M. A., Rhoads J. E., 2016, ApJS, 226, 5
Mac Low M.-M., Ferrara A., 1999, ApJ, 513, 142
Mac Low M.-M., Klessen R. S., 2004, Reviews of Modern Physics, 76, 125
Madau P., Dickinson M., 2014, ARA&A, 52, 415
Madore B. F., 1977, MNRAS, 178, 1
Madsen G. J., Reynolds R. J., Haffner L. M., 2006, ApJ, 652, 401
Magdis G. E. et al., 2016, MNRAS, 456, 4533
Maiolino R. et al., 2008, A&A, 488, 463
Mannucci F., Cresci G., Maiolino R., Marconi A., Gnerucci A., 2010, MNRAS, 408, 2115
Marino R. A. et al., 2013, A&A, 559, A114
Marri S., White S. D. M., 2003, MNRAS, 345, 561
Martin C. L., 1997, ApJ, 491, 561
Martínez-Delgado D. et al., 2012, ApJLett, 748, L24
Mas-Hesse J. M., Kunth D., 1999, A&A, 349, 765
Massey P., 2003, ARA&A, 41, 15
Matteucci F., 2003, The Chemical Evolution of the Galaxy
Matteucci F., 2012, Chemical Evolution of Galaxies
McCall M. L., Rybski P. M., Shields G. A., 1985, ApJS, 57, 1

McGaugh S. S., 1991, ApJ, 380, 140
McKee C. F., Ostriker E. C., 2007, ARA&A, 45, 565
McKee C. F., Ostriker J. P., 1977, ApJ, 218, 148
McQuinn K. B. W. et al., 2010, ApJ, 721, 297
Meurer G. R., Freeman K. C., Dopita M. A., Cacciari C., 1992, AJ, 103, 60
Meynet G., 1995, A&A, 298, 767
Meynet G., Maeder A., 2005, A&A, 429, 581
Michałowski M. J. et al., 2015, A&A, 582, A78
Milisavljevic D., Fesen R. A., 2008, ApJ, 677, 306
Minniti D., Zoccali M., 2008, in IAU Symposium, Vol. 245, Formation and Evolution of Galaxy Bulges, Bureau M., Athanassoula E., Barbuy B., eds., pp. 323–332
Mollá M., Cavichia O., Gavilán M., Gibson B. K., 2015, MNRAS, 451, 3693
Mollá M., García-Vargas M. L., Bressan A., 2009, MNRAS, 398, 451
Mollá M., Gavilán M., 2010, Mem. Soc. Astron. Ital., 81, 992
Mollá M., Vílchez J. M., Gavilán M., Díaz A. I., 2006, MNRAS, 372, 1069
Momose R. et al., 2013, ApJLett, 772, L13
Monreal-Ibero A., Relaño M., Kehrig C., Pérez-Montero E., Vílchez J. M., Kelz A., Roth M. M., Streicher O., 2011, MNRAS, 413, 2242
Monreal-Ibero A., Walsh J. R., Vílchez J. M., 2012, A&A, 544, A60
Morokuma-Matsui K., Muraoka K., 2017, ApJ, 837, 137
Morrissey P. et al., 2005, ApJLett, 619, L7
Nagao T., Maiolino R., Marconi A., 2006, A&A, 459, 85
Narayanan D., Cox T. J., Shirley Y., Davé R., Hernquist L., Walker C. K., 2008, ApJ, 684, 996
Narayanan D., Krumholz M. R., Ostriker E. C., Hernquist L., 2012, MNRAS, 421, 3127
Nicholls D. C., Dopita M. A., Sutherland R. S., Jerjen H., Kewley L. J., Basurah H., 2014, ApJ, 786, 155
Nicholls D. C., Dopita M. A., Sutherland R. S., Kewley L. J., Palay E., 2013, ApJS, 207, 21
Oey M. S. et al., 2007, ApJ, 661, 801
Oey M. S., Shields J. C., 2000, ApJ, 539, 687
Olmo-García A., Sánchez Almeida J., Muñoz-Tuñón C., Filho M. E., Elmegreen B. G., Elmegreen D. M., Pérez-Montero E., Méndez-Abreu J., 2017, ApJ, 834, 181
Osterbrock D. E., Ferland G. J., 2006a, Astrophysics of gaseous nebulae and active galactic nuclei
Osterbrock D. E., Ferland G. J., 2006b, Astrophysics of gaseous nebulae and active galactic nuclei
Ott J., Walter F., Brinks E., 2005, MNRAS, 358, 1453
Pagel B. E. J., 1997, Nucleosynthesis and Chemical Evolution of Galaxies. p. 392
Pagel B. E. J., Edmunds M. G., Blackwell D. E., Chun M. S., Smith G., 1979, MNRAS, 189,

95
Papaderos P., Izotov Y. I., Fricke K. J., Thuan T. X., Guseva N. G., 1998, A&A, 338, 43
Papaderos P., Loose H.-H., Fricke K. J., Thuan T. X., 1996a, A&A, 314, 59
Papaderos P., Loose H.-H., Thuan T. X., Fricke K. J., 1996b, A&AS, 120, 207
Peimbert A., Peimbert M., 2005, in Revista Mexicana de Astronomia y Astrofisica Conference Series, Vol. 23, Revista Mexicana de Astronomia y Astrofisica Conference Series, Torres-Peimbert S., MacAlpine G., eds., pp. 9–14
Peimbert A., Peimbert M., 2013, ApJ, 778, 89
Peimbert M., Peimbert A., Delgado-Inglada G., 2017, PASP, 129, 082001
Pérez-Montero E., 2014, MNRAS, 441, 2663
Pérez-Montero E., 2017, PASP, 129, 043001
Pérez-Montero E., Contini T., 2009, MNRAS, 398, 949
Pérez-Montero E., Hägele G. F., Contini T., Díaz Á. I., 2007, MNRAS, 381, 125
Pérez-Montero E., Kehrig C., Brinchmann J., Vílchez J. M., Kunth D., Durret F., 2013, Advances in Astronomy, 2013, 837392
Pérez-Montero E. et al., 2011, A&A, 532, A141
Pettini M., Pagel B. E. J., 2004, MNRAS, 348, L59
Pettini M., Zych B. J., Steidel C. C., Chaffee F. H., 2008, MNRAS, 385, 2011
Pilkington K. et al., 2012, A&A, 540, A56
Pilyugin L. S., Thuan T. X., 2005, ApJ, 631, 231
Porter R. L., Ferland G. J., Storey P. J., Detisch M. J., 2013, MNRAS, 433, L89
Pradhan A. K., Montenegro M., Nahar S. N., Eissner W., 2006, MNRAS, 366, L6
Prescott M. K. M. et al., 2007, ApJ, 668, 182
Prevot M. L., Lequeux J., Prevot L., Maurice E., Rocca-Volmerange B., 1984, A&A, 132, 389
Queyrel J. et al., 2012, A&A, 539, A93
Rahman N. et al., 2011, ApJ, 730, 72
Rahman N. et al., 2012, ApJ, 745, 183
Reynolds R. J., 1984, ApJ, 282, 191
Reynolds R. J., 1990, ApJLett, 349, L17
Ricciardelli E., Vazdekis A., Cenarro A. J., Falcón-Barroso J., 2012, MNRAS, 424, 172
Rossa J., Dettmar R.-J., 2003a, A&A, 406, 493
Rossa J., Dettmar R.-J., 2003b, A&A, 406, 505
Roy J.-R., Boulesteix J., Joncas G., Grundseth B., 1991, ApJ, 367, 141
Roy J.-R., Kunth D., 1995, A&A, 294, 432
Roychowdhury S., Chengalur J. N., Chiboucas K., Karachentsev I. D., Tully R. B., Kaisin S. S., 2012, MNRAS, 426, 665
Roychowdhury S., Huang M.-L., Kauffmann G., Wang J., Chengalur J. N., 2015, MNRAS, 449, 3700

Russell S. C., Dopita M. A., 1992, ApJ, 384, 508
Sage L. J., Salzer J. J., Loose H.-H., Henkel C., 1992, A&A, 265, 19
Saintonge A. et al., 2011, MNRAS, 415, 32
Salpeter E. E., 1955, ApJ, 121, 161
Sánchez S. F. et al., 2012, A&A, 538, A8
Sánchez S. F. et al., 2014, A&A, 563, A49
Sánchez S. F., Rosales-Ortega F. F., Kennicutt R. C., Johnson B. D., Diaz A. I., Pasquali A., Hao C. N., 2011, MNRAS, 410, 313
Sánchez Almeida J., Elmegreen B. G., Muñoz-Tuñón C., Elmegreen D. M., 2014a, A&A Rev., 22, 71
Sánchez Almeida J. et al., 2015, ApJLett, 810, L15
Sánchez Almeida J., Morales-Luis A. B., Muñoz-Tuñón C., Elmegreen D. M., Elmegreen B. G., Méndez-Abreu J., 2014b, ApJ, 783, 45
Sánchez Almeida J., Muñoz-Tuñón C., Elmegreen D. M., Elmegreen B. G., Méndez-Abreu J., 2013, ApJ, 767, 74
Sanders R. L., Shapley A. E., Zhang K., Yan R., 2017, ApJ, 850, 136
Sandstrom K. M. et al., 2013, ApJ, 777, 5
Sargent W. L. W., Searle L., 1970, ApJLett, 162, L155
Schaerer D., Contini T., Kunth D., 1999, A&A, 341, 399
Schaye J., Dalla Vecchia C., 2008, MNRAS, 383, 1210
Schlafly E. F., Finkbeiner D. P., 2011, ApJ, 737, 103
Schmutz W., Vacca W. D., 1999, New Astronomy, 4, 197
Schneider S. E., Thuan T. X., Mangum J. G., Miller J., 1992, ApJS, 81, 5
Schruba A. et al., 2011, AJ, 142, 37
Schuster K. F., Kramer C., Hitschfeld M., Garcia-Burillo S., Mookerjea B., 2007, A&A, 461, 143
Seaquist E. R., Bignell R. C., 1978, ApJLett, 226, L5
Searle L., Sargent W. L. W., 1972a, ApJ, 173, 25
Searle L., Sargent W. L. W., 1972b, ApJ, 173, 25
Seaton M. J., 1979, MNRAS, 187, 73P
Shetty R., Clark P. C., Klessen R. S., 2014, MNRAS, 442, 2208
Shetty R., Kelly B. C., Bigiel F., 2013, MNRAS, 430, 288
Shetty R., Kelly B. C., Rahman N., Bigiel F., Bolatto A. D., Clark P. C., Klessen R. S., Konstandin L. K., 2014, MNRAS, 437, L61
Shim H., Chary R.-R., Dickinson M., Lin L., Spinrad H., Stern D., Yan C.-H., 2011, ApJ, 738, 69
Shu F. H., Adams F. C., Lizano S., 1987, ARA&A, 25, 23
Sokal K. R., Johnson K. E., Indebetouw R., Reines A. E., 2015, AJ, 149, 115

Stasińska G., 1978, A&A, 66, 257
Stasińska G., 2002, in Revista Mexicana de Astronomia y Astrofisica Conference Series, Vol. 12, Revista Mexicana de Astronomia y Astrofisica Conference Series, Henney W. J., Franco J., Martos M., eds., pp. 62–69
Stasińska G., 2005, A&A, 434, 507
Stasińska G., 2006, A&A, 454, L127
Stasińska G., Izotov Y., Morisset C., Guseva N., 2015, A&A, 576, A83
Steigman G., 2007, Annual Review of Nuclear and Particle Science, 57, 463
Storchi-Bergmann T., Calzetti D., Kinney A. L., 1994, ApJ, 429, 572
Storey P. J., Sochi T., Bastin R., 2017, MNRAS, 470, 379
Stott J. P. et al., 2014, MNRAS, 443, 2695
Summers L. K., Stevens I. R., Strickland D. K., Heckman T. M., 2003, MNRAS, 342, 690
Sutherland R. S., Dopita M. A., 1993, ApJS, 88, 253
Swinbank A. M., Sobral D., Smail I., Geach J. E., Best P. N., McCarthy I. G., Crain R. A., Theuns T., 2012, MNRAS, 426, 935
Tan J. C., 2000, ApJ, 536, 173
Tasker E. J., Bryan G. L., 2006, ApJ, 641, 878
Tayal S. S., 2007, ApJS, 171, 331
Thacker R. J., Couchman H. M. P., 2000, ApJ, 545, 728
Theis C., Kohle S., 2001, A&A, 370, 365
Thilker D. A., Braun R., Walterbos R. A. M., 2000, AJ, 120, 3070
Thronson, Jr. H. A., Hunter D. A., Telesco C. M., Harper D. A., Decher R., 1987, ApJ, 317, 180
Thuan T. X., 2008, in IAU Symposium, Vol. 255, Low-Metallicity Star Formation: From the First Stars to Dwarf Galaxies, Hunt L. K., Madden S. C., Schneider R., eds., pp. 348–360
Thuan T. X., Hibbard J. E., Lévrier F., 2004, AJ, 128, 617
Thuan T. X., Izotov Y. I., Foltz C. B., 1999, ApJ, 525, 105
Thuan T. X., Izotov Y. I., Lipovetsky V. A., 1995, ApJ, 445, 108
Thuan T. X., Martin G. E., 1981, ApJ, 247, 823
Tremonti C. A., Calzetti D., Leitherer C., Heckman T. M., 2001, ApJ, 555, 322
Tremonti C. A. et al., 2004, ApJ, 613, 898
Vale Asari N., Stasińska G., Morisset C., Cid Fernandes R., 2016, MNRAS, 460, 1739
van Zee L., Haynes M. P., 2006, ApJ, 636, 214
van Zee L., Salzer J. J., Haynes M. P., 1998, ApJLett, 497, L1
Vazdekis A., Ricciardelli E., Cenarro A. J., Rivero-González J. G., Díaz-García L. A., Falcón-Barroso J., 2012, MNRAS, 424, 157
Verley S., Corbelli E., Giovanardi C., Hunt L. K., 2009, A&A, 493, 453
Vila Costas M. B., Edmunds M. G., 1993, MNRAS, 265, 199
Vílchez J. M., Iglesias-Páramo J., 1998, ApJ, 508, 248

Vincenzo F., Belfiore F., Maiolino R., Matteucci F., Ventura P., 2016, MNRAS, 458, 3466
Voges E. S., Walterbos R. A. M., 2006, ApJLett, 644, L29
Walter F., Brinks E., de Blok W. J. G., Bigiel F., Kennicutt, Jr. R. C., Thornley M. D., Leroy A., 2008, AJ, 136, 2563
Wang L.-L. et al., 2018, Monthly Notices of the Royal Astronomical Society, 474, 1873
Ward-Thompson D., Fraser H., Rawlings J., 2002, Astronomy and Geophysics, 43, 4.26
Werk J. K., Putman M. E., Meurer G. R., Thilker D. A., Allen R. J., Bland-Hawthorn J., Kravtsov A., Freeman K., 2010, ApJ, 715, 656
Westmoquette M. S., James B., Monreal-Ibero A., Walsh J. R., 2013, A&A, 550, A88
Wisnioski E. et al., 2015, ApJ, 799, 209
Wolfinger K., Kilborn V. A., Koribalski B. S., Minchin R. F., Boyce P. J., Disney M. J., Lang R. H., Jordan C. A., 2013, MNRAS, 428, 1790
Wong T., Blitz L., 2002, ApJ, 569, 157
Woosley S. E., Weaver T. A., 1995, ApJS, 101, 181
Wu Y., Charmandaris V., Hao L., Brandl B. R., Bernard-Salas J., Spoon H. W. W., Houck J. R., 2006, ApJ, 639, 157
Zaritsky D., Kennicutt, Jr. R. C., Huchra J. P., 1994, ApJ, 420, 87
Zhang K. et al., 2017, MNRAS, 466, 3217
Zinchenko I. A., Pilyugin L. S., Grebel E. K., Sánchez S. F., Vílchez J. M., 2016, MNRAS, 462, 2715
Zinnecker H., Yorke H. W., 2007, ARA&A, 45, 481